Dust and molecules in interstellar, circumstellar and extragalactic environments

Arfon McIndoe Smith

Thesis submitted to The University of Nottingham
for the degree of Doctor of Philosophy

September 2006

Abstract

Small-scale-structure variations in diffuse interstellar band strengths have been detected towards the ρ Ophiuchus complex of stars. Variations of $\sim$ 400 AU in the blue DIBs (λ < 5700 Å) have been detected for the first time with differences detected in eight of the ten bands analysed. Follow-up observations of the yellow/red diffuse bands (λ > 5700 Å) have confirmed the result of Cordiner (2005) and variations in the majority of the bands analysed. A comparison of the diffuse band variations over a 10 month timescale has been made with tentative evidence presented for tiny-scale-structure variations of the order of $\sim$ 3 AU. The behaviour of the diffuse bands with respect to each other and with atomic and molecular data from Pan *et al.* (2004) has been analysed; the results presented here, in some cases, conflicting with established diffuse band family classifications.

An investigation of diffuse band strengths in a selection of redshifted ($z \lesssim 0.5$) quasar absorption lines-of-sight has been made. Using the relationship between E_{B-V} and diffuse band strength in the Galaxy and the Magellanic Clouds, an attempt has been made to detect the diffuse band carriers at cosmological distances. Preliminary results are presented for five absorbers with a non-detection in all cases. Early analysis suggests that the diffuse band strengths are significantly lower than predicted suggesting that local diffuse band correlations may not be universal.

A search of infrared catalogues has been made for evolved stars with dusty discs. Prompted by the discovery of a selection of exotic evolved stars (e.g. Lloyd Evans 1997b), an automated search of the IRAS and 2MASS catalogues has been made based upon near-IR and mid-IR colours. By refining the selection criteria used and making use of the digitised sky survey images available, the success rate for detecting unusual stars has been significantly improved. Spectra have been recorded for over ninety targets; a summary of the stars and examples of their spectra is presented.

Acknowledgements

Firstly I'd like to thank my family and friends for their support and encouragement throughout my PhD. During my time in Nottingham I have had the opportunity to meet some truly amazing people and do some amazing things including marrying Laura! Your love and support has made the PhD process a much easier one. Thanks to Mark and Zoë for putting me up and making me feel at home during visits to Nottingham. Thanks to all the people in Nottingham chemistry that made lunchtimes fun and coffee breaks last too long. In no particular order, Dave, James, Ross, Phil, In-Ok, Tim, Darragh, Andy, Richard, Ben and anyone else I've forgotten....

Thanks to Peter Sarre for being an inspirational and ever enthusiastic supervisor and providing endless opportunities to visit far-away lands. Thanks to June McCombie for her friendship, scientific support and endless coffee breaks as well as some very fine cuisine! Thanks to all the past and present members of the Nottingham astrochemistry group for great office company, in particular my great friends Rad and Martin. Thanks to Steve Fossey for his excellent company on both AAT observing runs and his seemingly endless knowledge of all things astronomical. Thanks to Tom Lloyd Evans for his wisdom, scientific guidance and company whilst observing. Special thanks to Michael Murphy for introducing me to the early universe and helping to turn an idea into reality. Extra special very last minute thanks goes to Matt for his kind lend of the trusty G4 Powerbook in my hour of need - thanks man! I'd also like to thank Mike Merrifield, Alfonso Aragón-Salamanca and Steve Maddox of the Physics and Astronomy department for offering scientific advice and guidance.

Contents

Abstract **1**

Acknowledgements **2**

1 Introduction **6**

1.1 The Visible Universe . . . 6

1.2 The Interstellar Medium . . . 8

1.2.1 Phases of the ISM . . . 8

1.2.2 Chemistry of the ISM . . . 9

1.2.3 Diffuse interstellar clouds . . . 12

1.3 Large molecules in the ISM . . . 15

1.3.1 Unidentified Infrared Bands . . . 15

1.3.2 Diffuse Interstellar Bands . . . 16

2 Data Acquisition and Analysis **20**

2.1 Optical astronomy . . . 20

2.1.1 Telescopes . . . 20

2.1.2 Optical spectrographs . . . 21

2.2 CCD data reduction and analysis . . . 23

2.2.1 Software . . . 27

2.2.2 Terms and notation . . . 29

3 Small Scale Structure of the ISM **31**

3.1 Introduction . . . 31

3.1.1 Small Scale Structure . . . 31

3.2 Observational Techniques . . . 35

3.2.1 Searching for SSS variations . . . 37

3.2.2 Spectral ratios 37
3.3 Results and analysis 41
3.3.1 SSS probed through diffuse interstellar band observations . . 41
3.3.2 Tiny Scale Structure of the ISM 62
3.3.3 A common carrier for "C_2" features? 94
3.3.4 Profiles of blue diffuse bands 96
3.4 Diffuse Band Families 99
3.5 DIB variations and chemistry of ISM 109
3.6 Conclusions 125

4 A Search for Diffuse Band Carriers in the Early Universe 127
4.1 Introduction 127
4.1.1 Damped Lyman-α systems 130
4.1.2 Dust and diffuse bands in DLAs 132
4.1.3 Motivation for the study 136
4.1.4 Target selection 136
4.2 Observations 139
4.3 Results and Discussion 142
4.4 Analysis and conclusions 151

5 Post-AGB Stars with Dusty Discs 154
5.1 Introduction 154
5.1.1 Stellar evolution 155
5.1.2 Stars with discs 157
5.1.3 Identification of objects with discs - data sources 157
5.1.4 Identification of objects with discs - methodology 159
5.2 Survey 162
5.2.1 Selection by IRAS [12]-[25], [25]-[60] colour 162
5.2.2 Selection by near-IR colour excess 164
5.3 Observations 166
5.4 Results and discussion 173
5.4.1 Na I D emission line targets 173
5.4.2 Hα emission line targets 179
5.4.3 'Ordinary' stars 181

5.4.4 Review of selected targets 182
5.5 Conclusions and future strategy 184

6 Conclusions 186

Bibliography 189

List of Figures 195

List of Tables 200

Chapter 1

Introduction

1.1 The Visible Universe

The Earth is one of nine[1] planets orbiting the Sun, a low-mass G2 dwarf star some 4.7 billion years old. By mass, the Sun accounts for $\sim 99\%$ of the total mass of the solar system with the planets, asteroids and comets accounting for most of the other 1%.

Away from the light-polluted skies of towns and cities it is possible to identify in the night sky many thousands of individual stars of varying brightness and colour. With a dark adjusted eye it is also possible to see a 'band' of light spreading from one horizon to the other; this extra feature is our view through the plane of the disc of the Galaxy (see Figure 1.1). Our Sun is one of $\sim 10^{11}$ stars that together make up our galaxy, the Milky Way. Relative to the solar system, the Milky Way is vast. Light from the Sun takes just over 8 minutes to reach the Earth compared with 4.26 years it takes from our second closest star, Proxima Centauri. On larger scales, it takes $\sim 100,000$ years for light to travel from one edge of the Milky Way to the other giving some idea of the enormity of the Galaxy.

Just as stars form gravitationally bound clusters, galaxies can behave in a similar fashion. The Milky Way is one of the largest members of a group of 35 galaxies known as the 'Local Group'. Other members include the large Andromeda Galaxy (M31) the Triangulum Galaxy (M33) and the smaller Magellanic clouds. Just as there are $\sim 10^{11}$ stars in the Milky Way there are $\sim 10^{11}$ galaxies making up the visible Universe.

[1] Or, according to the IAU there are now eight planets and three "dwarf planets" including Pluto.

Figure 1.1: The Milky Way (http://skychasers.net/)

It is now widely held that the Universe began with the rapid expansion of a near-infinitesimally dense and small hot state some 13.7 billion years ago commonly referred to as the 'Big Bang'. Evidence for the Big Bang comes from, amongst other things, the findings of Edwin Hubble that the speed at which a galaxy is moving away from the Earth is proportional to the distance of the galaxy, i.e. the Universe is expanding. Further evidence for a hot early universe has been provided by the prediction (Gamow 1948) and subsequent discovery (Penzias & Wilson 1965) of a T = 2.735K blackbody spectrum that is believed to be the cooled relic radiation from the Big Bang.

Since the Big Bang of $\sim$ 13.7 billion years ago the Universe has evolved into an amazing mix of planets, stars and galaxies and other matter invisible to astronomers. This Thesis is primarily concerned with stars and the material that lies between them, the Interstellar Medium (ISM). Chapter 3 investigates the structure of the ISM by analysis of the dust and distribution of molecules in star forming regions. Chapter 4 investigates the possibility of using the wealth of knowledge acquired over many years of study of the Galaxy to identify and quantify the dust content of Damped Lyman-α absorbers. Finally, Chapter 5 describes an attempt to identify evolved stars with dusty discs by their near- and mid-IR colours through a systematic search of catalogue data.

1.2 The Interstellar Medium

The Interstellar Medium (ISM) is the matter *between* stars and within a galaxy. Characterised by, on average, extremely low particle densities, it is only because the ISM fills vast expanses of interstellar space that it accounts for $\sim 20\%$ of the baryonic mass of the galactic disc (Whittet 2003). Given the significant fraction of galactic mass the ISM represents, it is of little surprise that it has an important role in astrophysics. The ISM provides the reservoir of material from which stars form. Interstellar molecular clouds undergoing gravitational collapse eventually lead to clusters or 'nurseries' of hot young stars. Millions or billions of years later the ISM is replenished by the same stars coming to the end of their lives. Ejection of material from stellar winds and supernovae enriches the ISM with heavier elements, the product of nucleosynthesis, thus providing the material from which the next generation of stars form.

Close to 99% of the mass of the galactic ISM is gaseous, the remaining 1% is dust. Being the most abundant elements, the vast majority of the ISM gas is composed of hydrogen and helium with trace amounts of other species e.g. carbon, nitrogen and oxygen. It is these trace species that are partly responsible for the rich and varied chemistry of the ISM. Although only representing a small fraction of the total ISM mass, dust also plays a crucial role in facilitating chemical reactions in rarefied interstellar environments.

1.2.1 Phases of the ISM

The best vacuum that can be achieved in a terrestrial laboratory is termed Ultra-High Vacuum (UHV) and currently reaches pressures of $\sim 10^{-10}$ Torr[2] (1.33×10^{-7} Pa). Compared to atmospheric pressures of ~ 760 Torr and associated gas densities of $n \simeq 10^{19}$ cm^{-3}, UHV has a gas density of $\sim 10^{6}$ cm^{-3}. Remarkably, only the most dense regions of the ISM, the dark molecular clouds, have densities that begin to approach those of terrestrial UHV. Table 1.1 outlines the key distinct phases of the ISM and the parameters that define the phases.

Due to its dominant abundance, different regions of the ISM are often discussed in terms of the ionisation state of hydrogen. In the hot ionised medium the high tempera-

[2] 1 Torr = 133.322 Pa (N/m^2)

Phase	Temp (K)	Density (cm^{-3})	State
Hot Ionised	10^6	10^{-3}	highly ionised
Diffuse Ionised	10^4	0.03	highly ionised
H II regions	10^4	$1 - 10^4$	ionised hydrogen
Warm Ionised	$10^3 - 10^4$	0.01	ionised hydrogen
Warm Neutral	1000 – 5000	0.1 – 10	neutral hydrogen
Cold Neutral	50 – 100	$1 - 10^3$	neutral hydrogen
Molecular Clouds	20 – 50	$10^3 - 10^6$	hydrogen molecules

Table 1.1: Phases of the ISM

tures and extremely low number densities mean that all species including hydrogen are highly ionised. Moving to more dense regions such as cold neutral clouds, the density of atoms and molecules is sufficient that the periphery of the interstellar clouds begin to shield inner regions allowing for larger more complex molecules to form.

1.2.2 Chemistry of the ISM

On first inspection, it seems difficult to reconcile the physical conditions outlined in Table 1.1 with the rich and diverse chemistry known to be continually processing material in the ISM. Even in the most dense ISM environments, the dense molecular clouds, the mean free path[3] of an atom or molecule is $\sim$ 100 km making the chances of a three-body collision extremely low. In fact, the simultaneous collision of three bodies only becomes a viable chemical reaction mechanism for densities $\geq 10^{11}$ cm^{-3} (Lequeux 2005). The low densities of the ISM do not mean that gas-phase chemistry is not viable; instead, different types of reaction mechanisms must be considered.

Ion–molecule reactions

The low temperatures of molecular clouds essentially mean that endothermic reactions are impossible. Only *exothermic* reactions are likely to proceed but even so, if the kinetic temperature of the reactive species is so low that there is insufficient energy to surmount the activation barrier associated with the reaction, then no reaction will occur (Figure 1.2). It is not the case that reactions with an activation barrier do not occur *at*

[3]The mean free path of a particle is the average distance that a particle has to travel between collisions with other species.

all in the neutral medium, rather that it it unusual and regions require heating *via* e.g. shocks before they can occur.

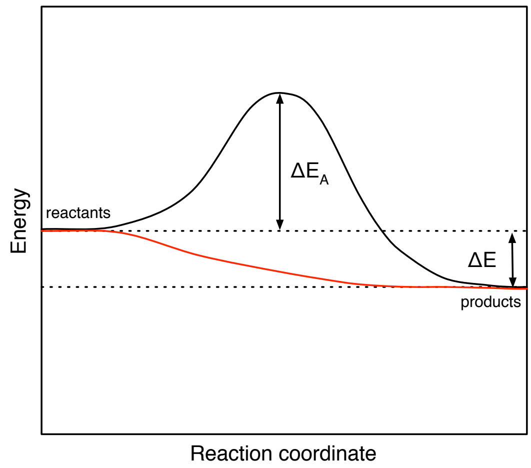

Figure 1.2: Reaction pathway for an exothermic reaction releasing energy ΔE, with an activation barrier (ΔE_A, black line) and without (red line).

In the neutral medium a reaction is required that follows a path similar to that of the red line in Figure 1.2. An example of such a reaction is an ion–molecule reaction. Ion–molecule reactions are important for the chemistry of the ISM as they typically have little or no barrier to reaction (ΔE_A Figure 1.2).

Ion–molecule reactions involve cations reacting with neutrals to produce a mix of charged and neutral products which, after subsequent recombination with free electrons produce further neutrals. The general reaction scheme is:

$$A^+ + B \longrightarrow C^+ + D \tag{1.1}$$

Ion–molecule reactions have low or zero activation energies because the ion induces an electric dipole on the neutral species that in turn attracts the neutral to the ion. Factors including the polarisibility of the neutral and the presence of a permanent electric dipole affect the interaction potential and thus the reaction rate.

Neutral–neutral reactions

At higher temperatures, in regions of shocked or turbulent material, neutral–neutral reactions can play a significant role in the chemistry of the ISM. Instead of the relatively strong ion–molecule interactions, neutral–neutral interactions rely upon van der Waals forces to bring reactive species together. If one of the reactive species possesses an unpaired electron (i.e. a radical) then the reaction rates can *increase* at lower temperatures.

Dissociative recombination

When a cationic species combines with an electron a combination of neutral species are produced.

$$AB^{+} + e \longrightarrow A + B \tag{1.2}$$

Two possible mechanisms exist for dissociative recombination: 1) the excitation of AB^{+} such that it has a potential energy curve crossing with a repulsive state of the neutral species or 2) excitation to an excited state of the neutral species (AB) which in turn has a curve crossing with a repulsive state thus leading again to dissociation of the species.

Dust grain chemistry

Although only representing a relatively small fraction of the total mass of the ISM, dust plays a crucial role in the chemistry of ISM environments. Ion–molecule two-body processes are possible for some species but significantly not for the formation of H_2 unless the degree of ionisation is very high. Dust grain surfaces offer an alternative route for the formation of molecules. By providing a surface onto which species can absorb, allowing species to 'meet' on the surface, react to form the new molecule and then, crucially, use the excess energy from reaction to drive the new molecule from the surface of the grain. Without the third-party involvement of a grain, species such as H_2 are unable to radiate away energy upon formation in a 2-body collision and so dissociate immediately after formation (e.g. Duley & Williams 1986).

Grain surfaces are important in the formation of other molecules. The formation of OH, CH, NH, CH_4, NH_3 and H_2O are just some of the many molecules whose formation is facilitated by reaction at grain surfaces. Evaporation and the release of the new species back into the gas phase once a reaction has occurred is a process that is not well understood (Lequeux 2005). For very small grains it is possible that the excess energy from the reaction of parent species is sufficient to thermally eject the daughter species. UV photon and cosmic ray heating of the grain offer alternative mechanisms for the desorption of a molecule. Recent studies of grain-mantle evaporation in molecular clouds has shown that the porosity of a grain surface can affect the process of evaporation and needs to be considered when modelling the chemistry of these regions (e.g. Collings *et al.* 2003).

Destructive processes

Just as molecules are readily formed in the diffuse ISM, they are also destroyed. The main destruction mechanisms are photoionisation and photodissociation. Both processes are most likely towards the outer regions of interstellar clouds where the ultraviolet (UV) radiation of the interstellar radiation field (ISRF) can reach the molecules. Photo-destructive processes are also possible towards the inner regions of molecular clouds but rely upon UV photons created locally *via* cosmic ray excitation of H_2 or He (Gredel *et al.* 1989).

1.2.3 Diffuse interstellar clouds

In the schema outlined in Table 1.1, diffuse clouds are most like the cold neutral medium. With number densities on average of ~ 300 cm^{-3} and temperatures between fifty and a few hundred Kelvin. The conditions in diffuse clouds are close to the density limits for chemistry to be feasible. The densities of diffuse clouds are such that they are optically thin i.e. they can be studied in the optical region of the electromagnetic spectrum and have typical colour excesses (E_{B-V}) of ~ 0.2 (Snow & McCall 2006).

Hydrogen is predominantly neutral and is atomic (H I) and molecular (H_2) in form in varying fractions[4] but with the atomic hydrogen at least 50%. The ISRF ionises other species present in diffuse clouds, the majority of which are singly ionised and carbon ions providing the main source of electrons.

Other than its role in the formation of H_2 it is not clear what effect dust has upon the chemistry of diffuse clouds. The chemistry in the diffuse medium is believed to be

[4] $f_{\mathrm{H}} = 2N(\mathrm{H_2})/[N(\mathrm{H\,I}) + 2N(\mathrm{H_2})]$

mostly gas phase and 'carbon dominated' (van Dishoeck & Black 1986); some of the key reactions outlined below:

$$C^+ + H \longrightarrow CH^+ + h\nu \tag{1.3}$$

$$C^+ + H_2 \longrightarrow CH_2^+ + h\nu. \tag{1.4}$$

The radiative association reactions 1.3 and 1.4 are extremely slow (k = 10^{-17} cm^{3}s^{-1}, Lequeux (2005)). Although ruled out in section 1.2.2 a reaction is possible between ionised carbon and H_2:

$$C^+ + H_2 \longrightarrow CH^+ + H. \tag{1.5}$$

Endothermic by 0.4 eV, it is thought that in regions of turbulence or shock fronts (supernovae) this reaction would become feasible (Hartquist & Williams 1978).

Further important reactions for diffuse clouds include the formation of CO and HCO^+ *via*:

$$C^+ + OH \longrightarrow CO + H^+ \tag{1.6}$$

$$C^+ + OH \longrightarrow CO^+ + H \tag{1.7}$$

followed by

$$CO^+ + H \longrightarrow CO + H^+ \tag{1.8}$$

$$CO^+ + H_2 \longrightarrow HCO^+ + H. \tag{1.9}$$

Or *via*:

$$C^+ + H_2O \longrightarrow HCO^+ + H. \tag{1.10}$$

Oxygen based molecules are generally formed through reaction with hydrogen rather than C^+:

$$H^+ + O \longrightarrow O^+ + H \tag{1.11}$$

then

$$O^+ + H_2 \longrightarrow OH^+ + H, \tag{1.12}$$

or *via* reaction with the triatomic molecule, H_3^+, the presence of which in diffuse clouds was only confirmed recently (McCall *et al.* 2002b):

$$H_2^+ + H_2 \longrightarrow H_3^+ + H \tag{1.13}$$

and

$$H_3^+ + O \longrightarrow OH^+ + H_2 \tag{1.14}$$

$$OH^+ + H_2 \longrightarrow H_2O^+ + H \tag{1.15}$$

$$H_2O^+ + e \longrightarrow OH + H. \tag{1.16}$$

Modelling of diffuse clouds

Chemical 'networks' incorporating many hundreds of different reactions have been developed over the last few decades, the most notable of which was by van Dishoeck & Black (1986). Models can readily be tested by comparing the predicted and observed abundances of species in individual lines of sight. To date the chemical models of diffuse clouds are immature compared with work on other phases of the ISM (Snow & McCall 2006). A model whereby the physical and chemical nature of a diffuse cloud is treated self consistently does not exist and is only likely to be considered in the next generation of chemical models. The failure of models to account for the high observed abundance of CH^+ and H_3^+ are notable problems with current models. The endothermicity of the reaction:

$$C^+ + H_2 \longrightarrow CH^+ + H \tag{1.17}$$

means that at diffuse cloud temperatures the reaction does not proceed. H_3^+ is believed to be produced by cosmic-ray ionisation of molecular hydrogen (Equation 1.13) and its abundance is currently under-predicted by many orders of magnitudes in most models.

Of particular relevance to this thesis is the recent modelling of the foreground ISM towards κ Velorum by Bell *et al.* (2005). Following repeated observations by Crawford (2000, 2002), Bell *et al.* attempted to incorporate small-scale ($\sim$ 10 AU) density variations into their chemical models to predict abundances of various molecular species. To date, parameters describing the small-scale structure of the ISM have not been included in the majority of diffuse cloud models but have been cited as a potentially important component (Black & van Dishoeck 1991). Observations have shown that the slab-like geometry used by most models is almost certainly not a complete description of the structure of the ISM (e.g. Crawford 2003, Cordiner 2005); Chapter 3 discusses this further.

1.3 Large molecules in the ISM

There is a component of the ISM that is composed of species much larger than those already discussed. Believed to be responsible for the Unidentified Infrared Band (UIR bands) and also the Diffuse Interstellar Bands, it is thought that there exist molecules in the ISM that are composed of many tens if not hundreds of atoms.

1.3.1 Unidentified Infrared Bands

The UIR bands are seen towards a range of astrophysical sources including planetary nebulae, evolved carbon stars and young stellar objects (YSOs). A sequence of emission features, the strongest of which are at 3.3, 6.2, 7.7, 8.6 and 11.3 μm, they are believed to be due to vibrations of large, carbonaceous molecules, which are most likely polycyclic aromatic hydrocarbons (PAHs) or some mix of aromatic species (Allamandola *et al.* 1989, Tokunaga 1997). Although there is some controversy as to the exact nature of the carriers (they remain unassigned), it is clear that they are due to significantly larger molecules than any currently identified species.

1.3.2 Diffuse Interstellar Bands

Seen most easily as a sequence of absorption features in the spectra of early-type stars, the Diffuse Interstellar Bands (DIBs) are a collection of $\sim$ 300 absorptions found mainly in the optical region of the electromagnetic spectrum and seen towards stars with intervening interstellar matter. The DIBs were first discovered in 1922 by Mary Heger (Heger 1922) as a pair of 'stationary' features at 5780 and 5797 Å in the spectra of binary stars. Stellar features, i.e. those absorptions due to atoms in the atmospheres of stars appear at wavelengths that vary depending upon the line-of-sight velocity of the star. In binary star systems where there are two stars in orbit about their shared centre of mass, the observed wavelengths of the stellar features vary due to the velocity shift introduced through their orbital motion. This is not the case for the DIBs are they are not associated with the star, but rather with the material between the star and the observer, and so are the termed 'stationary'. Diffuse band studies were significantly advanced by Merrill and co-workers (Merrill 1934, 1936) who noted additional 'stationary' features. At the time, this behaviour was not unknown; interstellar features due to atoms and small molecules behave in the same way. However, Merrill noted that the DIBs were '...somewhat widened and have rather diffuse edges'. The diffuse interstellar bands are discussed as such because of their 'diffuse' widths, i.e. they are *broader* than absorption lines due to atomic species in the same sight line and *interstellar* as they are associated with the interstellar material rather than the background illuminating source. Over eight decades since they were first discovered, the diffuse interstellar band spectrum remains unassigned; none of the $\sim$ 300 DIBs have been definitively assigned making it one of the greatest unsolved problems in spectroscopy.

Although the exact nature of the diffuse band carriers remains uncertain, a huge amount of effort has been devoted to solving the diffuse band problem.

Diffuse band behaviour

Merrill & Wilson (1938) noted that two DIBs, $\lambda5780$ and $\lambda6284$ varied in strength with the line-of-sight dust column, E_{B-V}. When the DIBs were first discovered, there was a general consensus that the DIBs were due to molecules in the ISM (e.g. Swings 1937, Eyster 1937). Later, partly due to their good correlation with E_{B-V} (Figure 1.3) and also because mechanisms for the production of large quantities of interstellar molecules were not known, solid state absorptions of grains became the most popular explanation for the DIBs (e.g. Herbig 1963, Duley 1968).

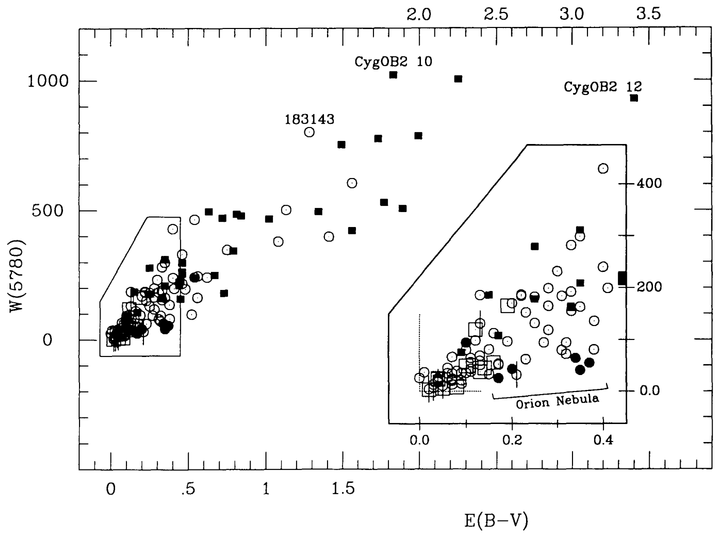

Figure 1.3: Herbig 1993 plot showing $\lambda5780$ – E_{B-V} correlation

Following the radio detection of molecules in the 1960s and 1970s (e.g. Rank *et al.* 1971) and the realisation that reaction mechanisms exist (e.g. ion–molecule, Section 1.2.2) that would have feasible reaction rates even in the extreme conditions of the diffuse ISM, the idea that molecules were responsible for the DIBs regained popularity (e.g. Douglas 1977). Whilst there exists evidence to favour solid state carrier species, the consistency of the central wavelengths, the invariance of the DIB profiles between sightlines and the existence of fine structure Sarre *et al.* (1995) in some bands argues strongly in favour of a molecular carrier.

Other DIB correlations are known to exist (e.g. Na I & H I Herbig 1993) although none so strong as that with E_{B-V}. It is worth noting that the scatter about the line in Figure 1.3 is real; for a given value of E_{B-V}, $W_{\lambda5780}$ can vary by a factor of two.

The broad spectral coverage, variety in shapes and lack of regularity in the spacing of the DIBs means that they almost certainly do not come from a single carrier species. Elemental abundance arguments also mean that the DIBs are probably composed of those elements most cosmically abundant, i.e. H, C, O etc. Due to the wide variety of environments in which the DIBs are seen and their clear preference for those regions occupied by H I gas (rather than more dense molecular environments, Herbig 1995), the DIB carriers must be able to withstand a fairly unattenuated interstellar radiation field. Likely candidates include large carbon-based aromatic species or carbon chains Snow (2001); both species have the required resilience to exist in the more diffuse atomic regions of the ISM.

Thorburn *et al.* (2003) have identified a suite of blue DIBs, the carriers of which, appear to reside in denser regions than their yellow/red cousins. A reasonable correlation was found between the C_2 molecule and a selection of relatively weak blue DIBs leading to them being referred to as the "C_2" DIBs. Like CN, C_2 is formed in the more dense regions of diffuse clouds (Federman *et al.* 1994). The fact that these "C_2" DIBs show a correlation with a more dense component of diffuse clouds makes them highly unusual.

Further evidence for molecular rather than solid state carriers of the DIBs comes from fine structure observed within the DIB profiles (e.g. Sarre *et al.* 1995). One of the most remarkable features of the diffuse band spectrum is the general lack of variation in the profiles of the DIBs *between* lines-of-sight. Westerlund & Krelowski (1988) demonstrated that the profiles of many strong DIBs could be decomposed into separate components based upon the profiles of Na I lines. The similarity of DIB profiles between lines-of-sight and the possible decomposition of their shapes has led to the idea of 'intrinsic' DIB profiles.

In an attempt to elucidate the nature of DIB 'intrinsic' profiles, authors have studied 'single-cloud' sightlines, i.e. those where the profile of the atomic species can be fitted with a single narrow Gaussian function. Single-cloud sightlines where only one component is observed even at the highest spectral resolution are rare. Instead, authors generally study *pseudo* single-cloud sight-lines where there is only one main component that far exceeds the minor components (e.g. Cami *et al.* 1997). Sarre *et al.* (1995) and Kerr *et al.* (1996) made the first ultra high resolution study of DIB profiles in single-cloud sightlines. At resolutions ($\lambda/\Delta\lambda$) of $\sim 10^6$ and high S/N, they discovered fine structure in strong yellow/red DIBs and modelled the triplet structure of λ6614 as a ro-vibronic transition of large symmetrical molecule. Just as there are DIBs that show fine structure (λ5797, λ5850, λ6234, λ6379, λ6614, λ6660, Sarre *et al.* 1995, Kerr *et al.* 1996, Krelowski & Schmidt 1997) there are many that do not; ultra-high resolution spectra of the strong λ4430 showed no sign of fine structure seen in other narrower DIBs (Snow 2002).

With the advent of modern detectors and the availability of large telescopes with high-resolution spectrographs, the quality of DIB spectra continues to improve. Large quantities of high-quality spectra (e.g. McCall *et al.* 2002a) mean that it is not only possible to characterise the diffuse band spectrum with unprecedented accuracy but also measure the DIB–'known species' correlations with increased confidence. If the DIB carriers are large organic species then the DIBs represent electronic transitions in these molecules. Unlike the UIR bands where the spectral features are characteristic of a certain type of chemical bond but not specific enough to be diagnostic of the particular molecules, electronic transitions such as the DIBs are likely characteristic of the specific molecule giving rise to the feature. Advances in the gas-phase spectroscopy of large molecules will hopefully identify specific DIB carriers and help us to understand the diffuse cloud chemistry that leads to the formation of large quantities of complex molecules in the ISM.

Chapter 2

Data Acquisition and Analysis

2.1 Optical astronomy

2.1.1 Telescopes

One of the most ancient sciences, the study of the night sky has been the pursuit of astronomers across the ages. Developing observational techniques still in use today the ancient Greek astronomers studied ‘astronomia’ meaning literally ‘law of the stars’ cataloguing positions of hundreds of stars and, together with their philosophical might, deduced that the world was in fact a sphere.

Although often wrongly credited with inventing the optical telescope, it was not until the Italian scientist Galileo Galilei in 1610 made use of his ‘telescopio’ to discover the four largest moons of Jupiter that a telescope-like instrument had been used in astronomy. Consisting of a combination of convex and concave lenses, Galileo’s use of a magnifying device in astronomy had begun a revolution in observational astronomy.

Due to problems associated with the construction of large lenses, almost all large modern research telescopes use mirrors to collect light. Broadly termed ‘reflecting telescopes’ and developed by Sir Isaac Newton to solve aberration[1] effects associated with refracting devices, ‘reflector’ telescope design has progressed to the point where the largest single mirror telescope currently in use is over 8 metres in diameter.

[1] Chromatic aberration is an image distortion effect caused by the difference in focal length of blue and red light when focussed with a lens.

Data for this thesis has been acquired on three telescopes; the 1.9 metre Radcliffe Telescope (SAAO, South Africa), the 3.9 metre Anglo-Australian Telescope (AAT, AAO, Australia) and the 8.2 metre Very Large Telescope (VLT, Paranal Observatory, Chile).

2.1.2 Optical spectrographs

Although first carried out at visible wavelengths, astronomical observations are now made at a variety of wavelengths across the electromagnetic spectrum from X-ray observations of massive black holes to radio observations of molecules in dense interstellar clouds. The work in this thesis is primarily based upon optical observations recorded by the author combined with some analysis of infra-red catalogue data.

Optical spectroscopy relies upon our ability to record the intensity of dispersed optical flux as a function of wavelength. With a function similar to that of a prism, modern spectrographs use a diffraction grating, a reflecting surface with many fine lines or grooves cut into its surface to diffract light into different wavelengths.

Light is collected by the telescope and focussed such that it passes into the spectrograph where it is diffracted by a diffraction grating and then recorded on a light sensitive device (see Figure 2.1).

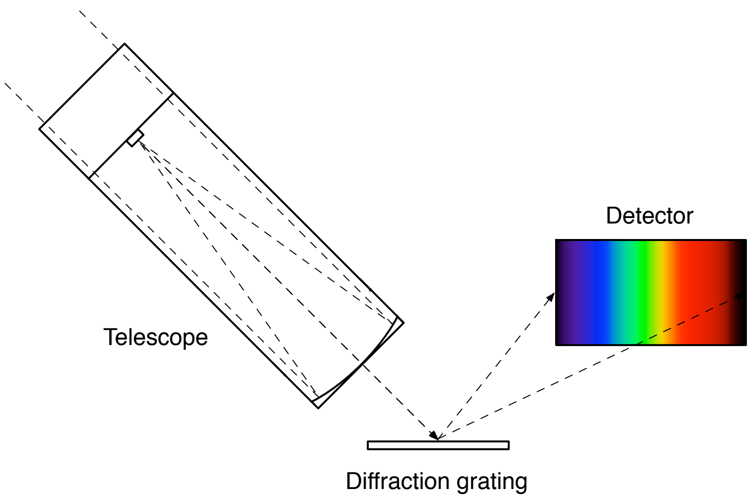

Figure 2.1: Basic layout of telescope and spectrograph.

Diffraction gratings come in a variety of forms with the resultant spectrum determined primarily by the number density of grooves/lines cut into its surface. The research in Chapters 4 and 5 in this thesis makes use of simple grating spectrographs i.e. data are recorded for a single diffraction order of the grating resulting in a spectrum of broad wavelength coverage (~ 3000 Å) but low spectral resolution. Data for Chapter 3 were recorded using an echelle spectrograph which gives a wide wavelength coverage (~ 6000 Å) and high resolution but requires more sophisticated data reduction techniques.

Characterising optical spectra

Optical spectra are characterised in numerous different ways using a variety of units for both historical and logical reasons. In this thesis spectra are generally characterised and discussed in terms of the following parameters:

I. **Wavelength coverage**

Measured in this thesis in angstroms (Å), wavelength coverage is the range in wavelength ($\lambda_{\text{minimum}} - \lambda_{\text{maximum}}$) that is recorded for a given combination of diffraction grating and detector. The combination of a large detector and relatively low 'spread' (dispersion) of the incident light can result in a wavelength coverage of many thousands of angstroms for single order spectrographs. Echelle spectrographs offer large wavelength coverage at high spectral resolution.

II. **Dispersion**

Defined as:

$$D = \frac{d\lambda}{dx} \tag{2.1}$$

and sometimes confused with spectral resolution, the dispersion of a spectrum describes how the wavelength is spread out on the detector. Usually measured in wavelength units per mm or pixel, a higher dispersion spectrum means that more light is spread across a detector than in a lower dispersion spectrum. When planning observations the dispersion scale of a spectrograph is important for determining the signal-to-noise requirements of the programme.

III. **Resolution**

Spectral resolution or resolving power, R, is the capacity of a spectrograph to resolve spectral features. It is defined as:

$$R = \frac{\lambda}{\Delta\lambda}, \tag{2.2}$$

where $\Delta\lambda$ is the $FWHM$ of the point spread function (PSF) of the spectrograph. For low resolution spectrographs such as FORS2 on the VLT, R is typically between 1000 and 2500. For higher resolution spectrographs, e.g. echelle-type spectrographs such as UCLES[2], $R \gtrsim 50,000$.

IV. **Signal-to-noise ratio**

The signal-to-noise (S/N) of a spectrum is defined as the signal strength relative to the background noise. For cases where there is Poisson noise the S/N is defined as:

$$S/N = \frac{I(\lambda)}{\sigma(\lambda)}, \tag{2.3}$$

where $I(\lambda)$ is the number of counts (intensity) at a given wavelength and $\sigma(\lambda)$ is the standard deviation of the noise. S/N is usually quoted either in terms of S/N per detector pixel or per resolution element of the spectrograph (usually many pixels).

2.2 CCD data reduction and analysis

The detector of choice for almost all modern astronomical observations is the Charged Coupled Device (CCD). A CCD is a photoelectric device consisting of an array of light-sensitive detector pixels that record photon 'hits'. Each pixel can be thought of as an electron 'bucket' collecting electrons until the CCD is 'read out' and the number of electrons (photons) measured. CCDs are constructed from metal insulator

[2]The University College of London Echelle Spectrograph (UCLES) used in this work is one of the main spectrographs in use at the 3.9 metre Anglo-Australian Telescope (AAT).

semiconductors that, at low temperatures, allow promotion of an electron from the filled valence band to the empty conduction band thus recording a photon hit.

Once an exposure is terminated, the CCD is read out row by row by the CCD controller and together with an Analogue to Digital (A/D) converter, stored as a fits (Flexible Image Transport System) image. The fits files then undergo processing to remove instrumental effects from the recorded data.

The aim of the data reduction process is that the final data product, be it a spectrum or image, is free of instrumental artefacts introduced by the telescope, spectrograph (or imaging device) or detector.

Whilst the operation of the telescope and instrument employed is generally carried out by the observatory staff, the analysis and reduction of CCD fits data is usually the responsibility of the end user. Properties or defects of the CCD detector that may affect the quality of the CCD data are now considered.

When a CCD is read out, the quantity recorded by the CCD controller and A/D converter is not solely due to the incident photon flux. Other factors including dark current, readout noise, photon gain and quantum efficiency can affect the recorded value for each pixel. The aim of CCD reductions is to characterise and preferably remove these effects.

Dark current

CCDs function by promoting electrons from the valence band to the conduction band. At temperatures above those close to absolute zero, there is a non-negligible contribution to the conduction band electron population due to thermal effects. Because of this effect, CCDs are normally kept at cryogenic temperatures with the detector attached to a cooling element immersed in liquid nitrogen ($\sim$ 77 K) thus minimising the effect of thermal noise. Modern CCDs suffer significantly less from the effects of dark current than their earlier counterparts. Provided that the CCD is kept at a constant low temperature (dark current varies with temperature), then, for normal observations of moderate S/N, the dark current contribution to the total signal is negligible and can be safely ignored.

Digitisation

When read out by the CCD controller, each pixel value is converted from the analogue readout charge to digital values. For a given A/D converter there is a conversion factor termed the 'analogue to digital unit' (ADU) factor that determines how many electrons are required to register 1 ADU. If for example 1 ADU = 10 electrons, then in the conversion from electron charge to ADU between 1 and 5 electron charges may be lost in digitisation of the data due to rounding errors.

Readout noise

CCDs are usually read out row by row with the same physical row being read out only and the charge transferred *between* rows as the CCD is read out. During the transfer of charge between pixel rows, random fluctuations in the total pixel charge are introduced by the CCD thus resulting in some uncertainty in the total charge value. This readout effect is usually combined with the digitisation uncertainty to produce an overall readout noise (R/O noise) value for the CCD. For modern detectors this value is typically less than 5 electrons per pixel.

Bias level and overscan

A perfect semiconductor detector would contain no electrons in the conduction band before the CCD exposure. Unfortunately this is not the case and in order to quantify the pre-exposure pixel values, the detector is read out (and the pixel values measured) without exposing it to any photon flux; this is the zero level noise associated with the CCD. Because of effects associated with the readout of the CCD, pixel values are distributed about a mean value close to zero but with some pixels having negative values. To prevent negative values from being recorded an arbitrary artificial offset called the bias level is applied to the CCD thus resulting in a bias image with pixel values fluctuating around the bias level.

Two main methods are used to determine the bias level of a CCD, 1) the recording of bias frames and 2) the addition of overscan regions to the CCD. Recording large numbers of CCD images where no light is incident upon the detector (and the integration time zero), the pixel value due to the bias level of the CCD can be accurately determined. Alternatively a strip of virtual pixels can be added onto the end of the CCD image. Because there are no physical pixels in the overscan region the pixel values are due only to the artificial bias level and the uncertainty within it. In practice astronomers usually record large numbers of bias frames that all have an overscan region. Averaging the pixel values in a large number of bias images and subtracting the resultant image from the data frames removes the zero level uncertainty in the CCD data.

Flat fielding

Ideally the response of each CCD pixel to incoming photons would be identical, i.e. the pixel-to-pixel sensitivity variation would be nil and the response uniform across the CCD array. This is not the case and in order to account for the slight differences in quantum efficiency of each pixel 'flat field' images are taken so that the response of the array can be characterised and the effect removed.

As the quantum efficiency of CCD pixels varies with wavelength, flat field images are obtained by illuminating the CCD with light from a continuum source such as a quartz lamp with the light following the same passage through the spectrograph as the photons from the astronomical source. In order that the quality of the science data is not degraded by the flat fielding process, numerous high S/N flat field images are obtained typically by illuminating the slit of the spectrograph with a projector lamp (projector flats) or by observing an illuminated white screen on the inside of the telescope dome (dome flats).

In cases where there is significant fringing in the CCD frame (caused by internal reflection of light in the CCD, Figure 2.2) careful flat fielding can be used to 'divide out' the shape of the fringing in the science frames.

CCD response

Although to a first approximation the response of a CCD is linear, the response of a CCD usually deviates from linearity by fractions of a percent with the total deviation depending upon the extent of the illumination of the CCD. For many astronomical observations any non-linearity effects can be safely ignored, however for the work

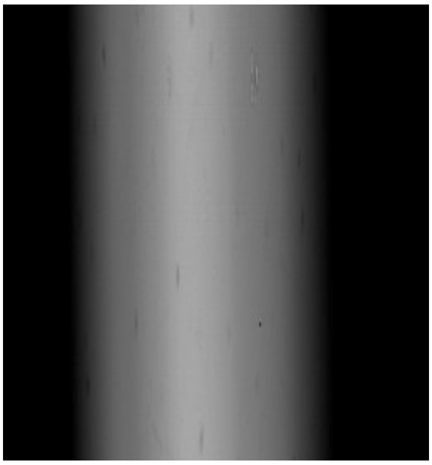

Figure 2.2: Moderate fringing of the red sensitive AAT MITTL3 CCD (left) compared with no fringing in the blue optimised EEV2 CCD (right). Note the presence also of a 'hot column' of pixels in the MITTL3 CCD (left).

described in Chapter 3, differences of fractions of a percent in spectral intensities are routinely encountered so a correction for this effect has to be made during the reduction process.

2.2.1 Software

With the wealth of sophisticated astronomical data reduction packages available, the reduction of CCD data is relatively straightforward provided that the user is aware of possible pitfalls. The data presented in this thesis have been analysed using the IRAF [3] (Image Reduction and Analysis Facility) data reduction suite. All data recorded and presented in this thesis are in the optical region of the electromagnetic spectrum. The reduction of the CCD data, regardless of the telescope/instrument configuration can broadly be summarised as follows:

I. **Linearise number counts**

IRAF task: **images.imutil.imarith, images.imutil.imfunc**

Using a combination of the IRAF tasks **imarith** (image arithmetic) and **imfunc** (image function) a IRAF script can be constructed to apply the transformation required to correct for the non-linearity of the CCD.

[3] IRAF is a general purpose software system for the reduction and analysis of astronomical data. IRAF is written by the IRAF programming group at the National Optical Astronomy Observatory (NOAO)in Tucson Arizona (http://www.noao.edu/).

II. **Bad pixel correction**

IRAF task: **proto.text2mask, proto.fixpix**

Using an image viewer such as DS9[4], individual, groups or sometimes even rows/columns of dead/hot pixels can be identified and a text file made of the XY co-ordinates of the bad pixels. The IRAF **text2mask** is then used to produce a bad pixel 'image' and passed to the **fixpix** task which interpolates and replaces the bad pixel values with those of nearby pixels.

III. **Cosmic ray correction**

IRAF task: **noao.imred.crutil.cosmicrays**

This task detects and removes (interpolates with nearby pixels) cosmic ray hits on the CCD.

IV. **Overscan/bias subtraction**

IRAF task: **noao.imred.ccdred.zerocombine, noao.imred.ccdred.ccdproc**

IRAF task **zerocombine** is used to combine the zero (bias) CCD frames creating a 'master' bias frame that is then subtracted from the CCD data images using the **ccdproc** task.

V. **Combination and normalisation of flat field images**

IRAF task: **noao.imred.ccdred.flatcombine, noao.twodspec.longslit.response or noao.twodspec.apextract.apflatten**

Using the IRAF task **flatcombine** flat field CCD images are combined to create a master flat field image. Depending upon the format of the data the flat field is then normalised using **response** (single slit observations) or **apflatten** (echelle data).

VI. **Flat fielding of CCD data**

IRAF task: **noao.imred.ccdred.ccdproc**

CCD data images are divided by the normalised flat field image from step V using the IRAF task **ccdproc**.

[4]DS9 is an astronomical imaging and data visualization application developed by Smithsonian Astrophysical Observatory (http://cfa-www.harvard.edu/sao-home.html).

VII. **Scattered light subtraction**

IRAF task: **noao.imred.echelle.apscatter**

Only required for echelle data reduction, this step removes the scattered light that falls on the detector between echelle orders. A particularly CPU intensive process, the IRAF task **apscatter** is used.

VIII. **Trace apertures and extract spectra**

IRAF task: **noao.imred.echelle.apall**

This task is used to extract the spectra from two dimensional images. For single slit observations **apall** only extracts one aperture, but for echelle data numerous (~ 60) apertures are extracted. For each science CCD image a calibration CCD image (arc) is extracted with the same aperture definition as for the object image. This task can also be used to subtract night sky emission lines in faint object spectra.

IX. **Identify arc spectra**

IRAF task: **noao.imred.echelle.ecidentify or noao.onedspec.identify**

Lines in the arc files are identified with reference to an arc atlas. Functions describing the wavelength solution are applied to the fit of the arc lines.

X. **Apply wavelength solution**

IRAF task: **noao.onedspec.refspectra, noao.onedspec.dispcor**

The wavelength solution of the arc file is applied to the object spectra also and the dispersion solution applied resulting in wavelength calibrated spectra.

2.2.2 Terms and notation

When analysing astronomical spectroscopic data a selection of key terms/descriptors are used to describe the data. The most commonly used term for defining the breadth of a spectral feature is its Full Width at Half Maximum ($FWHM$). Usually quoted in angstroms (Å), the $FWHM$ is marked in Figure 2.3. The wavelength at which the feature is observed (also marked in Figure 2.3) is the central wavelength.

When measuring the strength of a spectral feature authors typically quote the central depth (in percent, 10% for the example in Figure 2.3) or equivalent width. The equivalent width ($W_{feature}$) of a spectral line is defined as the width in wavelength units (Å in this case) of an imaginary feature that causes 100% absorption of the spectral energy such that the integrated area of the 100% absorption feature is the same as that of the actual feature.

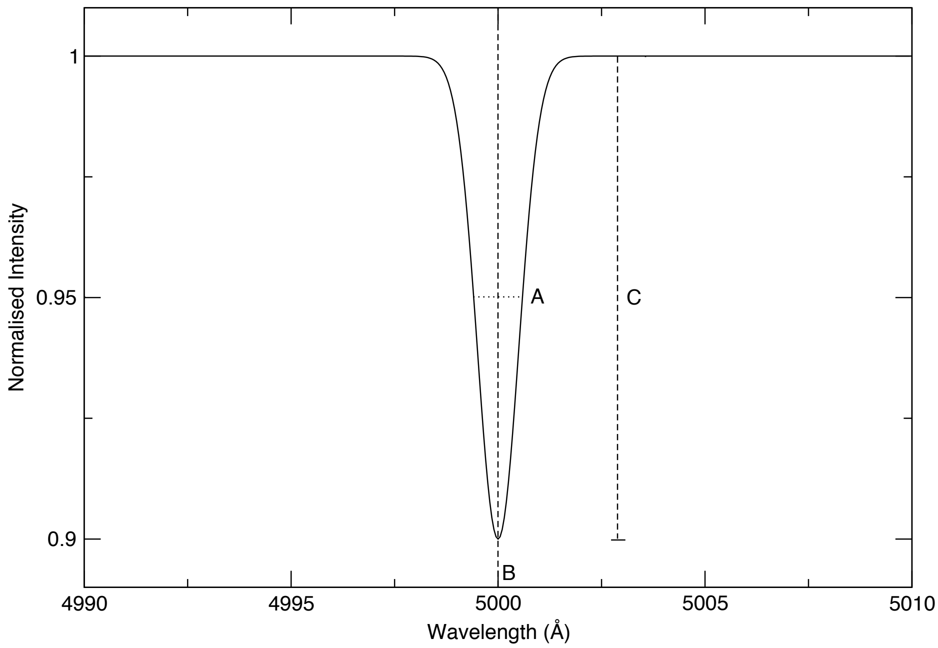

Figure 2.3: A synthetic spectral feature of $FWHM$ = A, $\lambda_{\mathrm{central}}$ = B and central depth = C.

Chapter 3

Small Scale Structure of the ISM

3.1 Introduction

Although typically at pressures many orders of magnitude lower than any terrestrial vacuum, the space in between stars is far from empty. This space, the Interstellar Medium (ISM), is thought to represent about one fifth of the baryonic mass of the galactic disc (Whittet 2003) and as such is an important and significant fraction of the total mass of the Universe. Regions of the ISM are characterised by their temperature, density and chemical species present. Chapter 1 introduces the different chemistry and phases of the ISM in more detail with this chapter being concerned with the *diffuse* interstellar medium; one of the more tenuous regions of the ISM.

3.1.1 Small Scale Structure

Identifying and characterising the small-scale-structure (SSS) of the ISM is important for a better understanding of the processing of material between interstellar (IS) environments. Current chemical models of diffuse IS clouds account for abundances of hundreds of different species linking them in reaction networks incorporating many thousands of chemical reactions (e.g. van Dishoeck & Black 1986). Even the most successful diffuse cloud models are unable to account for all species and their observed relative abundances. Noteworthy anomalies include H_3^+ (e.g. McCall *et al.* 2002b) and the troublesome quantities of observed CH^+, the reaction mechanism(s) responsible for its formation currently unknown.

In all but the most recent chemical models (Bell *et al.* 2005), the structure of IS clouds has been assumed homogeneous over parsec scales. The failure to incorporate small scale density/temperature/ionisation variations is partly due to the difficulties associated with identifying the size-scales involved in the structure. Prompted by the observed variation in K I strength towards κ Velorum (Crawford *et al.* 2000) on ~ 10 AU size-scales, Bell *et al.* (2005) modelled this region and, incorporating the observed density gradient in K I, predicted observable abundances of species such including C_2 thus offering observers an opportunity to test their model.

Whether or not there exists SSS in the ISM has been a question that until quite recently has proven difficult to answer. Given the wide variety of ISM environments that exist, from the hot (T $\sim 10^6$ K, N $\sim 10^{-3}$cm^{-3}) ionised intercloud medium to star forming, dense molecular clouds (T $\sim$ 10 K, N $>$ 300 cm^{-3}), a better question is probably 'in which species are SSS variations observed?'

Atomic species

Since the discovery of velocity structure in the interstellar (IS) Ca II H & K lines in 1943 (Adams 1943), it has been clear that there is differential distribution of atomic species in the ISM. Adams detected structure in over 80% of his programme stars with an example of such a detection shown in Figure 3.1.

Figure 3.1: Photographic images of the Calcium II H (right) and K (left) lines seen towards HD 167264. Figure taken from Adams (1943)

More recently, studies including VLBI[1] observations of quasar (QSO) lines-of-sight have identified SSS in the galactic H I distribution down to the angular resolution of

[1] Very Long Baseline Interferometry (VLBI) is radio astronomy combined with interferometry. High spatial resolution is possible (~ 0.1″), the extent of which related to the distance between the antennas.

the telescope (0.1″, ~ 70 AU, Dieter *et al.* 1976). Follow-up observations by Diamond *et al.* (1989) confirmed the earlier result of Dieter *et al.* observing significant variations in H I towards 3C 147, 3C 138 and 3C 380.

Using the sky projected separation of binary-star lines-of-sight, variations in Mg II and Mn II of size-scale ~ 2,800 AU have been identified by Meyer (1990). Utilising the same methodology, Watson & Meyer (1996) and Meyer & Blades (1996) observed variations in the distribution of Na I down to ~ 500 AU leading them to the conclusion that SSS in the ISM ubiquitous and 'the norm'.

Towards the B2 subgiant , κ Velorum, Crawford *et al.* (2000) observed a 40% increase in N(K I) over 8 years due to the transverse proper motion (PM) displacement of the star relative to the observer and foreground IS cloud. With a PM of ~ 2.5 AU yr^{-1} this ~ 20 AU variation represented the finest probe yet of SSS in the ISM. In a search for time-variable DIBs, Cordiner (2005) detected a further 35% increase in N(K I) since Crawford's observation of 2002. Travelling ~ 5 AU since the 2002 observation, this futher dramatic difference in N(K I) is the finest probe yet of the atomic component of the diffuse ISM.

Molecular species

In an approach similar to that of Watson & Meyer (1996), Pan *et al.* (2004, 2005) have identified variations in the observed quantities of small diatomics such as CH, CH^+ and CN towards binary and multiple lines of sight. At longer wavelengths, observations of SSS in the molecular component of the ISM have been detected using the transverse proper motion of the background source to search for SSS variations. H_2CO and HCO^+ differences have been detected by Marscher *et al.* (1993) and Liszt & Lucas (2000) respectively. In the UV, FUSE observations of H_2 have led authors to explain the observed abundances in terms of filamentary-like structure of size-scale ~ 40 AU (e.g. Richter *et al.* 2003).

Large molecules and dust

Even in some of the more dense diffuse cloud regions, the number density is so low that the probability of a three-body collision is extremely low meaning that even over the typical lifetime of a diffuse cloud, typical terrestrial gas-phase chemistry cannot account for the formation of the species observed. In order to facilitate the reactions between chemical species in diffuse clouds it is thought that dust grain surfaces may have a very important role to play (e.g. Collings *et al.* 2003). The chemisorption and/or physisorption of reactive species onto grain surfaces, their 'migration' across the grain surface and subsequent reaction whilst still attached to the grain mantle provides the reaction rates required to explain the known chemical abundances.

Given the importance of dust in the chemistry of the ISM, it is highly desirable to better understand the structure and distribution of the dust. Studies by e.g. Watson & Meyer (1996) and Pan *et al.* (2004) have demonstrated the ubiquity of SSS in the atomic and small-molecule distribution of the ISM. Due to the difficulties associated with accurately measuring line-of-sight dust column, until very recently, differences in dust distribution relied upon looking for variation in the reddening (E_{B-V}) of closely separated stars similar spectral type. Using this approach, Lodén (1973) identified differences in E_{B-V} over $\sim$ 10,000 AU but this approach is limited by the difficulties of accurate stellar classification and the likelihood of finding closely separated stars of similar spectral type.

At longer wavelengths, large-scale mapping of the ρ Ophiuchi *molecular* cloud (e.g. Johnstone *et al.* 2000, Stanke *et al.* 2006) has provided and alternative method for probing the distribution of material in molecular clouds. By detecting the submillimeter continuum emission of dust grains, searches of the ρ Oph cloud complex for protostars has revealed well over one hundred 'cores' with separations of $\sim$ 5000 AU (Stanke *et al.* 2006) including new classes of extremely young stellar objects (YSOs, André *et al.* 1993).

A novel method for identifying SSS dust distribution 'by proxy' was used by Cordiner *et al.* (2005). Using the diffuse interstellar bands (DIBs) and their close relation to dust reddening, E_{B-V}, Cordiner *et al.* recorded high S/N DIB spectra of binary and multiple sight lines looking for differences in the DIB strengths over distances ranging from 400 to 30,000 AU. Whilst it is not clear whether the DIB carriers *are* dust grains, current theory (Crawford *et al.* 1985, Leger & d'hendecourt 1985, Foing & Ehrenfreund 1994 and Salama 1999) suggests that the DIB carriers are very probably large molecules, i.e., the precursors to, or daughter species of IS dust grains. Cordiner *et al.* detected differences in the yellow and red ($\lambda_{\rm obs}$ > 5700 Å) DIBs for the majority of targets observed suggesting that, like the atomic and molecular species, SSS in the dust/large molecular component of the ISM may also be ubiquitous.

This Chapter describes an extension of the original Cordiner *et al.* (2005) study. The aims of this study were threefold: 1) to confirm the Cordiner *et al.* result and improve upon the data quality achieved in 2004, 2) to extend the spectral coverage to shorter wavelengths to look for variations, amongst others, in the suite of blue DIBs noted by Thorburn *et al.* (2003) as being related to the C_2 molecule and 3) use the proper motion displacement of the programme stars (typically ~ 3 AU yr^{-1}) between the 2004 and 2005 observations to search for DIB variations over very small scales.

3.2 Observational Techniques

As outlined in section 3.1, numerous methods have been used to probe the SSS of the ISM (e.g. Dieter *et al.* 1976, Watson & Meyer 1996, Crawford *et al.* 2000). This study is based upon the approach of Watson & Meyer, their approach being to make high S/N observations towards binary and multiple lines of sight (see Figure 3.2). For any given set of observations, the limit that can be placed on the size-scale of the structure is the separation of the closest stars, which, for this study is ρ Oph A and B (separation ~ 400 AU).

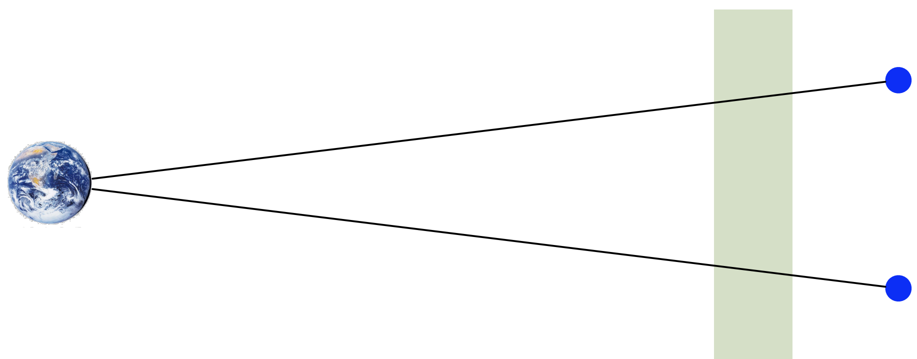

Figure 3.2: Binary pair separation give two discrete lines-of-sight through the interstellar cloud

Prompted in part by the discovery of variations in the column density of K I towards kappa Velorum (κ Vel) of size-scale ~ 5 AU (Crawford *et al.* 2000) due to the proper motion displacement of the star, it was realised that there was the possibility of searching for DIB variations due to the proper motion displacement of the binary and multiple systems observed in 2004 (see Figure 3.3). In April 2005 selected targets from the 2004 observing run were re-observed to search for such variations as well as providing an opportunity to assess the reproducibility of the 2004 result. Table 3.1 lists the targets observed, their parallax and proper motion displacement per year.

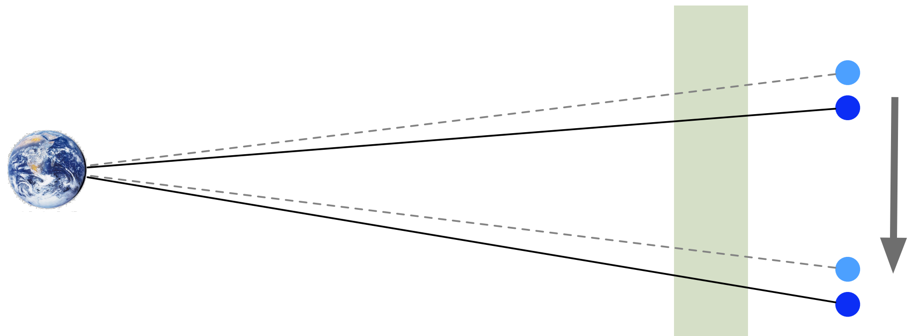

Figure 3.3: Finer probe of SSS due to proper motion displacement of the background stars .

Target	Spectral Type	Parallax(mas)	Distance (AU)	PM (mas yr^{-1} (AU))
ρ Oph A	B2/B3 V	8.27 ± 1.18	121 ± 16	25.7 (3.1)
ρ Oph B	B2 V	8.27 ± 1.18	121 ± 16	30.5 (3.7)
ρ Oph C	B5 V^a	7.76 ± 0.96	129 ± 15	28.3 (3.7)
ρ Oph DE	B3/B4 V	7.33 ± 1.37	136 ± 22	22.5 (3.1)
β^1 Sco	B0.5 V	6.15 ± 1.12	163 ± 26	25.8 (4.2)
β^2 Sco	B2 V	2.88 ± 12.99	347 ± 284	82.3 (29)
ν^1 Sco	B2 IV	7.47 ± 1.11	134 ± 17	27.0 (3.6)
ν^3 Sco	B8/B9 V	7.47 ± 1.11	134 ± 17	18.5 (2.5)

Table 3.1: Primary targets observed for the 2005 programme. Parallaxes and proper motions in milli-arcseconds (mas) are taken from the Hipparcos catalogue.

Apart from the probably erroneous value quoted for the proper motion of β^2 Sco, the majority targets observed in April 2005 are estimated to have moved $\sim$ 3 AU in the 10 months since their original observation in June 2004.

3.2.1 Searching for SSS variations

Which method to use in order to look for differences in DIB strengths (and potentially profiles) is, on first inspection, not obvious. One approach is to compare continuum normalised diffuse band profiles for each target star. With careful, systematic selection of the continuum regions surrounding the band then it should in principle be possible to discern differences in band strengths (see Figure 3.4).

Given the very high signal-to-noise of these data (S/N, up to ~ 2000) and that overlaying band profiles allows differences in their strengths and *shape*, this method is highly attractive. This technique is most reliable when the continuum regions surrounding the diffuse band are well behaved, i.e., the overall continuum of the background star on which the DIB is superimposed is free of stellar features that contaminate the DIB profile. It is for this reason that DIB observations are ideally carried out towards early spectral type, fast-rotating stars where there are relatively few contaminating spectral features and those that are present are smeared out by the fast-rotation of the star. Another factor that can make defining the continuum difficult is when the DIB is blended with another nearby feature.

When searching for differences in diffuse bands it is therefore desirable to study narrow, unblended DIBs towards a pair of closely separated, fast rotating bright stars of similar (early) spectral type. Unfortunately this scenario is rare and generally judgements have to be made as to where the true continuum lies. Given these potential difficulties it is possible that when small differences are detected using this method that the observed variation is due to the definition of the continuum and is not actually due to any *real* differences in the DIB strengths.

3.2.2 Spectral ratios

Given the somewhat subjective nature of the method outlined in section 3.2.1, that the differences in DIB strengths observed in 2004 are small (~ 5% difference in a ~ 10% absorption) and that differences due to the proper motion displacement of the stars are likely to be even *smaller*, a more robust, objective method is required for ‘tiny-scale’ structure investigations. Before deciding on a new method it is helpful to identify those steps in the analysis using overlaid spectra approach where a judgement is made by the

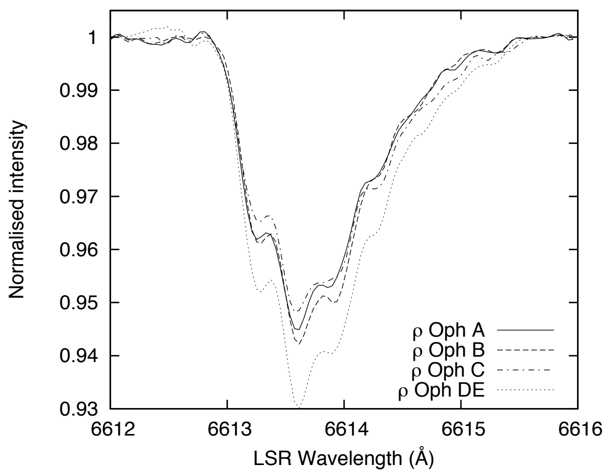

Figure 3.4: The λ6614 feature in the ρ Oph stars A, B, C and DE (from Cordiner 2005).

user.

When comparing DIB profiles, the DIB spectrum must be fully reduced i.e. standard CCD reductions, spectra extracted, wavelength calibrated, blaze corrected, telluric corrected and continuum normalised. Blaze correction, removal of telluric lines and continuum normalisation are all somewhat subjective steps of the reduction process that may, at each point, introduce differences in the final spectra that might be interpreted (incorrectly) as an indications of small- or tiny-scale structure (TSS).

If observations of pairs/multiples are carried out at similar air masses then the telluric features in each spectrum should be almost identical. Also, for a given night, if all observations are carried out with the same spectrograph configuration, i.e. using same central wavelength ($\lambda_{central}$) and cross disperser settings, then the shape of the blaze function introduced by the spectrograph in each exposure should be *identical*. To search for TSS variations, a new method was introduced whereby a direct division was made of spectra that had *not* undergone blaze, telluric or continuum correction. This method eliminates the three subjective reduction steps and should be significantly more robust.

An example of such a division is shown in Figure 3.5. The spectra in the upper two traces are of ρ Oph A and B. The curve in the continuum due to the blaze function of the spectrograph and some telluric features can clearly be seen. The bottom trace is of the direct division of these two 'raw' spectra, i.e., their ratio. Given their small

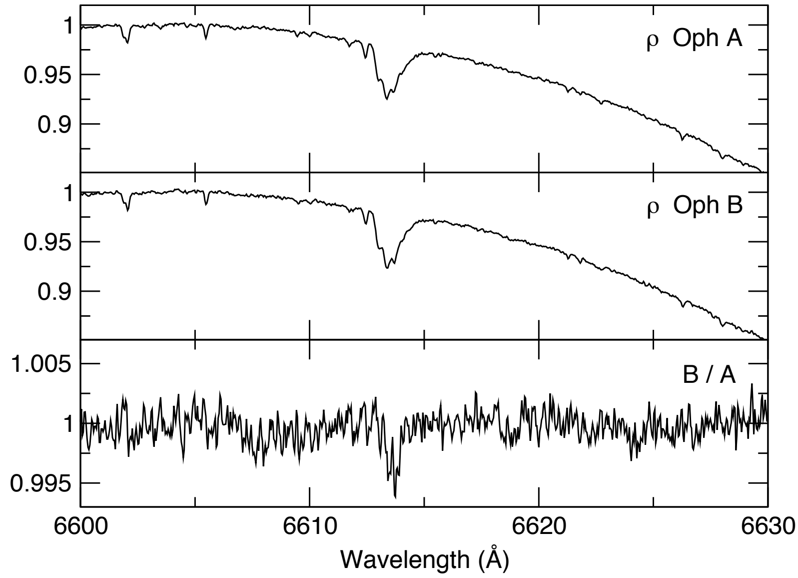

Figure 3.5: The spectral ratio of the λ6614 region from the 2004 data.

sky-projected separation ($\sim 3.5''$), differences in DIB strengths between ρ Oph A and ρ Oph B are expected to be small. Figure 3.4 suggests that there is a difference in the strengths of A and B and this is confirmed by Figure 3.5, clearly showing that λ6614 is stronger in ρ Oph B.

Examination of the overall 'continuum' of the spectral ratio shows that the telluric cancellation is excellent and that any shape due to the blaze function has been successfully removed. Any residual shape in the ratios can probably be accounted for by small differences in spectral type. If encountered, a simple fit with a low-order polynomial aids the presentation of the data.

It is with this new method of taking ratios of the spectra that have not undergone blaze or telluric correction that the data in this thesis are presented. Small-scale-structure differences in the DIBs are presented as a sequence of spectra and chosen ratios of the individual star spectra. In a search for 'tiny-scale' structure (TSS), results are presented as a comparison of the ratios of two stars from the 2004 and 2005 dataset and any difference between them. If there *are* TSS variations in the diffuse bands then this objective, highly sensitive method would be expected to reveal them.

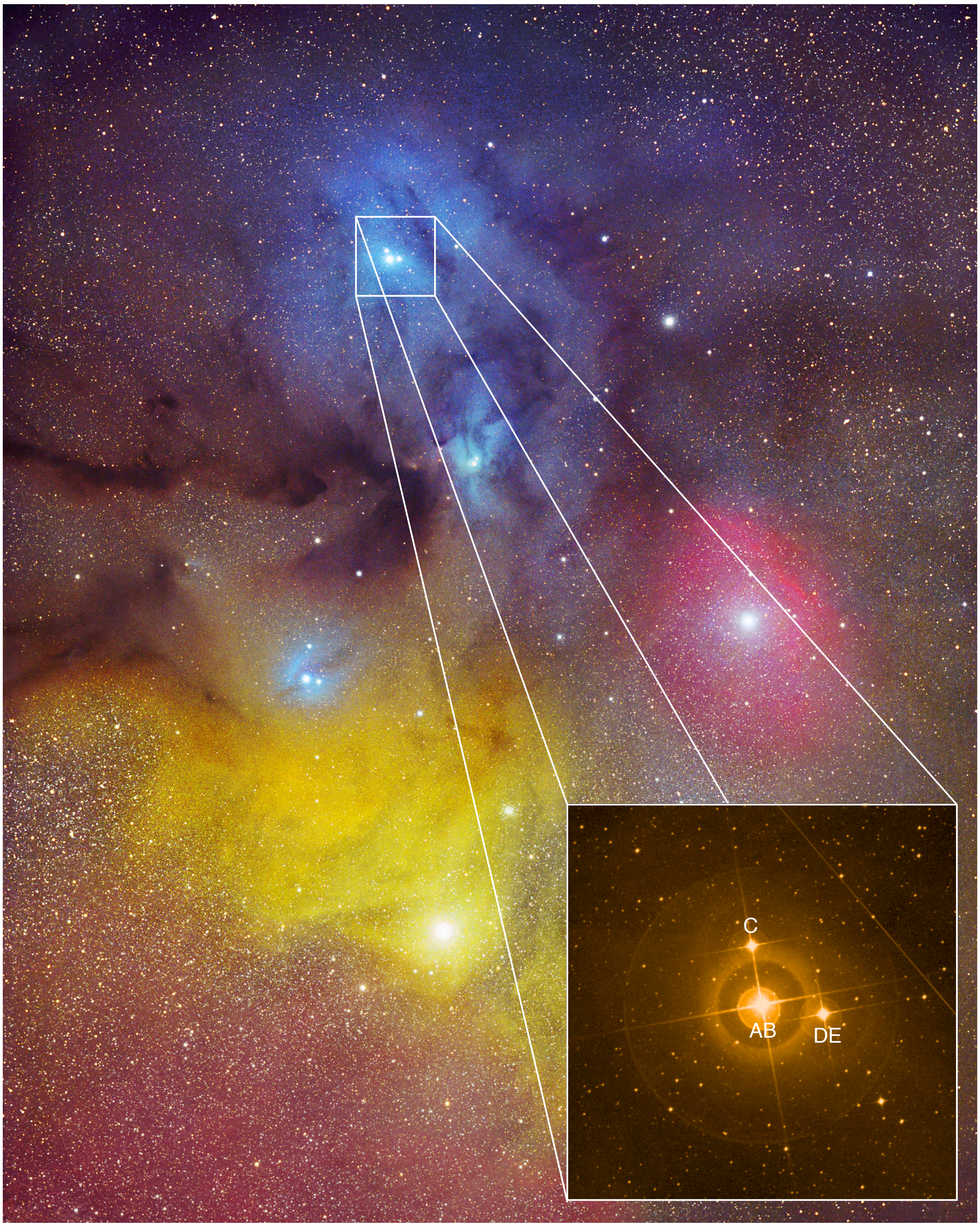

Figure 3.6: Image of the Scorpius–Ophiuchus constellations. ρ Oph stars are marked in Digitized Sky Survey (DSS2) R-Band image (bottom right). Colour image used with permission and courtesy of Daphne Hallas (www.astrophoto.com).

3.3 Results and analysis

3.3.1 SSS probed through diffuse interstellar band observations

After the success of the DIB-SSS project in 2004 it was an obvious extension of the study to search for variations in the diffuse bands at shorter wavelengths. Less studied than their yellow/red counterparts, the blue DIBs are generally weaker and hence more difficult to detect. Table 3.2 lists the selection of blue "C_2" DIBs studied in this work[2], their strengths (equivalent widths) in ρ Oph A and approximate *FWHM*.

Feature	W_λ (mÅ)	$FWHM$ (Å)
λ4726	121	3.8
λ4734	5.6	0.5
λ4964	23.5	0.6
λ4984	14.0	0.5
λ5170	7.1	0.5
λ5176	7.4	0.7
λ5418	13.7	0.6
λ5512	13.8	0.5
λ5541	5.5	0.5
λ5546	16.9	0.6

Table 3.2: Blue diffuse bands analysed in this study. Typical strengths and $FWHM$ values are as measured towards ρ Oph A.

For the 2005 observations, spectra were recorded in the wavelength range 4600 – 8400 Å for all targets listed in Table 3.1. As a consequence of the broad spectral range offered by the UCLES spectrograph, the majority of the yellow/red diffuse bands (redward of ~ 5700 Å) were recorded again in 2005 thus offering an opportunity to check the 2004 result (Cordiner 2005) and also look for variations *between* years. Table 3.3 lists the yellow/red DIBs studied here together with their strength and $FWHM$ towards ρ Oph A.

The relatively weak blue DIBs were only detected towards the ρ Oph stars and so they are therefore analysed only in these targets. The lack of blue DIBs towards the other targets is not surprising given that they are much more σ-like environments than ρ

[2]Due to their weakness, not all of the DIBs identified as "C_2" DIBs are analysed here. For a complete list of the "C_2" DIBs the reader is directed to Thorburn *et al.* 2003.

Feature	W_λ (mÅ)	$FWHM$ (Å)
λ5705	39.6	2.9
λ5780	188	2.0
λ5797	49.7	0.88
λ5850	29.8	0.71
λ6196	15.9	0.50
λ6203	42.0	1.7
λ6284	302	3.3
λ6376	14.8	0.62
λ6379	27.1	0.68
λ6426	2.7	0.20
λ6614	63.9	1.2
λ6660	0.9	0.61
λ7562	34.9	2.4

Table 3.3: Yellow/red diffuse bands analysed in this study. Typical strengths and $FWHM$ values are as measured towards ρ Oph A.

Oph[3] lines of sight.

Recent studies by Thorburn *et al.* (2003) suggested that some of the strongest blue DIBs were closely related to the C_2 molecule. This interesting study showed that out of the twenty-one DIBs analysed, seven were found to be "C_2" DIBs, that is, their normalised intensity ($W_{\mathrm{DIB}}/W_{\lambda 6196}$) is well correlated with $N(C_2)/E_{B-V}$. This is a potentially important result as Thorburn *et al.* also showed that some of the more 'famous' red DIBs at most only weakly correlate with $N(C_2)/E_{B-V}$. One interpretation of this result is that the red bands trace more diffuse regions than the blue features. This is discussed further in this chapter.

Figure 3.7 shows the λ4726 DIB seen towards ρ Oph A, B, C and DE (top to bottom) and the ratios $I_\lambda(B)/I_\lambda(A)$, $I_\lambda(C)/I_\lambda(A)$, $I_\lambda(DE)/I_\lambda(A)$ and $I_\lambda(C)/I_\lambda(DE)$. This relatively strong DIB ($\sim$ 120 mÅ in ρ Oph A, Table 3.2) has been identified as a blend of two or more features (Thorburn *et al.* 2003) and its unusual structure is clear. With their close spectral-type match, the spectra of ρ Oph A and B are remarkably similar and provide the best pair for comparison of the DIBs. Fortunately their sky-projected separation is also the lowest[4] of any of the binary and multiple stars observed in this programme

[3]The ρ Oph region lies somewhere between the σ and ζ classifications (Krełowski & Sneden 1995) having stronger λ5780 than λ5797 with a ratio ($W_{\lambda 5780}/W_{\lambda 5797}$) of $\sim$ 4. True 'σ'-type environments are characterised by a much higher ratio (weak λ5797 e.g. β Sco $W_{\lambda 5780}/W_{\lambda 5797} \simeq 9$), have low concentrations of small (diatomic) molecules and do not display the weak blue DIBs.

thus providing a sensitive probe of the structure of the ISM.

Figures 3.8 through to 3.23 have the same overall layout as Figure 3.7. The S/N in ρ Oph A and B clearly exceeds that of C and DE however differences in the DIB strengths are clearly visible in λ4726, λ4734, λ4964, λ4984, λ5418, λ5512, λ5546, λ5780, λ5797, λ5850, λ6196, λ6203, λ6284, λ6376, λ6379 and λ6614. Table 3.3.1 lists the DIB strengths in ρ Oph together with the atomic data (K I, Na I D_1 from this study) and other known species from Pan *et al.* (2004). Errors associated with the measurement of the DIBs can be approximated as the RMS noise in the continuum over the width of the feature measured i.e., $\sigma_{\mathrm{RMS}}\Delta_\lambda$ and typical values are quoted in Table 3.3.1.

Examination of Figures 3.7 through to 3.23 show that, particularly for ratios involving ρ Oph C, stellar features can introduce significant uncertainty in the ratios. In some cases (e.g. λ5170) there is also a large stellar feature in the composite spectrum of ρ Oph DE. A stellar feature in the spectrum of one of the stars being ratioed does not always mean that nothing can be learned from the ratio: for the λ5170 DIB and the ratio DE/A, there is clearly a stellar feature in DE, although the relatively smooth symmetrical shape of the feature in the residual shows that there is little difference in the relative DIB strengths.

It is immediately apparent from the spectra and the values listed in Table 3.3.1 that for the vast majority of the blue DIBs measured (λ < 5700 Å), their strengths are significantly lower towards ρ Oph DE than A, B or C with very little difference between the A and B values. Significantly the blue "C_2" DIBs behave as expected if they are related to the C_2 molecule. $N(C_2)$ values measured by Thorburn *et al.* (2003) are included in Table 3.3.1 and are higher towards ρ Oph A (stronger blue DIBs) than ρ Oph DE (weaker blue DIBs). This striking behaviour of the blue DIB strengths is very different from that observed in the yellow/red bands where, for the majority of features, the strength towards ρ Oph DE is significantly greater than A, B or C. It is clear that the factors influencing the strengths of yellow/red DIBs are different from those of the blue features.

[4]The ρ Oph DE pair have a smaller sky-projected separation than the AB pair but with a value of under 1″ it is not possible to record individual spectra of ρ Oph D and E without adaptive optics.

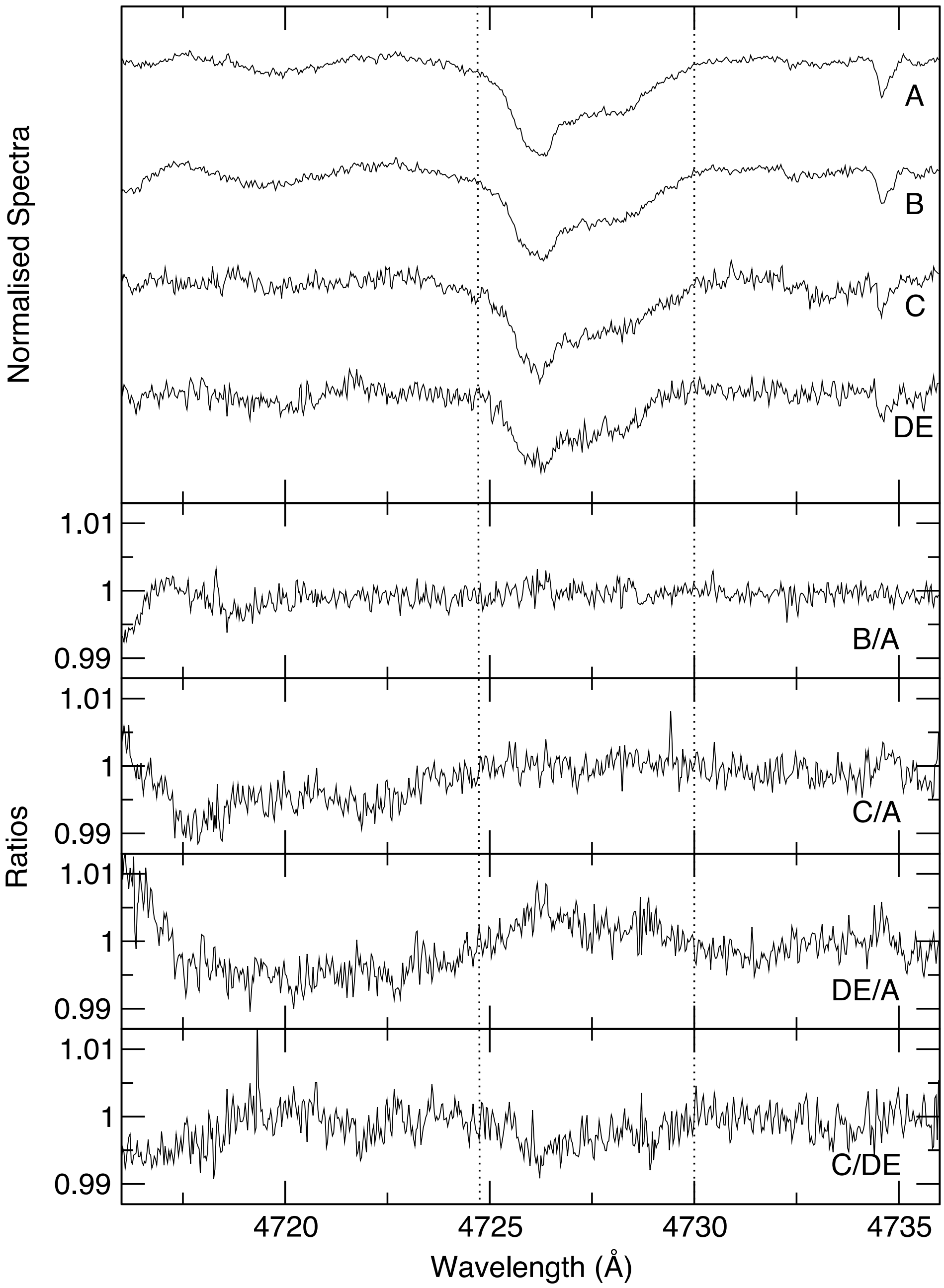

Figure 3.7: From top to bottom: Spectra of λ4726 recorded towards ρ Oph A, B, C and DE (upper panel) and the ratios B/A , C/A , DE/A and C/DE

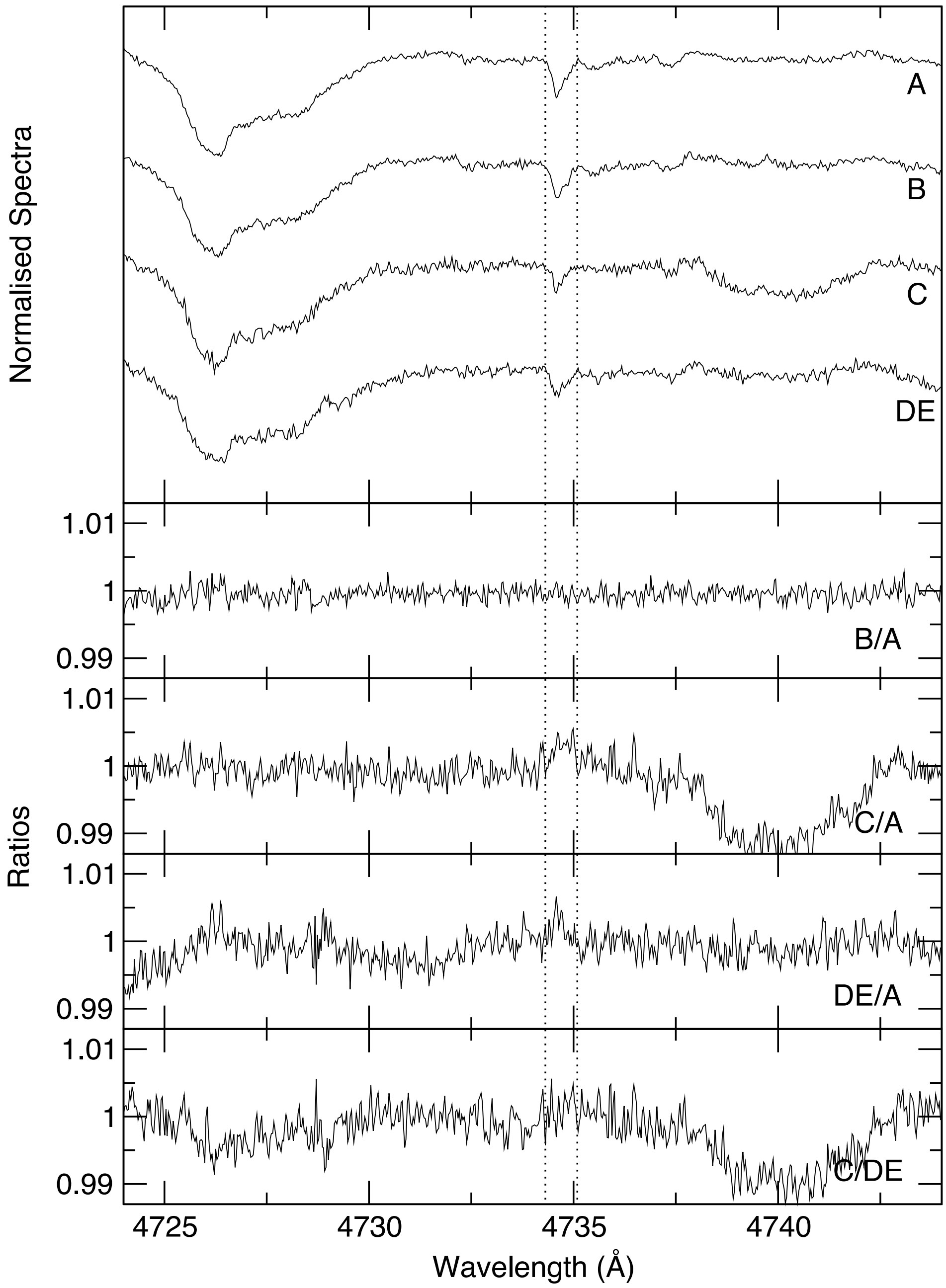

Figure 3.8: From top to bottom: Spectra of λ4734 recorded towards ρ Oph A, B, C and DE (upper panel) and the ratios B/A , C/A , DE/A and C/DE

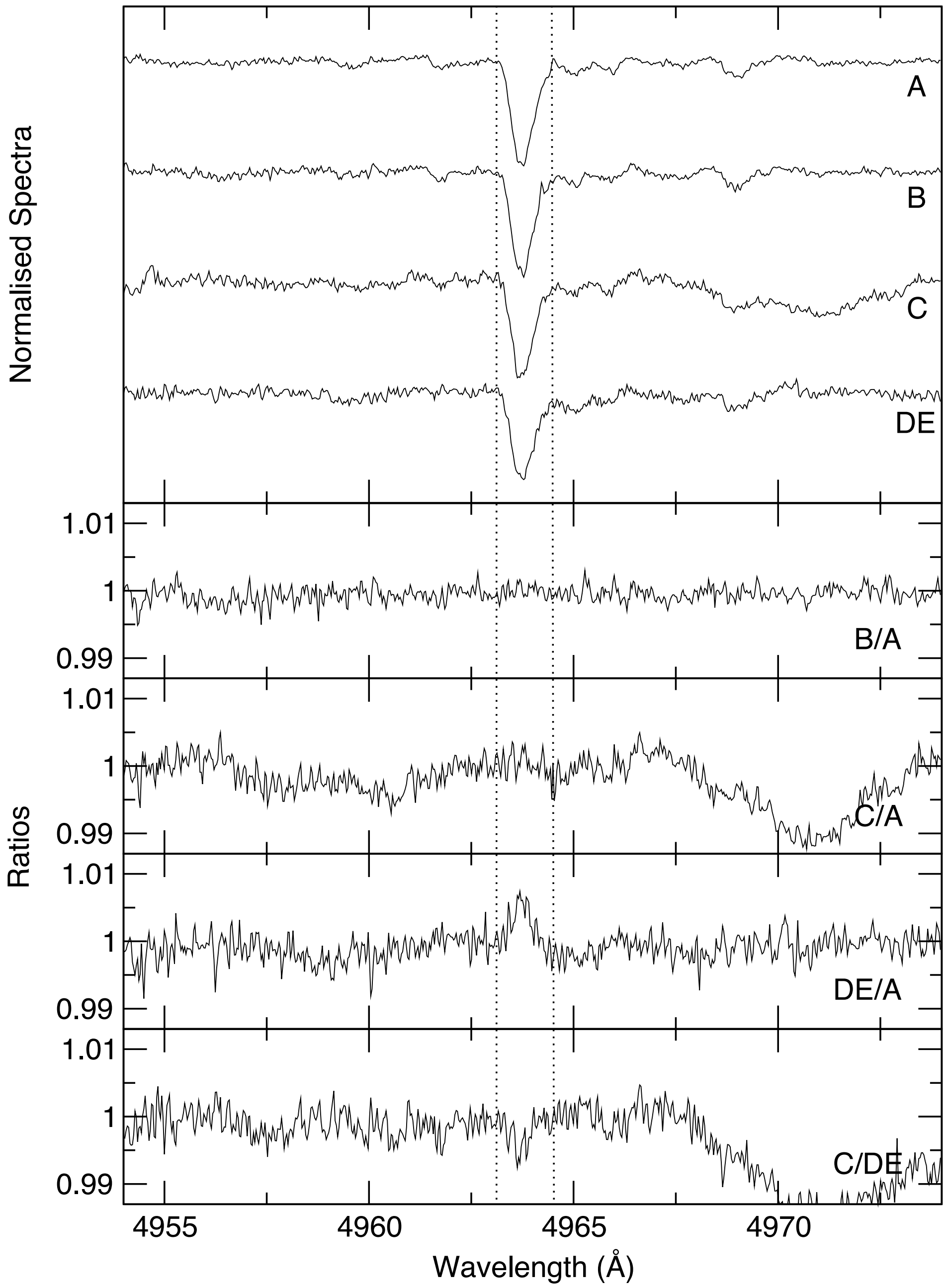

Figure 3.9: From top to bottom: Spectra of λ4964 recorded towards ρ Oph A, B, C and DE (upper panel) and the ratios B/A , C/A , DE/A and C/DE

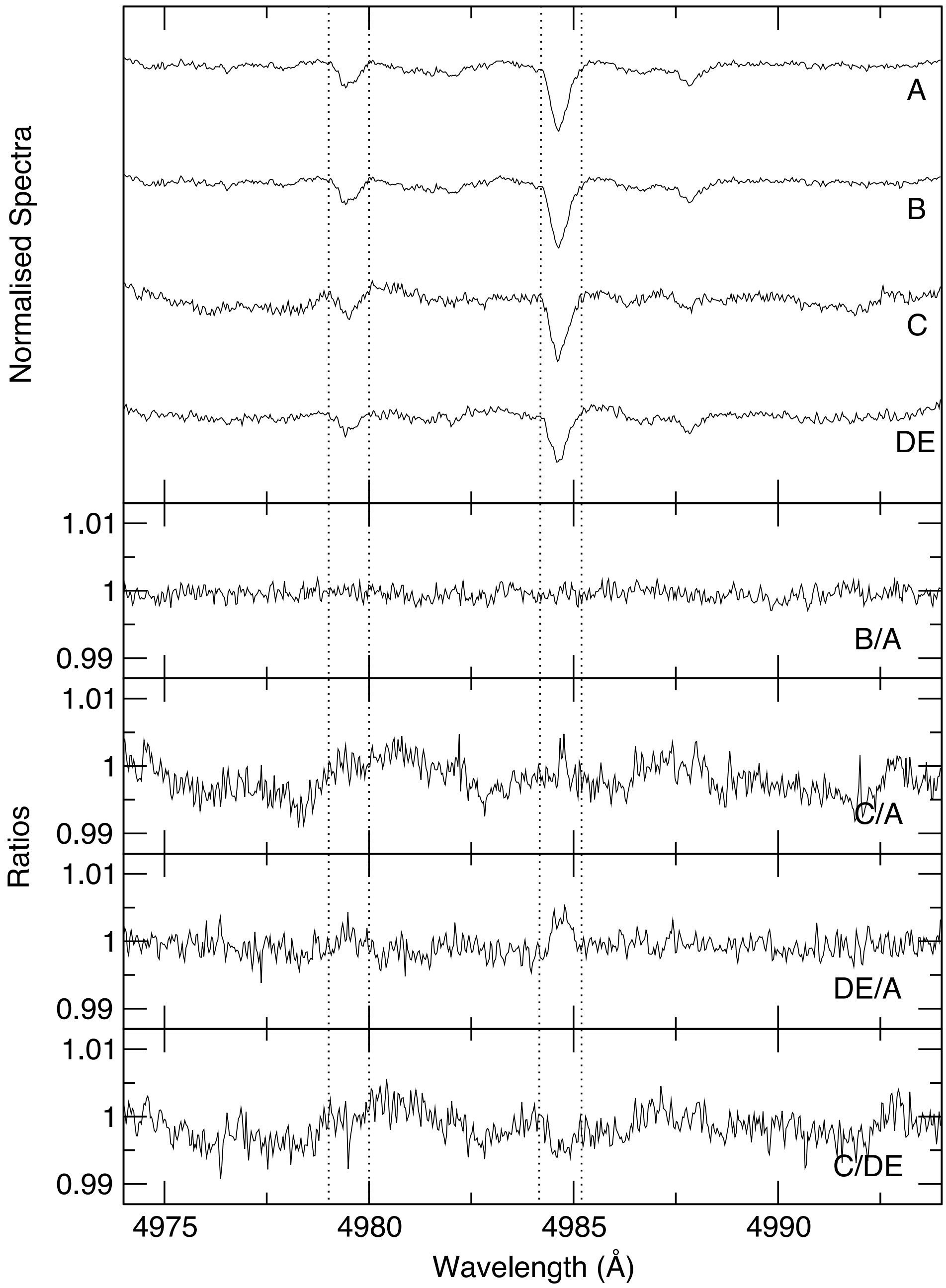

Figure 3.10: From top to bottom: Spectra of λ4984 recorded towards ρ Oph A, B, C and DE (upper panel) and the ratios B/A , C/A , DE/A and C/DE

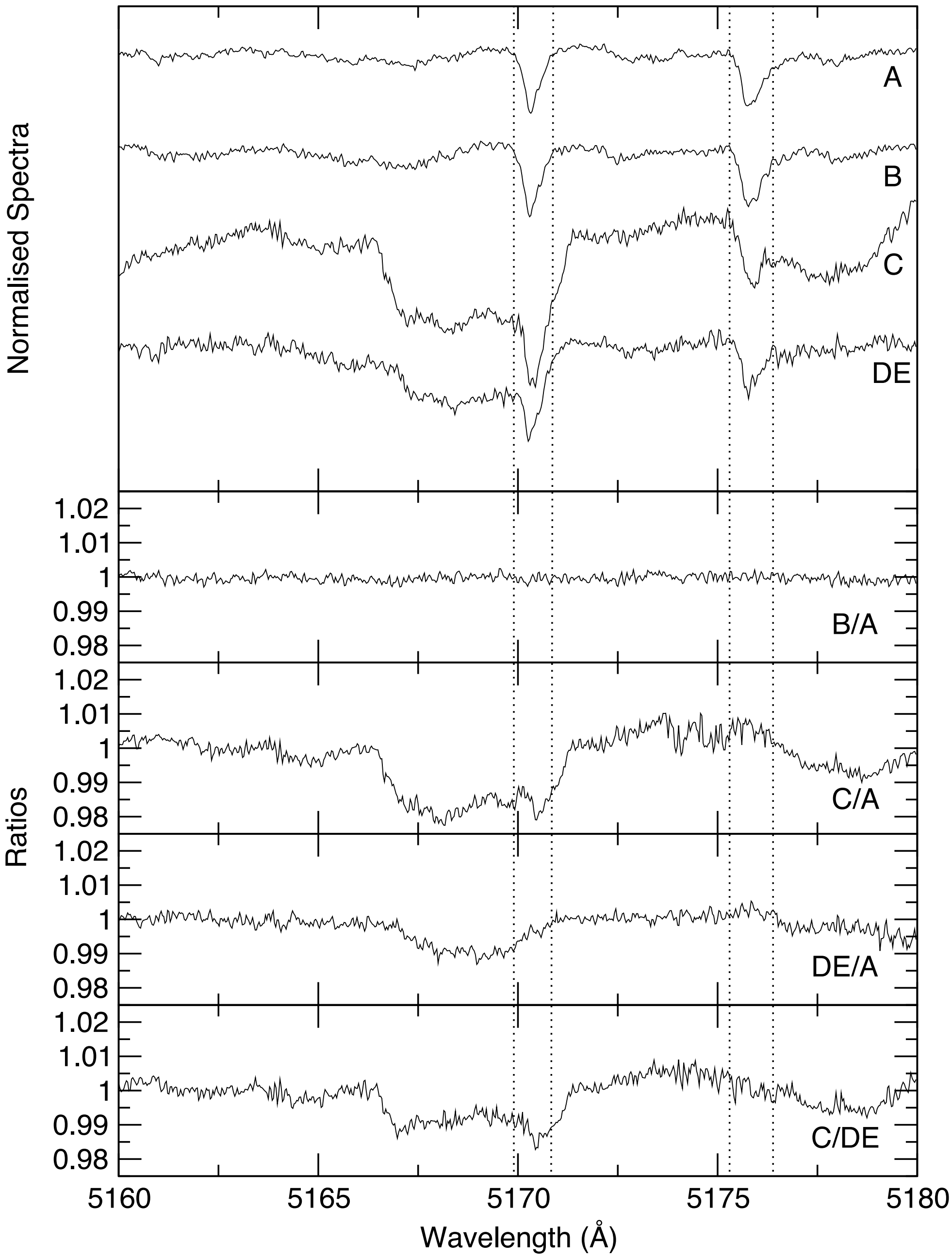

Figure 3.11: From top to bottom: Spectra of $\lambda5170$ and $\lambda5176$ recorded towards ρ Oph A, B, C and DE (upper panel) and the ratios B/A , C/A , DE/A and C/DE

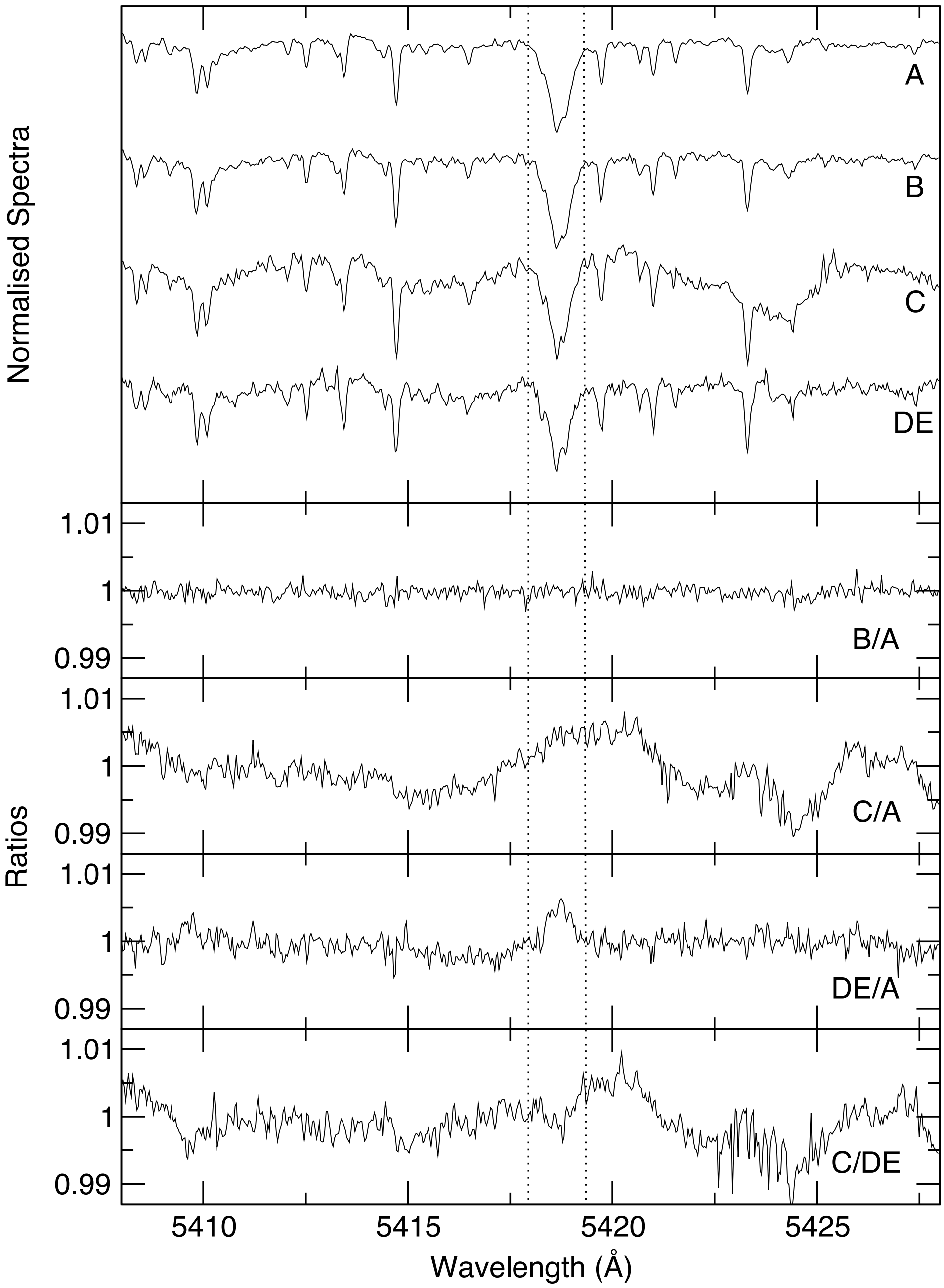

Figure 3.12: From top to bottom: Spectra of $\lambda 5418$ recorded towards ρ Oph A, B, C and DE (upper panel) and the ratios B/A , C/A , DE/A and C/DE

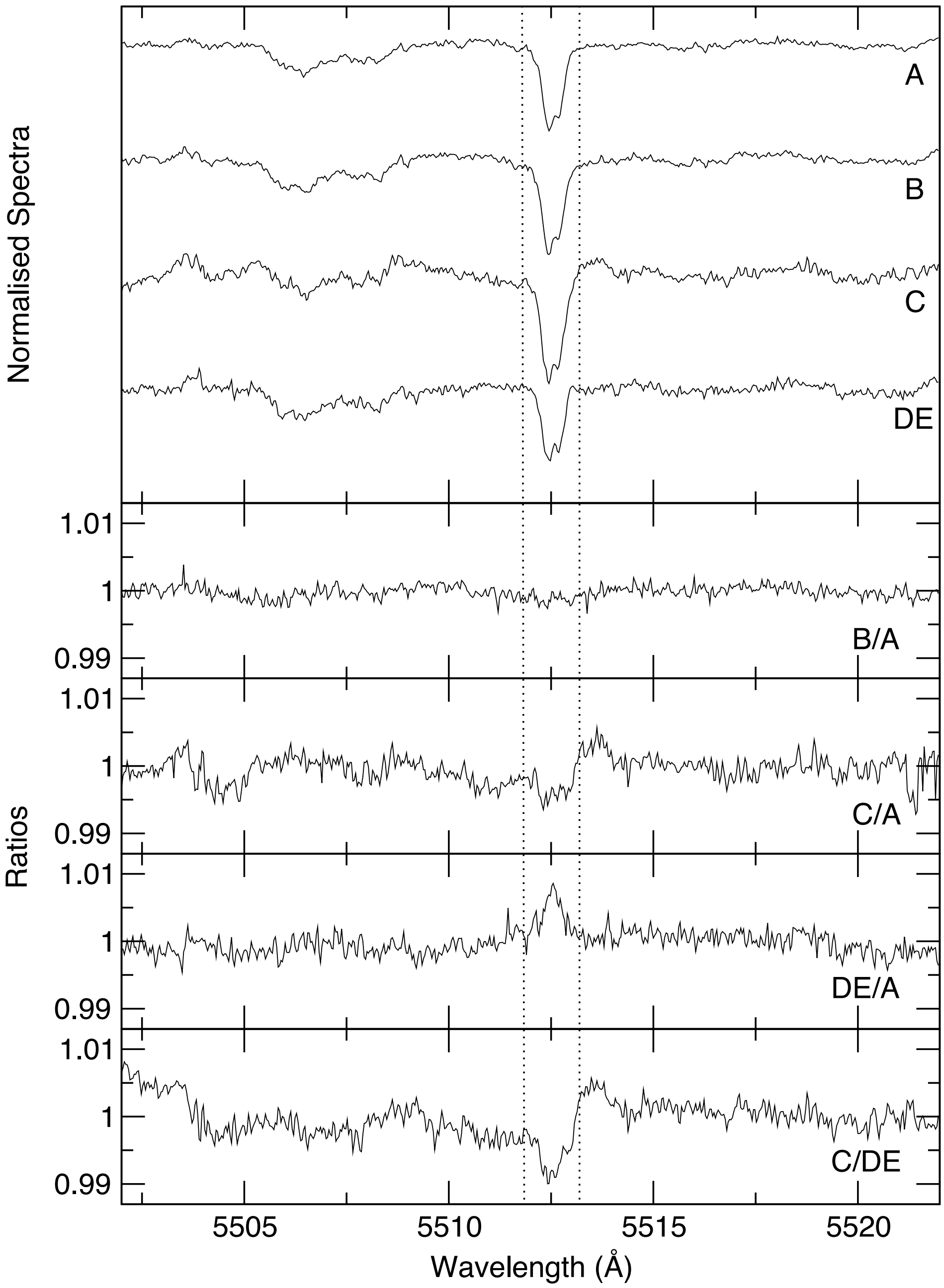

Figure 3.13: From top to bottom: Spectra of λ5512 recorded towards ρ Oph A, B, C and DE (upper panel) and the ratios B/A , C/A , DE/A and C/DE

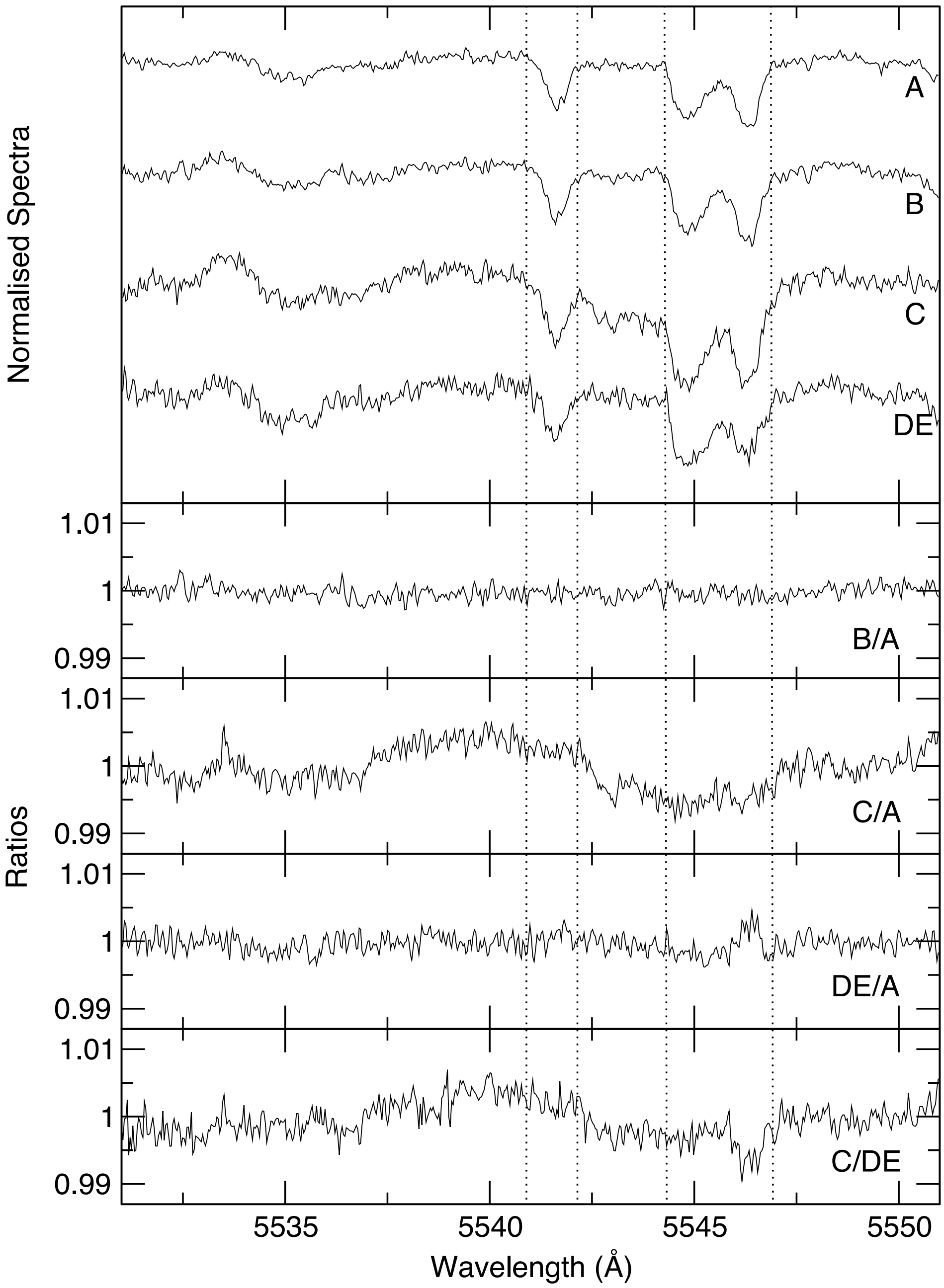

Figure 3.14: From top to bottom: Spectra of $\lambda5541$, $\lambda5544$ and $\lambda5546$ recorded towards ρ Oph A, B, C and DE (upper panel) and the ratios B/A , C/A , DE/A and C/DE

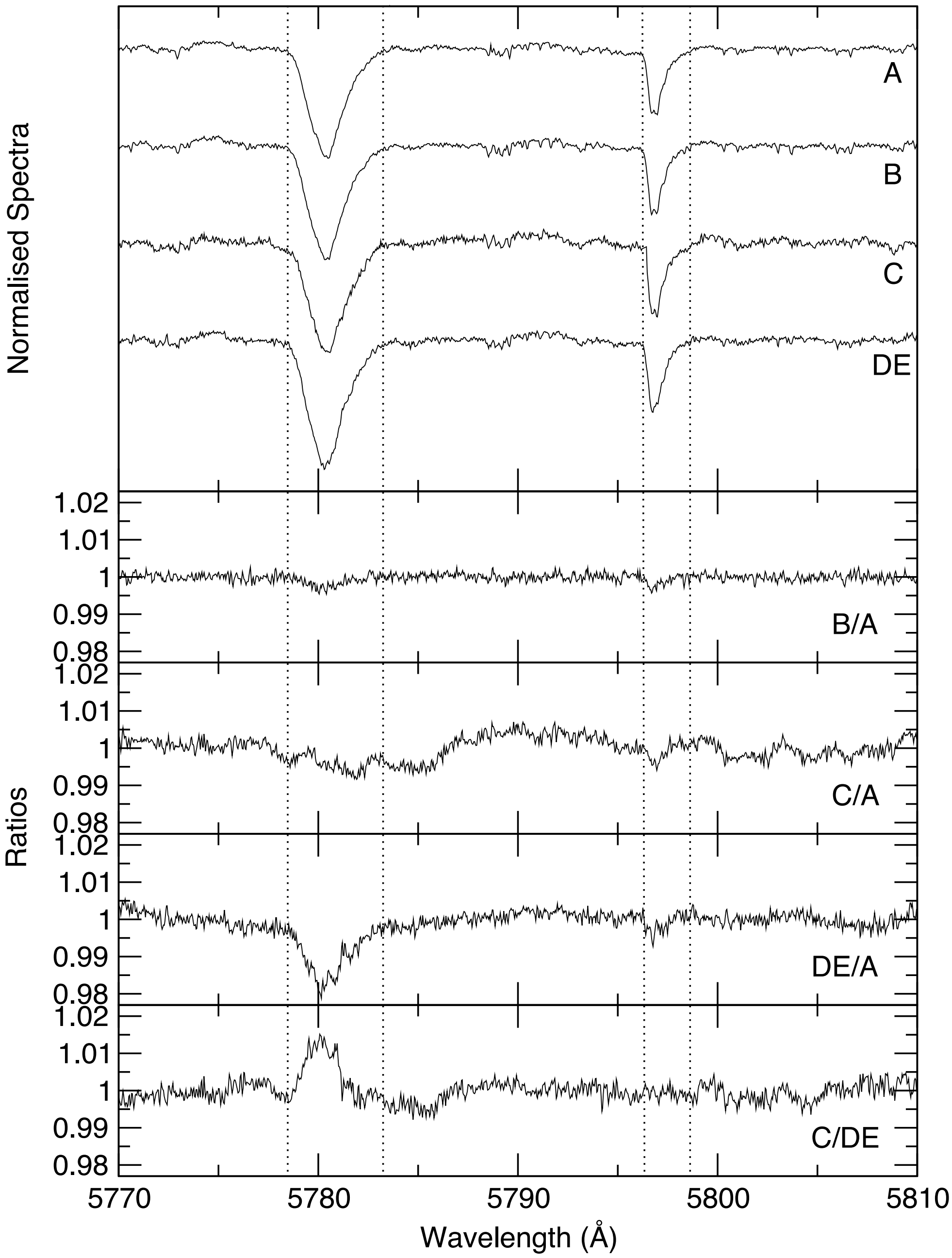

Figure 3.15: From top to bottom: Spectra of $\lambda5780$ and $\lambda5797$ recorded towards ρ Oph A, B, C and DE (upper panel) and the ratios B/A , C/A , DE/A and C/DE

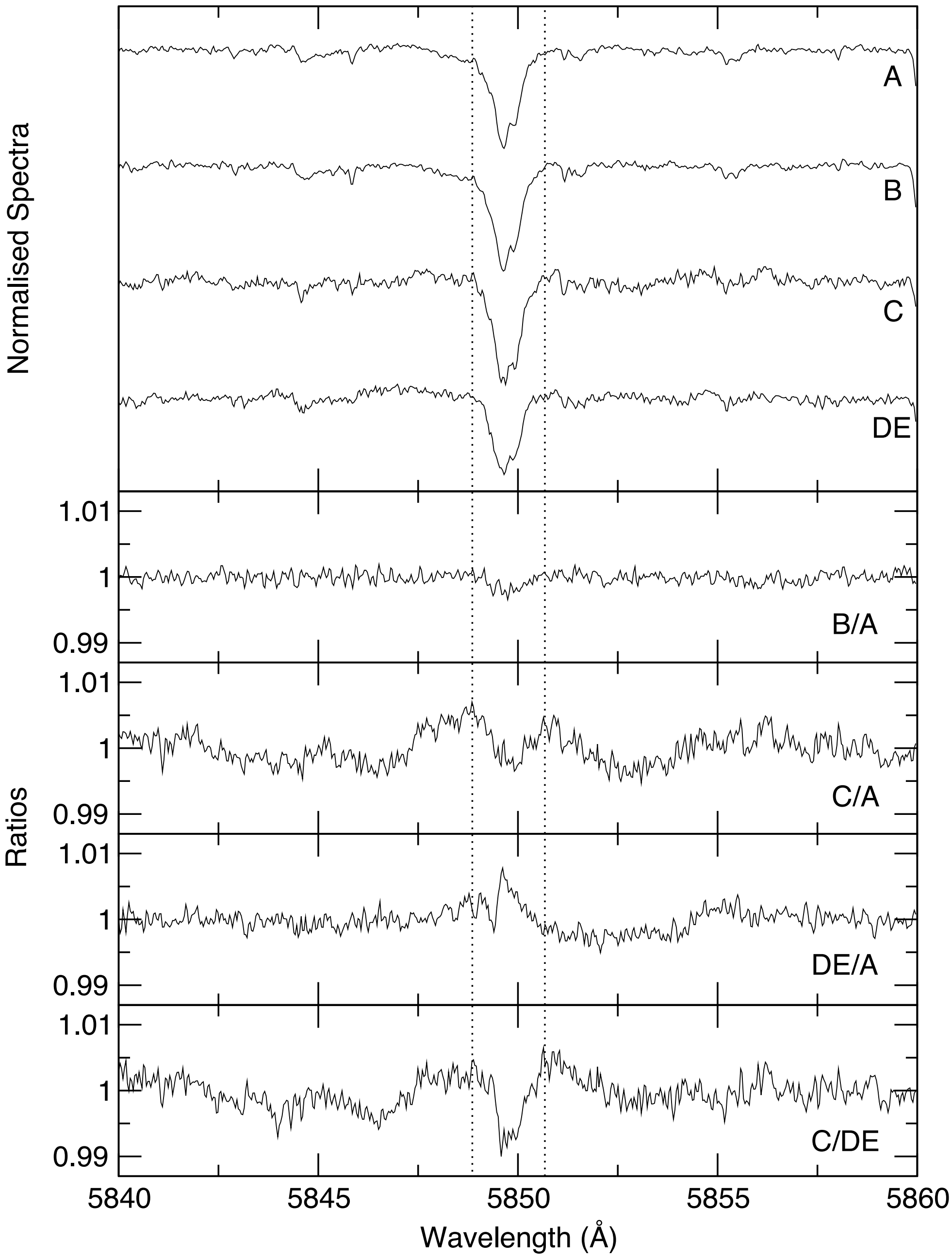

Figure 3.16: From top to bottom: Spectra of $\lambda 5850$ recorded towards ρ Oph A, B, C and DE (upper panel) and the ratios B/A , C/A , DE/A and C/DE

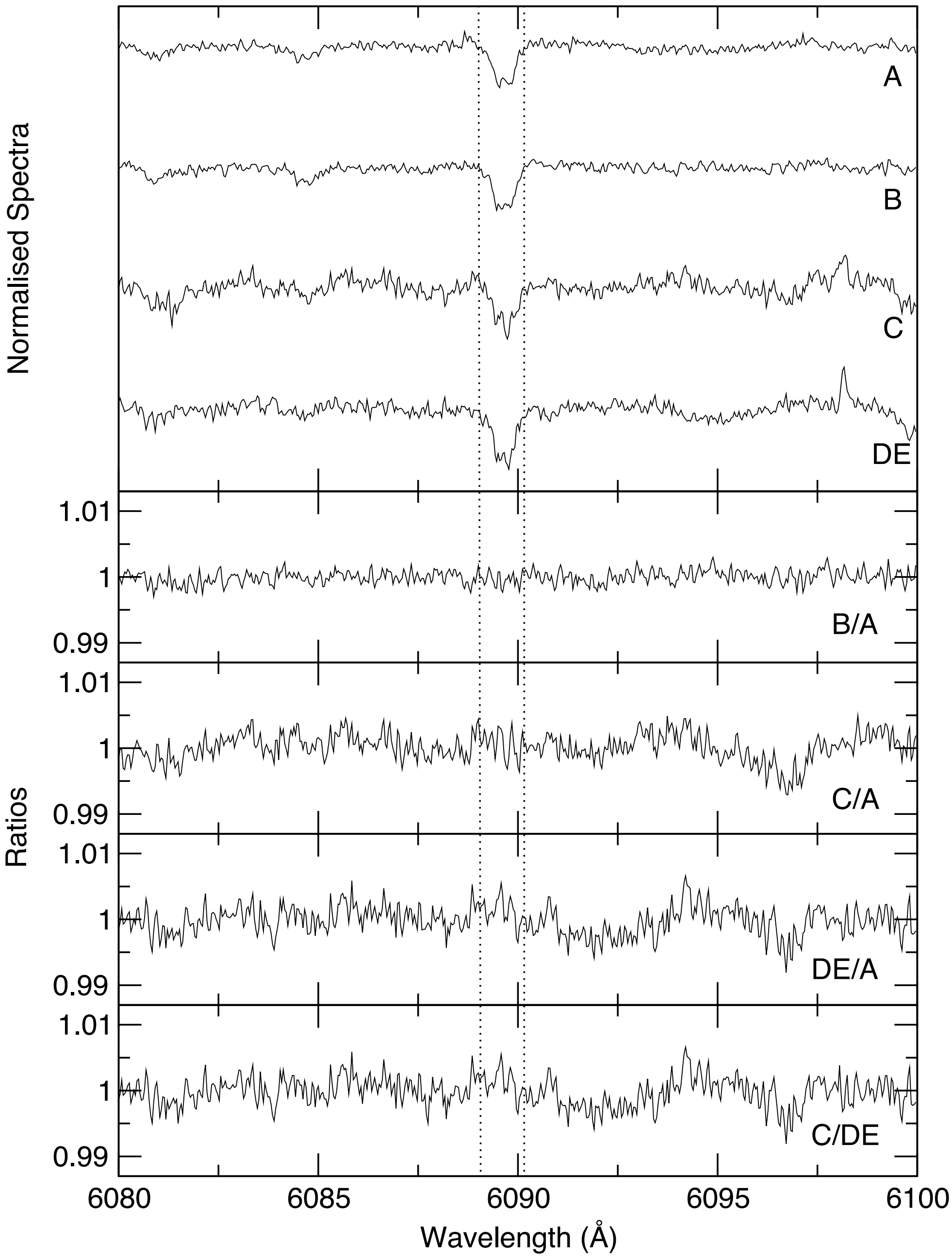

Figure 3.17: From top to bottom: Spectra of $\lambda 6090$ recorded towards ρ Oph A, B, C and DE (upper panel) and the ratios B/A , C/A , DE/A and C/DE

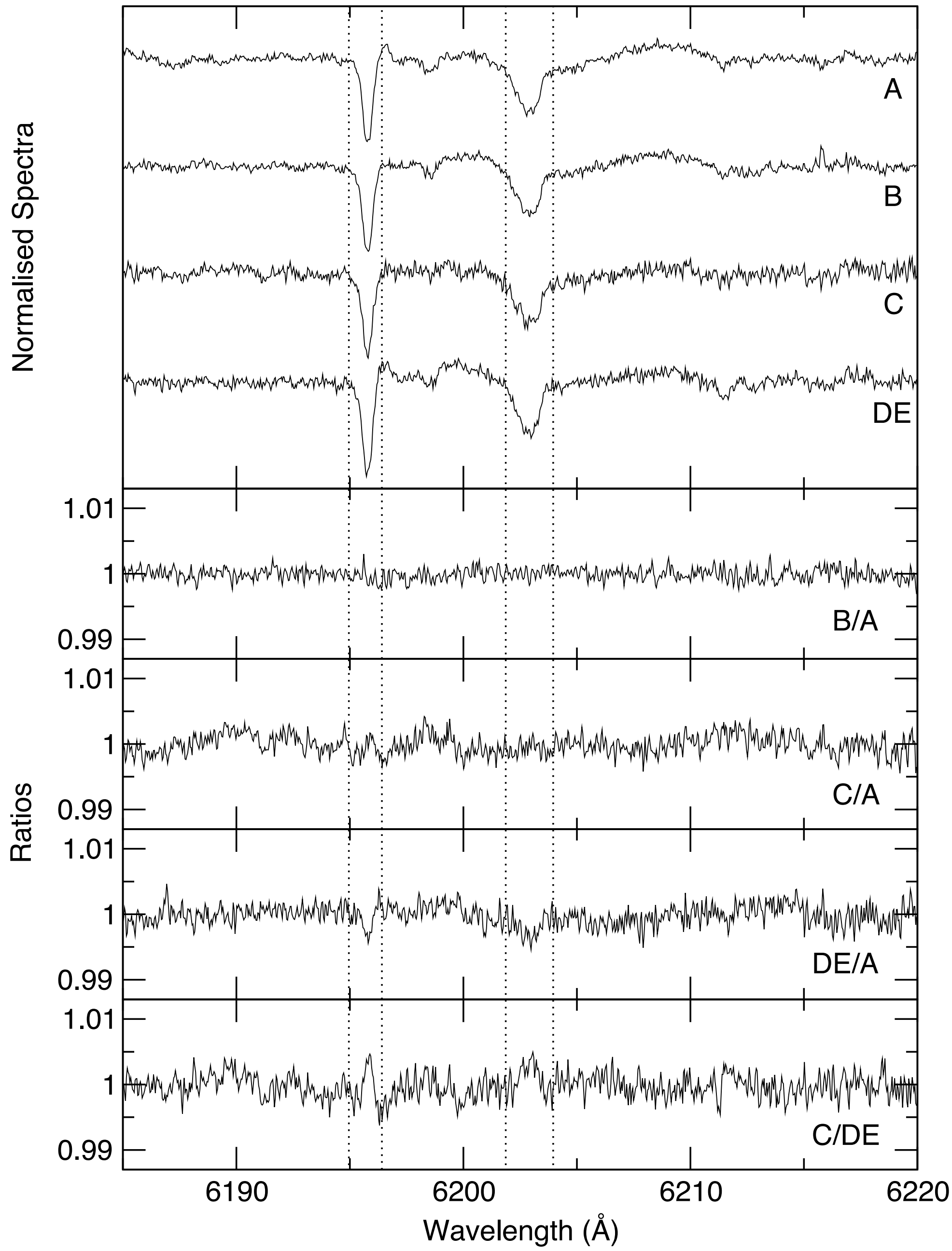

Figure 3.18: From top to bottom: Spectra of λ6196 and λ6203 recorded towards ρ Oph A, B, C and DE (upper panel) and the ratios B/A , C/A , DE/A and C/DE

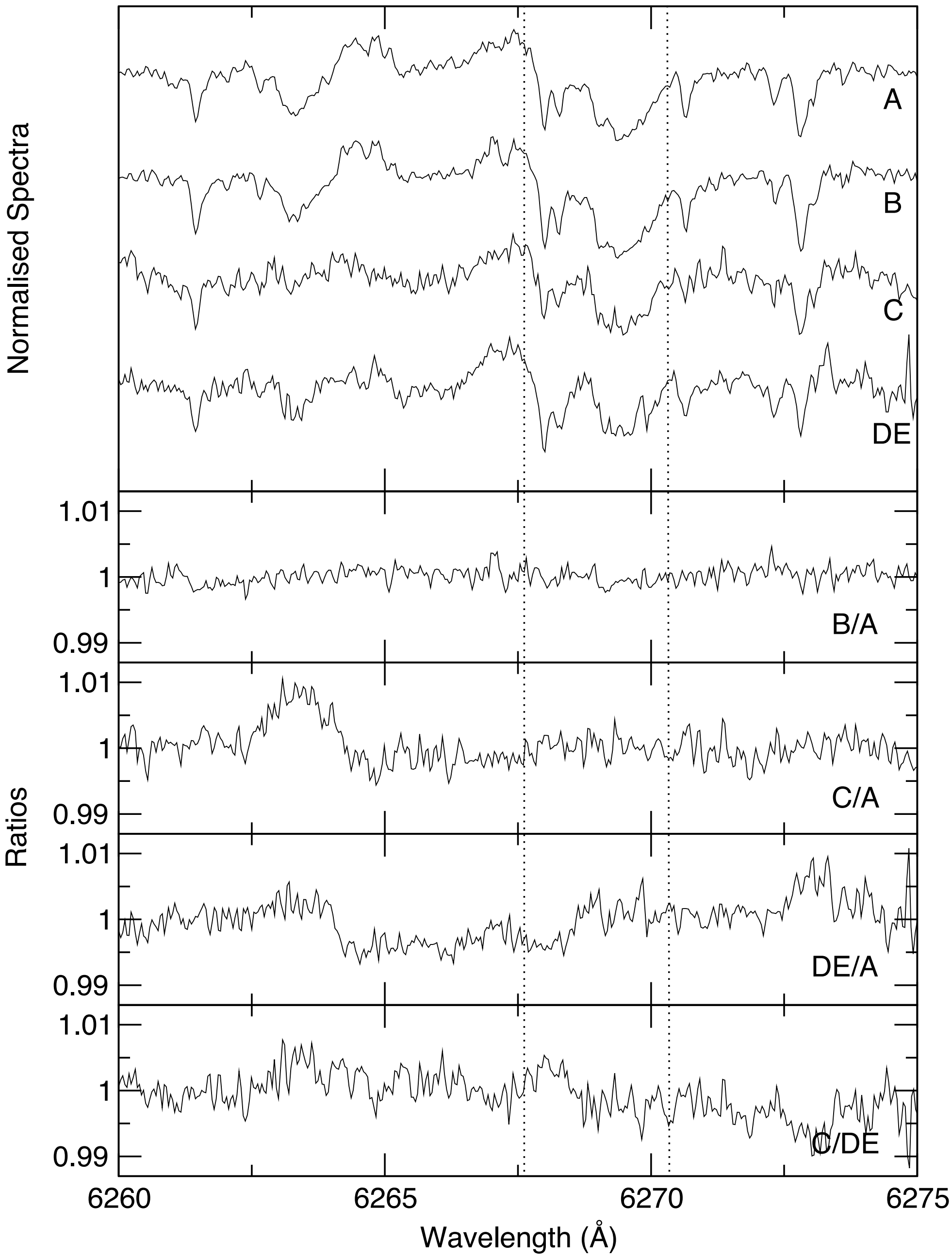

Figure 3.19: From top to bottom: Spectra of $\lambda6270$ recorded towards ρ Oph A, B, C and DE (upper panel) and the ratios B/A , C/A , DE/A and C/DE

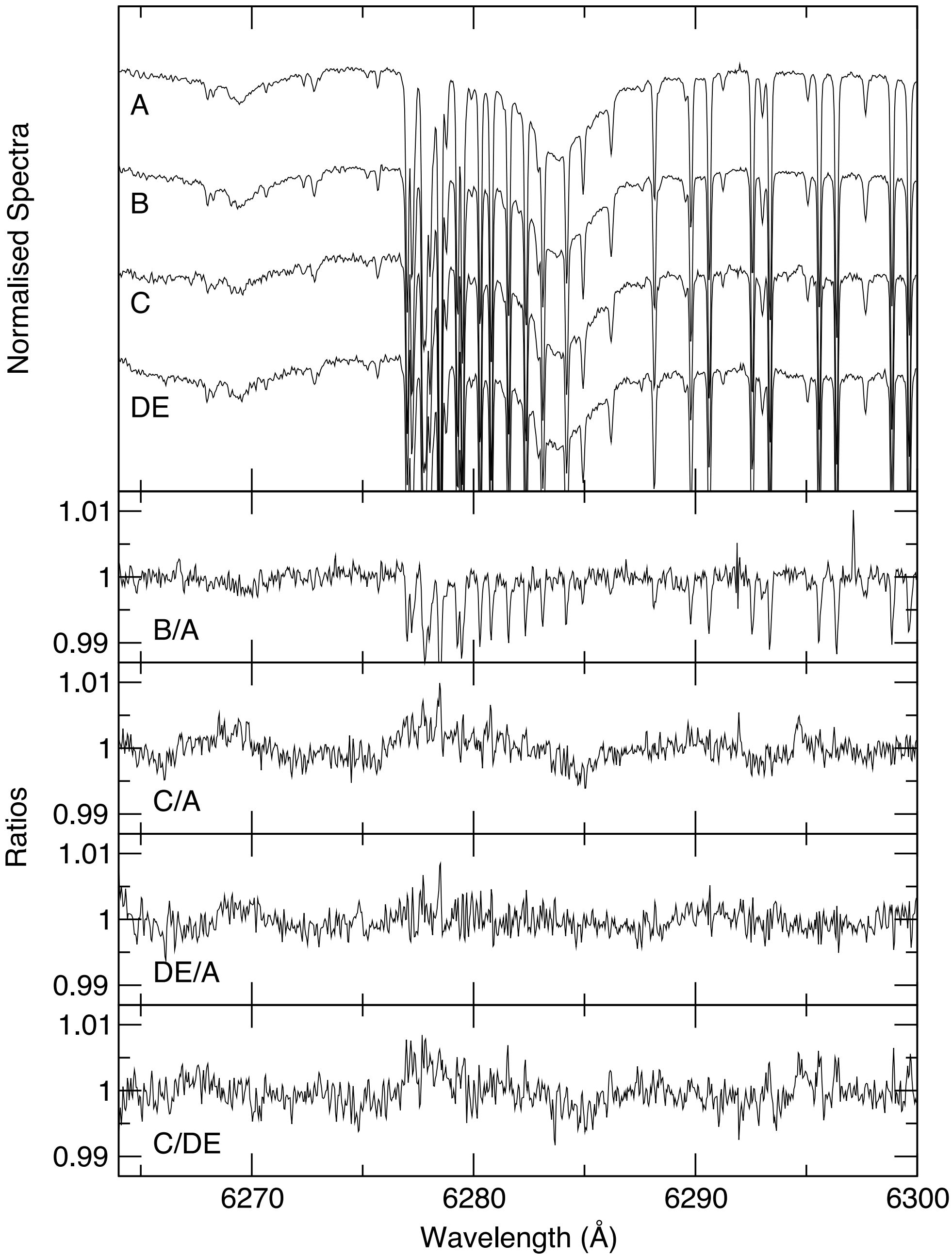

Figure 3.20: From top to bottom: Spectra of $\lambda6284$ recorded towards ρ Oph A, B, C and DE (upper panel) and the ratios B/A , C/A , DE/A and C/DE

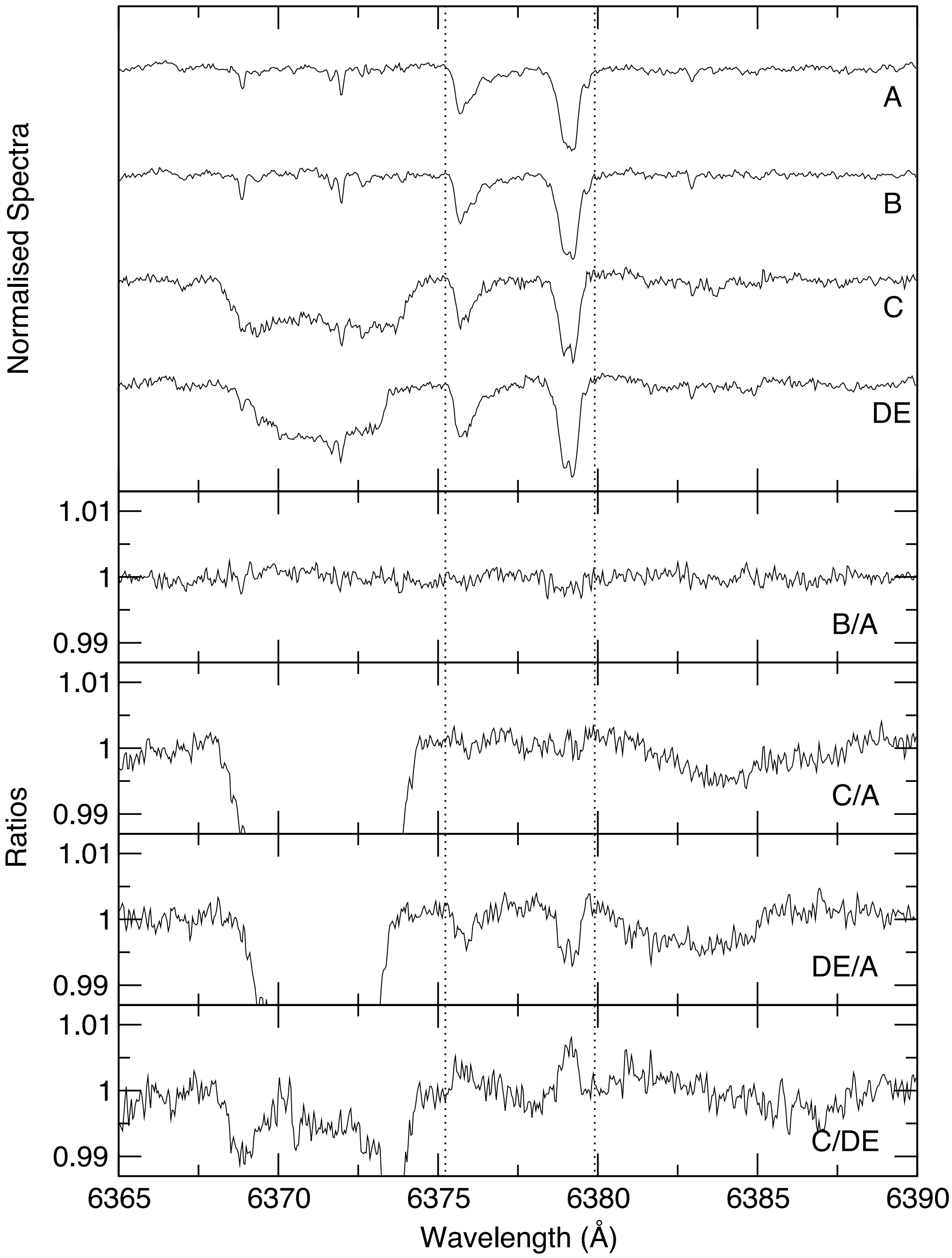

Figure 3.21: From top to bottom: Spectra of $\lambda6376$ and $\lambda6379$ recorded towards ρ Oph A, B, C and DE (upper panel) and the ratios B/A , C/A , DE/A and C/DE

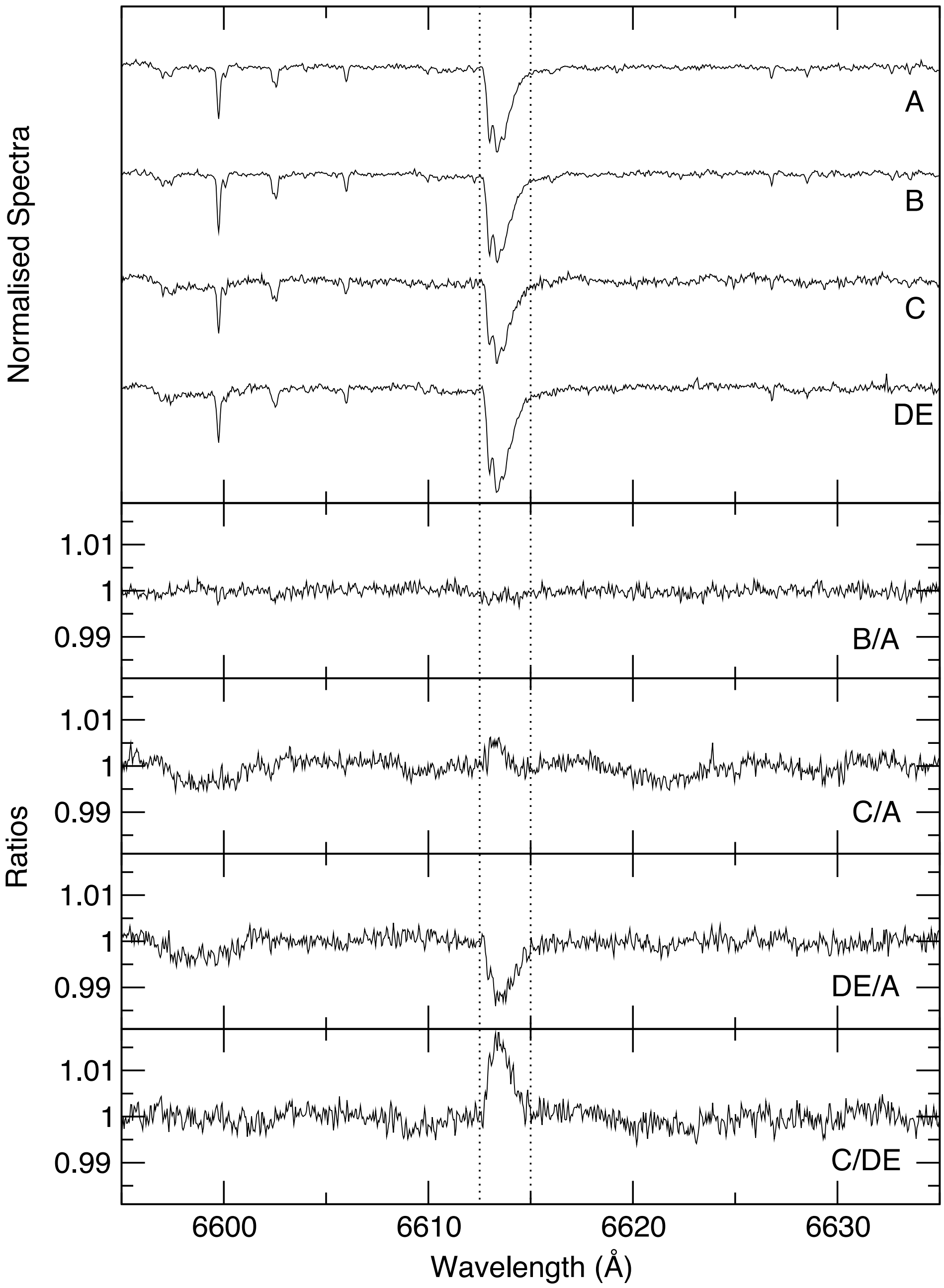

Figure 3.22: From top to bottom: Spectra of $\lambda 6614$ recorded towards ρ Oph A, B, C and DE (upper panel) and the ratios B/A , C/A , DE/A and C/DE

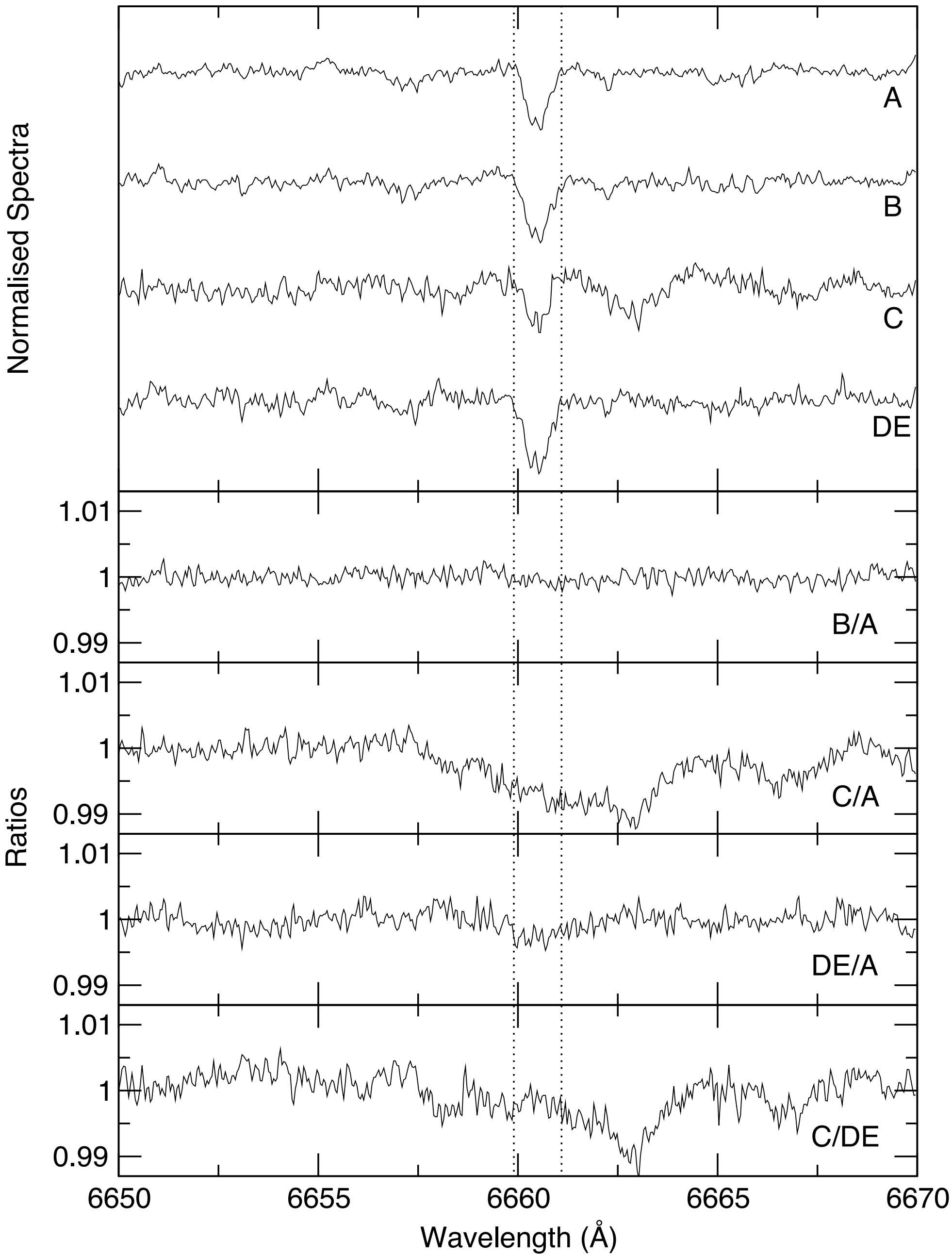

Figure 3.23: From top to bottom: Spectra of λ6660 recorded towards ρ Oph A, B, C and DE (upper panel) and the ratios B/A , C/A , DE/A and C/DE

	W_λ (mÅ)								
Feature	ρ Oph A	σ A	ρ Oph B	σ B	ρ Oph C	σ C	ρ Oph DE	σ DE	Blend?
λ4726	121	3.5	115	3.5	110	5.0	73	5.0	N
λ4734	5.6	0.8	5.1	0.8	2.5	1.2	4.1	1.2	N
λ4964	23.5	0.6	22.0	0.6	21.5	1.0	19.5	1.0	N
λ4984	14.0	0.7	14.0	0.7	11.0	0.9	10.7	0.9	N
λ5170	7.1	0.8	7.9	0.8	12.7	0.9	6.5	0.9	Y
λ5176	7.4	1.0	8.1	1.0	4.3	1.3	4.6	1.3	Y
λ5418	13.7	0.9	13.9	0.9	15.1	1.1	12.0	1.1	Y
λ5512	13.8	0.8	13.4	0.8	17.1	1.0	10.2	1.0	C
λ5541	5.5	1.0	5.4	1.0	6.2	1.2	5.6	1.2	C
λ5546	16.9	1.3	18.7	1.3	24.5	1.6	21.4	1.6	C
λ5705	39.6	3.0	40.0	3.0	34.3	3.5	46.9	3.5	N
λ5780	188	2.5	197	2.5	199	3.0	227	3	C
λ5797	49.7	1.5	54.2	1.5	56.0	2.0	55.2	2.0	C
λ5850	29.8	1.5	30.0	1.5	35.2	2.0	25.2	2.0	N
λ6196	15.9	1.5	15.6	1.5	15.0	2.5	18.8	2.5	N
λ6203	42.0	6.0	42.5	6.0	43.0	6.0	47.2	6.0	N
λ6284	302	5.0	304	5.0	336	6.0	300	6.0	C/T
λ6376	14.8	1.0	15.8	1.0	15.5	1.5	21.0	1.5	N
λ6379	27.1	1.0	28.3	1.0	28.5	1.5	34.7	1.5	N
λ6426	2.7	1.0	3.0	1.0	2.2	1.0	2.3	1.0	N
λ6614	63.9	1.0	67.7	1.0	62.1	1.5	84.9	1.5	N
λ6660	9.0	0.8	10.1	0.8	10.7	1.2	12.8	1.2	C
λ7562	34.9	2.5	33.4	2.5	36.0	3.5	37.5	3.5	N
K I λ7699	88.4	0.2	88.4	0.2	79.4	0.3	90.6	0.3	
Na I D_1	186.9	0.2	188.6	0.2	175.4	0.3	186.8	0.3	
log N(K I)	12.01	–	12.04	–	11.90	–	12.04	–	
log N(Ca I)	10.24	–	10.23	–	10.21	–	10.31	–	
log N(Ca II)	12.25	–	12.29	–	12.28	–	12.29	–	
log N(CH)	13.37	–	13.37	–	13.28	–	13.34	–	
log N(CH^+)	13.20	–	13.16	–	12.85	–	12.88	–	
log N(CN)	12.32	–	12.30	–	12.78	–	12.32	–	
log N(C_2)	13.69	–		–		–	13.59	–	

Table 3.4: Equivalent width measurements (mÅ) of the DIBs analysed in this study together with the K I and Na I D_1 strengths. Literature data for atomic and molecular species (Pan *et al.* 2004, Thorburn *et al.* 2003) for the same sight lines are also included. DIB strengths are quoted together with their associated error. The final column indicates if the measured values are affected by stellar features; 'N' means that there is no stellar contamination affecting the DIB measurements, 'C' indicates stellar contamination in ρ Oph C, 'Y' indicates that there is a stellar feature in more than one spectrum, and 'T' indicates probable contamination due to telluric features.

Table 3.4: DIB strengths in ρ Oph stars

3.3.2 Tiny Scale Structure of the ISM

ρ Oph stars 2004 - 2005

This section describes a search for variations in the DIB strengths and/or profiles over significantly smaller spatial scales than previously attempted. Using the method outlined in Section 3.2, complementary observations were made in 2005 of the targets observed in 2004 in order to search for variations in the DIBs due to the proper-motion displacement of the background stars. Not all stars have the same proper motions but in the $\sim$ 10 months since the original 2004 observations the majority of the targets observed are estimated to have moved by $\sim$ 3 AU relative to the absorbing IS cloud producing the DIB absorptions, (see Table 3.1). If identified, variations at this size-scale would be the very finest probe yet of the structure of the ISM.

As outlined previously (Section 3.2.2), taking ratios of two spectra that have not been corrected for the blaze function or telluric features is a objective method that should identify any differences in the DIB strengths between the two ratioed spectra (see Figure 3.5). When searching for variations due to the proper-motion displacement of the targets, it is even more important to use a robust method to search for the likely even *smaller* variations. The 'best' i.e., least subjective, most robust method is therefore required to test for 'tiny-scale' variations in the DIBs. It should be clear from the discussion in Section 3.2.2 that direct comparison of the same diffuse band in the same star *between* years would be difficult due to changes in the air masses, different instrumental set-up etc. It was decided therefore that the best method would be to compare the same ratio between years i.e. compare the ρ Oph B/A of 2004 with the same ratio in the 2005 data. Rather than looking directly for variations in each line of sight, this method identifies differences in the *ratios*. Whilst this method is likely far superior to direct comparison of DIB strengths, it is possible that a result could be missed if *both* lines of sight increased or decreased in strength by the same amount - in this case no difference in the ratio would be identified. It would be unfortunate to miss a potential result this way but the method chosen is believed to be an effective way in which to search for tiny-scale-structure variations in the DIBs.

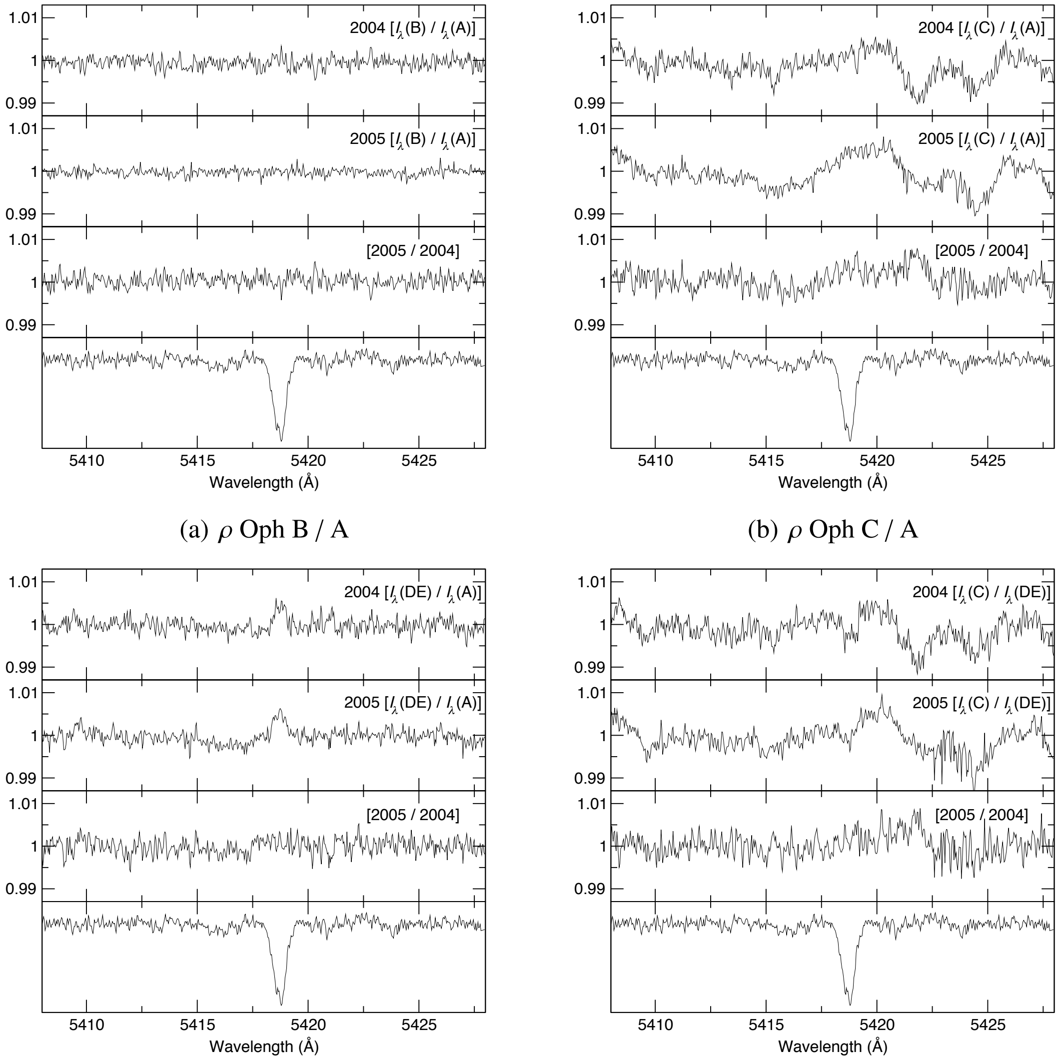

(a) ρ Oph B / A

(b) ρ Oph C / A

(c) ρ Oph DE / A

(d) ρ Oph C / DE

Figure 3.24: Plots of the ratios of λ5418 in 2004 and 2005 and their ratio. The lowest trace is a reference ρ Oph A λ5418 profile.

Figure 3.24 shows the λ5418 ratios for the ρ Oph suite of stars in 2004 and 2005. Examination of the plots reveals no obvious signs of a difference in the ratios between years for any of the spectral divisions. One of the aims of the 2005 observations was to at least match and preferably exceed the S/N achieved in all of the 2004 spectra; the 2005 ratios clearly show a reduced level of noise when compared to the 2004 plots. Due to problems associated with varying stellar features, any ratio involving ρ Oph C or DE may show some degree of change in the overall shape of the continuum and this is apparent in the C/A and C/DE ratios.

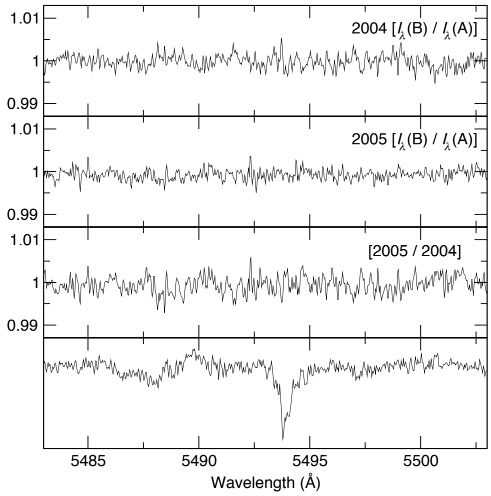

(a) ρ Oph B/A

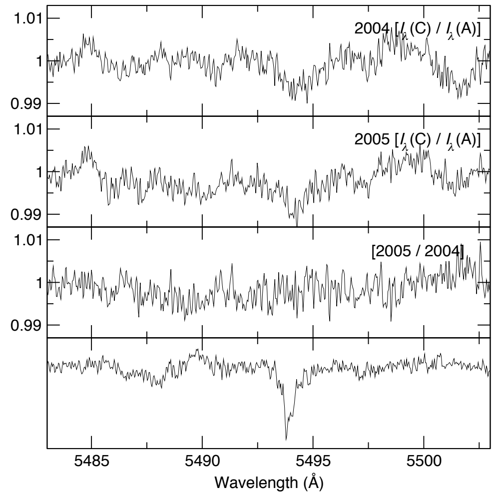

(b) ρ Oph C/A

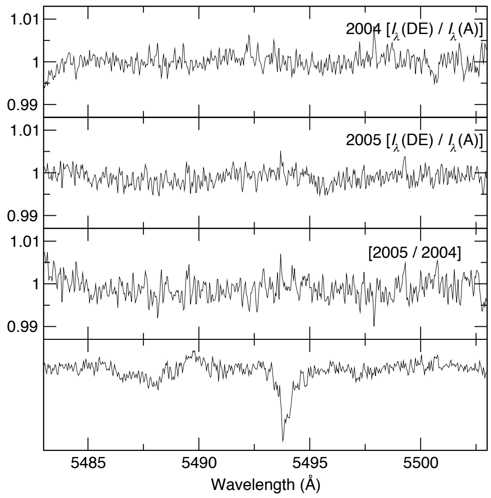

(c) ρ Oph DE/A

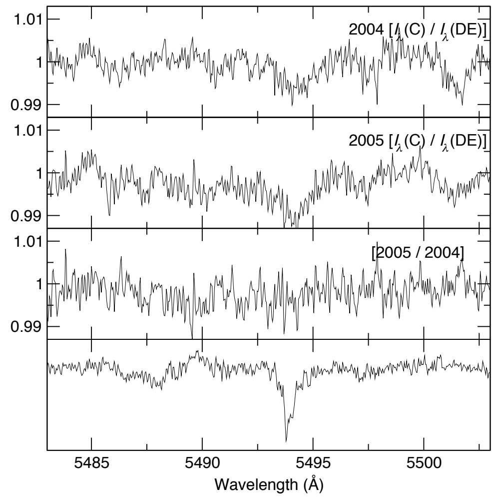

(d) ρ Oph C/DE

Figure 3.25: Plots of the ratios of $\lambda5493$ in 2004 and 2005 and their ratio. The lowest trace is a sample ρ Oph A $\lambda5493$ profile.

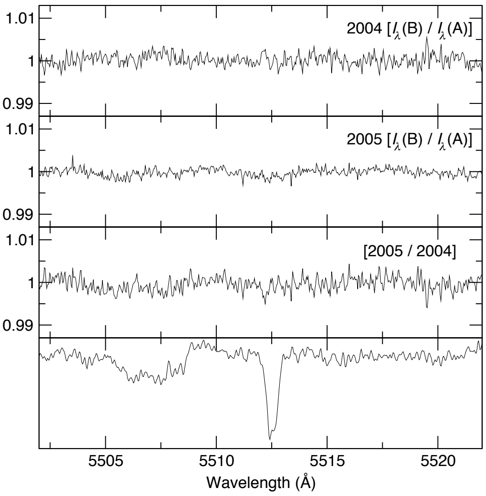

(a) ρ Oph B/A

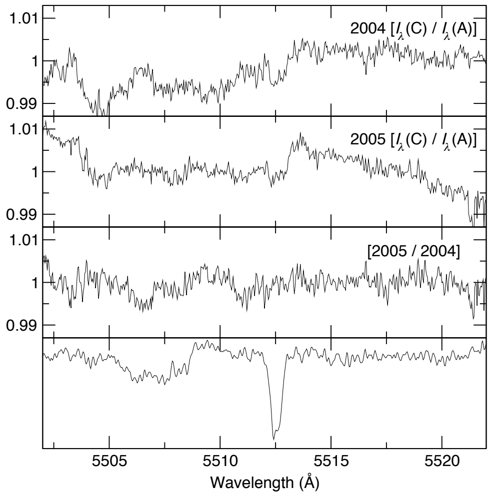

(b) ρ Oph C/A

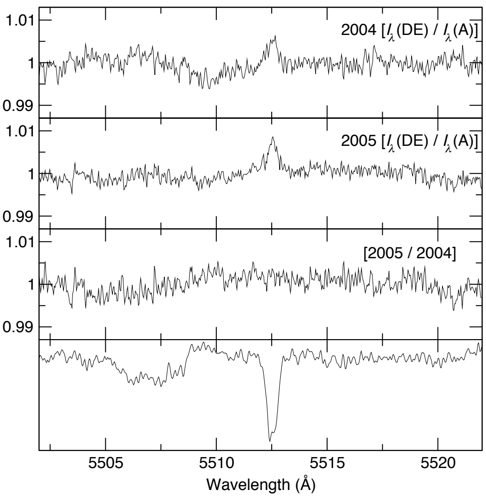

(c) ρ Oph DE/A

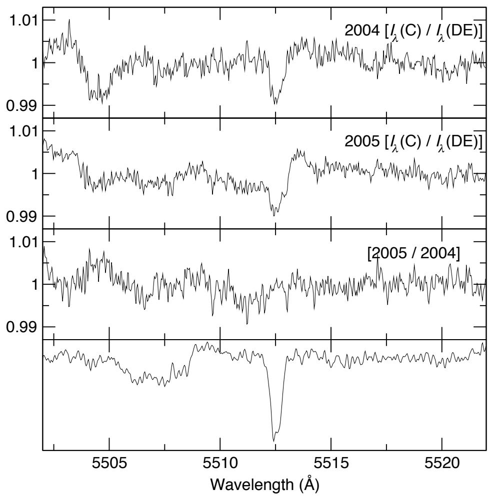

(d) ρ Oph C/DE

Figure 3.26: Plots of the ratios of λ5512 in 2004 and 2005 and their ratio. The lowest trace is a sample ρ Oph A λ5512 profile.

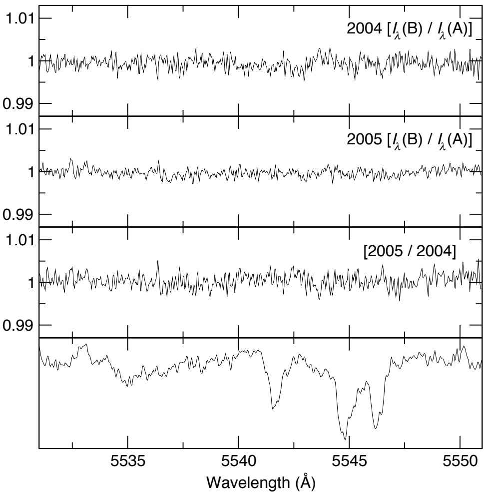

(a) ρ Oph B/A

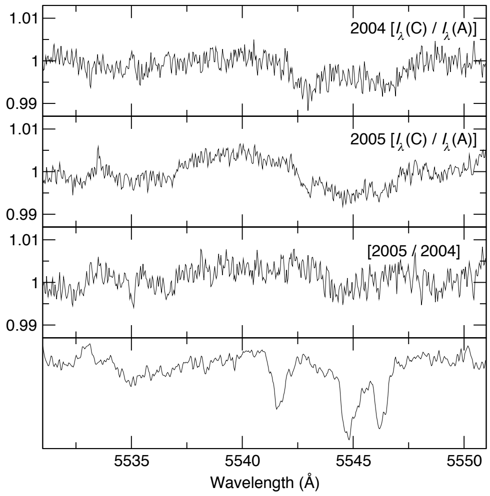

(b) ρ Oph C/A

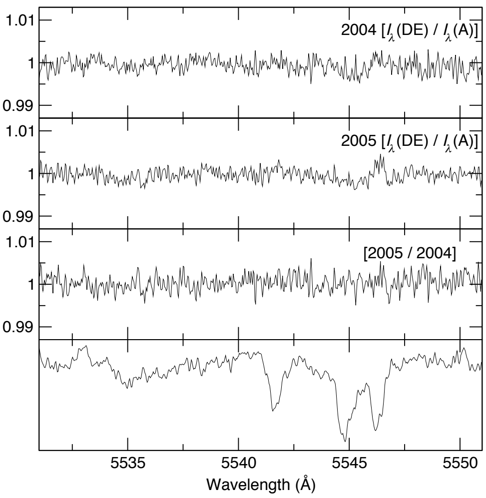

(c) ρ Oph DE/A

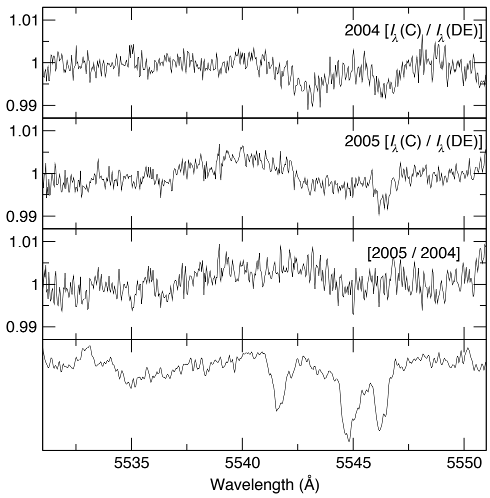

(d) ρ Oph C/DE

Figure 3.27: Plots of the ratios of $\lambda5541$, $\lambda5544$ and $\lambda5546$ in 2004 and 2005 and their ratio. The lowest trace is a sample ρ Oph A $\lambda5541$ profile.

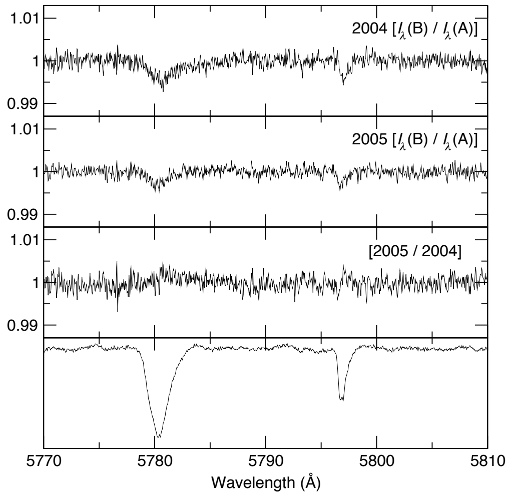

(a) ρ Oph B/A

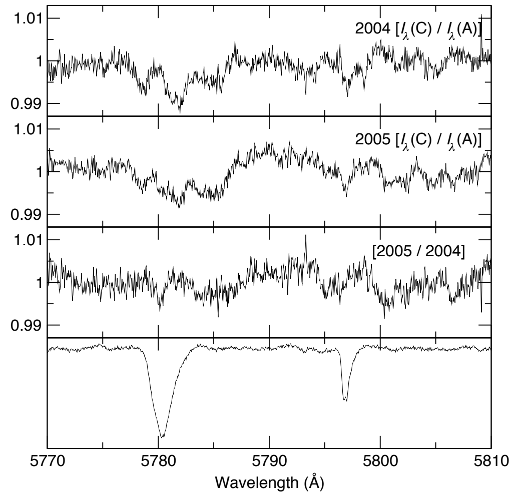

(b) ρ Oph C/A

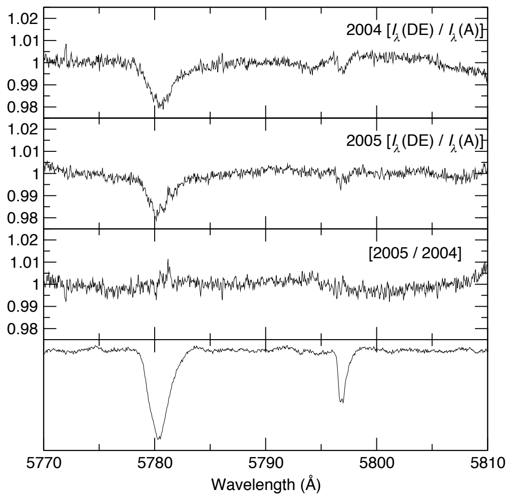

(c) ρ Oph DE/A

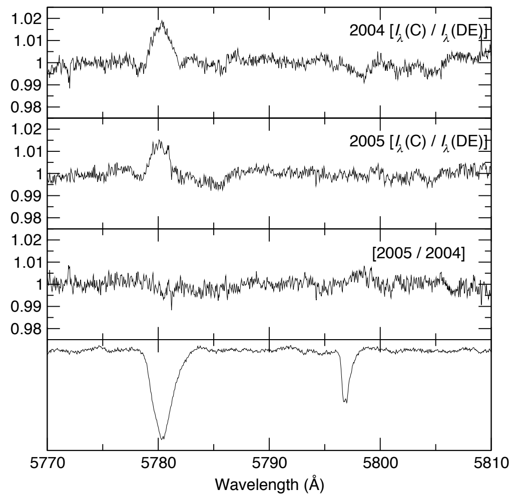

(d) ρ Oph C/DE

Figure 3.28: Plots of the ratios of λ5780 and λ5797 in 2004 and 2005 and their ratio. The lowest trace is a sample ρ Oph A λ5780 and λ5797 profiles.

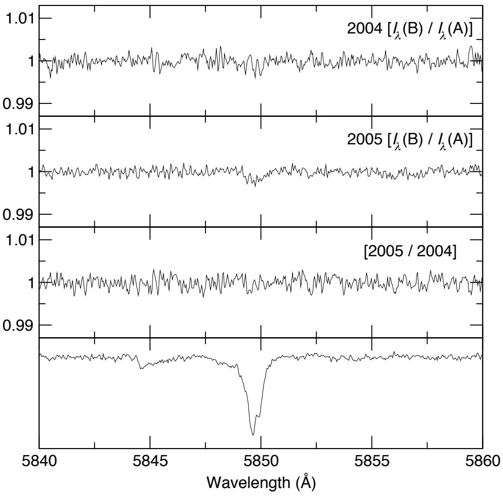

(a) ρ Oph B/A

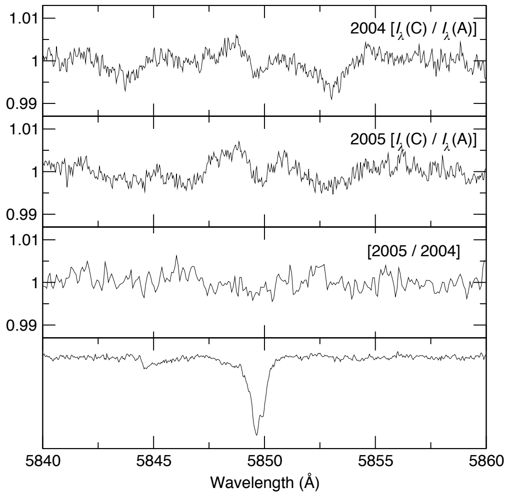

(b) ρ Oph C/A

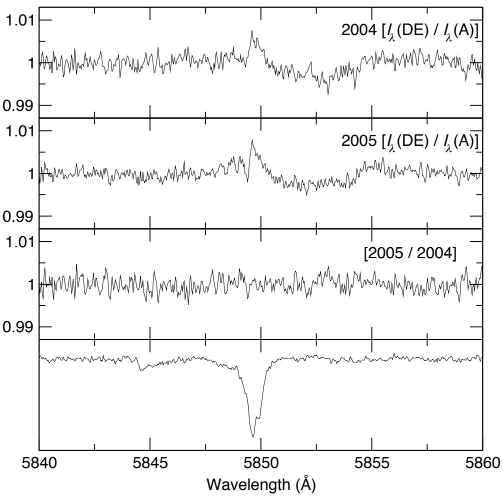

(c) ρ Oph DE/A

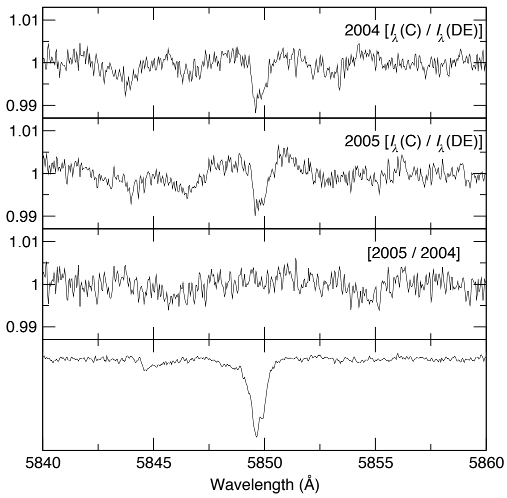

(d) ρ Oph C/DE

Figure 3.29: Plots of the ratios of λ5850 in 2004 and 2005 and their ratio. The lowest trace is a sample ρ Oph A λ5850 profile.

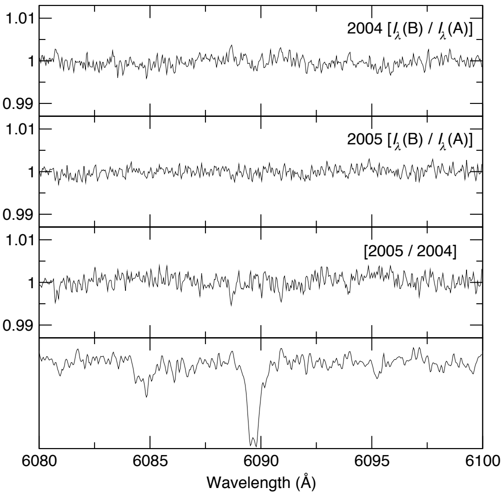

(a) ρ Oph B/A

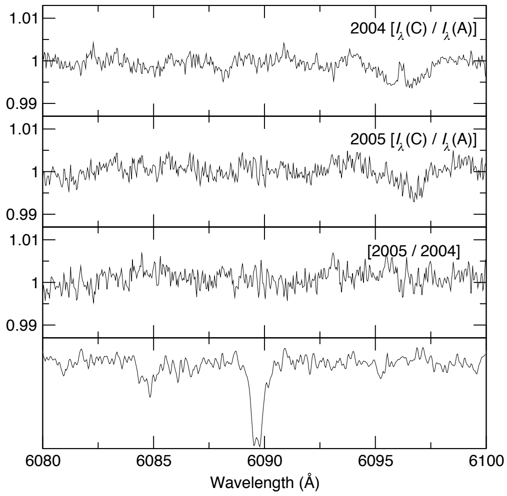

(b) ρ Oph C/A

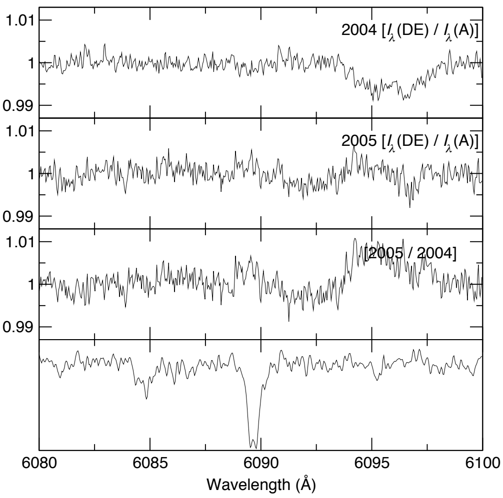

(c) ρ Oph DE/A

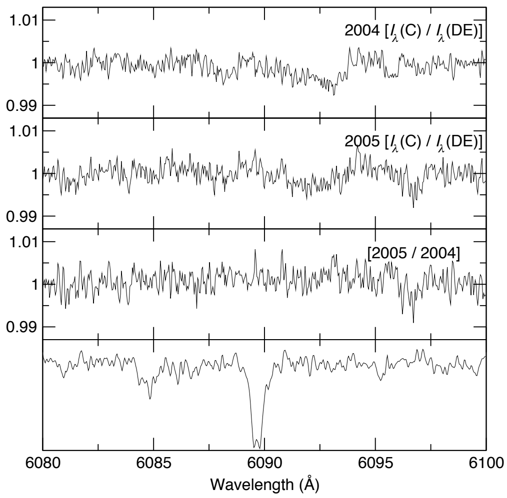

(d) ρ Oph C/DE

Figure 3.30: Plots of the ratios of λ6090 in 2004 and 2005 and their ratio. The lowest trace is a sample ρ Oph A λ6090 profile.

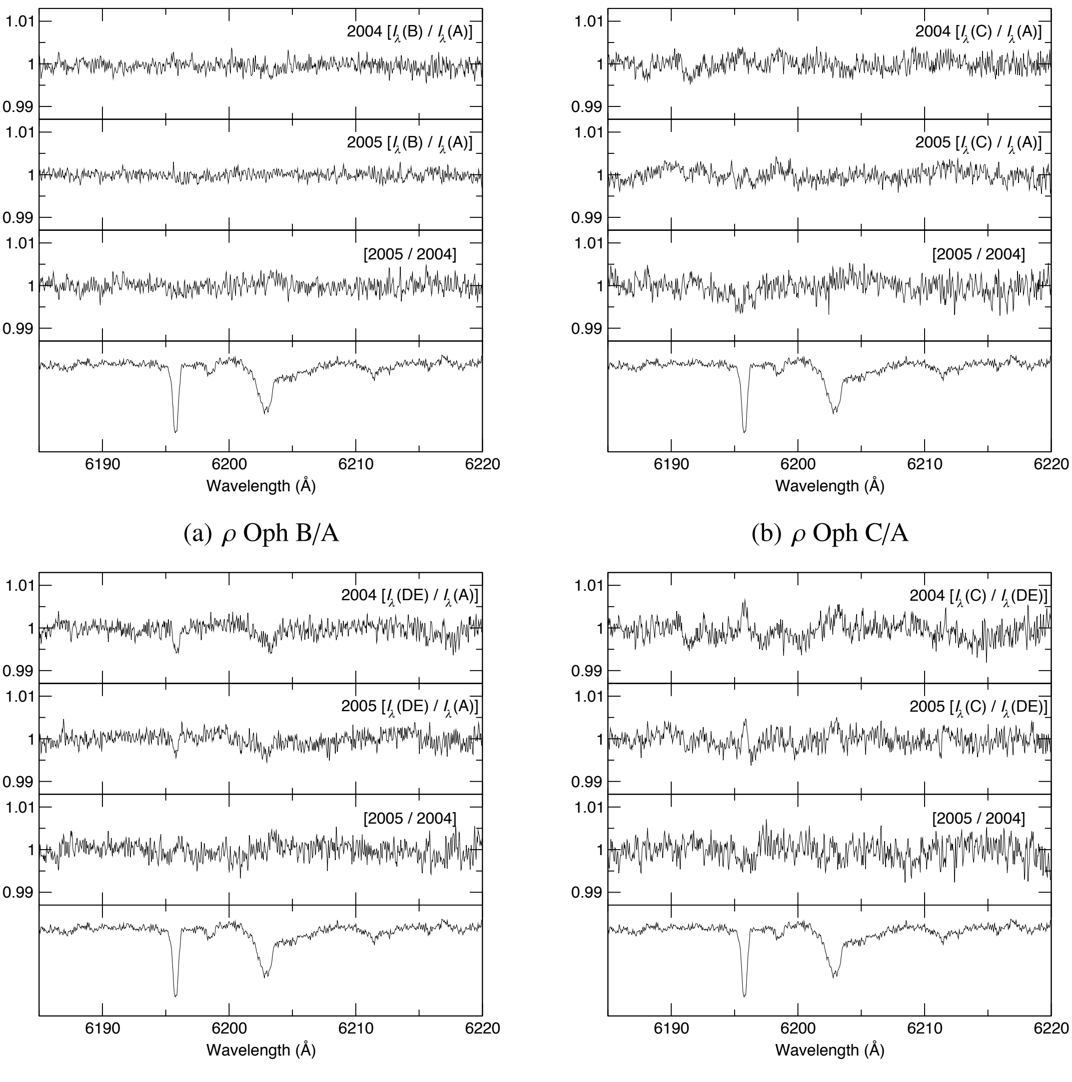

(a) ρ Oph B/A

(b) ρ Oph C/A

(c) ρ Oph DE/A

(d) ρ Oph C/DE

Figure 3.31: Plots of the ratios of λ6196 and λ6203 in 2004 and 2005 and their ratio. The lowest trace is a sample ρ Oph A λ6196 profiles.

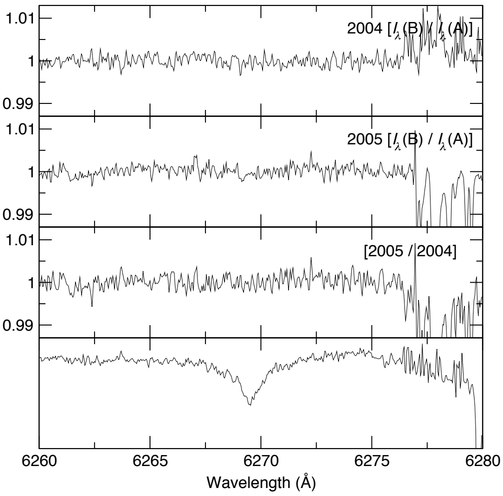

(a) ρ Oph B/A

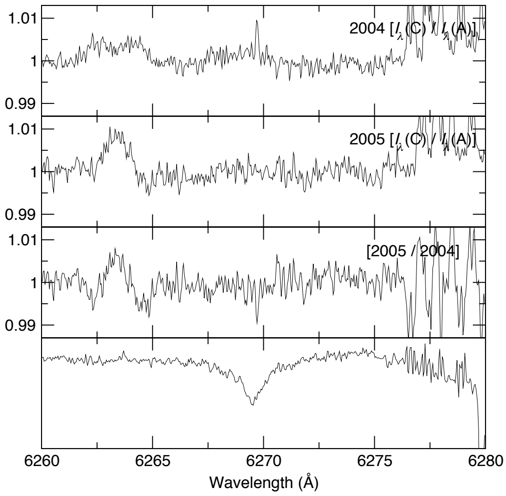

(b) ρ Oph C/A

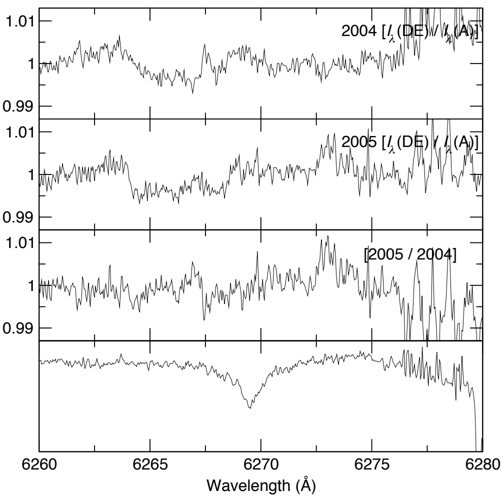

(c) ρ Oph DE/A

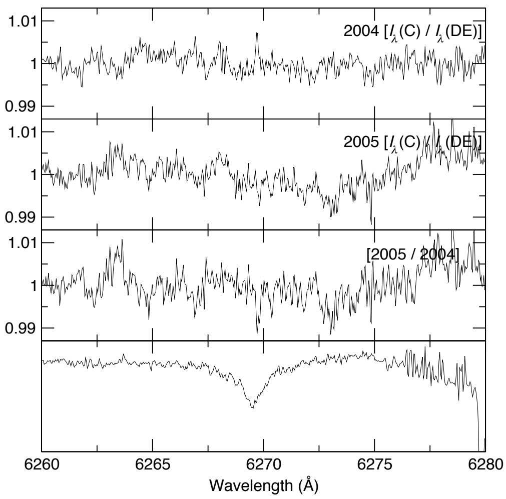

(d) ρ Oph C/DE

Figure 3.32: Plots of the ratios of λ6270 in 2004 and 2005 and their ratio. The lowest trace is a sample ρ Oph A λ6270 profile.

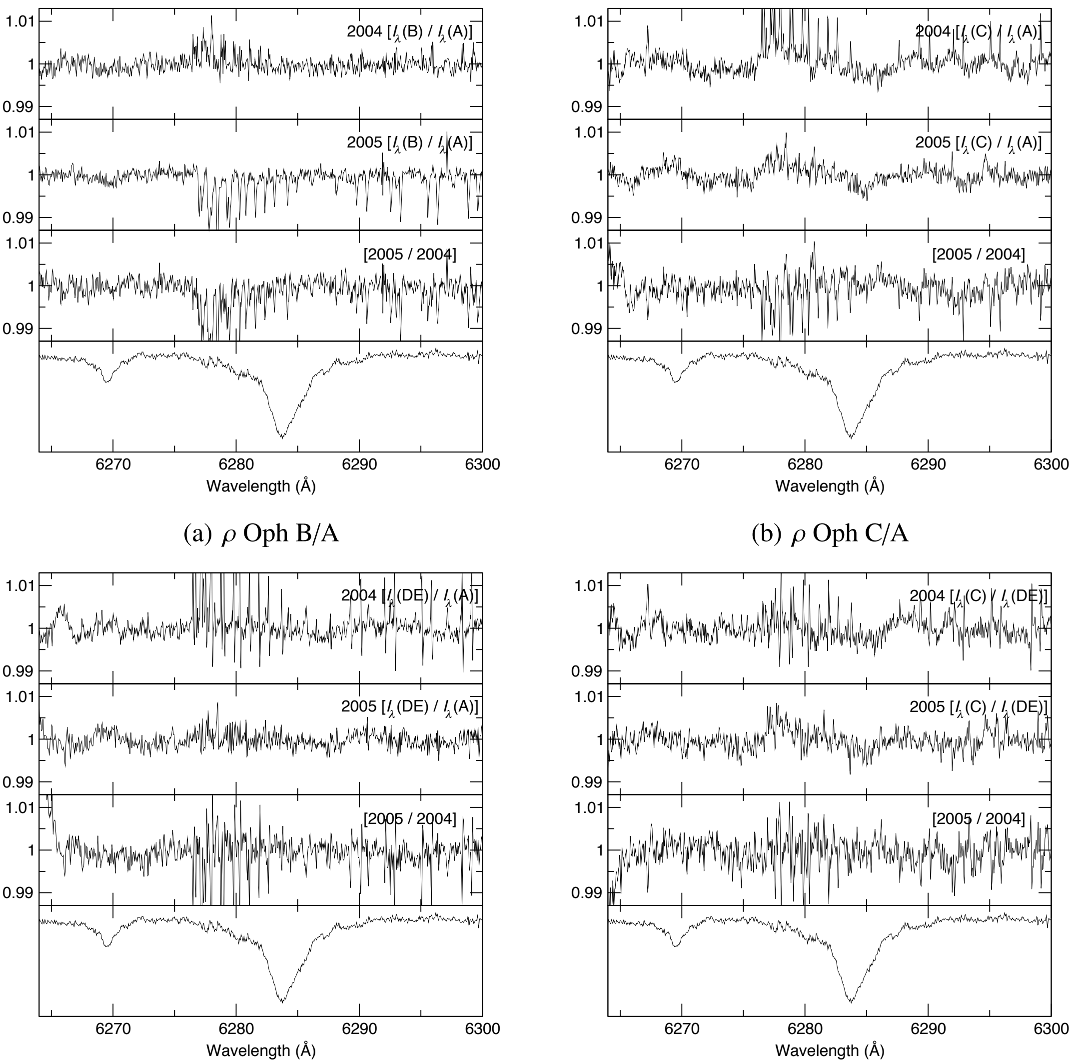

(a) ρ Oph B/A

(b) ρ Oph C/A

(c) ρ Oph DE/A

(d) ρ Oph C/DE

Figure 3.33: Plots of the ratios of λ6284 in 2004 and 2005 and their ratio. The lowest trace is a sample ρ Oph A λ6284 profile.

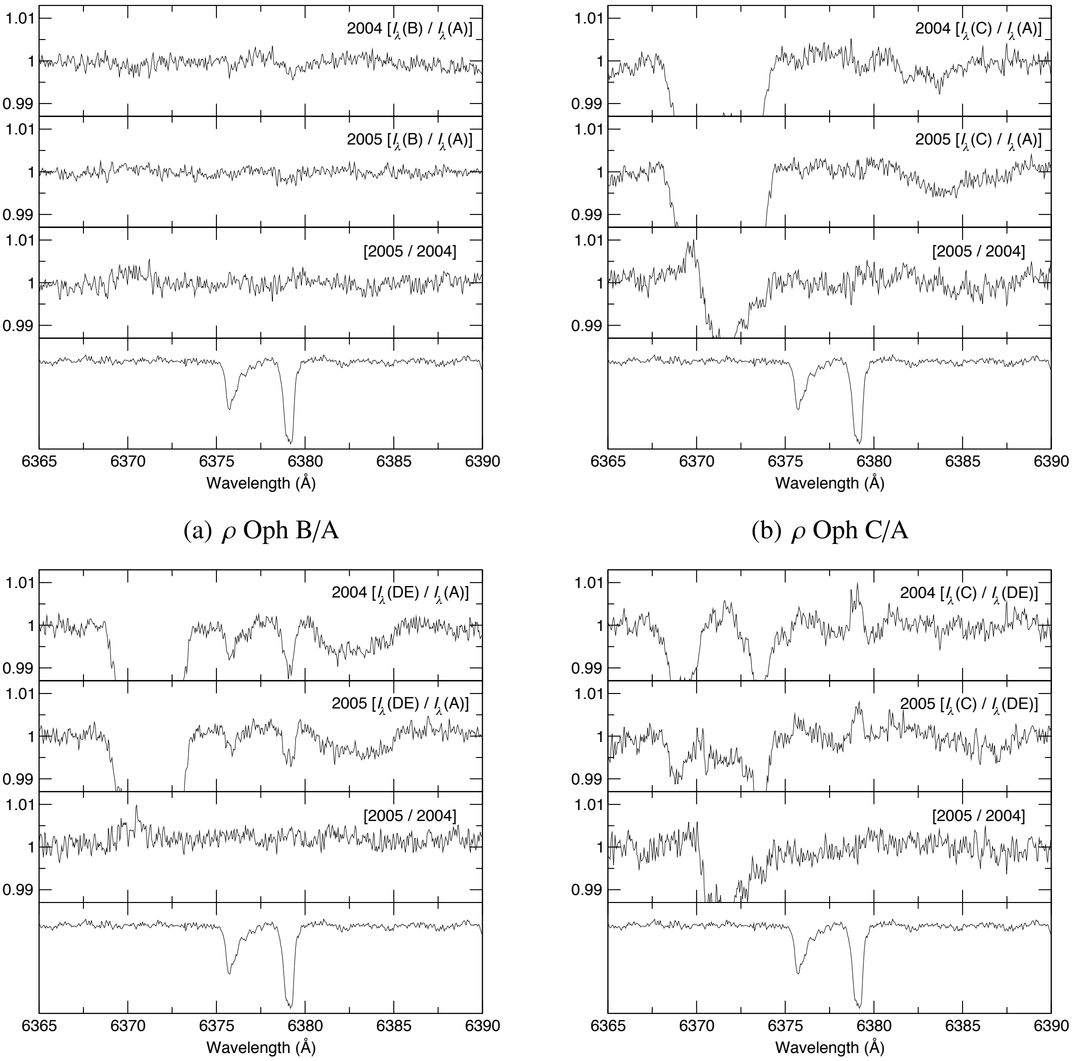

(a) ρ Oph B/A

(b) ρ Oph C/A

(c) ρ Oph DE/A

(d) ρ Oph C/DE

Figure 3.34: Plots of the ratios of $\lambda6376$ and $\lambda6379$ in 2004 and 2005 and their ratio. The lowest trace is a sample ρ Oph A $\lambda6376$ and $\lambda6379$ profile.

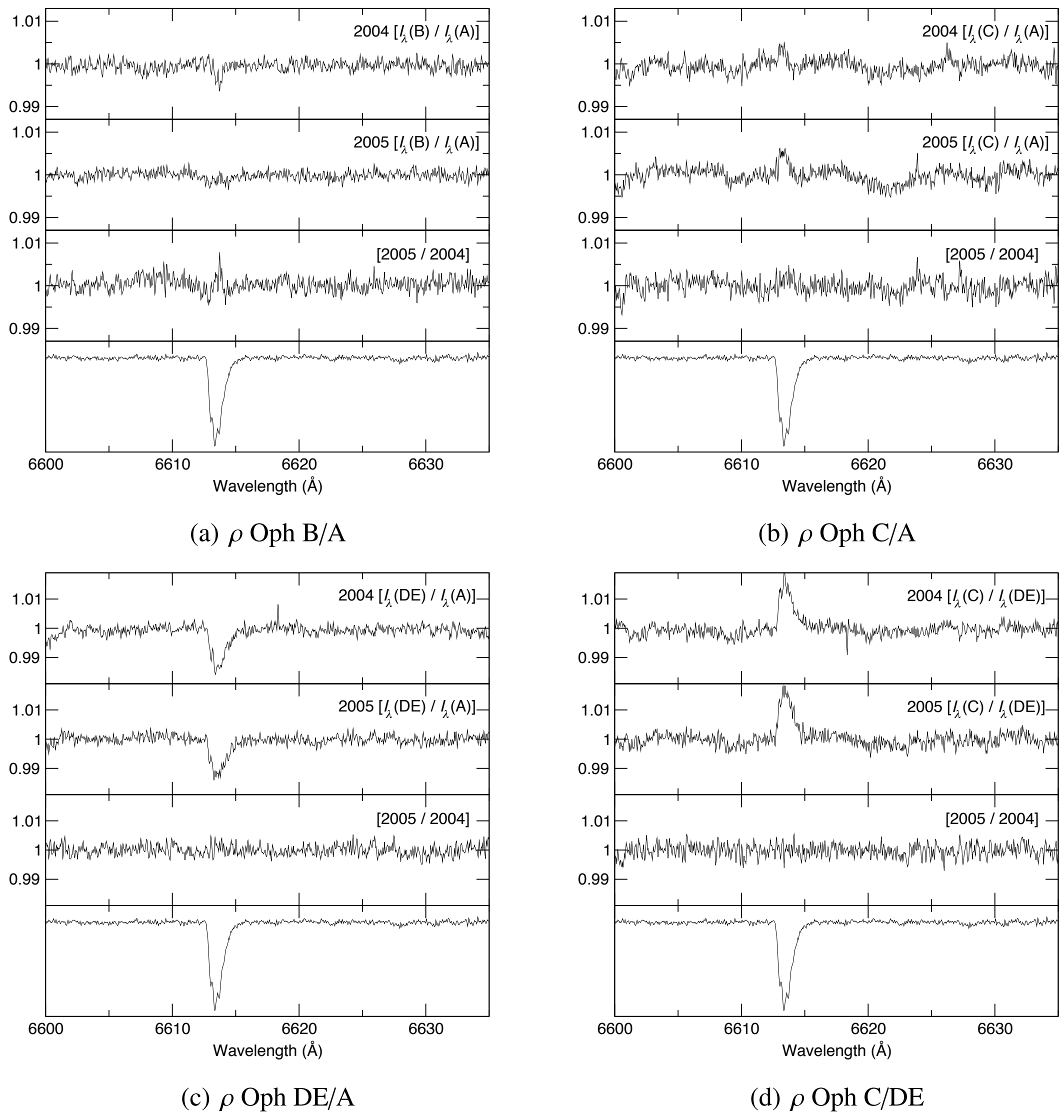

(a) ρ Oph B/A

(b) ρ Oph C/A

(c) ρ Oph DE/A

(d) ρ Oph C/DE

Figure 3.35: Plots of the ratios of λ6614 in 2004 and 2005 and their ratio. The lowest trace is a sample ρ Oph A λ6614 profile.

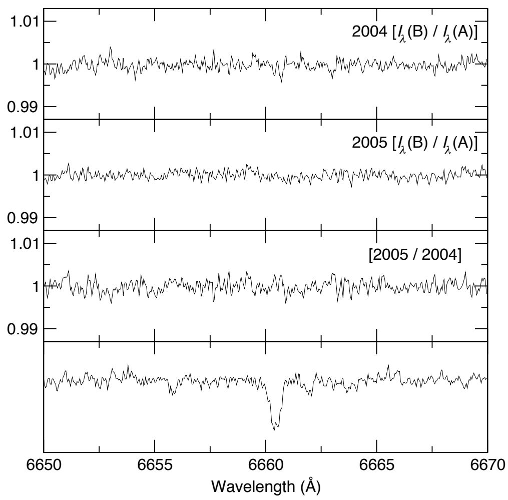

(a) ρ Oph B/A

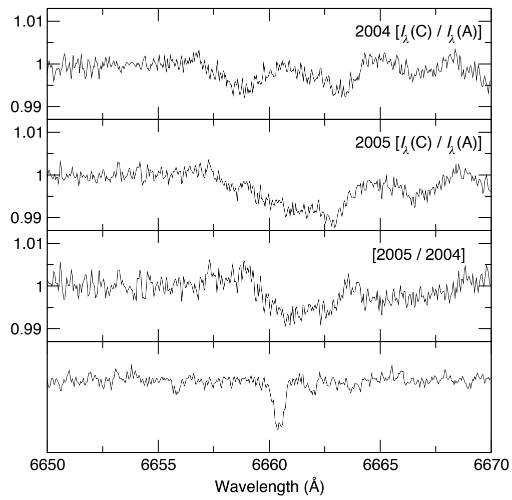

(b) ρ Oph C/A

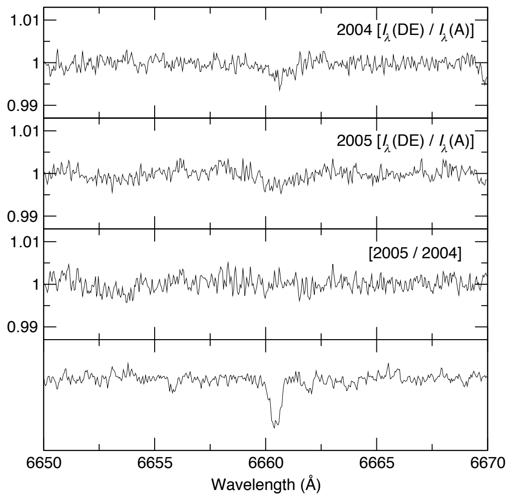

(c) ρ Oph DE/A

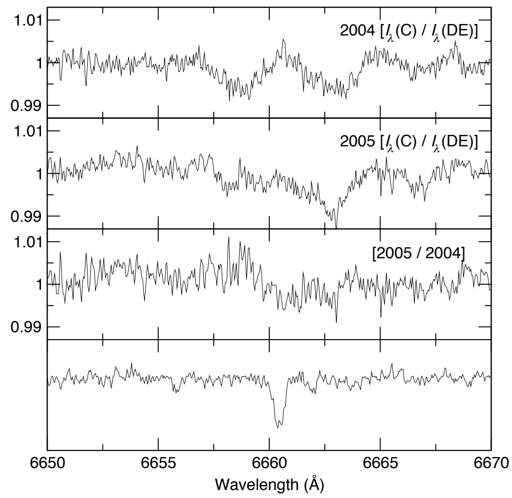

(d) ρ Oph C/DE

Figure 3.36: Plots of the ratios of λ6660 in 2004 and 2005 and their ratio. The lowest trace is a sample ρ Oph A λ6660 profile.

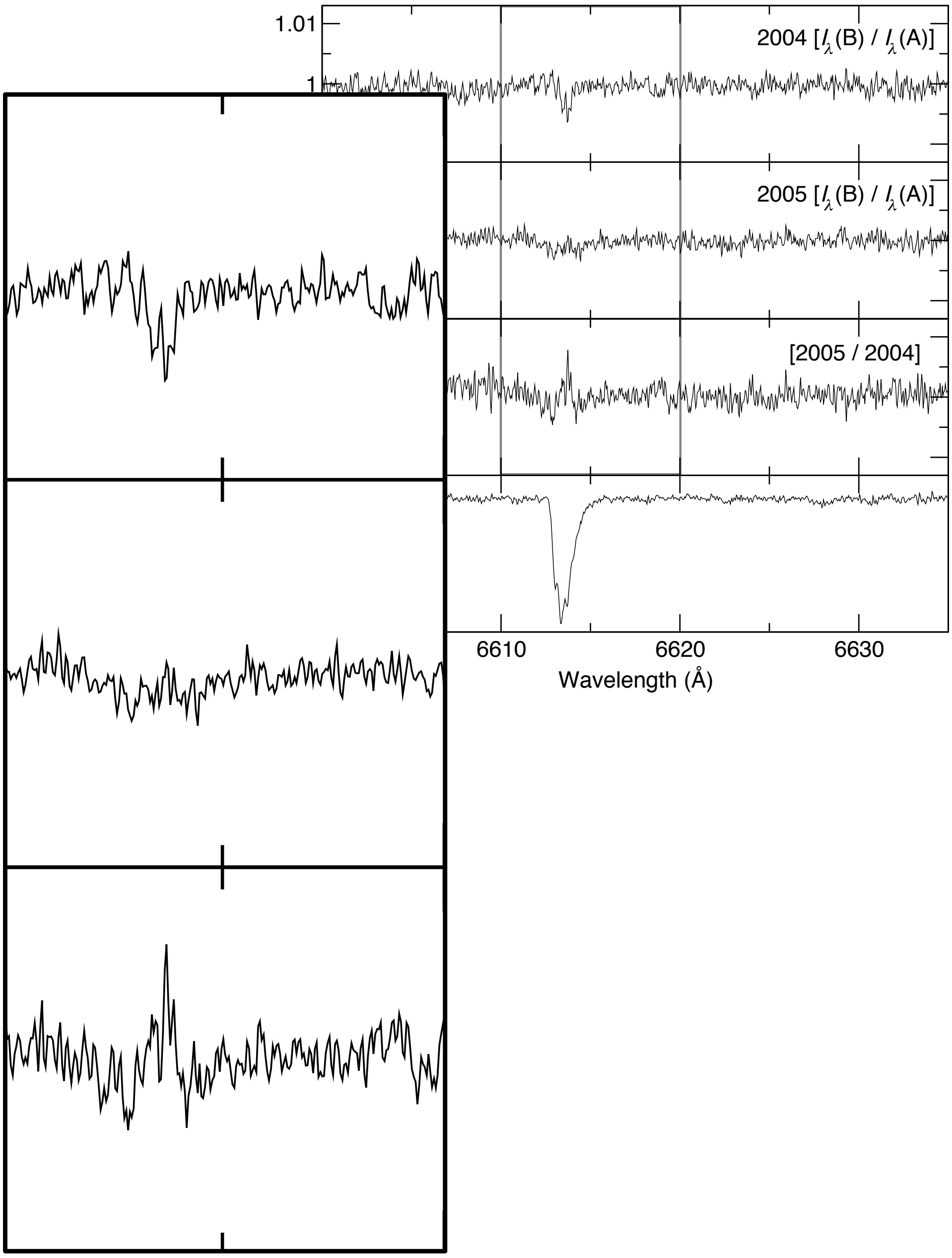

Figure 3.37: λ6614 ρ Oph B/A in 2004 and 2005, their division and an enlargement of the region surrounding the DIB for clarity.

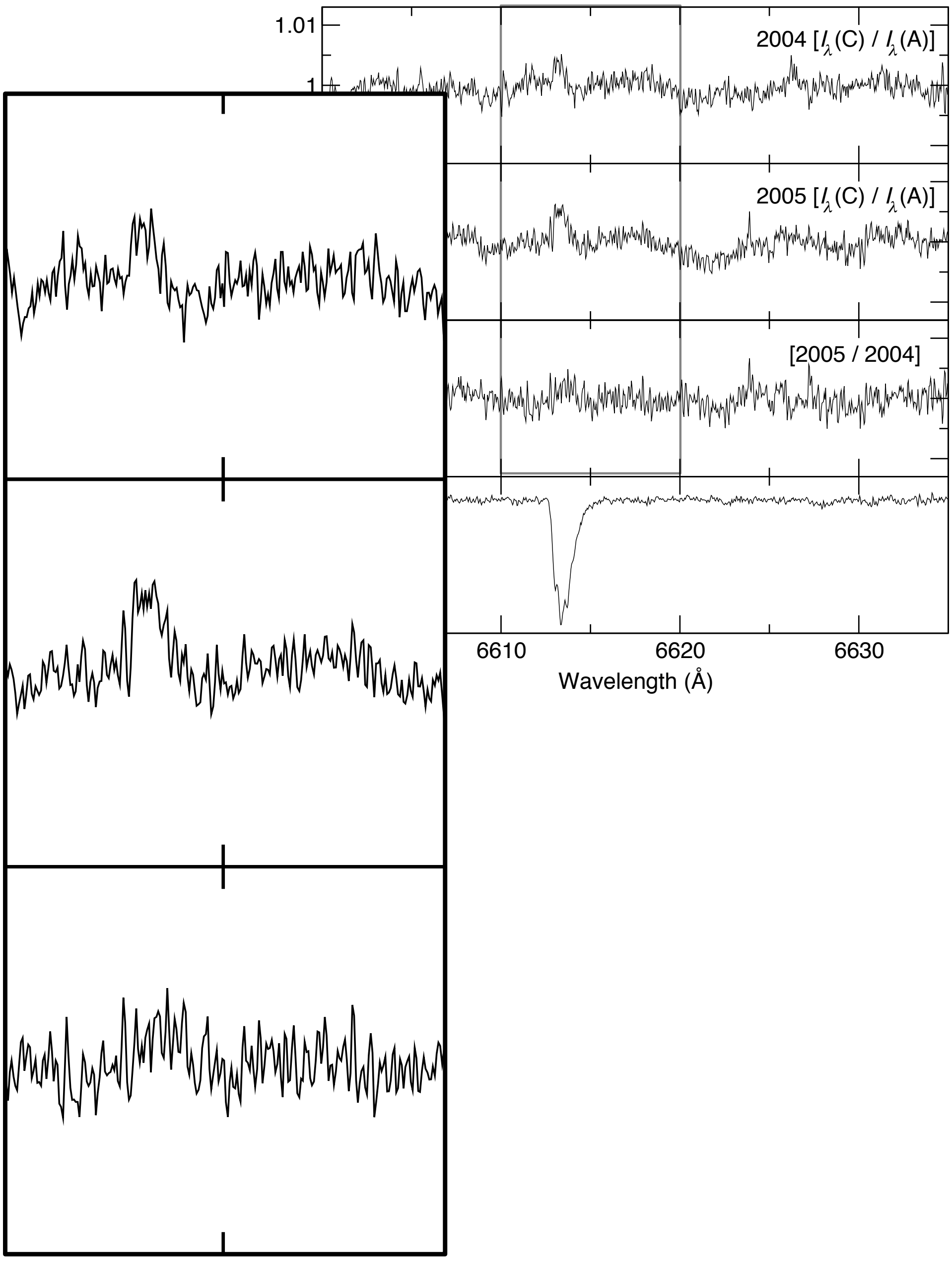

Figure 3.38: λ6614 ρ Oph C/A in 2004 and 2005, their division and an enlargement of the region surrounding the DIB for clarity.

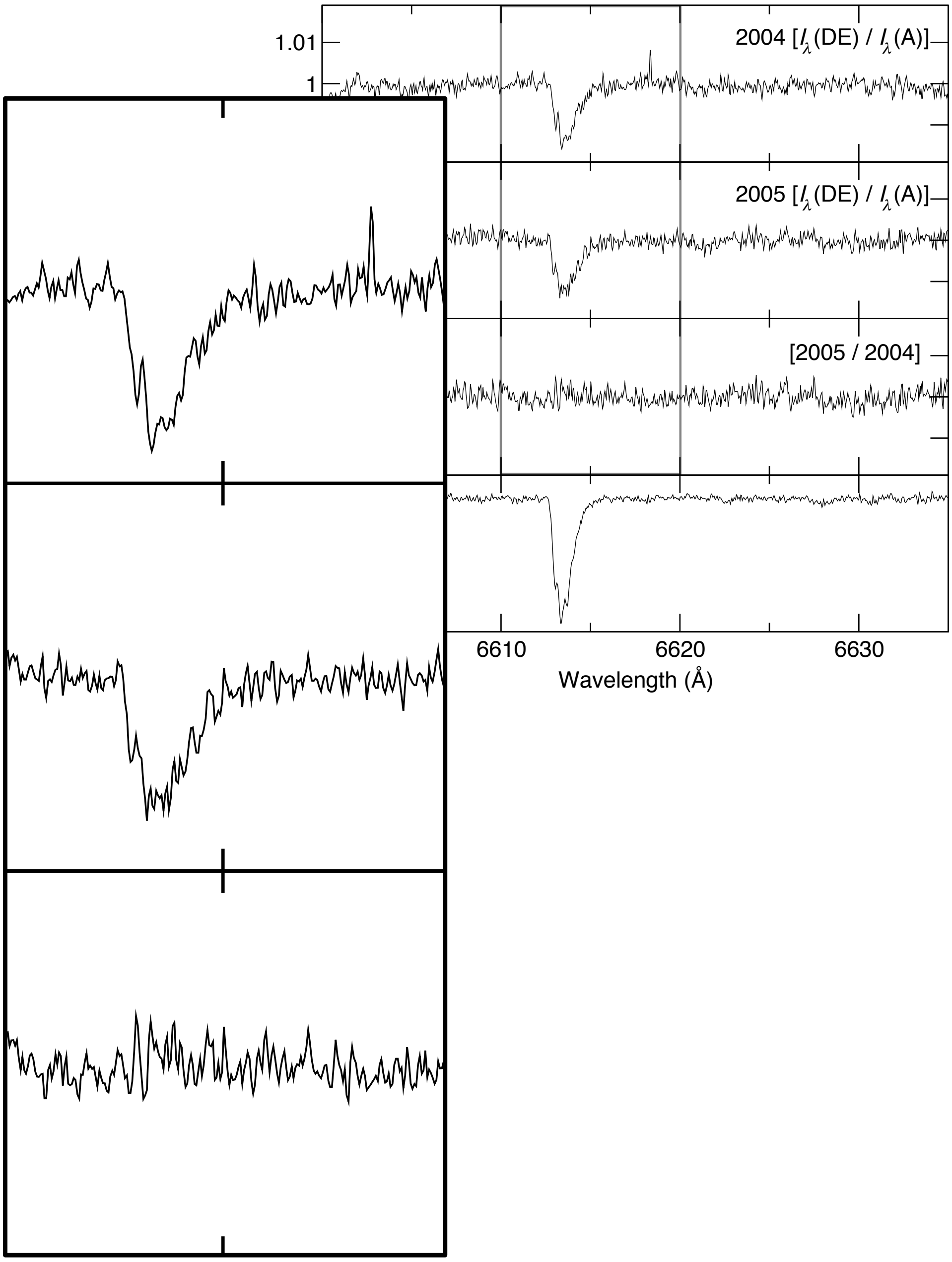

Figure 3.39: λ6614 ρ Oph DE/A in 2004 and 2005, their division and an enlargement of the region surrounding the DIB for clarity.

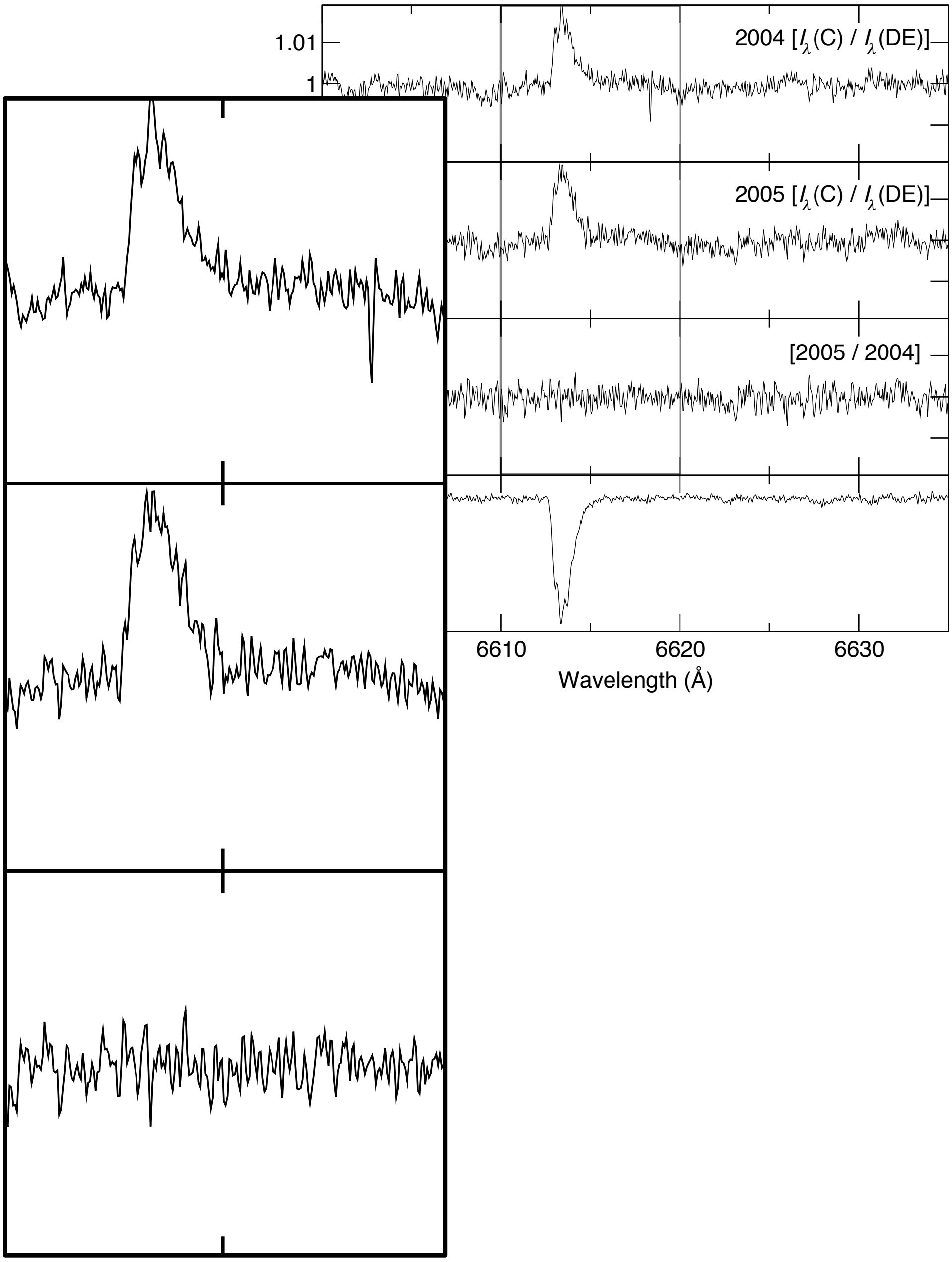

Figure 3.40: λ6614 ρ Oph C/DE in 2004 and 2005, their division and an enlargement of the region surrounding the DIB for clarity.

Figure 3.25 shows the $\lambda 5493$ ratios for the ρ Oph suite of stars in 2004 and 2005. As is the case for $\lambda 5418$ there is no obvious sign of tiny scale structure (TSS) variations in the DIB strength. This apparent lack of any variations in DIB ratios is also the case for $\lambda 5512$, $\lambda 5541$, $\lambda 6090$, $\lambda 6196$, $\lambda 6270$, $\lambda 6284$, $\lambda 6376$ and $\lambda 6660$. Whilst there is a lack of variation in DIB ratios *between* years it *does* demonstrate the repeatability of the 2004 data; the majority of the 2005 ratios are essentially higher S/N versions of their 2004 counterparts.

There are a few notable exceptions in the list of those DIBs not showing variations in their ratios between 2004 and 2005. As mentioned previously, the ρ Oph pair A and B are of very similar spectral type (B2/3 V). The similarity between the stellar continua of A and B and combined with their early spectral type (few stellar features) facilitates close comparison of DIB profiles between the two stars. They are also the most closely spaced pair of stars that could be resolved during observations ($\sim 3.1'' \simeq 400$AU at 130 pc). Examination of the ratios of the $\lambda 5780$, $\lambda 5797$ and $\lambda 6614$ (Figures 3.28 & 3.35) ratios reveals that there is some indication of a difference *between* years.

Figures 3.37 through to 3.40 contain enlargements of the region surrounding $\lambda 6614$ for each of the ρ Oph ratios. The top trace is the ratio of ρ Oph B/A in 2004, the middle ρ Oph B/A in 2005 and the lower the ratio of the *ratios* from each year i.e. 2005 ratio/2004 ratio. It is clear that there is a difference in the ratios between years for the division of B/A. In 2004 a sharp feature is present in the ratio centred at the wavelength of the DIB. In 2005 there is no longer such an obvious sharp difference in the strengths between the stars (although a broad difference is still detected in the B/A ratio). A difference in the ratio between 2004 and 2005 means that either the $\lambda 6614$ feature has changed in ρ Oph A or B (or both) since 2004.

Careful examination of the ratios B/A (Figure 3.37) and C/A (Figure 3.38) show signs of a difference in the ratios that could be interpreted as an increase in the DIB strength in ρ Oph A.

However, if a measurement is made of the ratio (EW) then we find that contrary to intuition there is *more* of a difference in the B/A ratio in 2005 than in 2004. The narrow difference in B/A in 2004 is replaced by a shallower, broader difference in 2005. Values are listed in Table 3.5. The error (σ) is quoted for each measurement can be understood as the upper limit for a non-detection of variation and is calculated as

$\sigma_{\rm RMS}\Delta\lambda$, i.e., the RMS noise in the ratio across the width of the feature been ratioed.

Table 3.5 also includes measurements of the additional ratios C/B and DE/B as the measurement of the ratio of B/A in 2004 and 2005 highlight that it is B that has strengthened relative to A between the years. The ratio of C/B is shown in Figures 3.41 and 3.42. Whilst there is no obvious difference in the ratios, the measurements suggest that B has strengthened relative to C between 2004 and 2005. Figure 3.41 and 3.43 show the ratios for DE/B in 2004 and 2005. Once again, there is little obvious difference between the two ratios although the measured values would suggest that B has weakened relative to DE.

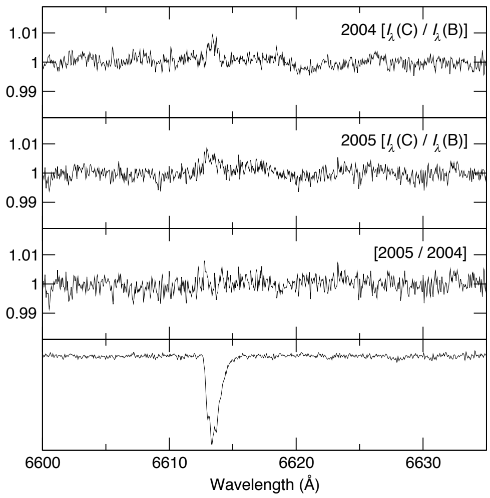

(a) ρ Oph C/B

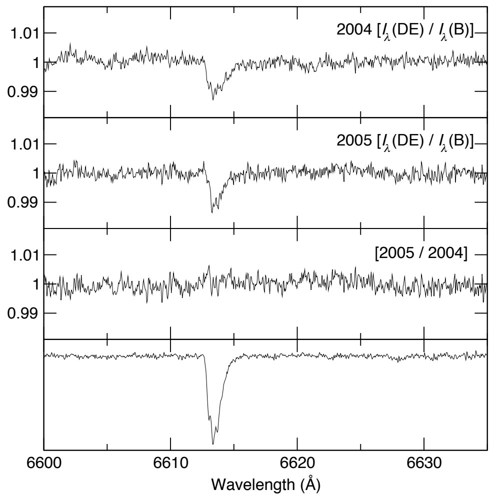

(b) ρ Oph DE/B

Figure 3.41: Plots of the ratios of λ6614 in 2004 and 2005 and their difference. The lowest trace is a sample ρ Oph A λ6614 profile.

	Integrated area			
Ratio	2004	σ	2005	σ
ρ Oph B/A	2.6	1.2	5.1	1.0
ρ Oph C/A	2.0	1.3	3.0	1.1
ρ Oph DE/A	19.5	1.3	18.4	1.3
ρ Oph C/DE	-19.6	1.3	-19.4	1.3
ρ Oph C/B	6.5	1.2	8.0	1.0
ρ Oph DE/B	16.7	1.1	13.8	1.0

Table 3.5: Measure of the λ6614 ratios in 2004 and 2005

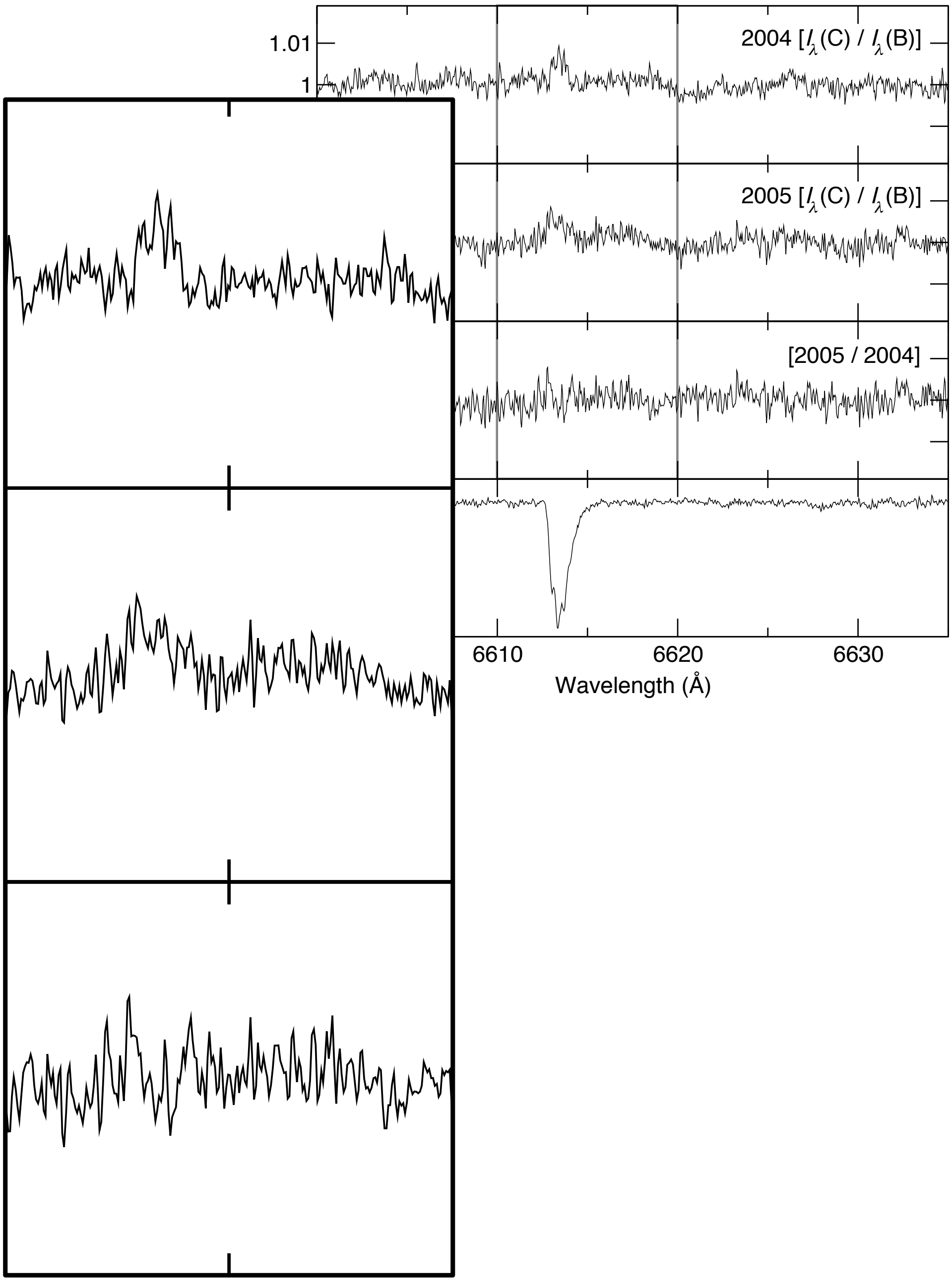

Figure 3.42: λ6614 ρ Oph C/B in 2004 and 2005, their division and an enlargement of the region surrounding the DIB for clarity.

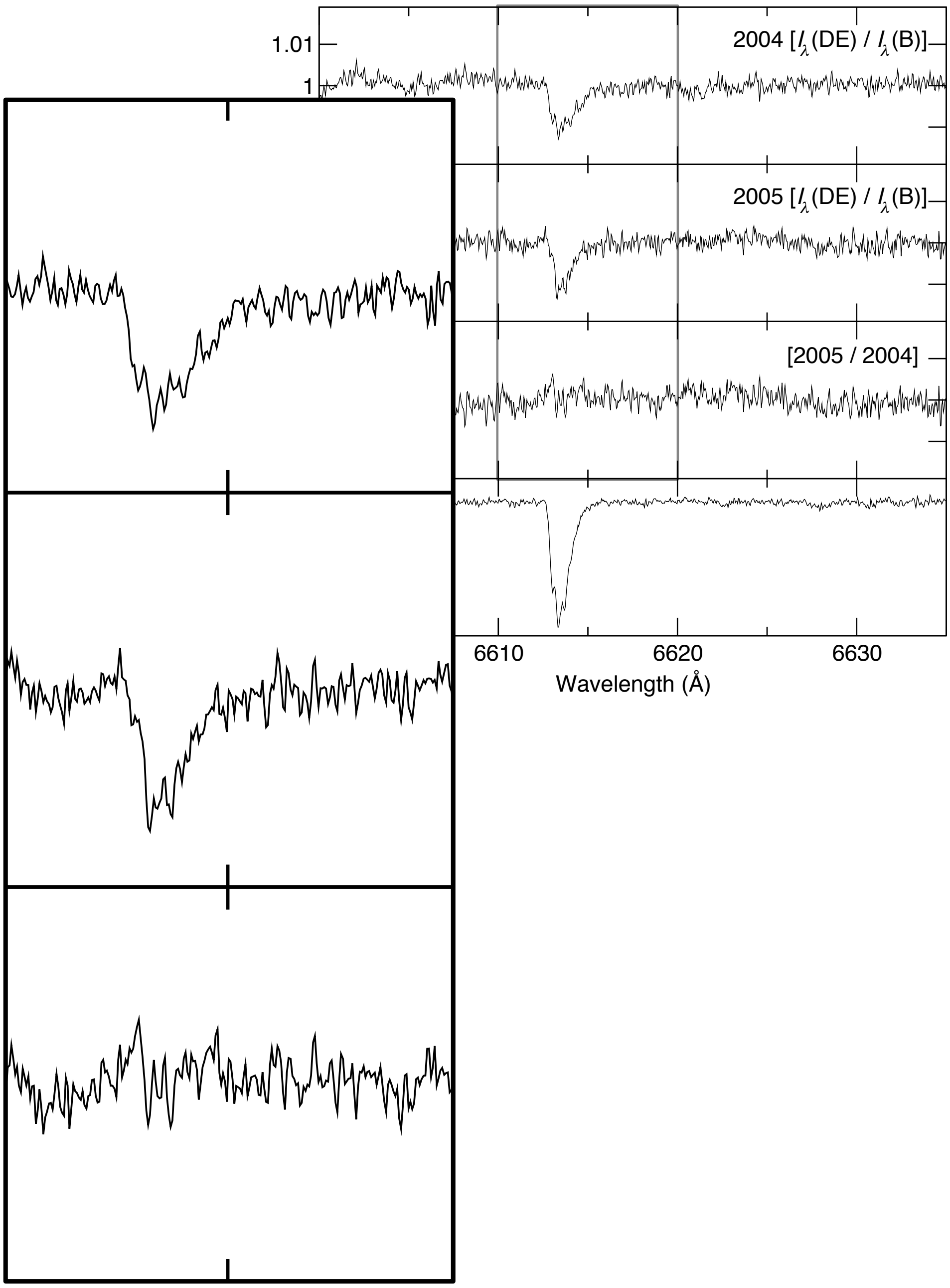

Figure 3.43: λ6614 ρ Oph DE/B in 2004 and 2005, their division and an enlargement of the region surrounding the DIB for clarity.

When considering any possible changes due to TSS variations all possible sources of confusion that might be incorrectly identified as a TSS variation must be considered and accounted for. An important example of such an issue is the different seeing in 2004 and 2005. Overall the seeing in 2005 was worse than that of 2004 (median seeing for ρ Oph observations $\sim 1.0''$ in 2004, $\sim 1.7''$ in 2005). The effect that seeing has upon the observations is threefold:

I. Seeing affects the throughput of the spectrograph; for these observations the aperture through which the light from a star enters the spectrograph was $1''$ wide. Should the seeing be much worse than $1''$ then a significant fraction of the light from the star is lost on the slit jaws and hence the number of counts per unit time of observing reduced. Whilst this loss of throughput is unfortunate it does not directly affect the TSS analysis other than requiring significantly longer integrations to achieve the desired S/N.

II. The limiting spectral resolution ($\Delta\lambda/\lambda$) of a given configuration of the spectrograph (e.g. slit width, grating) is determined by the width of the aperture through which the light enters. When the seeing is *better* than the width of the slit then the resolution achieved can actually be *higher* than that expected, the case if the object observed 'fills' the full width of the slit. The significantly better seeing in 2004 combined with a marginally narrower slit aperture meant that the resolving power of the data recorded was higher in 2004 than in 2005 (R = 58,000 vs. 52,000). If the difference between two DIBs were due to a change in fine structure in the DIB then at the lower R blending of the fine structure may occur resulting in a different ratio between years. An example of where this might be an issue is for the λ6614 B/A ratio in 2004 and 2005 and Figure 3.45 addresses this question by comparing the 2004 ratio (R = 58,000) with a blended version of the same ratio but at the resolution achieved in 2005 (R = 52,000). The ratio of the two ratios demonstrates that the reduced R in 2005 cannot account for the difference seen in the λ6614 ratios (e.g. Figure 3.37)

III. Where there are two closely separated stars that are treated as different lines of sight (e.g. ρ Oph A & B) it is important to establish that the light from one star does not contaminate the signal from the other. For the majority of stars observed in this program contamination from another source is not an issue, but one case where it is a possibility is ρ Oph A & B. Figure 3.44 shows the seeing intensity profiles of ρ Oph A & B for 2004 (red) and 2005 (black). Of concern for this project is the possibility that light from A might contaminate the spectrum of B *more* in 2005 than in 2004. If this is the case and there is more contamination in 2005 than 2004 and *less* of a difference in the ratio is observed then a possible explanation would be the difference in seeing rather than a change in the relative DIB strengths. Clearly there is more contamination in 2005 than 2004. The extent of the contamination introduced by the poorer seeing is outlined in Table 3.6.

It is possible that the larger overlap in the ρ Oph A & B profiles in 2005 might have an effect on the results. Figure 3.46 is a comparison of the B/A λ6614 profiles in 2004 and 2005. The left-hand panel is the same ratio as presented in Figure 3.35, the right-hand panel is the same ratio but this time taking into account the fractional contamination of the two stars in 2005. Each 'contaminated' spectrum is produced as a weighted addition of the two spectra, e.g., spectrum of A + 0.119% of B to produce the contaminated spectrum of A and A into B by 0.622% (Table 3.6). Comparison of the two ratios leads to the conclusion that even in the worst case scenario (that of the contamination of A into B in 2005), when the ratio of the 2004 data is 'blended' with the contamination of the 2005 data, the result still holds.

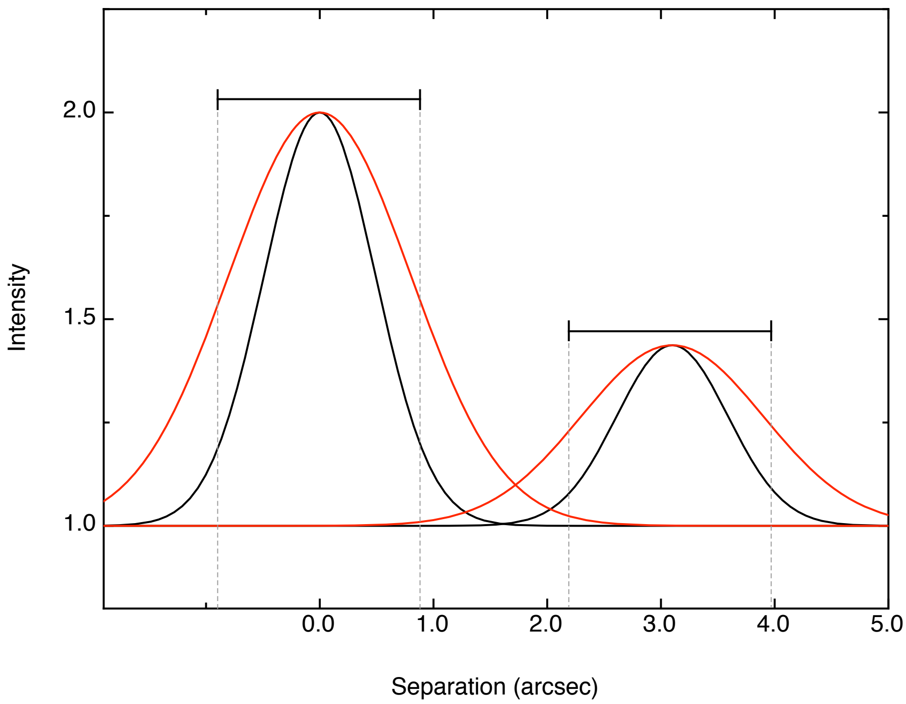

Figure 3.44: ρ Oph A & B 2004 (black lines) and 2005 (red lines) simulated star intensity profiles. Relative heights of two profiles reflect differences in magnitudes of pair (A brighter than B). Apertures used in the extraction of the spectra for both years are marked also.

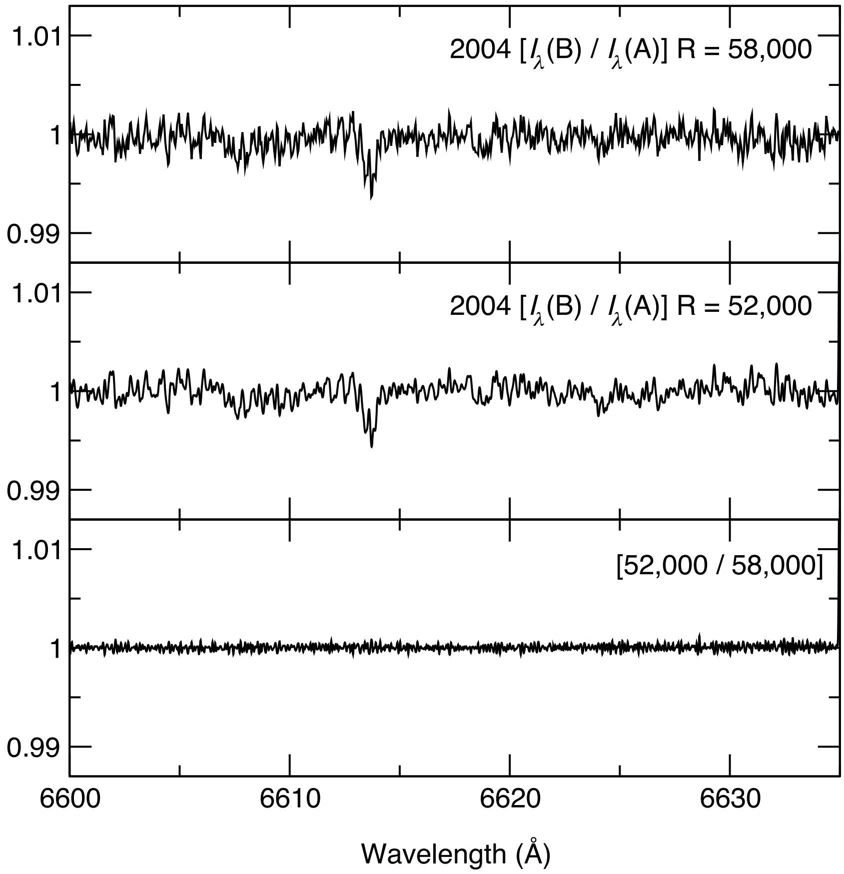

Figure 3.45: λ6614 ρ Oph B/A ratios. The upper panel is the original ratio at the 2004 spectral resolution (R) ~58,000, the middle trace is the same ratio but this time the original ρ Oph A and B spectra have been blended with a Gaussian function to simulate the lower R in 2005 (52,000). The bottom trace is the ratio of these ratios demonstrating that the lower R in 2005 does not have a significant effect.

Clearly there is an indication of TSS variations in the λ6614 diffuse band, but it is small. There is no consistent variation of the ratios indicating that the λ6614 DIB has changed towards only on of the ρ Oph stars. There is more of a difference in 2005 in the B/A ratio than in 2004; if it is assumed that this is due to the weakening of A then more of a difference in the C/A ratio would be expected also and this is the case. There is an indication that the DE/A ratio does not fit with this picture as there is *less* of a difference in the DE/A ratio in 2005 than in 2004 suggesting that A has strengthened relative to DE. With the errors associated with these minuscule changes and the uncertainty therein, in-depth discussion about a possible result is not warranted.

Table 3.7 lists the strengths of λ5780 and λ5797 in 2004 and 2005 together with the error in each measurement. There appears to be a significant difference in the λ5780 DIB

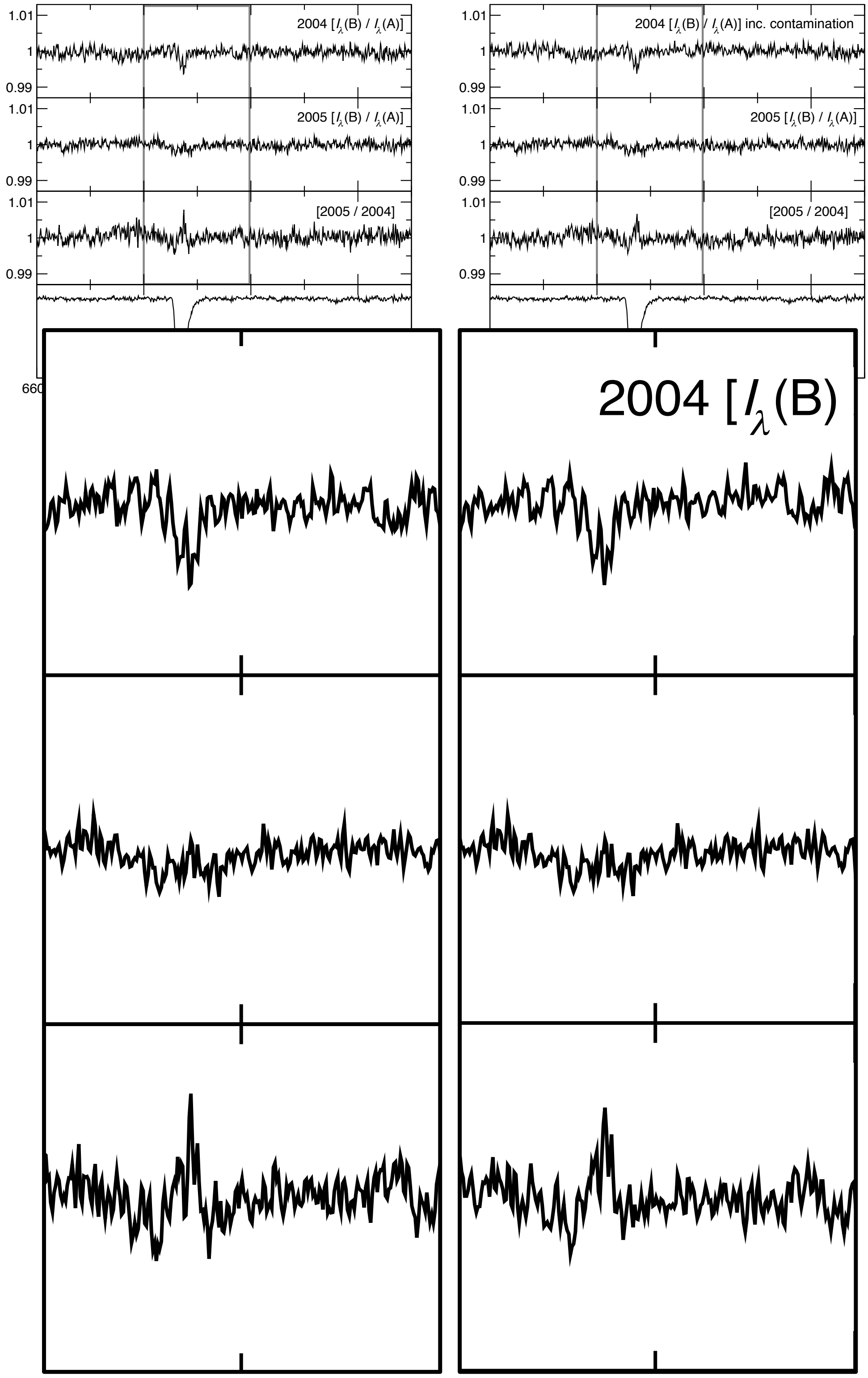

Figure 3.46: ρ Oph B/A in 2004 and 2005. The comparison is between the ratioed spectra ignoring the potential seeing-induced overlap in 2005 (left) and the 'contaminated' version of the 2004 data, incorporating the 2005 seeing overlap (right) using the values quoted in Table 3.6

Year	I_A	Cont. I_B in I_A (%)	I_B	Cont. I_A in I_B (%)
2004	2.290164	0.000001 (0.00004)	1.000000	0.000003 (0.00003)
2005	2.290164	0.002732 (0.11913)	1.000000	0.006256 (0.62173)

Table 3.6: ρ Oph A and B contaminations in 2004 and 2005. I_A is the total integrated intensity of the ρ Oph A profile between the aperture limits marked on Figure 3.44. Cont. I_B in I_A is the integrated intensity of the ρ Oph B profile in the ρ *Oph A aperture*, expressed as a percentage of the total ($I_A + I_B$) flux measured in the ρ Oph A aperture.

strength between years. The measured B/A ratio in 2005 for λ5780 is less than half that of 2004 with the λ5797 DIB also showing a reduction. The DE/A ratio between 2005 and 2004 also shows a dramatic reduction in 2005. Whilst these differences appear to be statistically significant, careful examination of the B/A ratios in Figure 3.28 show that there is a much broader component on the red wing of the λ5780 ratio in 2004 which is *not* present in 2005. This broad feature adds significantly to the measured differences (ratios) in 2004; there is some indication that this broad 'wing' is also present in the DE/A ratios in 2004 also. If it is assumed that this 'wing' is due to a feature in the stellar spectrum of ρ Oph A that is not present in 2005 then the differences in the ratios that involve A can be ascribed to a variation in the spectrum of A and not due to a decrease in the strength of the λ5780 DIB. This hypothesis is supported by the difference in the ratios (B/A 2005)/(B/A 2004) for λ5780 and the broad deviation in the continuum between $\sim$ 5782 – 5788 Å indicating that there is a feature in the 2004 ratio that *is not* present in 2005.

	Integrated area							
	2004				2005			
Ratio	λ5780	λ5797	$\sigma_{\lambda 5780}$	$\sigma_{\lambda 5797}$	λ5780	λ5797	$\sigma_{\lambda 5780}$	$\sigma_{\lambda 5797}$
ρ Oph B/A	14.5	3.6	2.6	0.8	6.2	2.9	2.3	0.7
ρ Oph C/A	–	4.3	–	1.1	–	3.2	–	1.2
ρ Oph DE/A	50.3	5.1	3.8	1.1	33.0	4.2	3.1	0.9
ρ Oph C/DE	-30.1	0.3	3.8	1.2	-24.5	-0.9	4.0	1.2

Table 3.7: λ5780 and λ5797 ratio measurements in 2004 and 2005.

In this wavelength region there is an indication that the λ5797 DIB has weakened in ρ Oph B (or strengthened in A) but with a difference of 0.7 ± 1.1 mÅ between the years the result is not statistically significant. The ratios C/A and DE/A also show a difference that could also be interpreted as an increase in the λ5797 strength towards A but again at 1.1 ± 1.6 mÅ (C/A) and 0.9 ± 1.4 mÅ (DE/A) there is no result of statistical significance.

So far only variations in the diffuse band strengths have been considered. In both 2004 and 2005 high S/N spectra of the K I and Na I D_1 atomic lines were recorded allowing an accurate measurement of their strengths in each line of sight. Measurements of the atomic species are an attractive route to pursue when looking for TSS variations as they are relatively strong and narrow permitting an accurate determination of their strengths. Figure 3.47 shows the overlaid K I and Na I D_1 absorption lines in 2004 and 2005. It is important to note that even though there appears to be a significant difference in strengths, particularly between the K I 2004 and 2005 data, this decrease in line central depth is actually due to the reduced spectral resolution in 2005. The data in Tables 3.8 and 3.9 lists the measured strengths of the atomic species between years and demonstrates that the decrease in the K I profile depth between years does not translate to a significant difference in measured equivalent widths (W_λ).

Table 3.8 shows that the only statistically significant variation in the K I strengths between years is towards ρ Oph A. Since the 2004 observations the $W_{\mathrm{K\ I}}$ has increased by ~1.7%. It is interesting that the TSS variations discussed earlier suggest that for at least some of the λ6614 and λ5797 ratios involving A one can invoke a scenario whereby the DIB strength towards A has also increased. The Na I D_1 lines show little variation outside the errors apart from ρ Oph C where a significant difference is measured.

	ρ Oph A	ρ Oph B	ρ Oph C	ρ Oph DE	σ_{W_λ}
2004	86.9	87.8	78.3	90.3	0.3
2005	88.4	88.4	79.4	90.6	0.3

Table 3.8: ρ Oph K I W_λ (mÅ)

	ρ Oph A	ρ Oph B	ρ Oph C	ρ Oph DE	σ_{W_λ}
2004	186.4	188.7	174.1	186.3	0.3
2005	186.9	188.6	175.4	186.8	0.3

Table 3.9: ρ Oph NaD1 W_λ (mÅ)

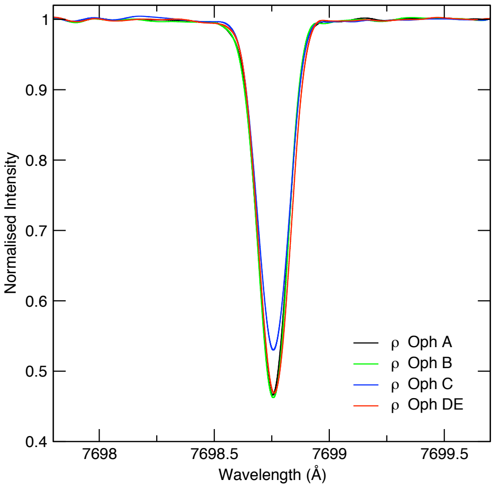

(a) ρ Oph 2004 K I

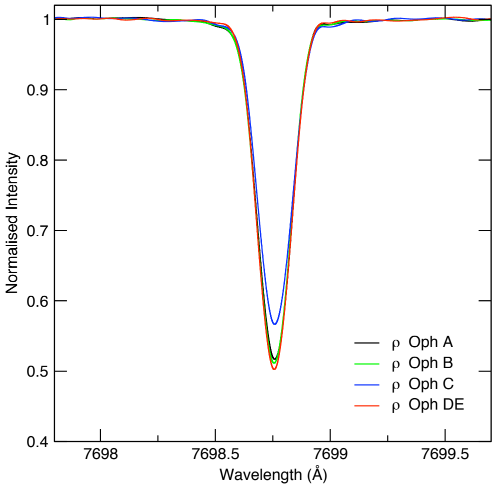

(b) ρ Oph 2005 K I

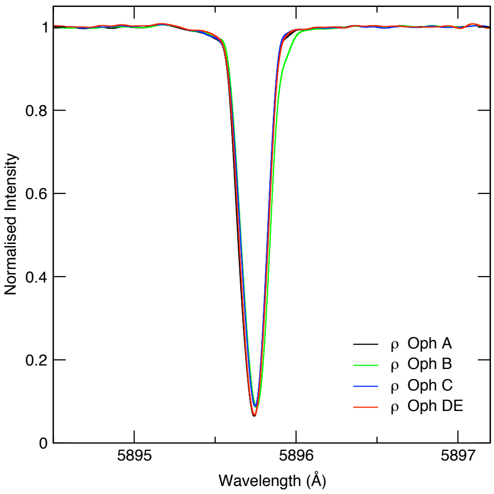

(c) ρ Oph 2004 Na I D_1

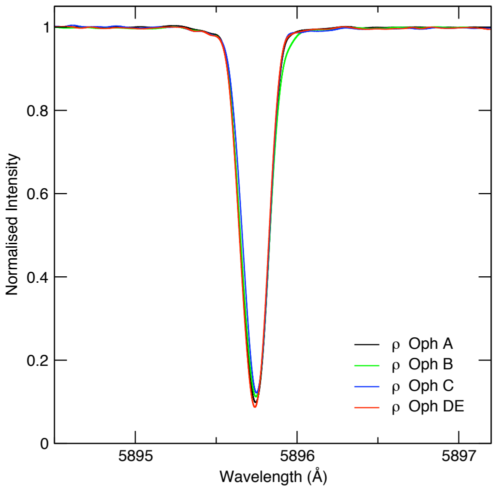

(d) ρ Oph 2005 Na I D_1

Figure 3.47: Plots of ρ Oph 2004 K I (top left) and 2005 K I (top right) together with ρ Oph 2004 Na I D_1 (bottom left) and ρ Oph 2005 Na I D_1 (bottom right). All spectra are continuum normalised and have been fitted with cubic spline polynomials.

β Sco 2004 - 2005

The continuum of β^2 Sco is plagued by stellar features making the comparison of β^2/β^1 diffuse band ratios between years virtually impossible. However, given the high quality of the data recorded, the direct comparison of DIB profiles from the *same* star between years is of interest. The ρ Oph results and discussion have shown that the differences sought are so small and as this method is so dependent on accurate, reliable and repeatable continuum definition around the DIB profile the results are inconclusive. Hence for the β Sco lines of sight have only been investigated in the atomic species K I and Na I D_1.

As was the case for the atomic line profiles in ρ Oph, the differences in spectral resolution between years, R $\sim$ 58,000 in 2004, $\sim$ 52,000 in 2005, produces slightly broader shallower features in 2005 making direct comparison of atomic line spectra impossible. However the equivalent width measurements are independent of the spectral resolution so these *can* be compared. Figure 3.48 shows the K I and Na I D_1 atomic line profiles for both years for β^1 and β^2 Sco. The profiles look remarkably similar (albeit shallower in 2005). This is reflected in the very similar values for their equivalent widths in Table 3.11.

Within the errors, no differences in the strengths of either Na I D_1 or K I is found between years towards the β Sco pair. While this is a negative result for the TSS part of this project, the remarkable repeatability of the SSS result i.e. differences between β^1 and β^2 Sco increase confidence in this earlier result.

Table 3.10: β Sco Na I D_1 and K I equivalent widths (mÅ)

	Na I D_1			K I		
	β^1 Sco	β^2 Sco	σ_{W_λ}	β^1 Sco	β^2 Sco	σ_{W_λ}
2004	146.6	154.0	0.5	21.7	23.8	0.3
2005	145.5	153.0	0.5	21.7	23.8	0.3

Table 3.11: β Sco Na I D and K I W_λ (mÅ)

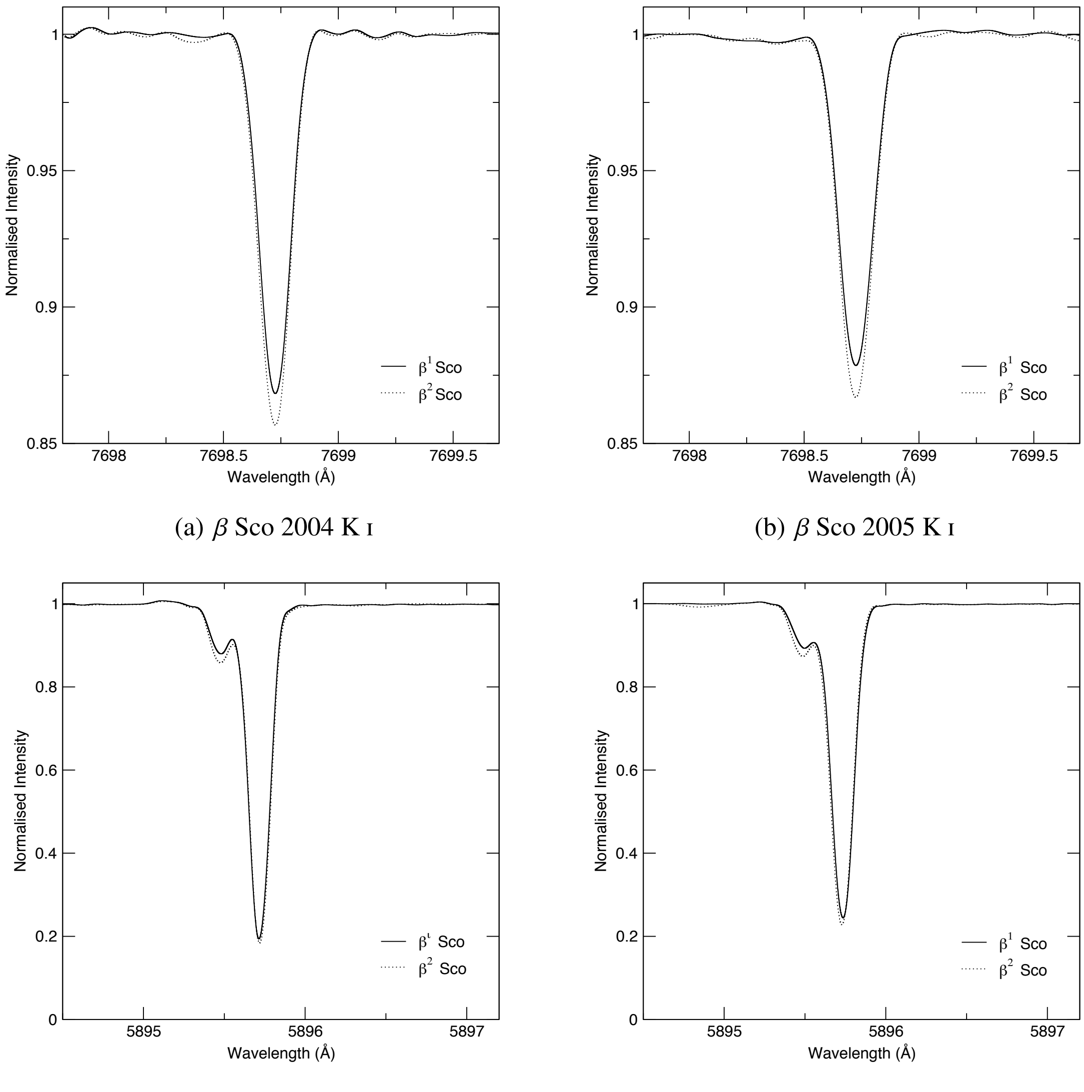

(a) β Sco 2004 K I

(b) β Sco 2005 K I

(c) β Sco 2004 Na I D_1

(d) β Sco 2005 Na I D_1

Figure 3.48: Plots of β Sco 2004 K I (top left) and 2005 K I (top right) together with β Sco 2004 Na I D_1 (bottom left) and 2005 Na I D_1 (bottom right). All spectra are continuum normalised and have been fitted with cubic spline polynomials.

ν Sco 2004 - 2005

As for β^1 and β^2 Sco, ratios of the spectra of ν^1 and ν^3 Sco are severely contaminated by the plethora of stellar features in ν^3 Sco making a diffuse band study difficult. In the search for TSS variations, a comparison of only the Na I D_1 lines and K I lines is made.

Table 3.12 lists equivalent width measurements for Na I D_1 and K I. As for β Sco, the values measured in 2005 are in good agreement with the 2004 values. The small differences in values are well within the uncertainties. It is therefore concluded that there is no indication of TSS variations in the Na I D_1 and K I strengths between 2004 and 2005.

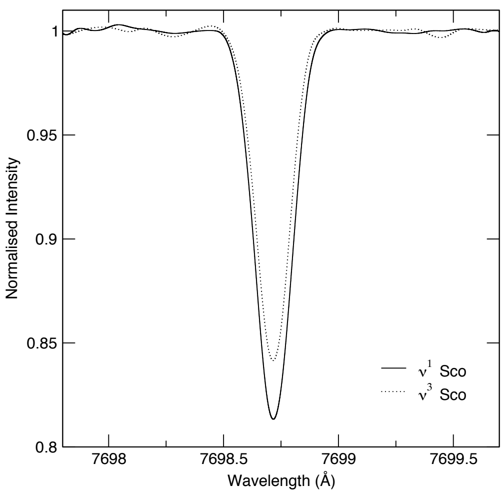

(a) ν Sco 2004 K I

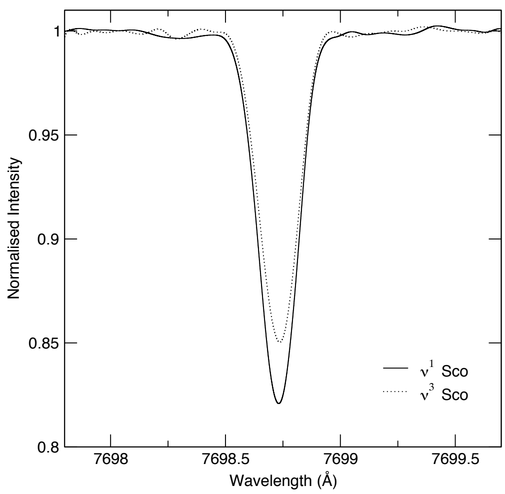

(b) ν Sco 2005 K I

Figure 3.49: Plots of (a) ν Sco 2004 K I (left) and (b) 2005 K I (right). All spectra are continuum normalised and have been fitted with cubic spline polynomials.

	Na I D_1			K I		
	ν^1 Sco	ν^3 Sco	σ_{W_λ}	ν^1 Sco	ν^3 Sco	σ_{W_λ}
2004	199.9	192.9	0.5	35.9	29.5	0.3
2005	200.5	192.8	0.5	36.2	29.4	0.3

Table 3.12: ν Sco Na I D_1 and K I equivalent widths (mÅ)

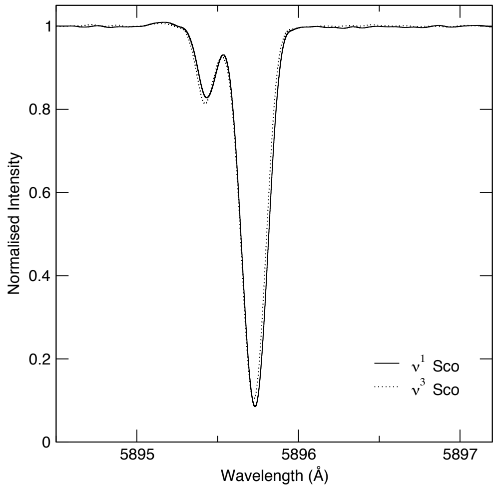

(a) ν Sco 2004 Na I D_1

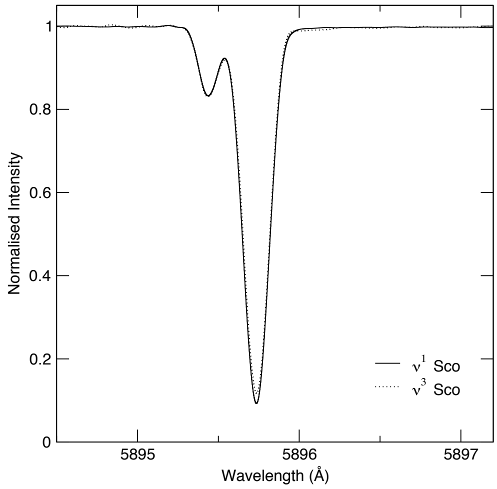

(b) ν Sco 2005 Na I D_1

Figure 3.50: Plots of (a) ν Sco 2004 Na I D_1 (left) and (b) 2005 Na I D_1 (right). All spectra are continuum normalised and have been fitted with cubic spline polynomials.

3.3.3 A common carrier for "C_2" features?

It is important that while analysing the DIB spectrum researchers attempt to find pairs or multiples of DIBs that may be related in some way. It is unlikely that there is a different carrier for each of the many hundreds of DIBs now discovered and so attempts to find consistent splitting in DIB pairs are worthwhile.

During their investigation of the "C_2" bands Thorburn *et al.* (2003) noted that some of the features form pairs with roughly equal splitting of ~ 20 cm^{-1}. The pairs are λ4964 & λ4969, λ4979 & λ4984 and λ5170 & λ5176. It was suggested that the splitting is reminiscent of a spin-orbit interaction in a linear molecule. If this is the case then there should be a correlation between the summed pairs of band strengths if this splitting is in the ground electronic state. Given the high quality of our data recorded towards ρ Oph a test was made of this hypothesis.

Figure 3.51 shows the EW of the summed pairs of DIBs from AB, C and DE. The spectra of ρ Oph A and B were combined for this analysis as the S/N achieved when producing a composite spectrum and combining all of the data (including poor seeing) allowed for a more accurate assessment of the hypothesis. Table 3.13 lists the $\lambda_{\rm central}$ values for the DIBs analysed, the difference in their wavelengths ($\Delta\lambda$) and the equivalent value in wavenumbers (cm^{-1}). The agreement with Thorburn *et al.* for the λ4979

– λ4984 and λ5170 – λ5196 pairs is excellent. For both of these pairs the splitting measured in wavenumbers is 20.7 cm^{-1}. The λ4964 – λ4949 splitting in the UCLES spectra is 21.2 cm^{-1} which is slightly different from the value of 20.9 cm^{-1} reported by Thorburn *et al.* Unfortunately as these DIBs are only present in the ρ Oph stars it has not been possible to further test the relationship between these features. The relatively weak nature of these DIBs and uncertainties associated with measuring the central wavelengths of the features means that it has not been possible to prove or disprove this interesting hypothesis. Further investigation of this possible relationship in more lines of sight seems worthwhile.

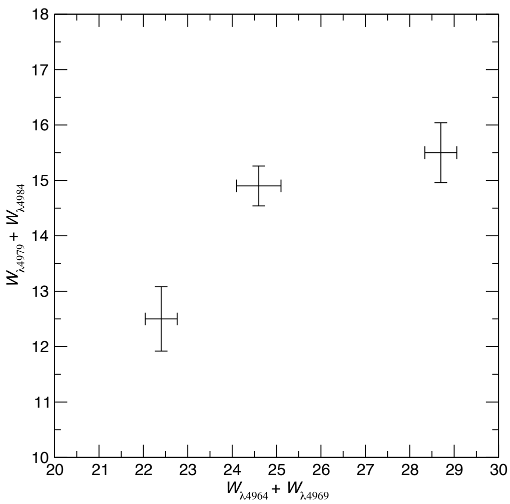

(a) (λ4979 + λ4984) vs (λ4964 + λ4969)

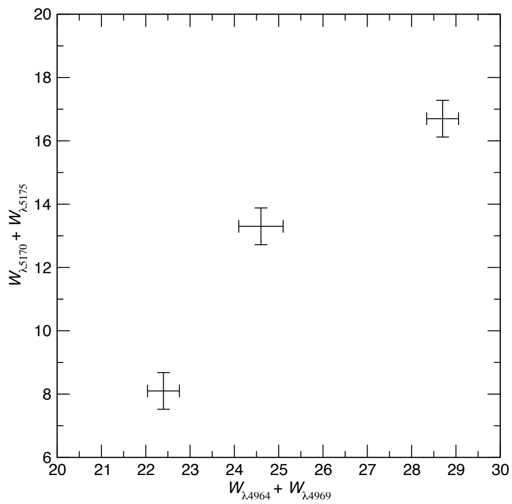

(b) (λ5170 + λ5176) vs (λ4964 + λ4969)

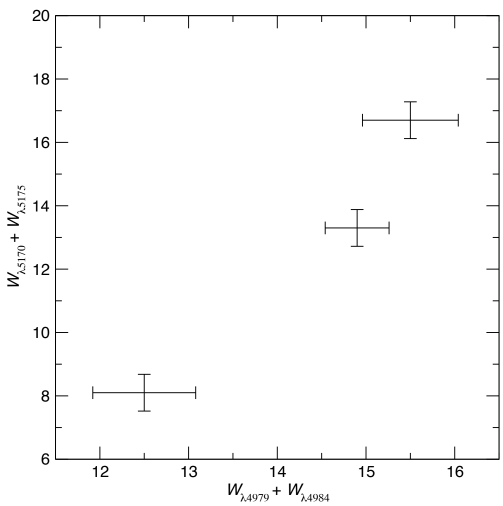

(c) (λ5170 + λ5176) vs (λ4979 + λ4984)

Figure 3.51: Plots of the summed equivalent widths of the pairs of DIBs listed in Table 3.13.

DIB_1 (Å)	DIB_2 (Å)	$\Delta\lambda$ (Å)	$\Delta\sigma_{\text{(This study)}}$ (cm^{-1})	$\Delta\sigma_{\text{(Thorburn } et\ al)}$ (cm^{-1})
4963.77	4968.99	5.22	21.2	20.9
4979.50	4984.66	5.16	20.7	20.7
5170.36	5175.92	5.56	20.7	20.7

Table 3.13: "C_2" DIB splittings

3.3.4 Profiles of blue diffuse bands

Probably due to their relative weakness compared to the well-known (and studied) yellow and red DIBs (e.g. λ5780, λ5797, λ6614), relatively little is known about the 'blue' features studied in this Thesis. Recently, Słyk *et al.* (2006) published high resolution (R ~ 120,000) profiles of some of the stronger blue DIBs. Their aim was to look for fine structure, something often interpreted as evidence for a molecular carrier, in the profiles of the features. This well-studied phenomenon has been considered by many authors (e.g. Kerr *et al.* 1996, Kerr *et al.* 1998) at the highest spectral resolutions available (< 1 kms^{-1}, UHRF (Diego *et al.* 1995)). Given the unprecedented S/N achieved in these UCLES data, DIB profiles for the features are presented in order to investigate fine structure and to make comparison with the structure seen in the DIB profiles of Słyk *et al.* (2006).

Figures 3.52 and 3.53 show the profiles of the blue DIBs studied here. The UCLES data S/N exceeds that of the Słyk *et al.* data and fine structure hinted at in the higher resolution but lower S/N profiles of Słyk *et al.* are confirmed in our data (e.g. λ4964 and λ5541). Słyk *et al.* suggested that there is evidence for extremely narrow fine structure in the profile of λ5418 as seen in Figure 3.53. Whilst there is clearly structure in the λ5418 DIB in our UCLES data, the narrow spikes seen by Słyk *et al.* are not detected. This leads to the conclusion that either the spectral resolution of the UCLES data is insufficient to resolve these features or that they are in fact noise. Of the nine DIBs presented there is clear fine structure within six of them. The λ4726 DIB has a curious shape and is likely a blend of two separate features, whether or not there is fine structure within the two blended components is not obvious. There is a hint of fine structure within the weak λ4984 DIB profile, unfortunately it appears that this DIB needs to be observed at high resolution to confirm this.

Diffuse band studies are almost always a compromise between spectral resolution and

S/N in the observing time available. Comparison of the UCLES profiles with those presented by Słyk *et al.* demonstrate that achieving the highest possible spectral resolution is desirable but not at the expense of S/N. Many of the Słyk *et al.* profiles show signs of fine structure but the S/N is not good enough to be certain of this. These UCLES profiles showcase what is possible at moderate resolution and extremely high S/N. The detection of fine structure in the majority of the blue DIBs here means that further study at higher resolution and high S/N is warranted.

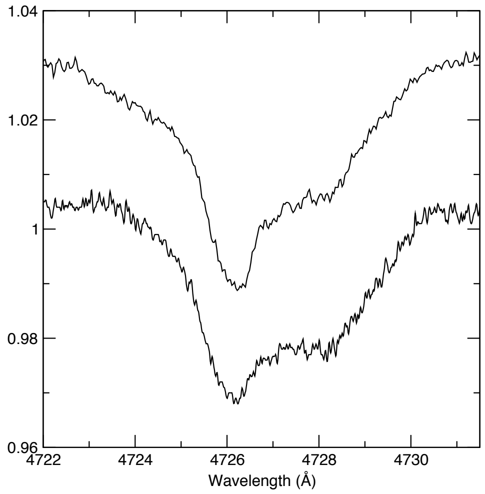

(a) λ4726

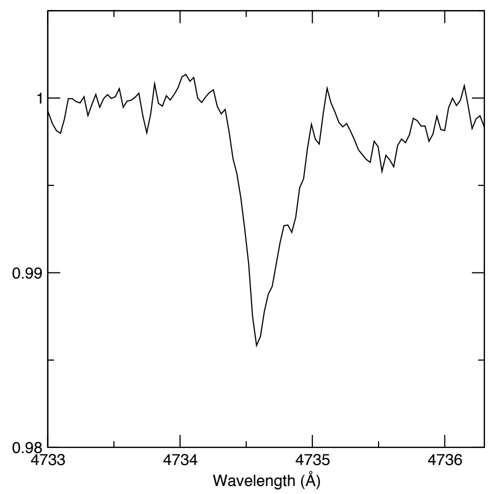

(b) λ4734

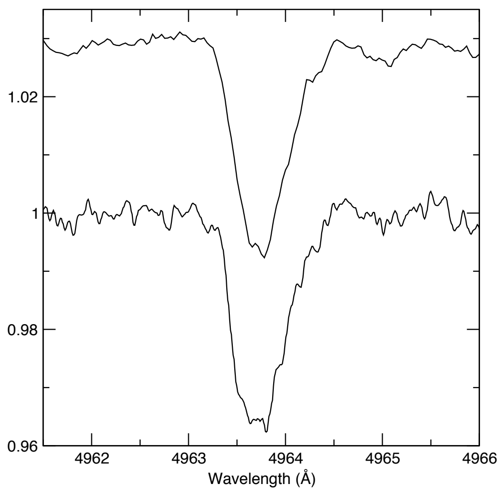

(c) λ4964

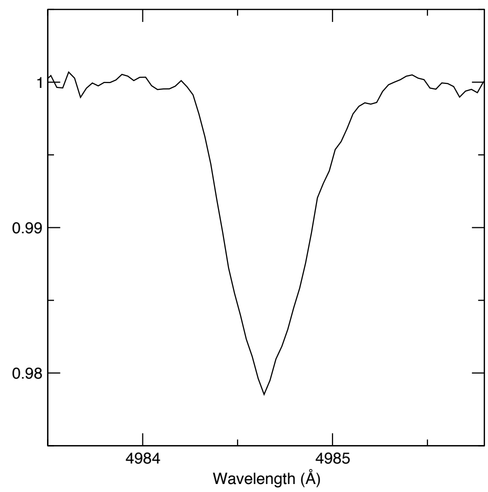

(d) λ4984

Figure 3.52: Combined spectrum of ρ Oph A and B in 2005 data of λ4726, λ4734, λ4964, λ4984, λ5170 and λ5176 at R ~ 50,000 (upper traces) compared with the same DIB profile in (Słyk *et al.* 2006) at R ~ 120,000 (lower trace)

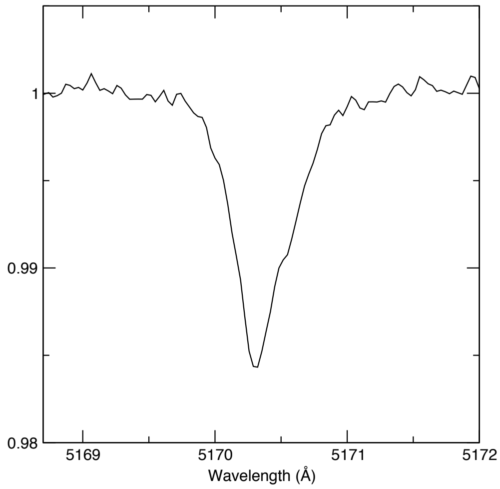

(a) $\lambda5170$

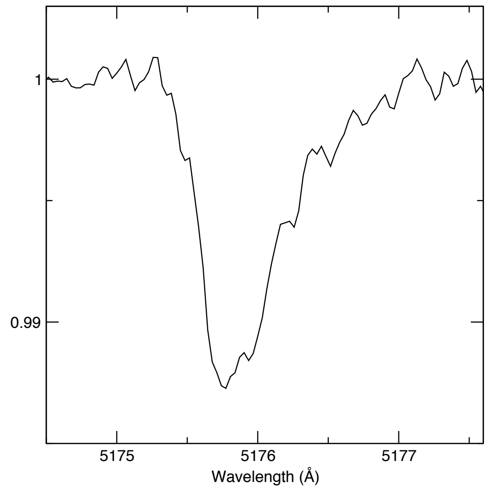

(b) $\lambda5176$

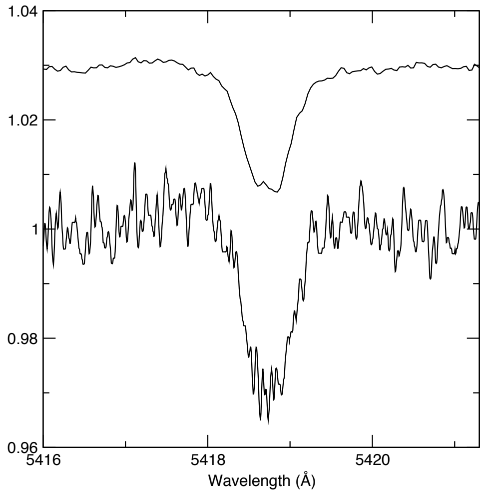

(c) $\lambda5418$

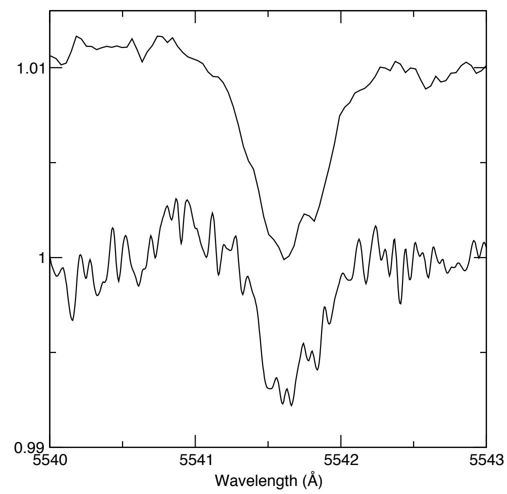

(d) $\lambda5541$

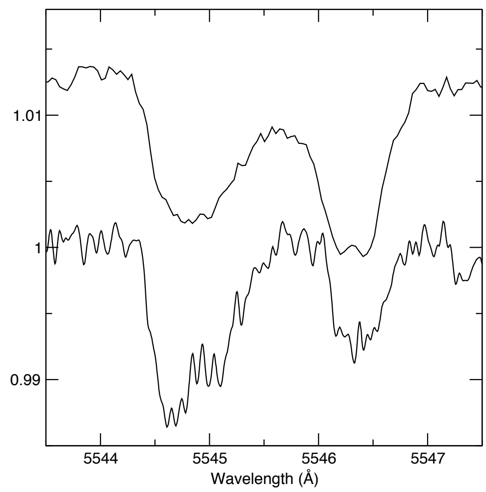

(e) $\lambda5544$ / $\lambda5546$

Figure 3.53: Combined spectrum of ρ Oph A and B in 2005 data of $\lambda5170$, $\lambda5176$ $\lambda5418$ and $\lambda5541$ and $\lambda5544$/$\lambda5546$ at R ~ 50,000 (upper traces), compared with the same DIB profile in (Słyk *et al.* 2006) at R ~ 120,000 (lower trace)

3.4 Diffuse Band Families

In an effort to simplify the problem of identifying the carriers of the diffuse bands, researchers have attempted to pool different bands into groups or 'families'. The most widely used classification scheme is that of Krełowski and Walker 1987 and is based upon differences in DIB intensity ratios seen towards nearby stars. Whilst other authors have introduced their own classification schemes (e.g. Chlewicki *et al.* 1987), the Krełowski and Walker approach is likely superior as their observations were made towards stars obscured by single clouds, thus avoiding the potential confusion and uncertainty associated with multi-cloud lines of sight.

Krełowski and Walker grouped various DIBs into three families based upon intensity ratios of pairs of DIBs (KW I, KW II and KW III). These families can be described as follows:

> I. Broad and shallow DIBs are almost all in this family, the archetypal member being λ4430. The strengths of these DIBs, relative to DIBs in other families, varies significantly leading to the conclusion that the carriers must be sensitive to the conditions of the IS cloud in which they reside. The broad, shallow nature of these bands makes precise measurement of their EWs difficult.
>
> II. This family is composed mostly of strong bands that have relatively symmetric profiles. A typical member of this family is the strong λ5780 diffuse band. Like the bands in KW I, the KW II DIBs can be sensitive to the physical conditions of their environment.
>
> III. The third Krełowski and Walker family consists mainly of relatively sharp asymmetric DIBs. Unlike the other two families, KW III DIBs are relatively insensitive to the physical condition of their environment leading to the conclusion that their carriers are more 'hardy'.

One of the main problems associated with putting DIBs into families arises when observations are made towards heavily reddened lines of sight where the DIB carriers reside in multiple clouds. Correlations identified in such sight lines are plagued by the

KW I	KW II	KW III
λ4430, λ4882, λ6180	λ4763, λ4780, λ5362 λ5449, λ5487, λ5535 λ5780, λ6196, λ6203 λ6269, λ6284	λ4726, λ5494, λ5508 λ5545, λ5797, λ5850 λ6376, λ6379, λ6614

Table 3.14: Some DIBs and their Krełowski and Walker family members.

uncertainty introduced by having multiple DIB environments, each presumably with different physical conditions that favour individual carriers. It is clear therefore that, in order to classify the DIBs in a meaningful way, correlation studies must be performed towards single-cloud[5] lines of sight.

Follow-up investigations of single clouds (e.g. Cami *et al.* 1997, Moutou *et al.* 1999) have added more DIBs to the relatively small number originally considered. Cami *et al.* (1997) calculated the EW correlation coefficients of 44 DIBs in high S/N, high-resolution spectra recorded along single-cloud lines of sight with very different conditions. They interpreted their results in terms of DIB-carrier response to the local UV field strength and argued that the differentiation of interstellar clouds into ζ , σ and Orion type originates in UV field strength difference.

Moutou *et al.* (1999) performed a similar analysis to that of Cami *et al.* but in their study used the central depths (CD) of the DIBs as an indicator of band strength. It was argued that in single-cloud environments the band-width difference should be negligible and for moderate quality data the error associated with CD measurements is smaller than that for EW measurements. As in the study by Cami *et al.* the best DIB-DIB correlation was found to be between the λ6196 and λ6614 diffuse bands ($R^2 \simeq 0.95$) leading them to the conclusion that there may be a single carrier for the two bands. McCall *et al.* (2005) have also reported a R-squared value of 0.985 for the λ6196 and λ6614 correlation in their ongoing APO survey. However, the story is not complete as recent work by Galazutdinov *et al.* (2002) questions whether the two bands come from the same carrier; ratios of high S/N, high resolution spectra do not appear to always be

[5]Single-cloud environments are those where the interstellar atomic species (e.g. Na, Ca) show only one component, even at the highest resolution and are extremely rare. For the purposes of identifying related DIBs *pseudo* single-cloud environments are sufficient and are defined as those where there is only one *major* component in the interstellar Na and Ca lines which outweigh other components in strength by at least an order of magnitude.

the same.

This extremely high quality (S/N >1000 for ρ Oph A & B) dataset provides a unique opportunity to test the family hypotheses and individual DIB-pair correlations identified by other authors (e.g. λ6196 - λ6614 Cami *et al.* 1997, Moutou *et al.* 1999). Whilst there is one *main* component in the ρ Oph set of stars it is probably not quite the 'pseudo' single-cloud type environment studied by Cami *et al.* (1997). As there is no way around this issue, for the purposes of this DIB-family investigation the ρ Oph suite of stars are each considered a single-cloud line of sight.

Figure 3.54 is matrix plot of the correlation coefficients (R-squared) for DIB–DIB correlation plots for 22 different DIBs in the ρ Oph stars. Numbers in black represent a positive correlation i.e. the strength of one DIB increases with the other, numbers in red represent a negative correlation. Immediately obvious in Figure 3.54 is that the upper left-hand region of the plot, i.e. the R-squared values for the "C_2" blue DIB–DIB correlations are almost all positive. Conversely, in the upper right-hand region, the vast majority of the R-squared values are red, that is, there is little overall correlation between the blue and yellow/red diffuse bands.

The behaviour of the blue DIB correlations is not perfect however as there are some pairs, e.g. λ4734 vs. λ5541, where there appears to be a fairly strong *negative* correlation even though both DIBs are believed to belong to the same "C_2" DIB family (Thorburn *et al.* 2003).

A helpful approach when looking for pairs or groups of DIBs that behave in the same way is to trace down the vertical columns of two or more DIBs looking for consistent behaviour. An example of such a pair are λ6376 and λ6379 where the behaviour of the two DIBs is remarkably similar; in all cases where there is a strong positive correlation with one of the DIBs the other has a similarly strong R-squared value. This behaviour is reflected in the R-squared value for the λ6376–λ6379 correlation of 0.99.

A common misconception is that the DIBs belonging to the same Krełowski and Walker family come from the same carrier however this is not the case. The initial work by Krełowski and Walker (1987) demonstrated that some DIBs 'go with' each other, i.e., behave in the same way when exposed to different physical environments. A problem with placing DIBs in groups determined by their behaviour between very different physical conditions is that additional factors that might affect DIB strengths may be missed. The ρ Oph suite of stars offer 4 similar lines of sight; even though there are differences in the DIB strengths, these sight lines are, to a first approximation very similar. It is only at the extremely high S/N recorded in these data that the subtle differences in DIB strengths are realised. These targets offer an opportunity to test the Krełowski and Walker families as those DIBs belonging to the same family should in principle behave in a similar fashion.

Figure 3.55 includes the same correlation data as Figure 3.54 with some Krełowski and Walker family members also marked. Those squares marked blue belong to KW II, those marked in red KW III. As mentioned previously, the λ6376/λ6379 pair behave very similarly and both belong to KW family III. Their behaviour with respect to other KW III family members is mixed; λ6614 is another KW III family member and the correlation with λ6376 and λ6379 is strong (> 0.9). Their correlation with λ5797 is positive but weak and with KW III member λ5850 negative. This behaviour is clearly seen in Figures 3.16 and 3.21 where λ5850 is significantly stronger towards ρ Oph A than DE and λ6376 & λ6376 are significantly weaker towards A. In the ρ Oph sightlines λ5850 does not behave in a similar fashion as other members of the KW III family (λ5797, λ6376, λ6379 and λ6614).

Of those family members listed in Figure 3.55, the KW II DIBs (marked with blue boxes) behave more consistently than the KW III DIBs. λ5780 appears to correlate extremely well with λ6203 and reasonably well with λ6196. λ6196 shows a moderate negative correlation with λ6284.

It is clear that there are discrepancies in the behaviour of KW family members. λ5850 appears to be the most anomalous DIB showing a negative correlation with three other KW III family members. It should be kept in mind that the R-squared values come from plots containing only four points, the statistical significance of a correlation is therefore questionable. Figure 3.56 shows the correlations for thirteen yellow/red DIBs including the four ρ Oph sightlines as well as β^1 Sco, ν^1 Sco, HD 150135 and HD 164863.

	4726	4734	4964	4984	5170	5176	5418	5512	5541	5705	5780	5797	5850	6196	6203	6284	6376	6379	6426	6614	6660	7562	
4726	1.00	0.09	0.89	0.57	0.10	0.41	0.59	0.48	0.00	0.58	0.99	0.27	0.44	0.83	1.00	0.06	0.98	0.98	0.15	0.89	0.94	0.67	4726
4734	0.09	1.00	0.25	0.69	0.67	0.74	0.15	0.23	0.87	0.15	0.11	0.64	0.27	0.01	0.07	0.73	0.03	0.06	0.27	0.00	0.22	0.28	4734
4964	0.89	0.25	1.00	0.67	0.00	0.48	0.31	0.26	0.04	0.33	0.94	0.60	0.21	0.54	0.86	0.00	0.83	0.88	0.07	0.69	0.99	0.53	4964
4984	0.57	0.69	0.67	1.00	0.14	0.96	0.03	0.00	0.46	0.02	0.56	0.55	0.00	0.21	0.54	0.20	0.42	0.50	0.49	0.24	0.69	0.79	4984
5170	0.10	0.67	0.00	0.14	1.00	0.21	0.72	0.80	0.82	0.72	0.07	0.25	0.84	0.44	0.11	0.99	0.19	0.13	0.06	0.36	0.01	0.00	5170
5176	0.41	0.74	0.48	0.96	0.21	1.00	0.00	0.01	0.60	0.00	0.38	0.42	0.01	0.12	0.39	0.30	0.27	0.34	0.64	0.12	0.50	0.78	5176
5418	0.59	0.15	0.31	0.03	0.72	0.00	1.00	0.97	0.34	0.99	0.53	0.01	0.97	0.92	0.62	0.64	0.71	0.64	0.01	0.85	0.37	0.22	5418
5512	0.48	0.23	0.26	0.00	0.80	0.01	0.97	1.00	0.48	0.99	0.46	0.01	0.99	0.82	0.51	0.74	0.62	0.55	0.01	0.80	0.30	0.10	5512
5541	0.00	0.87	0.04	0.46	0.82	0.60	0.34	0.48	1.00	0.38	0.00	0.30	0.50	0.11	0.00	0.90	0.01	0.00	0.37	0.10	0.03	0.18	5541
5705	0.58	0.15	0.33	0.02	0.72	0.00	0.99	0.99	0.38	1.00	0.54	0.00	0.98	0.89	0.61	0.66	0.71	0.64	0.00	0.87	0.38	0.17	5705
5780	0.99	0.11	0.94	0.56	0.07	0.38	0.53	0.46	0.00	0.54	1.00	0.36	0.40	0.77	0.98	0.04	0.97	0.99	0.10	0.87	0.97	0.59	5780
5797	0.27	0.64	0.60	0.55	0.25	0.42	0.01	0.01	0.30	0.00	0.36	1.00	0.03	0.02	0.24	0.26	0.20	0.25	0.00	0.10	0.51	0.14	5797
5850	0.44	0.27	0.21	0.00	0.84	0.01	0.97	0.99	0.50	0.98	0.40	0.03	1.00	0.81	0.47	0.78	0.58	0.50	0.00	0.76	0.25	0.10	5850
6196	0.83	0.01	0.54	0.21	0.44	0.12	0.92	0.92	0.11	0.89	0.77	0.02	0.81	1.00	0.85	0.35	0.90	0.86	0.09	0.95	0.61	0.48	6196
6203	1.00	0.07	0.86	0.54	0.11	0.39	0.62	0.51	0.00	0.61	0.98	0.24	0.47	0.85	1.00	0.07	0.98	1.00	0.16	0.90	0.92	0.67	6203
6284	0.06	0.73	0.00	0.20	0.99	0.30	0.64	0.74	0.90	0.66	0.04	0.26	0.78	0.35	0.07	1.00	0.14	0.09	0.12	0.30	0.00	0.01	6284
6376	0.98	0.03	0.83	0.42	0.19	0.27	0.71	0.62	0.01	0.71	0.97	0.20	0.58	0.90	0.98	0.14	1.00	0.99	0.09	0.96	0.96	0.56	6376
6379	1.00	0.06	0.88	0.50	0.13	0.34	0.64	0.55	0.00	0.64	0.99	0.25	0.50	0.86	1.00	0.09	0.99	1.00	0.11	0.92	0.92	0.61	6379
6426	0.15	0.27	0.07	0.49	0.06	0.64	0.01	0.01	0.37	0.00	0.10	0.00	0.00	0.09	0.16	0.12	0.09	0.11	1.00	0.03	0.12	0.72	6426
6614	0.89	0.00	0.69	0.24	0.36	0.12	0.85	0.80	0.10	0.87	0.87	0.10	0.76	0.95	0.90	0.30	0.96	0.92	0.03	1.00	0.74	0.40	6614
6660	0.94	0.22	0.99	0.69	0.01	0.50	0.37	0.30	0.03	0.38	0.97	0.51	0.25	0.61	0.92	0.00	0.88	0.92	0.12	0.74	1.00	0.61	6660
7562	0.67	0.28	0.53	0.79	0.00	0.78	0.22	0.10	0.18	0.17	0.59	0.14	0.10	0.48	0.67	0.01	0.56	0.61	0.72	0.40	0.61	1.00	7562
	4726	4734	4964	4984	5170	5176	5418	5512	5541	5705	5780	5797	5850	6196	6203	6284	6376	6379	6426	6614	6660	7562	

Figure 3.54: Correlation plot of 22 DIBs in the ρ Oph stars

	4726	4734	4964	4984	5170	5176	5418	5512	5541	5705	5780	5797	5850	6196	6203	6284	6376	6379	6426	6614	6660	7562
4726	1.00	0.09	0.89	0.57	0.10	0.41	0.59	0.48	0.00	0.58	0.99	0.27	0.44	0.83	1.00	0.06	0.98	1.00	0.15	0.89	0.94	0.67
4734	0.09	1.00	0.25	0.69	0.67	0.74	0.15	0.23	0.87	0.15	0.11	0.64	0.27	0.01	0.07	0.73	0.03	0.06	0.27	0.00	0.22	0.28
4964	0.89	0.25	1.00	0.67	0.00	0.48	0.31	0.26	0.04	0.33	0.94	0.60	0.21	0.54	0.86	0.00	0.83	0.88	0.07	0.69	0.99	0.53
4984	0.57	0.69	0.67	1.00	0.14	0.96	0.03	0.00	0.46	0.02	0.56	0.55	0.00	0.21	0.54	0.20	0.42	0.50	0.49	0.24	0.69	0.79
5170	0.10	0.67	0.00	0.14	1.00	0.21	0.72	0.80	0.82	0.72	0.07	0.25	0.84	0.44	0.11	0.99	0.19	0.13	0.06	0.36	0.01	0.00
5176	0.41	0.74	0.48	0.96	0.21	1.00	0.00	0.01	0.60	0.00	0.38	0.42	0.01	0.12	0.39	0.30	0.27	0.34	0.64	0.12	0.50	0.78
5418	0.59	0.15	0.31	0.03	0.72	0.00	1.00	0.97	0.34	0.99	0.53	0.01	0.97	0.92	0.62	0.64	0.71	0.64	0.01	0.85	0.37	0.22
5512	0.48	0.23	0.26	0.00	0.80	0.01	0.97	1.00	0.48	0.99	0.46	0.01	0.99	0.82	0.51	0.74	0.62	0.55	0.01	0.80	0.30	0.10
5541	0.00	0.87	0.04	0.46	0.82	0.60	0.34	0.48	1.00	0.38	0.00	0.30	0.50	0.11	0.00	0.90	0.01	0.00	0.37	0.10	0.03	0.18
5705	0.58	0.15	0.33	0.02	0.72	0.00	0.99	0.99	0.38	1.00	0.54	0.00	0.98	0.89	0.61	0.66	0.71	0.64	0.00	0.87	0.38	0.17
5780	0.99	0.11	0.94	0.56	0.07	0.38	0.53	0.46	0.00	0.54	1.00	0.36	0.40	0.77	0.98	0.04	0.97	0.99	0.10	0.87	0.97	0.59
5797	0.27	0.64	0.60	0.55	0.25	0.42	0.01	0.01	0.30	0.00	0.36	1.00	0.03	0.02	0.24	0.26	0.20	0.25	0.00	0.10	0.51	0.14
5850	0.44	0.27	0.21	0.00	0.84	0.01	0.97	0.99	0.50	0.98	0.40	0.03	1.00	0.81	0.47	0.78	0.58	0.50	0.00	0.76	0.25	0.10
6196	0.83	0.01	0.54	0.21	0.44	0.12	0.92	0.92	0.11	0.89	0.77	0.02	0.81	1.00	0.85	0.35	0.90	0.86	0.09	0.95	0.61	0.48
6203	1.00	0.07	0.86	0.54	0.11	0.39	0.62	0.51	0.00	0.61	0.98	0.24	0.47	0.85	1.00	0.07	0.98	1.00	0.16	0.90	0.92	0.67
6284	0.06	0.73	0.00	0.20	0.99	0.30	0.64	0.74	0.90	0.66	0.04	0.26	0.78	0.35	0.07	1.00	0.14	0.09	0.12	0.30	0.00	0.01
6376	0.98	0.03	0.83	0.42	0.19	0.27	0.71	0.62	0.01	0.71	0.97	0.20	0.58	0.90	0.98	0.14	1.00	0.99	0.09	0.96	0.88	0.56
6379	1.00	0.06	0.88	0.50	0.13	0.34	0.64	0.55	0.00	0.64	0.99	0.25	0.50	0.86	1.00	0.09	0.99	1.00	0.11	0.92	0.92	0.61
6426	0.15	0.27	0.07	0.49	0.06	0.64	0.01	0.01	0.37	0.00	0.10	0.00	0.00	0.09	0.16	0.12	0.09	0.11	1.00	0.03	0.12	0.72
6614	0.89	0.00	0.69	0.24	0.36	0.12	0.85	0.80	0.10	0.87	0.87	0.10	0.76	0.95	0.90	0.30	0.96	0.92	0.03	1.00	0.74	0.40
6660	0.94	0.22	0.99	0.69	0.01	0.50	0.37	0.30	0.03	0.38	0.97	0.51	0.25	0.61	0.92	0.00	0.88	0.92	0.12	0.74	1.00	0.61
7562	0.67	0.28	0.53	0.79	0.00	0.78	0.22	0.10	0.18	0.17	0.59	0.14	0.10	0.48	0.67	0.01	0.56	0.61	0.72	0.40	0.61	1.00

Figure 3.55: Correlation plot of 22 DIBs in the ρ Oph stars including the KW II and KW III families

The R-squared values in Figure 3.56 are therefore derived from plots containing eight points compared with four in Figures 3.54 and 3.55. DIBs in the same KW familiy should behave consistently over all sightlines; the data incorporated into Figure 3.56 is therefore a more significant test of the KW families. With the extra four data points the discrepancies seen in Figure 3.55 between KW III family members disappear. As a group, the KW III DIBs now all show mutual positive correlation. The KW II family members still appear to behave moderately well although there is no correlation between λ5780 and λ6203 and λ6284. A comparison of the R-squared values in Figure 3.55 and Figure 3.56 demonstrates that there is scope for error when working with small datasets. Given that the number of lines-of-sight doubles between the two figures and that there is more variety in the sightlines in Figure 3.56 then these correlation values should be considered more significant.

Figure 3.57 highlights those DIBs where there is a correlation of > 0.8. DIBs that appear to be strongly related include λ5705, λ5780, λ6376, λ6379 and λ6614. Although clearly related and with a R-squared value of 0.81, λ6196 and λ6614 are not as strongly correlated as might have been expected (Cami *et al.* 1997). The notion that λ6376 and λ6379 may be related (first noted in Figure 3.54) is given further support by Figure 3.57 where the two DIBs behave virtually identically once again. This remarkably similar behaviour is not only apparent in the ρ Oph sightlines but also in the additional σ-like environments. Whilst there have been many studies of DIB-family behaviour and the λ6376 & λ6379 pair do belong to the same KW family, there does not appear to be any suggestion in the literature that the two bands are so closely related.

An alternative approach for identifying those DIBs that behave in a similar fashion is to compare the *ratios* of DIBs between pairs of stars. If one carrier is responsible for more than one of the DIBs then those bands should behave in *exactly* the same way in *all* cases.

Table 3.15 lists the DIBs measured in the 2004 and 2005 datasets for ρ Oph A, B, C and DE. For each ratio taken the strongest component is stated e.g. for a ratio of B/A in λ5780 the DIB is stronger towards B hence an entry of ‘B’ in the ‘A or B’ column. DIBs belonging to the KW II family are coloured blue and those belonging to KW III red. In the case where there is no difference in the DIB ratios there is a dash, when there is contamination due to stellar features preventing a definitive answer the value

	5705	5780	5797	5850	6196	6203	6284	6376	6379	6426	6614	6660	7562	
5705	1.00	0.89	0.65	0.37	0.70	0.02	0.05	0.88	0.85	0.18	0.95	0.72	0.46	5705
5780	0.89	1.00	0.72	0.51	0.54	0.00	0.01	0.97	0.96	0.06	0.88	0.77	0.35	5780
5797	0.65	0.72	1.00	0.77	0.36	0.02	0.06	0.65	0.65	0.19	0.54	0.33	0.17	5797
5850	0.37	0.51	0.77	1.00	0.08	0.07	0.01	0.52	0.57	0.05	0.26	0.21	0.04	5850
6196	0.70	0.54	0.36	0.08	1.00	0.35	0.46	0.46	0.43	0.26	0.81	0.67	0.87	6196
6203	0.02	0.00	0.02	0.07	0.35	1.00	0.96	0.02	0.03	0.26	0.05	0.01	0.30	6203
6284	0.05	0.01	0.06	0.01	0.46	0.96	1.00	0.00	0.00	0.30	0.10	0.04	0.44	6284
6376	0.88	0.97	0.65	0.52	0.46	0.02	0.00	1.00	0.99	0.04	0.85	0.78	0.30	6376
6379	0.85	0.96	0.65	0.57	0.43	0.03	0.00	0.99	1.00	0.04	0.81	0.77	0.30	6379
6426	0.18	0.06	0.19	0.05	0.26	0.26	0.30	0.04	0.04	1.00	0.15	0.05	0.17	6426
6614	0.95	0.88	0.54	0.26	0.81	0.05	0.10	0.85	0.81	0.15	1.00	0.86	0.61	6614
6660	0.72	0.77	0.33	0.21	0.67	0.01	0.04	0.78	0.77	0.05	0.86	1.00	0.67	6660
7562	0.46	0.35	0.17	0.04	0.87	0.30	0.44	0.30	0.30	0.17	0.61	0.67	1.00	7562
	5705	5780	5797	5850	6196	6203	6284	6376	6379	6426	6614	6660	7562	

Figure 3.56: Correlation plot of yellow/red DIB equivalent widths in a selection of stars including the KW II and KW III families

	5705	5780	5797	5850	6196	6203	6284	6376	6379	6426	6614	6660	7562	
5705	1.00	0.89	0.65	0.37	0.70	0.02	0.05	0.88	0.85	0.18	0.95	0.72	0.46	5705
5780	0.89	1.00	0.72	0.51	0.54	0.00	0.01	0.97	0.96	0.06	0.88	0.77	0.35	5780
5797	0.65	0.72	1.00	0.77	0.36	0.02	0.06	0.65	0.65	0.19	0.54	0.33	0.17	5797
5850	0.37	0.51	0.77	1.00	0.08	0.07	0.01	0.52	0.57	0.05	0.26	0.21	0.04	5850
6196	0.70	0.54	0.36	0.08	1.00	0.35	0.46	0.46	0.43	0.26	0.81	0.67	0.87	6196
6203	0.02	0.00	0.02	0.07	0.35	1.00	0.96	0.02	0.03	0.26	0.05	0.01	0.30	6203
6284	0.05	0.01	0.06	0.01	0.46	0.96	1.00	0.00	0.00	0.30	0.10	0.04	0.44	6284
6376	0.88	0.97	0.65	0.52	0.46	0.02	0.00	1.00	0.99	0.04	0.85	0.78	0.30	6376
6379	0.85	0.96	0.65	0.57	0.43	0.03	0.00	0.99	1.00	0.04	0.81	0.77	0.30	6379
6426	0.18	0.06	0.19	0.05	0.26	0.26	0.30	0.04	0.04	1.00	0.15	0.05	0.17	6426
6614	0.95	0.88	0.54	0.26	0.81	0.05	0.10	0.85	0.81	0.15	1.00	0.86	0.61	6614
6660	0.72	0.77	0.33	0.21	0.67	0.01	0.04	0.78	0.77	0.05	0.86	1.00	0.67	6660
7562	0.46	0.35	0.17	0.04	0.87	0.30	0.44	0.30	0.30	0.17	0.61	0.67	1.00	7562
	5705	5780	5797	5850	6196	6203	6284	6376	6379	6426	6614	6660	7562	

Figure 3.57: Correlation plot of yellow/red DIB equivalent widths in a selection of stars highlighting those stars with high R-squared values.

'ST' is entered.

Table 3.15 demonstrates that the family groupings do not universally hold for all of the DIBs measured. Table 3.16 groups the DIBs listed in Table 3.15 by their behaviour; it is possible to distinguish 5 or possibly 6 different groups within the set. If the Krełowski and Walker family behaviours were strictly followed then all of the KW II family members (blue) should appear in the same group in Table 3.16 but this is *not* the case; the KW II and III family members are spread across all 5 of the distinct groups identified here.

The high S/N of the data acquired for this project means that ratios of DIBs between different lines-of-sight highlight differences in the DIB behaviour in very specific cases (e.g. λ6196 & λ6614 between ρ Oph A and B). Correlations between DIBs are likely significant as the data is of high S/N, high resolution, has been recorded on the same instrument/telescope and reduced/measured by the same individual. Potential conflicts with the Krełowski and Walker classification scheme arose when only the ρ Oph data were considered. The addition of more lines of sight doubled the number of data points and removed the majority of conflicts. KW II family members λ5780, λ6203 and λ6284 appear, within the limits of this study, to show little or no correlation suggesting that they should not be grouped together.

DIB	A or B	C or A	DE or A	C or DE
λ4726	–	–	A	C
λ4763	–	A	A	–
λ4964	–	–	A	C
λ4984	–	A	A	C
λ5170	ST	ST	ST	ST
λ5418	–	–	A	C
λ5493	–	C?(ST)	–	C?(ST)
λ5512	–	C?(ST)	A	C
λ5541	–	–	A?	C?
λ5544	–	ST	ST	ST
λ5546	–	ST	A	C
λ5705	B?	A	DE	DE
λ5780	B	C	DE	DE
λ5797	B	C	DE	DE
λ5850	B	C	A	C
λ6196	–	–	DE	DE
λ6203	B?	C?	DE	DE
λ6270	–	–	–	–
λ6284	–	C	–	C
λ6376	B	C	DE	DE
λ6379	B	C	DE	DE
λ6426	–	–	–	–
λ6439	B	C	A	C
λ6445	-	C	DE	DE
λ6614	B	A	DE	DE
λ6660	B	C	DE	DE
λ7224	B	C	DE	DE
λ7562	–	–	–	–
K I	B	A	DE	DE
Na I D_1	B	A	A	DE
Ca I	A	A	DE	DE
Ca II	B	C	DE	DE
CH	–	A	A	DE
CH^+	A	A	A	DE
CN	A	C	–	C
C_2	N/A	N/A	A	N/A

Table 3.15: Table showing behaviour of each DIB between different pairs of stars. Entry is 'A' in column 'A or B' if the DIB is stronger seen towards ρ Oph A than B. Those entries coloured blue are members of the KW II family, those coloured red are KW III. An entry of 'ST' highlights cases where stellar features due to the background star prevent a conclusion from being drawn, N/A applies to those cases where there are no data.

I	II	III	IV	V
λ4726, λ4734	λ5705, λ6614	λ5780, λ5797	λ5850, λ6439	λ5544, λ6270
λ4964, λ4984	K I	λ6203, λ6376	λ6284	λ6426, λ7562
λ5418, λ5512		λ6379, λ6445		
λ5541, λ5546		λ6660, λ7224		

Table 3.16: AMS family groupings based upon behaviour in Table 3.15. DIBs coloured blue are members of the KW II family, those coloured red are KW III

3.5 DIB variations and chemistry of ISM

It is clear that there are significant differences in the relative DIB strengths for the majority of the lines-of-sight measured in this study. Section 3.4 has demonstrated the power of studies of this kind for identifying those DIBs that behave in a similar way. Although such DIBs may not be due to the same carrier they likely favour similar environments. A majority of the yellow/red ($\lambda > 5700$ Å) DIBs are stronger towards B than A and stronger again towards DE giving rise to the order:

$$W_\lambda^{DE} > W_\lambda^B > W_\lambda^C > W_\lambda^A$$

Notable exceptions to this order are λ5850, λ6284 and λ6439 where $W_\lambda^{DE} \simeq W_\lambda^A$ or in some cases actually *weaker* towards DE. The λ6196 DIB shows no difference between A, B or C but is much ($\sim 30\%$) stronger towards DE whereas λ6426 and λ7562 show no variation between all four sight lines.

When diffuse bands blueward of 5700 Å are considered, the majority of the blue DIBs their strengths follow the order:

$$W_\lambda^A > W_\lambda^B > W_\lambda^C > W_\lambda^{DE}$$

This remarkable difference in behaviour especially for ρ Oph DE (W_λ^{DE} strongest for red DIBs, weakest for blue) deserves further investigation.

A key aim of diffuse band studies is to assign the spectrum. Apart from a few DIBs in the near-IR suggested to be due to the C_{60}^+ molecule, 'Buckminsterfullerene' (Foing & Ehrenfreund 1994, Ehrenfreund & Foing 1997), there have been no firm DIB assignments. How to approach this problem? A good starting point is to relate DIB strengths and characteristics to known atomic and molecular species residing in the same region as the DIB carriers. Parameters such as ionisation (e.g. Ca I, Ca II balance), density (CN-to-CH ratio) and temperature (e.g. from C_2 and H_2 data) can, with the appropriate observations, be determined relatively easily. Studies of atomic and molecular species are usually carried out at very high spectral resolution (> 1 kms^{-1}) so that different components (i.e. discrete gas clouds) can be identified and the relationship between different species investigated. Fortunately for this study Pan *et al.* (2004 and 2005) have made high resolution observations of the ρ Oph stars as part of a larger investigation into the chemistry of star-forming regions. Atomic and molecular data recorded by Pan *et al.* are listed in Table 3.17.

The quantity of data in Table 3.17 is impressive. For each of the ρ Oph stars there are at least four different velocity components, each having different molecular and atomic species present at that velocity. Closer inspection reveals that for all four sight lines there are in fact only two major velocity components (gas clouds) that contain most of the atomic and molecular species along that line of sight. For ρ Oph A, B and C there is a component at V_{LSR} = 1.9 kms^{-1} which, given the small velocity shift and the resolution of the data, is almost certainly the same component that is seen in DE at V_{LSR} = 2.0 kms^{-1}. The second major component is seen at V_{LSR} = 3.5 kms^{-1} in ρ Oph A and B and at V_{LSR} = 3.6 kms^{-1} towards C and DE. There is a third component seen at V_{LSR} = 0.2 kms^{-1} towards all of the stars that appears to be more significant for ρ Oph DE than any other.

Given what is known about the variations in the diffuse bands along these four lines of sight it is of interest to search for any relationship between DIB strengths and the column densities of *known* species. The data of Pan *et al.* is of enormous interest for this study; without it, reference could only be made to the atoms recorded in the current data (Na I D_1, K I).

As a first step it is important to investigate any direct relationship between the individual DIB strengths and the atomic and molecular species. Figures 3.58, 3.59, 3.60 and 3.61 are plots of select DIBs plotted against the line-of-sight column densities of C_2, K I, Ca I, Ca II, CH, CH^+ and CN. The ρ Oph A data are in black, B in green, C in blue and DE in red.

	CN		CH		CH^+		Ca I		K I		Ca II	
V_{LSR}	N^b ($10^{12}cm^{-2}$)	b	N^b ($10^{12}cm^{-2}$)	b	N^b ($10^{12}cm^{-2}$)	b	N^b ($10^{9}cm^{-2}$)	b	N^b ($10^{11}cm^{-2}$)	b	N^b ($10^{12}cm^{-2}$)	b
ρ Oph A (HD 147933)												
-20.6	...		...		...		...		...		0.3	2.0
-16.6	...		...		...		...		...		0.2	2.1
-2.8	...		...		...		...		0.1	0.7	0.5	1.5
0.2	...		2.4	1.0	...		...		0.6	0.9	1.6	1.0
1.9	2.1	0.7	14.9	0.8	8.8	2.0	14.1	1.1	7.5	1.0	12.5	1.1
3.5	...		6.4	0.9	7.1	1.7	3.2	0.9	2.1	0.6	2.3	1.0
8.8	...		...		...		...		...		0.2	2.0
ρ Oph B (HD 147934)												
-20.6	...		...		...		...		...		0.2	2.0
-2.8	...		...		...		...		0.1	1.1	0.3	1.5
0.2	...		2.4	1.1	...		...		0.7	0.9	2.0	1.1
1.9	2.0	0.9	16.8	0.8	9.5	2.0	14.5	1.0	9.1	0.9	14.7	1.1
3.5	...		4.0	0.8	4.8	1.5	2.4	0.9	1.0	0.7	2.0	1.0
8.8	...		...		...		...		...		0.4	1.1
ρ Oph C (HD 147932)												
-2.8	...		...		...		...		0.1	1.0	0.3	1.5
0.2	...		...		...		3.3	1.0	0.9	1.0	3.6	1.1
1.9	6.0	0.8	19.2	0.9	3.7	1.5	12.9	1.1	6.3	0.9	12.7	1.1
3.6	...		...		3.3	2.0	...		0.7	0.6	2.6	1.0
ρ Oph DE (HD 147888)												
-20.6	...		...		...		...		...		0.2	1.9
-2.8	...		...		...		...		0.1	0.9	0.4	1.5
0.2	...		2.3	1.0	1.0	1.7	2.4	1.0	0.9	1.0	2.4	1.0
2.0	2.1	0.8	19.5	0.9	6.5	2.0	17.8	1.2	9.4	1.0	14.2	1.1
3.6	...		...		...		...		0.6	0.7	2.2	1.0

Table 3.17: Atomic and molecular data from Pan *et al.* (2004) for ρ Oph A, B, C and DE

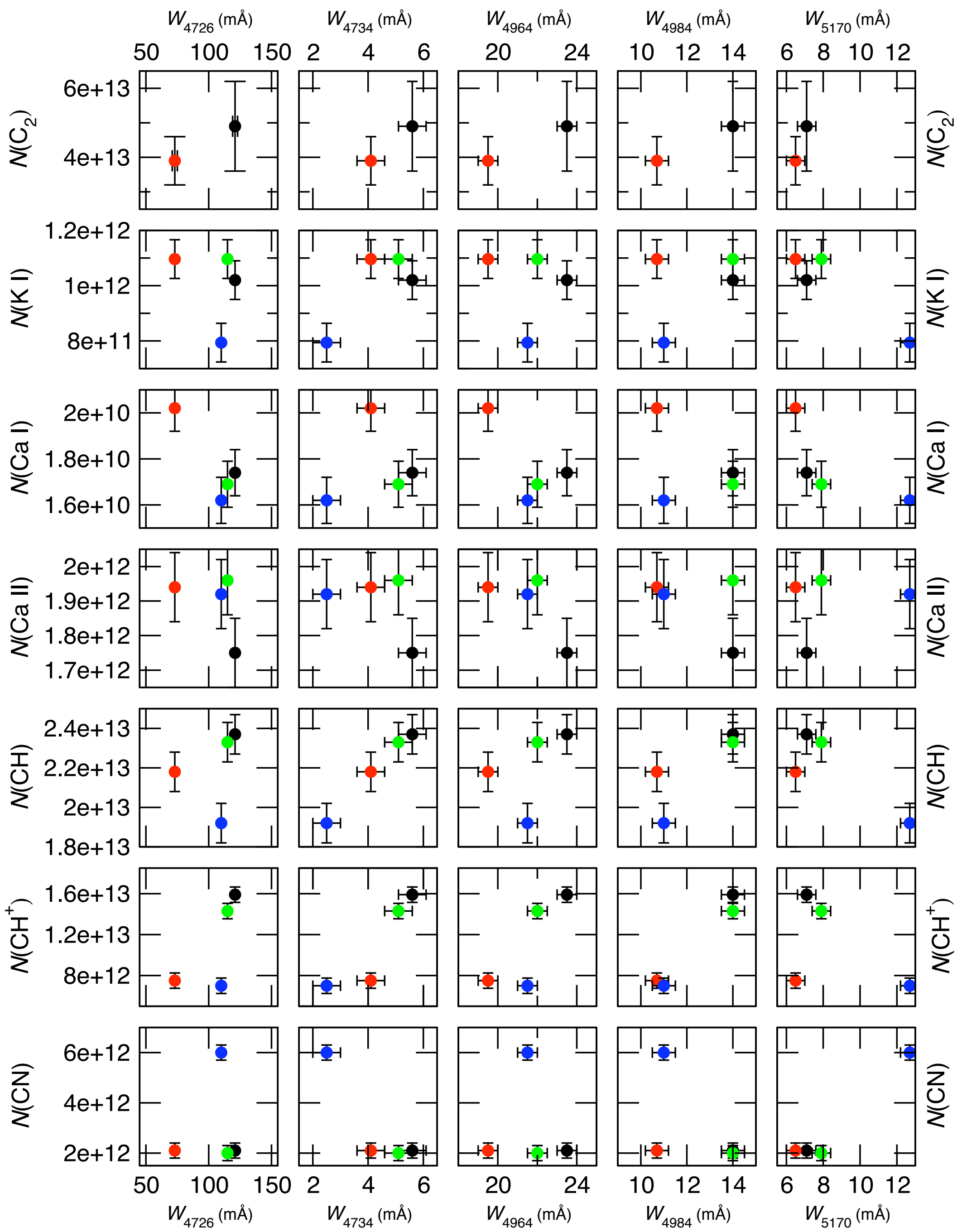

Figure 3.58: ρ Oph atomic and molecular data (cm^{-2}) (Pan *et al.* 2004) plotted against a variety of DIB strengths widths. ρ Oph A data are in black, B are in green, C are in blue and DE in red.

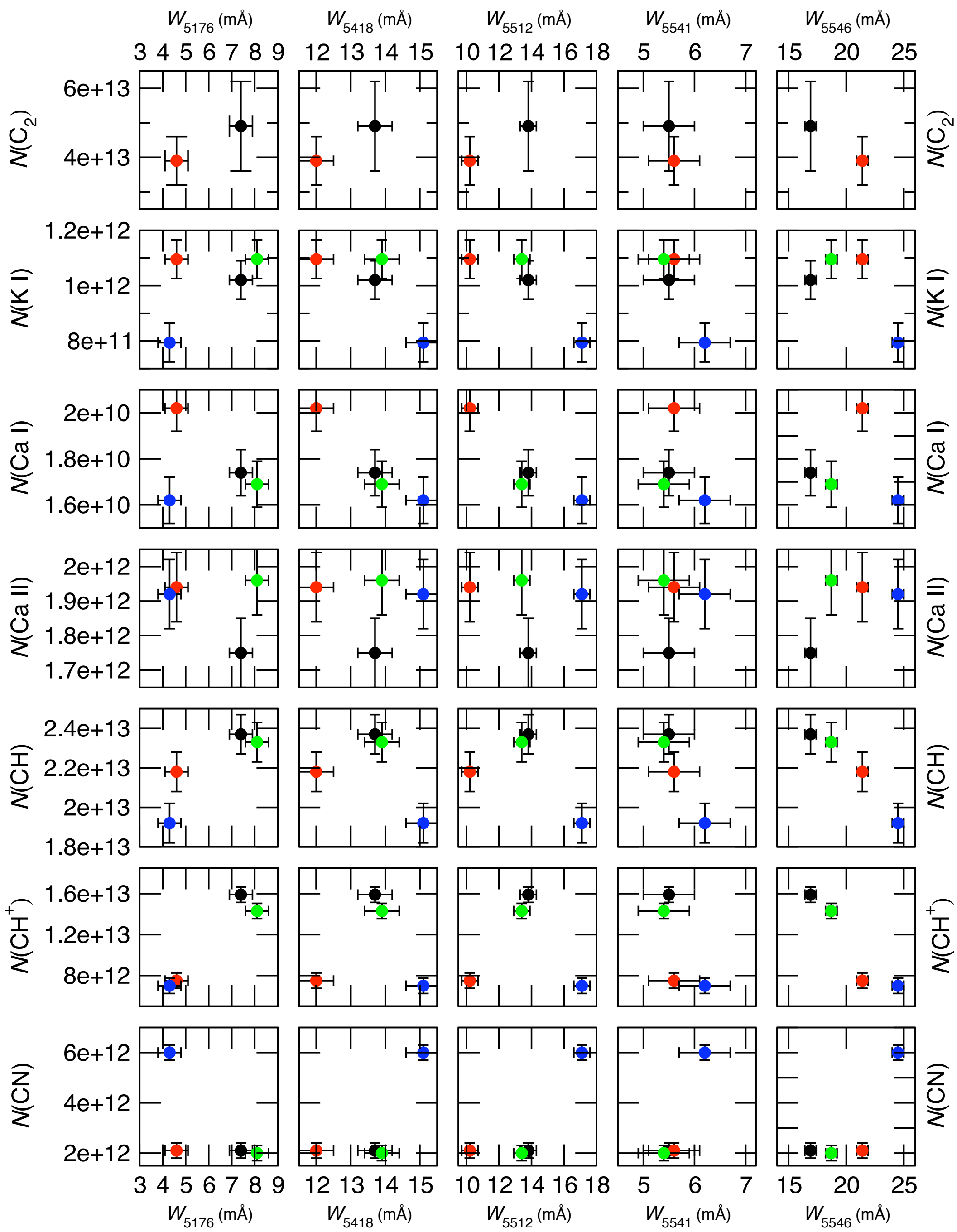

Figure 3.59: ρ Oph atomic and molecular data (cm^{-2}) (Pan *et al.* 2004) plotted against a variety of DIB strengths widths. ρ Oph A data are in black, B are in green, C are in blue and DE in red.

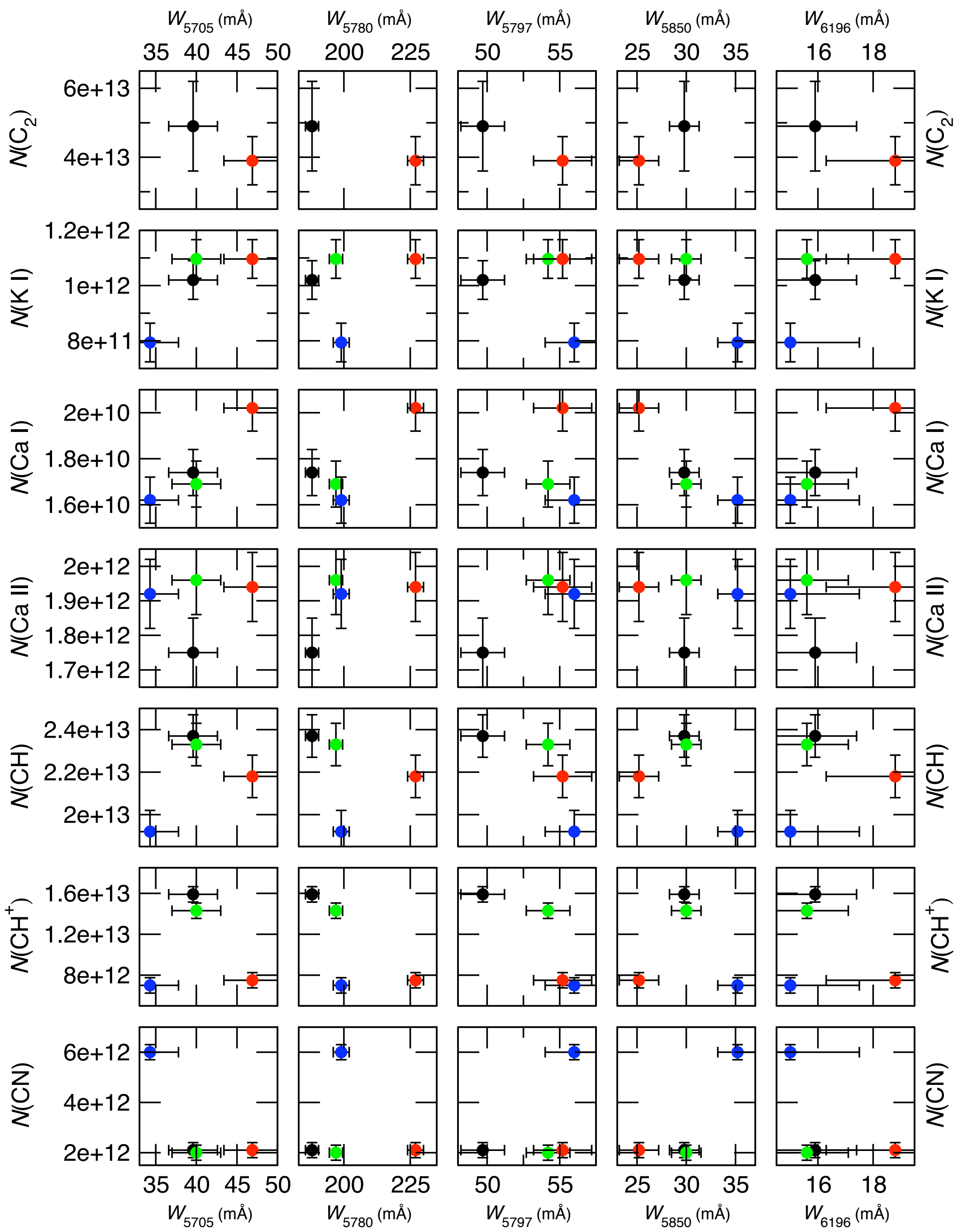

Figure 3.60: ρ Oph atomic and molecular data (cm^{-2}) (Pan *et al.* 2004) plotted against a variety of DIB strengths widths. ρ Oph A data are in black, B are in green, C are in blue and DE in red.

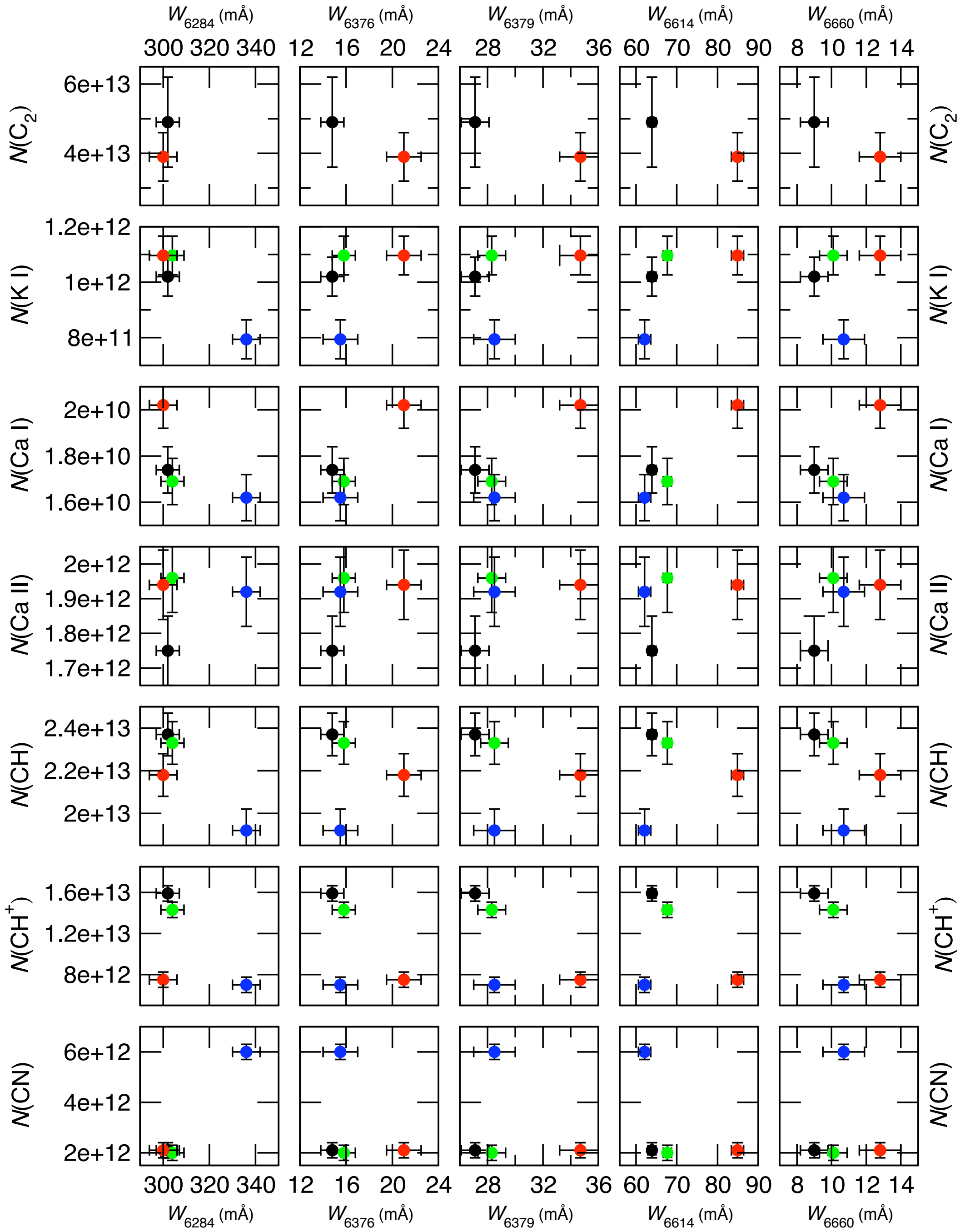

Figure 3.61: ρ Oph atomic and molecular data (cm^{-2}) (Pan *et al.* 2004) plotted against a variety of DIB strengths widths. ρ Oph A data are in black, B are in green, C are in blue and DE in red.

Correlation with C_2

Found mainly in relatively dense regions of diffuse clouds (e.g. Thorburn *et al.* 2003) the diatomic C_2 molecule, with its lack of a permanent electric dipole moment, offers a probe of the thermal (kinetic) temperature of an interstellar cloud through analysis of its rotational lines. An investigation of possible correlations between C_2 column densities and a set of relatively weak blue diffuse band strengths was presented by Thorburn *et al.* (2003). They showed that seven of the twenty-one DIBs correlate well with $N(C_2)/E_{B-V}$when the DIB strength is normalised by $W_{\lambda6196}$. This result has led to these DIBs being referred to as the "C_2" DIBs, a term that, more recently, Galazutdinov *et al.* (2006) have argued is not secure. They showed that some of the assumptions that Thorburn *et al.* made about DIB strength vs. E_{B-V} were not always valid. Together with their own analysis of C_2 and the strengths of the weak blue DIBs Galazutdinov *et al.* have suggested that these features are at best *slightly* related to C_2.

It is of interest to see what, if any, correlation exist between $N(C_2)$ for each of the ρ Oph stars and DIB strengths.

The data for $N(C_2)$ are from Thorburn *et al.* (2003) and were taken as part of their survey at the Apache Point Observatory (APO). Unfortunately data were only recorded for ρ Oph A and DE. A thorough search of the literature reveals that there are no published values for $N(C_2)$ towards ρ Oph B and C. Consequently, there are therefore only two values for $N(C_2)$ with which to investigate any correlation with DIB strengths. The uppermost row of plots in Figures 3.58 and 3.59 shows a plot of DIB strength (mÅ) with $N(C_2)$. Interestingly, there is a positive correlation (albeit with a large error on ρ Oph A measurement) of blue DIB strength with $N(C_2)$ for all blue DIBs *apart* from λ5541 and λ5546. These two DIBs are, according to Thorburn et al. *not* related to C_2. Figures 3.60 and 3.61 show that the vast majority of the yellow/red DIBs show a negative correlation with $N(C_2)$, that is, they are strongest towards ρ Oph DE where $N(C_2)$ is lowest.

The lack of C_2 data for ρ Oph B and C is unfortunate as is the large error associated with the Thorburn *et al.* measurements. Absorption lines due to the Phillips bands of C_2 ($A^1\Pi_u - X\ ^1\Sigma_g^+$) are present in some of our UCLES data, however, due to severe fringing in the MITTL chip in the far red it is not possible to measure their strengths reliably. Further analysis with respect to C_2 may be possible however as Federman *et al.* (1994) demonstrated with their modelling of diffuse cloud chemistry that they could accurately predict the relative abundances of CH, C_2 and CN. With knowledge of the CH and CN abundances towards the four ρ Oph sight lines, Pan *et al.* (2005) modelled the chemistry of the major component (V_{LSR} = 1.9 kms^{-1}) and produced *predicted* abundances for $N(C_2)$ in all sight lines.

Table 3.18 lists the physical parameters and chemical abundances calculated by Pan *et al.* in their modelling of the ρ Oph region. Entries headed by N_p(X) are predicted abundances should be compared with N_o(X), the *observed* values. The values listed in Table 3.18 are not the total abundance of each species, rather they are the derived abundances for the main cloud/velocity component at V_{LSR} = 1.9 kms^{-1}. Note that the density of the ρ Oph DE sight line is the the lowest, which might be significant when trying to understand the difference in DIB strengths.

	τ_{UV}	T (K)	n (cm^{-3})	N_o(CH) (10^{12}cm^{-2})	$N_o(C_2)$ (10^{12}cm^{-2})	$N_p(C_2)$ (10^{12}cm^{-2})	N_o(CN) (10^{12}cm^{-2})	N_p(CN) (10^{12}cm^{-2})
ρ Oph A	2.04	50	625	14.9	26.0	21.4	2.1	2.6
ρ Oph B	2.04	50	450	16.8	...	18.0	2.0	2.0
ρ Oph C	2.04	40	1100	19.2	...	44.4	6.0	6.0
ρ Oph DE	2.08	50	425	19.5	...	18.7	2.1	2.1

Table 3.18: Physical parameters and molecular abundances derived from modelling of ρ Oph region from Pan *et al.* (2005).

Federman *et al.* (1994) showed that the formation of CN in diffuse clouds involves CH reacting to form C_2 and then finally CN. Plots of log $N(C_2)$ vs. log N(CH), log N(CN) vs. log $N(C_2)$ and log N(CN) vs. log N(CH) all show strong linear correlations. Knowing the relationship between these species, it is then possible to predict the column density of C_2 in all four sight lines based upon the known abundances of CH and CN.

	1.9 kms^{-1}		0.2 kms^{-1}		3.5 kms^{-1}	
	N_o(CN) (10^{12}cm^{-2})	$N_p(C_2)$ (10^{12}cm^{-2})	N_o(CH) (10^{12}cm^{-2})	$N_p(C_2)$ (10^{12}cm^{-2})	N_o(CH) (10^{12}cm^{-2})	$N_p(C_2)$ (10^{12}cm^{-2})
ρ Oph A	2.1	21.3	2.4	1.3	6.4	4.3
ρ Oph B	2.0	20.6	2.4	1.3	4.0	2.4
ρ Oph C	6.0	41.8	...	...	...	...
ρ Oph DE	2.1	21.3	2.3	1.3	...	...

Table 3.19: 'Predicted' C_2 strengths based upon relationships derived by Federman *et al.* (1994).

Table 3.19 lists the observed CN and CH (N_o(CN), N_o(CH)) for the four ρ Oph sight lines. Federman *et al.* (1994) demonstrated that CN and C_2 likely coexist; given what is known about the CN column density in the 'main' IS cloud at V_{LSR} = 1.9 kms^{-1} can the amount of C_2 for this component be predicted? For the other two clouds here (V_{LSR} = 0.2 kms^{-1} and V_{LSR} = 3.5 kms^{-1}) CN was not detected so the CH column density has been used to predict the C_2 component.

	$N_p(C_2)$ (10^{12}cm^{-2})	$N_o(C_2)$ (10^{12}cm^{-2})
ρ Oph A	26.9	49±13
ρ Oph B	24.4	...
ρ Oph C	41.8	...
ρ Oph DE	22.6	39±7

Table 3.20: Total predicted ($N_p(C_2)$ and observed ($N_o(C_2)$ column densities of C_2 towards the four ρ Oph stars. Predicted values are based upon correlations with other species from Federman *et al.* (1994), observed values are from APO survey (Thorburn *et al.* 2003)

Clearly there is a discrepancy between the observed values of $N(C_2)$ and the predicted values. Pan *et al.* (2005) noted that their predicted values were lower limits and usually within 30% of the observed values. This difference was attributed to the modelling of individual components of the absorption, i.e. modelling the *main* CN/C_2 cloud thus not accounting for the presence of these species with the minor velocity components. Table 3.20 includes the predicted C_2 values from all the velocity components seen towards the ρ Oph stars that contain CH. This being the case the predicted values for $N(C_2)$ should be approaching the observed values of Thorburn *et al.* Even taking into account the large errors associated with the Thorburn *et al.* measurement there is still a discrepancy and the model values appear to still be a lower limit.

It may be a rather large assumption to state that all the CH in each cloud is participating in CN production. Pan *et al.* (2005) showed that there is 'CH^+ like CH' and 'CN like CH'. If it is assumed that the reality is that the 'CN like CH' which is involved in CN production in dense regions and the 'CH^+ like CH' is associated with more diffuse regions of the cloud, predicted values of $N(C_2)$ are obtained and shown in Table 3.21.

Table 3.21 demonstrates that even when the components that have CH *and* CH^+ (but no CN) are removed from the total predicted value of $N(C_2)$ the general trend is maintained, that is:

$$N(C_2)_{\rho\ \text{Oph C}} > N(C_2)_{\rho\ \text{Oph A}} > N(C_2)_{\rho\ \text{Oph B}} > N(C_2)_{\rho\ \text{Oph DE}}$$

	$N_p(C_2)$ (10^{12}cm^{-2})	$N_o(C_2)$ (10^{12}cm^{-2})
ρ Oph A	22.6	49±13
ρ Oph B	22.0	...
ρ Oph C	41.8	...
ρ Oph DE	21.3	39±7

Table 3.21: Total predicted ($N_p(C_2)$) and observed ($N_o(C_2)$) column densities of C_2 towards the four ρ Oph stars taking into account 'CH$^+$ like CH' and 'CN like CH' differences.

Correlation with density

Compared to the other three sight lines the ρ Oph C environment is clearly very different. It has a predicted density about twice that of A, B and DE. With its exceptionally high value of N(CN) the predicted value for $N(C_2)$ is also significantly greater than for the others. If the blue "C_2" DIBs did correlate perfectly with $N(C_2)$ then it might be expected that the ρ Oph C sight line would show by far the strongest blue DIBs but this is *not* the case. If however the ρ Oph C sight line is ignored then qualitatively the blue "C_2" DIBs do correlate with the predicted (and observed) quantities of $N(C_2)$ in A, B and DE. If it is assumed that the correlation of these blue features with $N(C_2)$ means that these DIBs are associated with a more dense component of the diffuse clouds then the results from the modelling of these regions again supports this hypothesis. Ignoring ρ Oph C and only considering the densities of the A, B and DE sight lines the blue and yellow/red DIB strengths can be understood using density arguments.

$$n_{\rho\ \text{Oph A}} > n_{\rho\ \text{Oph B}} > n_{\rho\ \text{Oph DE}}$$

$$W^A_{\lambda\ \text{blue}} > W^B_{\lambda\ \text{blue}} > W^{DE}_{\lambda\ \text{blue}}$$

$$W^A_{\lambda\ \text{red}} < W^B_{\lambda\ \text{red}} < W^{DE}_{\lambda\ \text{red}}$$

These trends suggest that the blue "C_2" DIBs favour more dense regions and so are strongest towards ρ Oph A and weakest towards ρ Oph DE. Conversely the yellow/red DIBs favour *less* dense environments and so are strongest towards ρ Oph DE. This argument can be pursued in considering the extent to which the ρ Oph A, B, C and DE environments behave like ζ or σ clouds.

Introduced at the same time as the idea of diffuse band families, Krelowski & Walker (1987) demonstrated that, for a given value of E_{B-V} the ratio of λ5780/λ5797 could vary by up to a factor of three. For cases where λ5780 is strong relative to λ5797 (like towards σ Sco), the IS clouds giving rise to the DIBs were called 'σ-type' clouds. Where λ5797 is strong relative to λ5780 (as is the case towards ζ Oph) the term 'ζ-type' was used instead. Although this differentiation of IS environments was based purely upon the λ5780/λ5797 ratio, it was quickly realised that σ and ζ-type clouds have many differences (Krełowski & Sneden 1995). Of particular relevance for this discussion is that ζ-type environments are rich in molecular species (e.g. CN) whereas σ-type environments are not.

Knowing only that σ-type clouds have fewer molecules than ζ-type then ρ Oph DE might be predicted as more 'σ-like' than A or B and indeed this *is* the case. The ratios of $W_{\lambda5780}/W_{\lambda5797}$ for the four ρ Oph sight lines are A = 3.82, B = 3.80, C = 3.86 and DE = 4.33. The ρ Oph A, B and C data all have a similar ratio of $W_{\lambda5780}/W_{\lambda5797}$ whereas DE is significantly larger. Typical values are $\lesssim 3$ for ζ-type environments and $\gtrsim 4$ for σ. Enhanced λ5797 strength (more ζ-like) has been interpreted as being the result of the carrier of λ5797 favouring denser environments where the UV radiation is weaker. The λ5780 DIB carrier is therefore reasoned to prefer less dense, more highly UV irradiated environments than the species responsible for the λ5797 feature. Although λ5797 is strongest towards ρ Oph DE (13% stronger than towards A) λ5780 is 28% stronger towards DE than A. It is clear then that the DIB-producing environment(s) towards ρ Oph DE are less dense and have a less attenuated UV flux than the other three sightlines thus giving rise to strong red/yellow DIBs (favour less dense regions) and weak "C_2" DIBs (which favour more dense regions).

Correlation with known species

Given the previous discussion on DIB correlations with small molecules in the ρ Oph sight lines (e.g. CN, CH, C_2) it is also important that the correlations with atomic species are considered. Figures 3.58, 3.59, 3.60 and 3.61 plot the blue DIBs studied against the total line of sight column densities from Pan *et al.* (2004). Cordiner

(2005) found that, not surprisingly (e.g. Herbig 1995), the yellow/red DIBs correlate better with N(K I) and N(Ca I) than with small molecules. Interestingly the situation is reversed for the blue DIBs. Most of the positive correlations in Figures 3.58 and 3.59 are with the small molecules and *not* with atomic species (e.g. K I). The λ5170, λ5418, λ5512 and λ5541 bands all show a clear negative correlation with N(K I) and N(Ca I) whereas at least some of these DIBs show a significant positive correlation with N(CH).

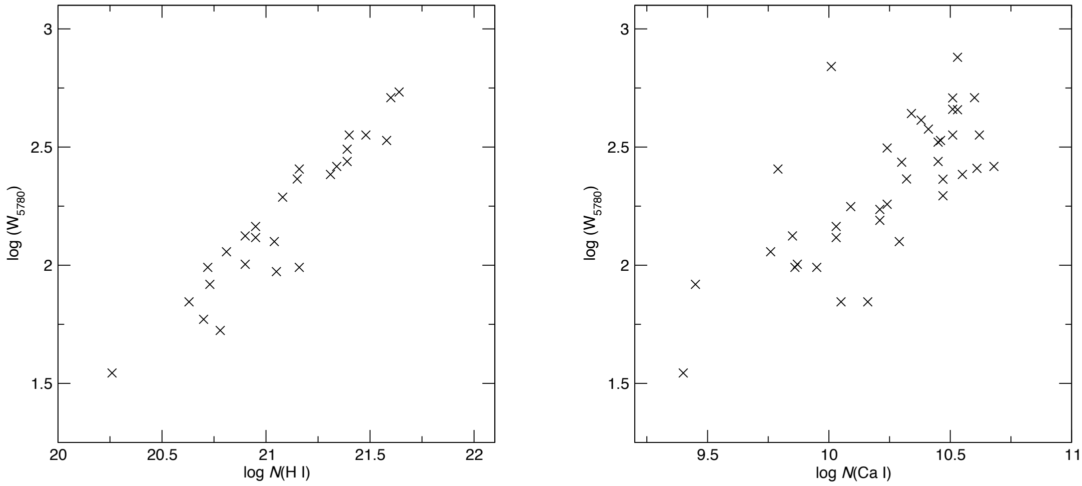

Figure 3.62: A comparison of the H I vs. W_{5780} and Ca I vs. W_{5780} relations.

Figure 3.62 plots the strength of λ5780 against H I and Ca I in a selection of galactic sightlines. As expected the correlation with H I is strong (e.g. Herbig 1995). Whilst there is significantly more scatter in the plot of Ca I vs. W_{5780}, there is still a significant positive correlation suggesting that indications of a positive correlation in the ρ Oph sightlines applies to other environments.

Although perhaps not as significant as with CH, the correlation between the blue DIBs and CH^+ appears to be marginally better than with the yellow/red DIBs (Figures 3.58, 3.59, 3.60 and 3.61). Pan *et al.* (2005) demonstrated that the AOD profiles of CH^+ are typically broader than those of CH or K I. With a similar width to Ca I, CH^+ probably spans a larger density range and larger volume of clouds than K I.

Diffuse band environments

Figure 3.63 plots each of the different species analysed by Pan *et al.* (2004) for each of the ρ Oph sight lines. For each given velocity component the diameter of the circle is proportional to the column density of the species in that component. This sequence of plots illustrates the complex nature of the absorbing material in the ρ Oph region. Examination of these plots demonstrates that the velocity component at V_{LSR} = 1.9 kms^{-1} (2.0 kms^{-1} in DE) is the dominant diffuse cloud containing the majority of all of the species measured. If this is the case for the known species then is it a reasonable assumption that the majority of the DIBs are associated with this component also? This is almost certainly the case and for the majority of diffuse band studies it would not be necessary to consider the other components. However it is known from this study that differences in DIB strengths have been detected that conceivably may not be due to variations within a single cloud but rather due to contributions from minor clouds not considered to be the dominant 'DIB producer'.

Disentangling this problem is not trivial; determining the relative contributions of each component may not in fact be possible. However, there are some aspects that are well founded: On average, the yellow/red diffuse bands are slightly stronger towards ρ Oph B than A. Given that the two sight lines essentially pass through the same diffuse cloud this difference can be easily explained in terms of density. The ρ Oph B sight line is slightly less dense than that towards A (as determined by CN/CH ratio) and assuming that yellow/red DIB carriers prefer this lower density then the difference is explained. The argument holds for the blue "C_2" DIBs also. The blue DIBs are, on average, slightly *weaker* towards B than A. Given that these DIB carriers are predicted to favour more dense environments then the A/B difference seems to be well understood.

This same argument can be used to understand the differences in ρ Oph DE. The yellow/red DIBs are, on average, significantly enhanced in strength towards DE when compared to A and B. Conversely, the blue DIBs are weaker towards DE and the density towards DE in the main velocity component is significantly lower than that towards A or B. It would seem reasonable that the differences observed, be they larger or smaller relative to A/B, can be also understood in terms of density.

Throughout this study, the ρ Oph C sight line has presented a more challenging situation. If the density arguments hold then with by far the highest density, ρ Oph C should have the strongest blue "C_2" DIBs and the weakest yellow/red bands. But this is not the case. ρ Oph C has significantly more CN (and predicted C_2) than A, B or DE but it also has *less* Ca I, CH^+ and K I. In order to explain the apparent lack of blue "C_2" DIB enhancement towards ρ Oph C then it is necessary to conclude that, although it is entirely conceivable that these DIB carriers favour more dense environments, they *do not* reside in exactly the same environment as the CN and C_2. Perhaps the observed density enhancement in ρ Oph C is a geometric/orientation effect due to the SSS in these clouds. It is possible that, for ρ Oph C the line of sight passes down the major axis of a filament or sheet of material therefore giving rise to an increase in the molecules that exist in the more dense environments but not for the more diffuse ones.

Based upon careful analysis of the shape (i.e. width, structure) and distribution of velocity components, Pan *et al.* (2005) produced Figure 3.64 to represent the distribution of species within diffuse clouds. This schema puts Ca II as the most widely distributed of all species (that they measured), Ca I and CH^+ sharing similar environments, K I and CH having significant overlap and CO, CN and C_2 existing in only the most dense environments. How does this fit in with the DIB variations? Given that the yellow/red DIBs are thought to favour less dense environments, then, unsurprisingly, the species with which they show some correlation are some of the more widely distributed 'diffuse' species in Figure 3.64, that is, K I and Ca I and not those that exclusively occupy the most dense regions. The lack of DIB correlation with Ca II can be understood as this widely distributed component is presumably able to withstand even harsher environments than the DIB carriers or indeed K I and Ca I. No correlation with the yellow/red DIBs was found with CH or CN and this is presumably because these molecules trace environments where, even though the parent molecules of the yellow/red DIBs may be being formed, the actual species giving rise to the yellow/red DIBs do not yet exist, perhaps because of insufficient ionisation or de-hydrogenation.

Figures 3.58 and 3.59 demonstrate that the at least some of the blue DIBs studied here correlate more strongly with the molecular species than with the atoms. λ5170, λ5418, λ5512 and λ5541 are all "C_2" DIBs and they all anti-correlate with K I and Ca I but do correlate to some degree with CN, C_2 (Thorburn *et al.* 2003) and CH (this study). Interpreting these correlations with the picture described by Figure 3.64 then it may be concluded that whilst not existing in exactly the same environments as C_2, CO and CN, the blue "C_2" DIBs most probably reside in the regions where the more diffuse

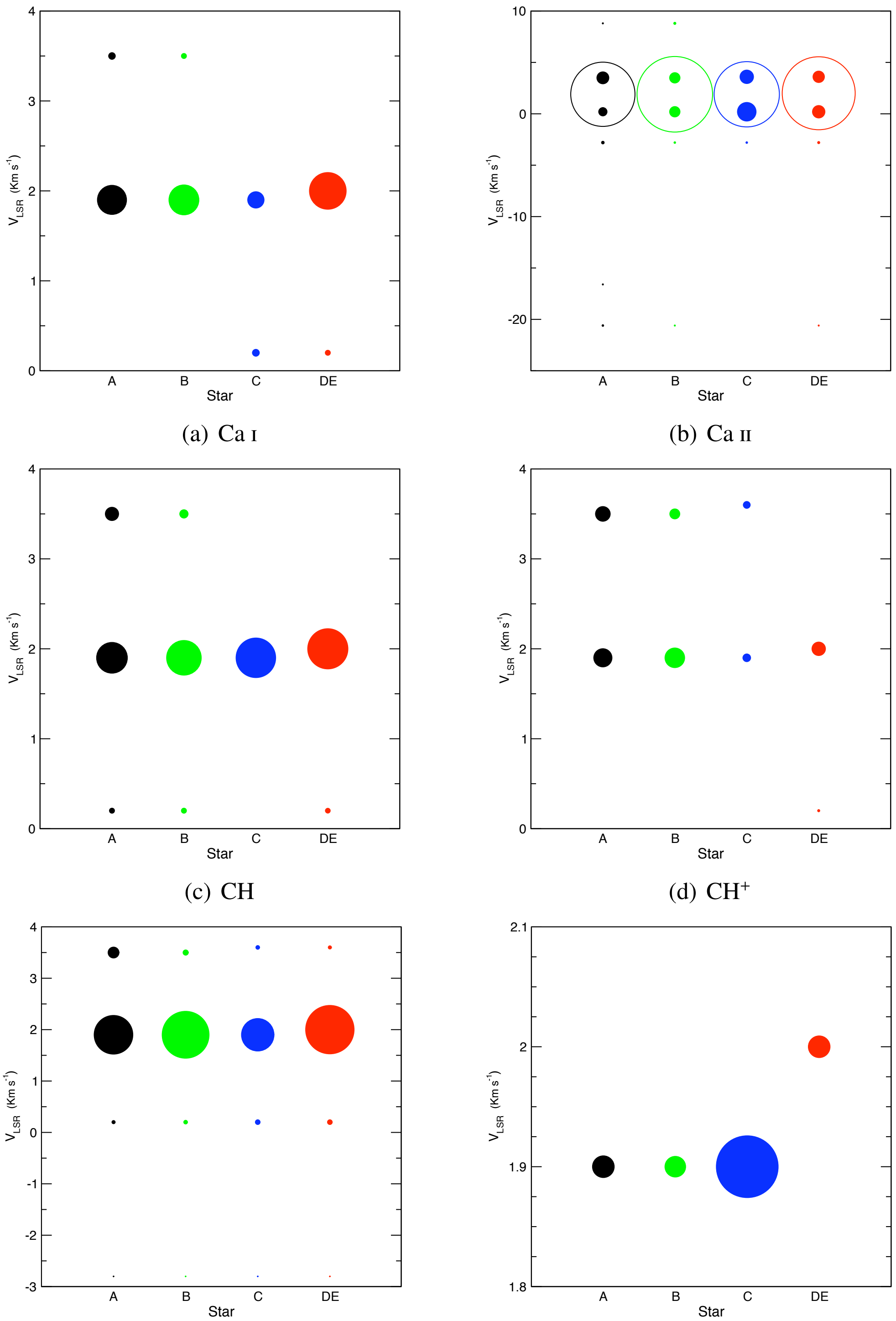

(a) Ca I (b) Ca II

(c) CH (d) CH^+

(e) K I (f) CN

Figure 3.63: Overview of individual velocity components of Ca I, Ca II, CH, CH^+, K I and CN towards the four ρ Oph stars. Data taken from Pan *et al.* (2004). Diameter of circle of each component is directly proportional to N(X) of the that component relative to the others.

boundary region of the CO, CN and C_2 overlaps with the CH.

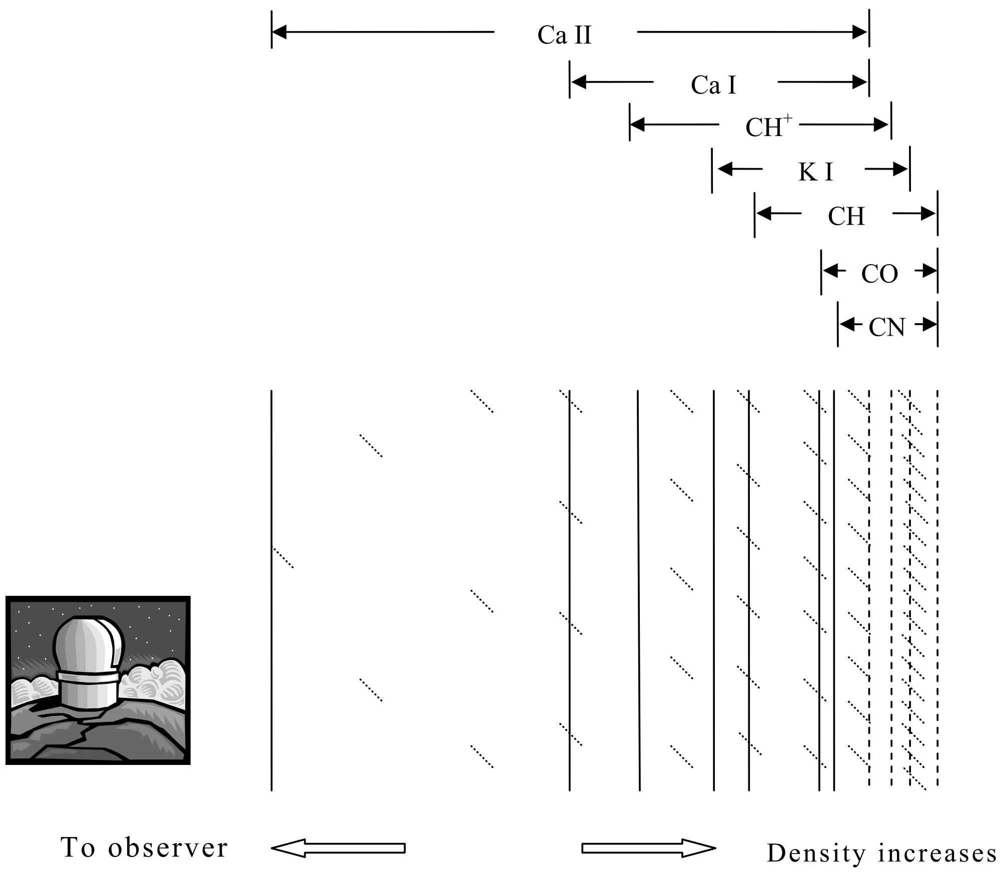

Figure 3.64: Illustration of the different environments in which 'known' species reside. Figure taken from Pan *et al.* (2005).

3.6 Conclusions

Small-scale-structure variations in diffuse interstellar band strengths have been detected towards four of the ρ Ophiuchus complex of stars. SSS variations down to ~ 400 AU in the blue DIBs (λ < 5700 Å) have been detected for the first time with differences detected in eight of the ten DIBs analysed. Follow-up observations of the yellow/red DIBs (λ > 5700 Å) have confirmed the result of Cordiner (2005) and SSS variations in the majority of the DIBs analysed.

A search has been made for tiny-scale-structure (~ 3 AU) variations in the DIB carrier distributions/strengths by making complimentary observations in 2005 of select targets from the 2004 (Cordiner 2005) AAT observing programme. Problems associated with stellar features in the spectra of β Sco and ν Sco stars have prevented a search for TSS variations towards these stars in anything other than atomic species. A comparison has been made of DIB ratios in the ρ Oph suite of stars between years with indications of differences in λ5780, λ5797 and λ6614. A thorough assessment had been made of possible contaminating factors in the TSS study; TSS variations in λ6614 profiles/strengths appear to be real.

Extremely high S/N (> 2000) profiles of select blue DIBs have been presented and compared with the profiles of Słyk *et al.* (2006). Fine structure appears to be present in five of the nine DIBs presented with some displaying 'molecular' profiles remarkably similar to that λ5797 (e.g. λ5418). Extremely narrow 'spikes' presented in some of the Słyk *et al.* (2006) profiles have not been detected although the lower spectral resolution of the UCLES data may account for any differences.

DIB strengths towards the ρ Oph stars and other extremely high S/N data have been analysed with respect to atomic and molecular data from Thorburn *et al.* (2003), Pan *et al.* (2004) and Pan *et al.* (2005) as well as with each other. Significant differences in the behaviour of the blue and yellow/red DIBs have been demonstrated with the blue DIBs showing a clear preference for more dense regions than their yellow/red cousins. The suggestion of Thorburn *et al.* (2003) that many of the blue DIBs are related to the C_2 molecule has been analysed within the ρ Oph dataset; blue DIBs strengths do appear to be broadly correlated with C_2 although whether this indicates any chemical relation or rather a mutual preference for denser environments remains unclear.

Krełowski and Walker (Krelowski & Walker 1987) DIB families have been tested for ρ Oph and other sightlines with significant deviations from predicted behaviour detected in many cases. Factors determining the absolute behaviour of the DIBs over such small spatial scales clearly outweigh the 'bulk' observed trends of DIB family behaviour. Exceptionally similar behaviour of λ6376 and λ6379 has been detected towards the ρ Oph stars and other lines-of-sight. With an R-squared value of 0.995, the λ6376–λ6379 correlation is extremely strong and seems worthy of further investigation.

Chapter 4

A Search for Diffuse Band Carriers in the Early Universe

4.1 Introduction

Although the carriers of the Diffuse Interstellar Bands (DIBs) remain unassigned, the resilience of the carriers and their ability to withstand a broad variety of interstellar environments constrains their possible nature. Based upon elemental abundance arguments and the requirement that the DIB carriers must be able to exist in a range of interstellar environments, there is a consensus amongst most of the astrophysical community that the DIB carriers are large organic[1] molecules.

Polycyclic aromatic hydrocarbons (PAHs), fullerenes and carbon chains have been suggested as likely candidates for the DIB carriers (Crawford *et al.* 1985, Leger & d'hendecourt 1985, Foing & Ehrenfreund 1994 and Salama 1999) as these large molecules are able to withstand harsh interstellar environments, absorbing high-energy UV photons and dissipating the energy of the photon through internal conversion.

In the Galaxy, some of the best DIB - 'known species' correlations are with N(H I) and E_{B-V}. Herbig (1993, Figure 4.1) demonstrated that λ5780 correlates strongly with the line-of-sight dust reddening index, E_{B-V}. This relationship is not unique to λ5780; it is one of the few 'certainties' of diffuse band studies that, on average, DIB strength

[1]The term "organic" meaning primarily composed of carbon.

increases with the amount of reddening.[2] Herbig (1993) also identified the DIB - N(H I) relation, Figure 4.2 again showing a good correlation with λ5780.

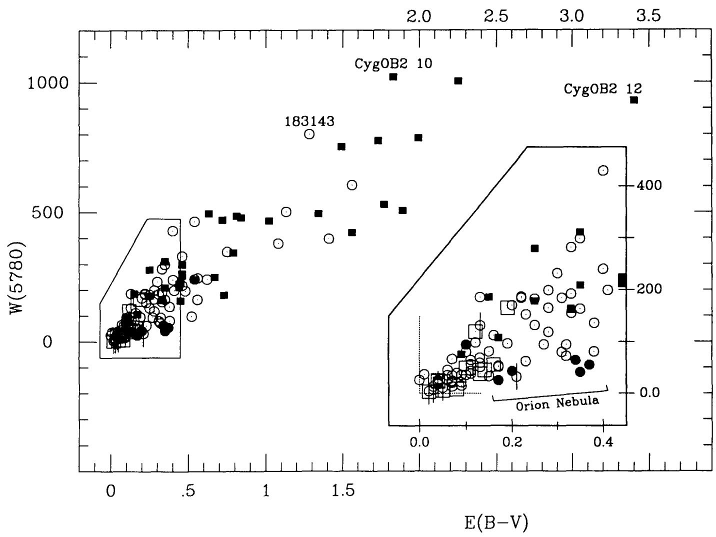

Figure 4.1: The relationship between $W_{\lambda 5780}$ and E_{B-V}. Figure taken from Herbig (1993)

Whilst there are numerous studies investigating the relationship between DIBs and atomic and molecular species, one of the least understood factors is the effect that the metallicity of a region has on the abundance of the DIB carriers. Whilst the Galaxy provides a range of different interstellar environments to study the DIBs, each with its own temperature, density etc., the research is limited by the fact that it is all carried out in the same galaxy. The situation is particularly limited for studies of the possible DIB - metallicity relation as even in the most unusual Milky Way environments the metallicity (Z) differs by only $\sim$ 10% from solar ($Z_{\odot}$) values. It is clear that if we wish to investigate how DIB strengths vary in relatively 'extreme' environments then observations need to be made outside the Milky Way.

DIB studies of our nearest galactic neighbours, the Large and Small Magellanic Clouds (LMC & SMC), have recently flourished (Cox *et al.* 2006, Welty *et al.* 2006 and references therein) and have demonstrated that DIB behaviour can be very different in

[2]It has been shown that the DIB vs. E_{B-V} relationship holds until $E_{B-V} \sim 1$, after which the DIB strength increases more slowly. This 'flattening' of the correlation has been attributed to the so called 'skin-effect' (Adamson *et al.* 1991) because the DIB carriers are thought to exist towards the edges of diffuse clouds.

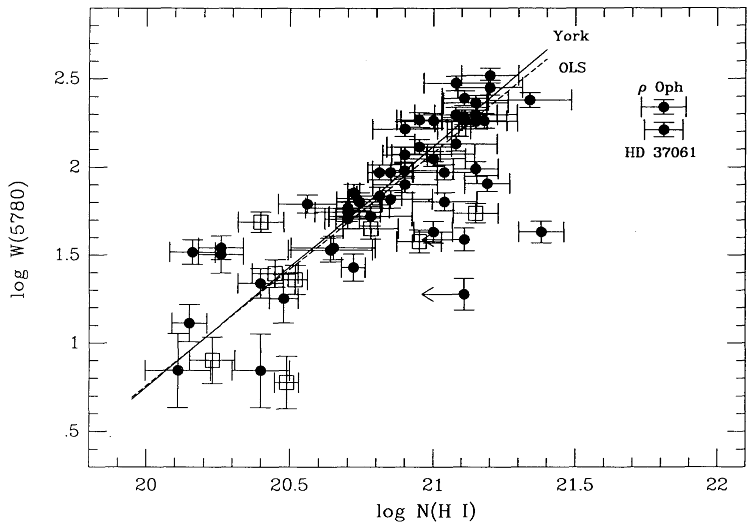

Figure 4.2: The relationship between $W_{\lambda 5780}$ and N(H I). Figure taken from Herbig (1993)

these low-metallicity, high gas-to-dust ratio[3] environments. Significantly, the galactic relationship between $W_{\lambda 5780}$ and N(H I) was found *not* to hold with the λ5780 DIB being $\sim$ 10 times weaker in LMC sight-lines than would have been predicted based on the Milky Way N(H I) relationship (Figure 4.2). This difference in behaviour is not seen however when the MC λ5780 strengths are plotted as a function of E_{B-V}. Welty *et al.* (2006) have shown that the LMC and SMC λ5780 values show good agreement with the galactic relation.

The Magellanic Clouds (MCs) have provided an opportunity to study the diffuse bands in two distinct extragalactic environments. The stars observed are relatively bright (V Mag 11–13) and the MCs are so close ($\sim$ 50 kpc) that it is possible to observe single stars in each galaxy thus investigating the behaviour of the DIBs across the whole galaxy. Other extragalactic DIB studies include the investigation of dusty starburst galaxies (e.g. M82, NGC 2146) by Heckman & Lehnert (2000), a spiral galaxy (NGC 1448, Sollerman *et al.* 2005) and the z = 0.5 Damped Lyman-α (DLA) system seen towards AO 0235+164 (Junkkarinen *et al.* 2004, York *et al.* 2006). In all of these other studies the distance scales are such that the spectra recorded are averaged over a large area of the galaxy.

Whilst studies of external galaxies have shown that there is much to be learned from studying the DIBs in new and different environments, one of the most exciting recent

[3] A measure of the amount of atomic hydrogen per unit dust reddening, i.e. $G = N(\text{H I})/E_{B-V}$.

results was the discovery of the λ4430 DIB in the Damped Lyman-α absorber (DLA, Section 4.1.1) seen towards AO 0235+164 (Junkkarinen *et al.* 2004). Subsequent investigation of the same line of sight has lead to the discovery of the λ5705 and λ5780 DIBs (York *et al.* 2006). This significant discovery shows that the DIB carriers which are probably large organic molecules, were present in the Universe over 5 Gyr ago. If the diffuse band behaviour in extragalactic environments is to be fully understood then DLA systems may provide the variety of physical and chemical conditions sought to better understand DIB chemistry.

This Chapter describes a search for the diffuse interstellar bands in quasar absorption lines of sight, DLAs. However, before presenting any results it is useful to describe the nature of DLAs and why it would be particularly interesting to find DIBs in these systems.

4.1.1 Damped Lyman-α systems

Originally discovered in the early 1970's (Lowrance *et al.* 1971, 1972), it was quickly realised that DLA systems arise due to large quantities of neutral hydrogen presumably associated with galaxies and proto-galaxies in the early Universe. Damped Lyman-α (DLA) systems are a particular class of quasar (QSO) absorber that are identified by their high column density of neutral atomic hydrogen. For a QSO absorber to be designated a DLA, the column density of hydrogen, N(H I), must exceed 2×10^{20} cm^{-2}. Figure 4.3 shows an example of the spectrum recorded towards a DLA sightline. The DLA in this picture is the spiral galaxy.

The term 'damped' refers to the shape of the H I Lyman-α line seen in absorption and is a consequence of the very high column density of H I contained within the DLA and the radiation damping that ensues. DLAs are one of many different types of H I absorption systems; Lyman-α forest (N(H I) $< 10^{17}$ cm^{-2}) and Lyman limit (N(H I) $< 10^{20}$ cm^{-2}, Péroux *et al.* 2003) absorbers are examples with lower N(H I). Although initially selected as a 'cut-off' for the definition of a DLA, the N(H I) limit of $> 2 \times 10^{20}$ cm^{-2} actually corresponds to a fundamental difference in the classes of H I absorbers; the hydrogen in DLAs is predominantly neutral whereas in Lyman-α forest and Lyman limit absorbers it is almost entirely ionised. This difference in ionisation state is of fundamental importance given that DLAs and the gas within them

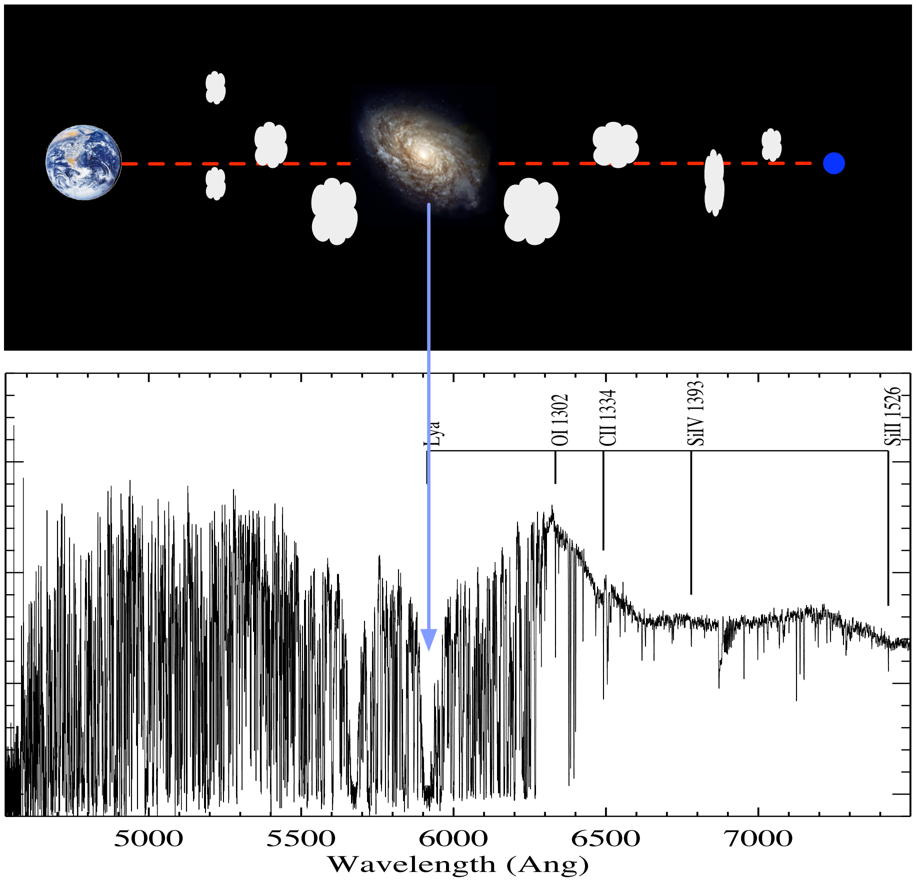

Figure 4.3: A QSO (right, blue) absorption line-of-sight. Light from the background QSO is absorbed by the intervening material giving rise to the Lyman-α 'forest' of lines blueward of the Lyman-α emission line due to the QSO. The strongest absorption feature is due to the intervening galaxy. Absorptions due to other species are also present at the same redshift.

represent a significant fraction of the baryonic mass of the early Universe available for star formation (Wolfe *et al.* 1995). As stars are unlikely to form from the warm ionised gas present in the Lyman-α forest and Lyman limit absorbers, DLAs are thought to be the principal reservoirs of neutral material from which stars form (Wolfire *et al.* 2003).

DLAs are most easily identified through the Lyman-α transition of hydrogen at 1216 Å. With the advent of the Sloan Digital Sky Survey[4] (SDSS) and enormous quantities of high quality spectra, over 500 DLAs have been identified (Prochaska & Herbert-Fort 2004) using the 1216 Å Lyman-α transition. The opaque nature of the Earth's atmo-

[4]Funding for the SDSS and SDSS-II has been provided by the Alfred P. Sloan Foundation, the Participating Institutions, the National Science Foundation, the U.S. Department of Energy, the National Aeronautics and Space Administration, the Japanese Monbukagakusho, the Max Planck Society, and the Higher Education Funding Council for England. The SDSS Web Site is http://www.sdss.org/.

sphere makes detection of this UV transition impossible for absorbers with $z \lesssim 1.65$[5]. Detection of DLAs at $z < 1.65$ requires a space telescope but with the failure of the Space Telescope Imaging Spectrograph (STIS) in August 2004, the astronomical community is no longer able to identify low redshift DLAs directly. This has led authors to seek alternative methods for identifying DLAs. Realising that Mg II lines (2796 Å & 2804 Å) are observed in every DLA known, Rao & Turnshek (2000) have used the Mg doublet to search for DLAs by 'proxy'. With a success rate of $\sim 40\%$ this method has increased the number of known absorbers to ~ 40 (Nestor *et al.* 2005).

Understanding the relationship between the luminous galaxies that can be observed directly and the nature of DLAs is of prime importance if a better understanding of galaxy evolution and star formation is to be achieved. Direct imaging of DLA absorbers only becomes feasible for DLAs of $z \lesssim 1$ and so the low-to-moderate redshift ($z < 1$) DLAs are arguably the most important group to study.

4.1.2 Dust and diffuse bands in DLAs

If DLAs really are the principal source of material that was available for star formation in the early Universe then characterising and quantifying the role that dust may play in DLAs is a crucial step towards understanding the star formation and galaxy evolution in primordial times (Pei & Fall 1995). Since the early realisation of their importance, authors have used a variety of methods for identifying dust reddening in DLAs. Given the relatively difficult nature of DLA observations as the targets are faint, studies of the dust in DLAs are rudimentary compared to those carried out in the galactic interstellar medium (ISM).

In order to detect dust it is necessary to consider the effect(s) of a dusty DLA environment on the spectrum recorded of the background QSO. One major effect is the differential depletion of metals onto the surfaces of dust grains (Savage & Sembach 1996, Pettini *et al.* 1997). Atomic spectra for refractory elements such as Fe are weakened relative to more volatile non-refractory species such as Zn in dusty environments. With the aid of high-resolution spectroscopy an estimate of the amount of reddening of the DLA can be made based upon the different abundances of these metals. Pettini *et al.* (1994, 1997) using the relative strengths of Cr and Zn lines, showed that,

[5] At a redshift (z) of 1.65 the 1216 Å Lyman-α transition is shifted to $(1 + z) \times 1216$ Å = 3222 Å

compared to the galactic ISM the dust depletion in DLAs is significantly less.

Another effect of dust is that it reddens the background QSO spectrum. As at least some of the dust grains are of a similar size to the bluer wavelengths of the optical spectrum, the individual grains preferentially absorb and scatter blue light thus reddening the overall spectral energy distribution (SED) of the background QSO. Making use of this SED reddening an alternative technique to search for dust is by fitting the SEDs of samples of DLA QSO spectra and then comparing those SEDs with a sample of non-DLA QSO spectra (Fall *et al.* 1989, Pei *et al.* 1991). Using this approach, Pei *et al.* (1991) showed that, to a 4σ significance level, the 20 QSOs *with* DLAs were redder than the 46 non-DLA QSOs in their control sample. More recently however, Murphy & Liske (2004) demonstrated that there is little or no dust reddening of $z = 3$ QSOs in the SDSS.

There are problems with both of the methods outlined above; in order to measure accurately the relative abundances of refractory and non-refractory species, expensive[6] observations are required. This severely limits the number of targets that can be readily observed with anything other than the largest telescopes. The SED fitting method relies on having large samples of QSOs and so is only coming to maturity with the advent of the SDSS and the huge database of QSO spectra that have been recorded. As with most statistical studies of trends in large datasets, information about individual lines of sight is lost in the bulk statistics of the study.

Given these difficulties it is not surprising that many authors have sought alternative methods for identifying dust in DLAs. One such example is the search for the 2175 Å feature. Seen towards reddened MW lines-of-sight, the 2175 Å feature is believed to be a *spectroscopic* signature of carbon dust grains. A comparison of the MW UV extinction curve with that of LMC and SMC reveals that the MC sight-lines generally show very little sign of the 2175 Å feature. In a survey of DLA sight-lines, Pei *et al.* (1991) failed to detect the 2175 Å dust feature leading them to the conclusion that the dust in DLAs is more MC-type than Galactic.

Malhotra (1997) detected a broad 2175 Å feature in a composite spectrum of 96 in-

[6] 'Expensive' meaning requires significant amounts of telescope time. Because QSO sight-lines are inherently faint objects and there is a requirement for high-resolution spectra, recording a QSO-DLA spectrum can take many hours using an 8-metre class telescope.

dividual Mg II absorbers, each shifted to the rest wavelength of the absorber. More recently, Motta *et al.* (2002) reported the detection of a 2175 Å feature at $z = 0.83$ in the gravitationally lensed QSO SBS 0909+532. This was detected by taking the ratio of the two lensed spectra thus removing the underlying shape of the QSO spectrum and leaving only the residual dust absorption feature.

More recently, Wang *et al.* (2004) detected the 2175 Å dust feature in the SDSS spectra of three Mg II absorbers in the redshift range $1.4 \lesssim z \lesssim 1.5$. Galactic extinction parameters were found to fit the shape of the 2175 Å feature best although with overall smaller dust grain sizes predicted.

The 2175 Å feature is not the only spectroscopic signature of dust: the strong Galactic and MC DIB – E_{B-V} correlation (Figure 4.1) means that where DIBs are seen, dust is also present. It was only with the recent discovery of the 2175 Å dust feature and the λ4430 DIB in the DLA towards the BL Lac object AO 0235+164 (Junkkarinen *et al.* 2004) that the true potential of using the strengths of DIBs in DLAs as a proxy for measuring the dust content of these systems was realised.

DLA target selection

The lack of a 2175 Å absorption feature in their sample of DLAs (Pei *et al.* 1991) and the recent results of Murphy & Liske (2004) have shown that the majority of DLAs have very little dust. Utilising the Galactic relationship between $W_{\lambda 5780}$ and N(H I) Lawton *et al.* (2005) recorded spectra of six high N(H I) ($\geqslant 10^{20}$ cm^{-2}) DLAs with the expectation that they would detect the λ5780 DIB; unfortunately this was not the case. Lawton *et al.* were only able to place upper limits on the strengths of DIBs in their targets and this study demonstrated that the cherished Galactic DIB correlations do not necessarily hold in extragalactic environments. It is not clear why the DIBs were not detected in these DLAs. Considering what has been learnt from studies of the LMC and SMC, it is possible that the (presumably) lower metallicities are severely reducing the DIB carrier column densities. It is also possible that higher levels of radiation in the DLA sight-line may be sufficient to destroy the DIB carriers. Based on the dramatically lower DIB strengths in DLAs it is clear that to have *any* chance of detecting DIBs in DLAs it is essential to target systematically the highest column density, highest metallicity and most dust-reddened sight-lines.

Ca II absorbers in the SDSS

Lawton *et al.* (2005) have shown that having a high N(H I) requirement when targeting QSO absorbers is clearly not sufficient when trying to detect the diffuse bands. A more promising avenue might be to use the DIB – E_{B-V} relationship that has been shown to hold for extragalactic as well as Galactic environments (e.g. Welty *et al.* 2006). Recently, a study by Wild & Hewett (2005) demonstrated that QSO absorbers selected from the SDSS using the Ca II H & K lines ($\lambda_{\rm rest}$ 3934 Å, 3969 Å) showed significant reddening of the background QSOs. In the redshift range targeted ($0.84 < z_{\rm abs} < 1.3$) a detection was made not only of the Ca II lines but also the Mg I, Mg II and Fe II lines. This lead Wild & Hewett to conclude that the majority of the 31 Ca II absorbers detected were DLAs.

A key question is how much dust is there in these Ca II absorbers? Wild & Hewett calculated that the average dust reddening, E_{B-V}, was ~ 0.06 with LMC and SMC-type extinction curves fitting the (absorption) spectrum best. Significantly they also showed that there exists a trend of increasing E_{B-V} with increasing $W_{\rm Ca\,II}$. Splitting their sample into two groups, low $W_{\rm Ca\,II}$ (< 0.7 Å) and high $W_{\rm Ca\,II}$ (> 0.7 Å), they calculated E_{B-V} values of ~ 0.025 and ~ 0.1 respectively.

Utilising the huge statistical power of the SDSS (> 50,000 QSOs) Wild & Hewett found probably the dustiest sub-sample of QSO absorbers in the whole SDSS thus making them the ideal place to start a search for DIBs. Unfortunately, for the redshift range in which Ca II absorption ($0.84 < z_{\rm abs} < 1.3$) was detected, even the λ4430 DIB lies beyond 8000 Å and other strong DIBs are shifted into the near-IR. Working in collaboration with Michael Murphy at the Institute of Astronomy, Cambridge, a sample of ~ 40 Ca II absorbers at lower redshifts ($z_{\rm abs} < 0.5$) was identified[7]. Since these absorbers are likely to have high N(H I), high metallicity and are also likely to be some of the dustiest DLAs in the entire SDSS catalogue of QSOs, they represent probably the best known candidates in which to carry out a search for DIBs in the early Universe.

[7]The analysis of SDSS spectra and search for low-z Ca II absorbers was carried out by Michael Murphy.

4.1.3 Motivation for the study

This Chapter describes a first attempt to find DIBs in DLAs that have been selected not only because of their high probable $N(\text{H I})$, but based on their significant dust content and high metallicity. The key questions are:

I. Do Galactic DIB-strength correlations (e.g. $N(\text{H I})$, E_{B-V}) hold for extragalactic environments or are they merely a consequence of the IS chemistry of the Galaxy? Investigating DIB strengths in galaxies with very different histories from the Galaxy should help in identifying the most important DIB correlations.

II. Are the DIB carriers present in a wide range of galaxies with different star formation rates? In the SDSS images of the QSO field the galaxy hosting the absorption is visible for many of the targets selected. Multi-colour imaging of the galaxies would reveal the rates of star formation and it might be possible to relate this to DIB strengths.

III. DIB families? Are the DIBs that appear to show a correlation with each other (e.g. Krelowski & Walker 1987) in the Galaxy *actually* related or are the correlations unique to the Galaxy? Investigating relative DIB strengths in extra-galactic environments may help reveal the extent to which those DIBs correlations hold.

IV. Can the DIB-metallicity relationship be constrained by investigating these DLAs? Studies are underway[8] to obtain the emission-line metallicities of those targets where the host galaxy can be seen in the SDSS image.

4.1.4 Target selection

Targets were selected from the Sloan Digital Sky Survey Data Release 3 (SDSS DR3) which contains over 50,000 QSOs. Using the 'matched-filter' technique pioneered by

[8]FORS2 proposal submitted by Michael Murphy, IoA

Hewett *et al.* (1985) a search was made of the QSO spectra for the Ca II doublet. Of the many tens of thousands of spectra analysed, 224 Ca II absorbers were found to have rest $W_{\mathrm{Ca\ II}} > 0.3$ Å at greater than 4σ significance. In order to give the best chance of detecting the DIBs it was necessary to target those absorbers with the highest $W_{\mathrm{Ca\ II}}$ noting that Wild & Hewett (2005) showed that E_{B-V} increases with $W_{\mathrm{Ca\ II}}$.

Once an initial selection had been made based upon $W_{\mathrm{Ca\ II}}(> 0.5$ Å), target spectra were visually inspected for signs of reddening which was noticeable by significant deviation of the spectrum away from a power law in the blue (see Figure 4.4). A further refinement of the targets was then made by choosing those targets for which the DIBs of interest (λ4430, λ5780, λ6284, λ6614), did not fall in regions of strong telluric features or where undulations in the QSO continuum might cause confusion.

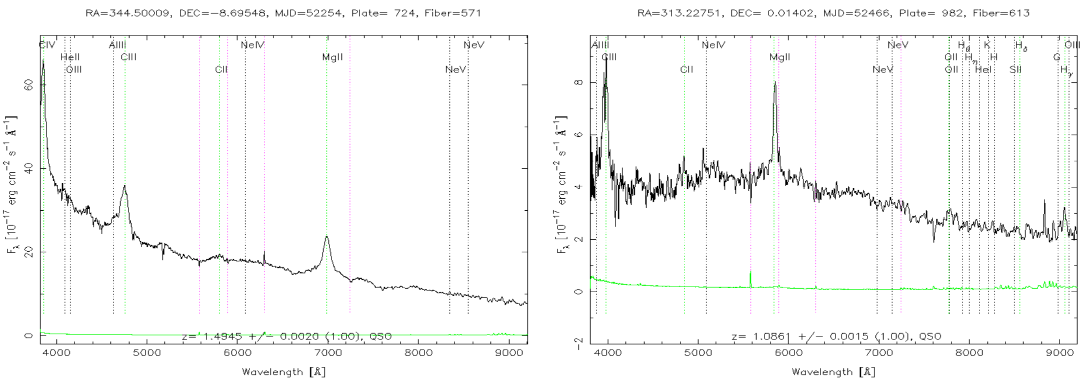

Figure 4.4: SDSS spectra of SDSSJ225800.02-084143.7 (left) with rest $W_{\mathrm{Ca\ II}}$ = 0.260 Å and SDSSJ205254.60+000050.4 (right) with rest $W_{\mathrm{Ca\ II}}$ = 1.971 Å. The left-hand QSO spectrum shows a clear power law in the blue whereas in the right-hand spectrum the blue flux is severely reduced.

As the targets were selected from a survey primarily carried out in the Northern hemisphere (SDSS), the ideal telescope–instrument configuration for this project would be Gemini North–GMOS. Unfortunately Gemini North is one of the most over-subscribed telescopes in the World and a request for 19 hours of observing time to record the spectra of 7 targets was not successful. An award of 4 hours was granted by the time-allocation committee but as of the time of writing, no data have been taken. At the same time as the Gemini-N proposal was submitted, a complementary proposal was submitted to the Very Large Telescope (VLT) for 22 hours of FORS2 time. This proposal was successful and is analysed in this Chapter. Table 4.1 lists the targets observed during P77 (Program ID 077.C-0737) (April – October 2006) for this project.

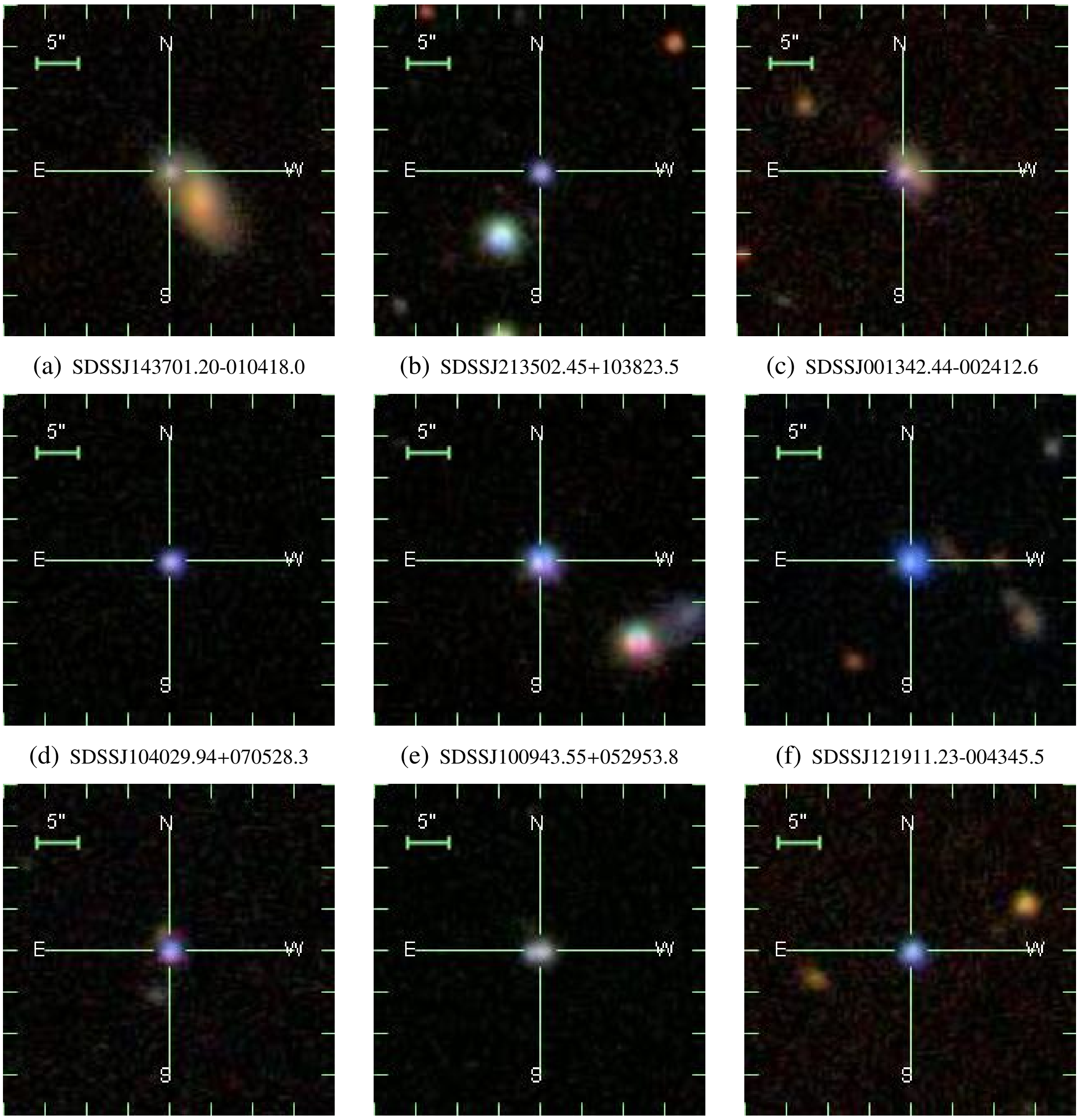

(a) SDSSJ143701.20-010418.0

(b) SDSSJ213502.45+103823.5

(c) SDSSJ001342.44-002412.6

(d) SDSSJ104029.94+070528.3

(e) SDSSJ100943.55+052953.8

(f) SDSSJ121911.23-004345.5

(g) SDSSJ113702.03+013622.1

(h) SDSSJ122608.02-000602.2

(i) SDSSJ225913.74-084419.6

Figure 4.5: SDSS images of the QSOs studied in this Chapter. QSO is marked by NSEW crosshairs. The likely candidate absorber can be seen for at least 5 of the 9 targets.

Target	R_{mag}	z_{em}	z_{abs}	$W_{\text{Ca II } 3934}$	$\Delta W_{\text{Ca II } 3934}$
SDSSJ143701.20-010418.0	19.1	0.2860	0.07254	1.065	0.203
SDSSJ213502.45+103823.5	18.8	1.5110	0.09839	0.897	0.192
SDSSJ001342.44-002412.6	18.6	1.6440	0.15555	1.208	0.149
SDSSJ104029.94+070528.3	18.6	1.5320	0.20626	0.607	0.122
SDSSJ100943.55+052953.8	16.9	0.9420	0.38622	0.506	0.048
SDSSJ121911.23-004345.5	18.0	2.2930	0.44847	0.565	0.079
SDSSJ113702.03+013622.1	18.6	1.6410	0.44916	0.540	0.117
SDSSJ122608.02-000602.2	18.4	1.1250	0.51793	0.455	0.107
SDSSJ225913.74-084419.6	18.4	1.2900	0.52931	0.453	0.087

Table 4.1: VLT targets observed, their SDSS R-band magnitude, the redshift of the background QSO (z_{em}) of the absorber z_{abs}, and the strength of the Ca II 3934 Å line (rest frame). All equivalent widths are quoted in Å

4.2 Observations

Observations of the targets listed in Table 4.1 were carried out during period 77 (April – October 2006) using the FOcal Reducer/low dispersion Spectrograph (FORS) spectrograph on the Antu (UT1) telescope of the VLT. FORS is a multi-purpose instrument capable of direct imaging, single- and multi-object spectroscopy and polarimetry. Two versions of FORS (Appenzeller *et al.* 1998) exist: FORS1 & FORS2, the only difference is that the newer FORS2 spectrograph has higher resolution gratings available and is mounted at the Cassegrain focus of Antu (UT1) rather than Kueyen (UT2). Table 4.2 lists the gratings available and those used for this programme on FORS2.

Grating	$\lambda_{central}$	λ_{range}	dispersion	$\lambda/\Delta\lambda$
GRIS 600B+22	4650	3300 – 6210	0.75	780
GRIS 600I+25 (5)	7950	6630 – 9390	0.66	1500
GRIS 300V+20	5900	3300 – 8700	1.68	440
GRIS 300I+21	8600	6000 – 11000	1.62	660
GRIS 200I+28 (2)	7450	5600 – 11000	2.43	380
GRIS 150I+27	7200	3300 – 11000	3.45	260
GRIS 1400V+18 (4)	5200	4560 – 5860	0.31	2100
GRIS 1200R+93	6500	5750 – 7310	0.38	2140
GRIS 1028z+29	8600	7730 – 9480	0.42	2560
GRIS 600RI+19 (4)	6780	5120 – 8450	0.83	1000
GRIS 600z+23	9010	7030 – 10700	0.81	1390

Table 4.2: Gratings available for use on FORS2. $\lambda_{central}$ and λ_{range} are in angstroms (Å). Dispersions are quoted in Å/pixel, spectral resolutions are measured at $\lambda_{central}$. Those gratings marked bold were used for this observing programme.

Table 4.3 lists the individual observations made for each of the targets. As with all spectroscopic observations there is a trade-off between S/N and resolving power. Given that the majority of our targets are fainter than $R_{mag} \sim 18.5$ even with the large collecting area of an 8-metre telescope it was not feasible to use the highest resolution gratings.

Target	Obs 1	Obs 2	DIBs
SDSSJ143701.20-010418.0	1200R (3.0)	–	λ5780, λ6284, λ6614
SDSSJ213502.45+103823.5	600B (3.0)	–	λ4430
SDSSJ001342.44-002412.6	1200R (1.5)	–	λ5780, λ6284
SDSSJ104029.94+070528.3	600I (1.5)	–	λ5780, λ6284, λ6614
SDSSJ100943.55+052953.8	1028z (0.75)	600RI (1.1)	λ4430, λ5780, λ6284, λ6614
SDSSJ121911.23-004345.5	600RI (0.75)	–	λ4430, λ5780
SDSSJ113702.03+013622.1	600RI (1.5)	–	λ4430, λ5780
SDSSJ122608.02-000602.2	600RI (1.5)	–	λ4430
SDSSJ225913.74-084419.6	600RI (1.5)	–	λ4430

Table 4.3: VLT/FORS2 targets and the observations carried out. Column 'Obs 1' lists the grating used and (in parentheses) the number of hours on-target integration. Column 'Obs 2' details, if applicable, the second grating used for the target. The final column lists the main DIBs targeted for the observation.

Predicted DIB strengths

The aim was to be able to search for λ4430 and λ5780 DIBs at greater than 5-sigma significance. Given the lack of previous DIB detections in DLAs and their low metallicities (Murphy & Liske 2004), it was not immediately clear just how strong the DIBs would be. DIB studies in the Magellanic clouds have shown (Welty *et al.* 2006, Cox *et al.* 2006) that the λ5780 - E_{B-V} relationship in the Galaxy extends at least to these extragalactic (MC) environments. However, these studies together with the work of Lawton *et al.* (2005) have demonstrated that the Galactic λ5780-N(H I) *does not* hold for external galaxies. DIB-strengths have therefore been estimated from the λ5780 - E_{B-V} (Herbig 1993) and λ4430 - E_{B-V} (Snow *et al.* 2002) relationships.

Wild & Hewett (2005) showed that for the strongest Ca II absorbers the average reddening (E_{B-V}) is ~ 0.1. The targets selected by Wild & Hewett were in the redshift range $0.84 < z < 1.3$. The targets observed in this programme are of $z \lesssim 0.5$ and have a range of $W_{\mathrm{Ca\,II}\,3934}$ strengths ($0.45 < W_{\mathrm{Ca\,II}\,3934} < 1.2$ Å). Given that the targets observed are of lower z than those selected by Wild & Hewett and the degree of reddening apparent in the SDSS spectra of the QSOs, a uniform value of $E_{B-V} = 0.1$ has been used to predict the DIB strengths and hence calculate the S/N requirements and exposure times of the programme.

The S/N requirements for a 5-sigma DIB detection depends upon whether or not the feature is resolved[9]. Table 4.4 lists the S/N requirements of the observing programme for each available DIB in each of the targets. When predicting the strengths of the DIBs the Galactic DIB - E_{B-V} relationship has been used. One charcteristic of observing spectral features at cosmological distances is that the strength of the feature scales with $(1+z)$ such that $W_{\mathrm{DIB(observed)}} = W_{\mathrm{DIB(rest)}} \times (1+z_{\mathrm{abs}})$. This increase in the observed strength of a feature means that a target of higher z may not require higher S/N to detect a feature to the same degree of significance as a lower-z target.

Target	λ4430	λ5780	λ6284	λ6614
SDSSJ143701.20-010418.0	–	75	80	160
SDSSJ213502.45+103823.5	65	–	–	–
SDSSJ001342.44-002412.6	–	66	65	–
SDSSJ104029.94+070528.3	–	97	94	230
SDSSJ100943.55+052953.8	73	62/112	139	–
SDSSJ121911.23-004345.5	66	111	–	–
SDSSJ113702.03+013622.1	67	113	–	–
SDSSJ122608.02-000602.2	64	–	–	–
SDSSJ225913.74-084419.6	64	–	–	–

Table 4.4: VLT/FORS2 S/N per pixel requirements for a 5-sigma detection of a given DIB. Predicted DIB strengths based upon the Galactic E_{B-V}-DIB strength relationship. N.B. there are two entries for λ5780 towards SDSSJ100943.55+052953.8 as the λ5780 DIB is covered with both of the gratings used (1028z & 600RI)

The values quoted in Table 4.4 are a 'best estimate' of how strong the DIBs might be. The exact nature of these Ca II absorbers is not yet clear and with the lack of a suitable UV spectrograph for measuring N(H I) is impossible to say whether all of the target absorbers are *bona fide* DLAs. However, the intrinsic weakness of Ca II absorption means that their detection indicates significant quantities of enriched material. Hence these targets are very probably the best QSO absorbers in which to begin a search for

[9]The term 'resolved' has a different definition in astronomy than chemistry. For the purposes of this discussion the term means that for a feature to be resolved then the $FWHM$ of the feature being investigated must be spread across two or more resolution elements of the spectrograph.

DIBs at cosmological distances.

At the time of writing all of the observations for Program ID 077.C-0737 have been completed. However, with the P77 semester running from April – October 2006 data for this chapter was provided on 28/07/06, i.e. before the end of P77 so that a preliminary reduction could be performed and results reported. The data for the remaining four targets will be analysed elsewhere.

4.3 Results and Discussion

SDSSJ143701.20-010418.0

With an absorber redshift (z_{abs}) of 0.07254, the Ca II QSO absorber seen towards SDSSJ143701.20-010418.0, (J143701 from now on), is the lowest z target observed in this programme and as a consequence this target is one of those selected in which a potential candidate for the Ca II absorption can be seen in the image in Figure 4.6.

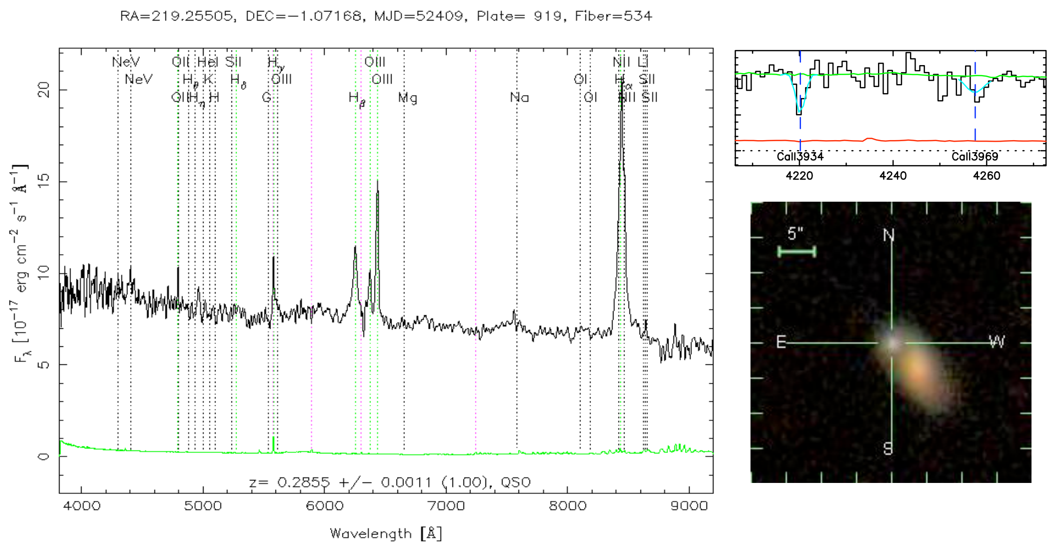

Figure 4.6: SDSS spectrum of SDSSJ143701.20-010418.0, the region around the Ca II lines (courtesy of Michael Murphy) and the SDSS image of the field.

The Ca II 3934 Å absorption feature is very strong in this target with a measured equivalent width (EW) of 1.06 ± 0.20 Å. As might have been expected the SDSS spectrum of J1430701 is clearly reddened showing little evidence of a power law in the blue.

Because of the significant obscuration of the background QSO, J1430701 was also one of the faintest targets observed (R_{mag} = 19.1) thus requiring a significant amount of integration to achieve the S/N requirements of the programme. With a low z_{abs} this target was used as an opportunity to search for the λ5780, λ6284 and λ6614 diffuse bands with even the reddest λ6614 DIB still in the optical region at 7094 Å. Given the relative narrowness of these three DIBs ($FWHM_{\rm rest} \sim 2,\ 2.5$ & 1 Å respectively) the 1200R grating was chosen in order to at least partially resolve the features.

The brightness of the galaxy visible in the SDSS acquisition (Figure 4.6) image of J1430701 is such that it was possible to record a spectrum of both the QSO and the galaxy (see Figure 4.7).

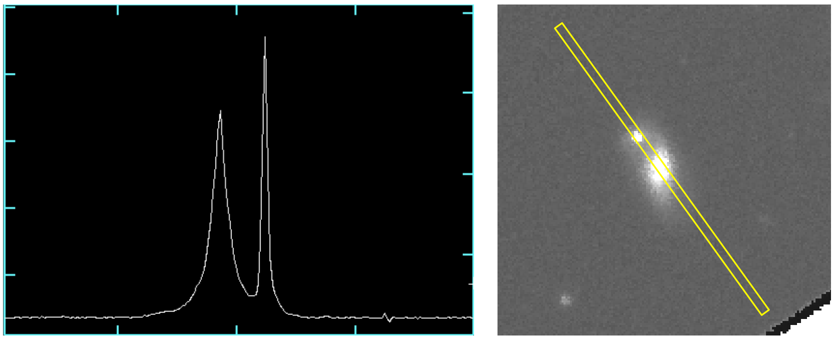

Figure 4.7: IRAF screen grab of a slice through a CCD frame of SDSSJ143701.20-010418.0 clearly showing the broad profile of the foreground galaxy (left) and the narrow background QSO profile (right) together with the FORS2 acquisition image and approximate slit position.

Figure 4.8 shows the regions surrounding λ5780, λ6284 and λ6614 for the galaxy (red line) and the QSO line-of-sight (black) together with the predicted DIB profile. The predicted DIB profile is a Gaussian feature of the same $FWHM$ as quoted by Tuairisg *et al.* (2000), of W_λ as predicted by the Herbig λ5780 – E_{B-V} relation (see Figure 4.1, Herbig 1993) and convolved with the instrument profile of FORS2 with the 1200R grating. λ6284 and λ6614 predicted profiles have been produced in the same way with the predicted $W_{\rm DIB}$ based upon the strength of the DIB relative to λ5780 in the Galaxy.

All spectra in Figure 4.8 have been shifted to rest as defined by the Na I D lines also arising from the absorber. With average seeing of 0.65″ during exposure on J143701, S/N requirements were achieved. The 0.65″ seeing allowed for extraction of the QSO and galaxy traces to be performed with minimal contamination of individual profiles. Visual inspection of the spectra in Figure 4.8 reveals that λ6284 and λ6614 have not been detected in either the QSO or galaxy, at least at the *predicted* strength. $\lambda5780$ appears to have been detected in the galactic sight line (red) with a strong ($W_\lambda \sim 0.9$ Å) feature centred around 5781 Å.

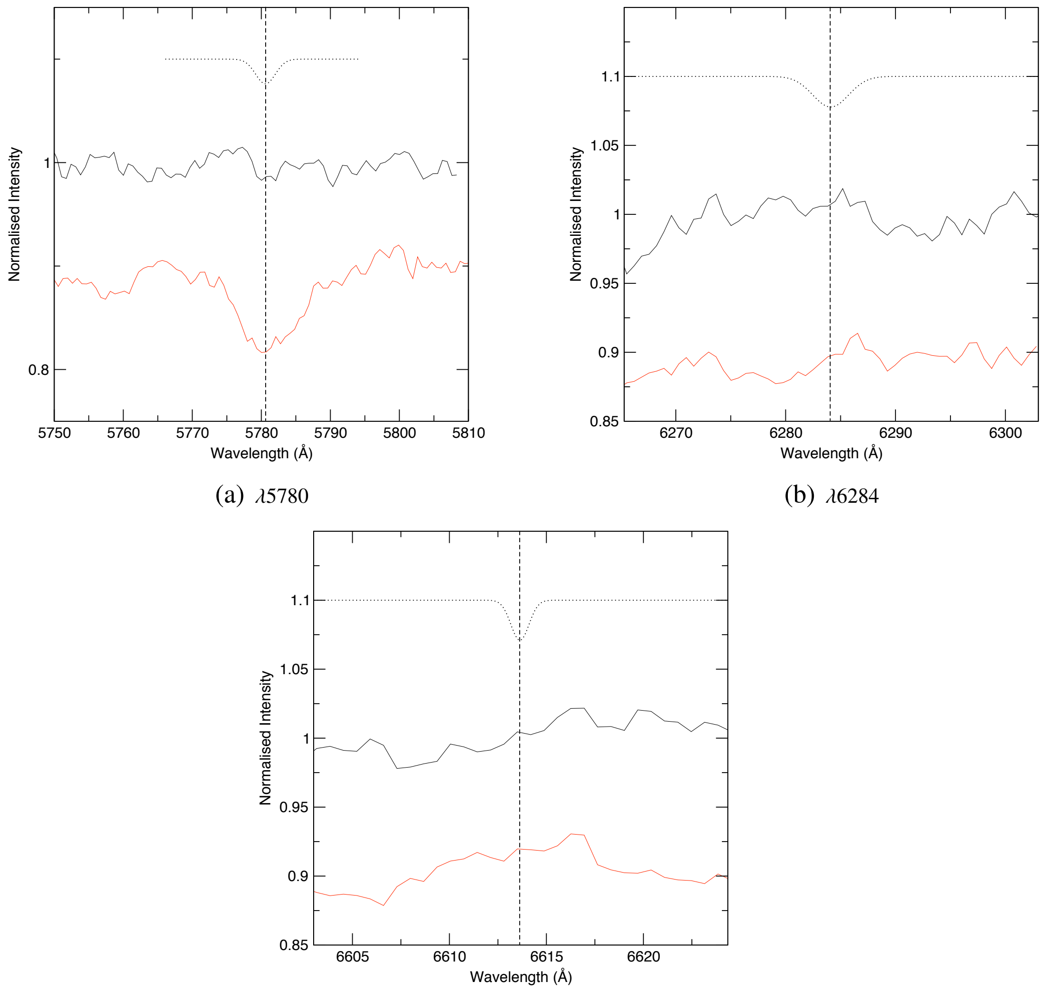

(a) $\lambda5780$ (b) $\lambda6284$

(c) $\lambda6614$

Figure 4.8: Plots of the spectral region encompassing $\lambda5780$, $\lambda6284$ and $\lambda6614$ for SDSSJ143701.20-010418.0. The top trace is the predicted DIB profile based upon E_{B-V} and including the instrumental profile. The QSO spectrum is shown in black and the galaxy spectrum in red. All spectra have been shifted to rest.

A strong feature was also detected at 5708 Å and was originally thought to be a possible detection of $\lambda5705$ (York *et al.* 2006). The absorbing foreground galaxy of J143701 appears to be some kind of barred spiral galaxy where the dominant stellar population are K-type giants. The spectra of such stars are dominated by metal lines due to, amongst others Fe. It is to be expected then that the spectrum of the J143701 foreground galaxy bulge is dominated by the metal lines present in K giant spectra. Unfortunately there are two strong lines due to Fe I at 5709 and 5782 Å. The features centred at ~ 5781 Å in Figure 4.8 are almost certainly not due to the λ5780 diffuse band. Even if λ5780 is present in this system, the overwhelming strength of the Fe I lines prevent any possibility of achieving a detection.

With a $FWHM$ of ~ 9 Å and W_λ ~ 0.9 Å and the failure to detect λ6284 and λ6614 made the 'detection' of λ5780 in J143701 suspicious. The broadness of the feature at 5781 Å (~ 550 kms^{-1}) can likely be accounted for by the motion of stars within the galaxy and the summation of all of the exposed CCD pixels across the full profile of the spectral trace.

SDSSJ100943.55+052953.8

At R_{mag} = 16.9, SDSSJ100943.55+052953.8 (J100943) was one of the brightest targets observed in this programme. The 600RI grating was used to cover λ4430 and λ5780 in one spectrum.

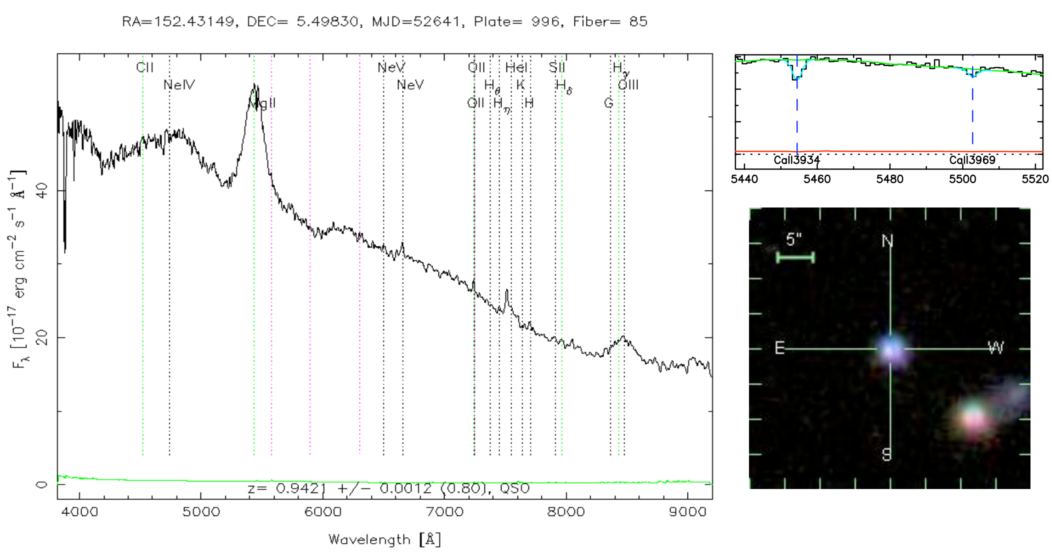

Figure 4.9: SDSS spectrum of SDSSJ100943.55+052953.8, the region around the Ca II lines (courtesy of Michael Murphy) and the SDSS image of the field.

As well as the QSO there is another source approximately 10″ away in the SDSS field image (Figure 4.9). The SDSS spectrum in Figure 4.9 is not obviously reddened and with $W_{\mathrm{Ca\,II}\,3934}$ = 0.506 Å, J100943 is at the lower end of the range in Ca II absorption strength.

Figure 4.10 shows the spectral regions surrounding $\lambda4430$ and $\lambda5780$. Once again there is no obvious detection of either DIB, limiting strengths are listed in Table 4.5.

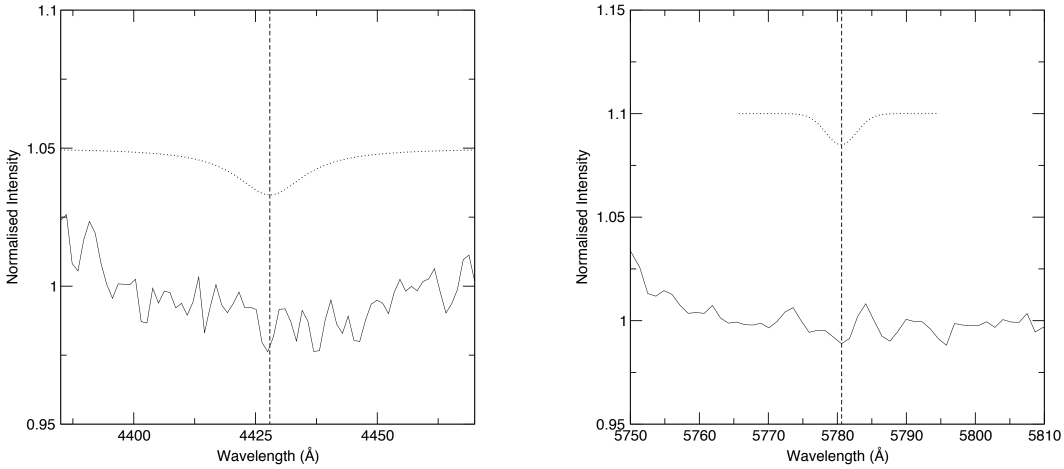

(a) $\lambda4430$ (b) $\lambda5780$

Figure 4.10: Plots of the spectral region encompassing $\lambda4430$ and $\lambda5780$ for SDSSJ100943.55+052953.8. The top trace is the predicted DIB profile based upon E_{B-V} and including the instrumental profile. The QSO spectrum is shown in black. All spectra have been shifted to rest.

SDSSJ121911.23-004345.5

The foreground Ca II absorber towards SDSSJ121911.23-004345.5 (J121911) is not immediately obvious from the SDSS image in Figure 4.11 although there are a number of potential candidates within 5-10″.

The SDSS spectrum of J121911 appears to obeys a clear power law to the blue and the SDSS image showing little sign of reddening with the QSO appearing compact and blue.

The 600RI (Table 4.2) grating was used to cover $\lambda4430$ and $\lambda5780$ and the spectra are shown in Figure 4.12. No detection was made of either DIB; non-detection limits are listed in Table 4.5.

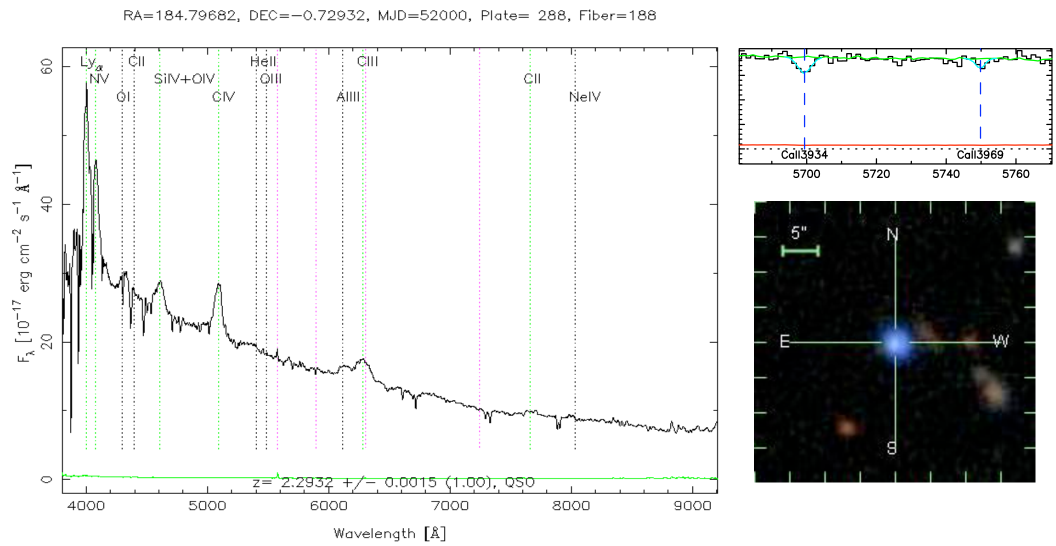

Figure 4.11: SDSS spectrum of SDSSJ121911.23-004345.5, the region around the Ca ii lines (courtesy of Michael Murphy) and the SDSS image of the field.

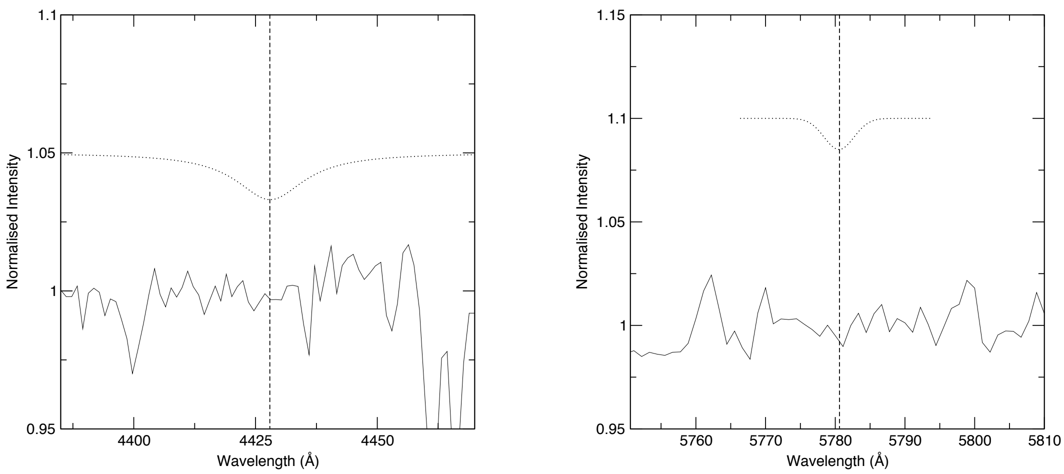

(a) λ4430 (b) λ5705

Figure 4.12: Plots of the spectral region encompassing λ4430 and λ5780 for SDSSJ121911.23-004345.5. The top trace is the predicted DIB profile based upon E_{B-V} and including the instrumental profile. The QSO spectrum is shown in black. All spectra have been shifted to rest.

SDSSJ113702.03+013622.1

An attempt was made to have a selection of Ca II absorbers with a range of redshifts for observation. The limiting redshift was $\sim$ 0.75, after which even the bluest DIB (λ4430) enters regions seriously contaminated with sky emission lines and atmospheric absorptions.

With a $z_{\rm abs}$ = 0.44916, the absorber towards SDSSJ113702.03+013622.1 (J113702) was the highest z target for which is was still feasible to observe λ5780.

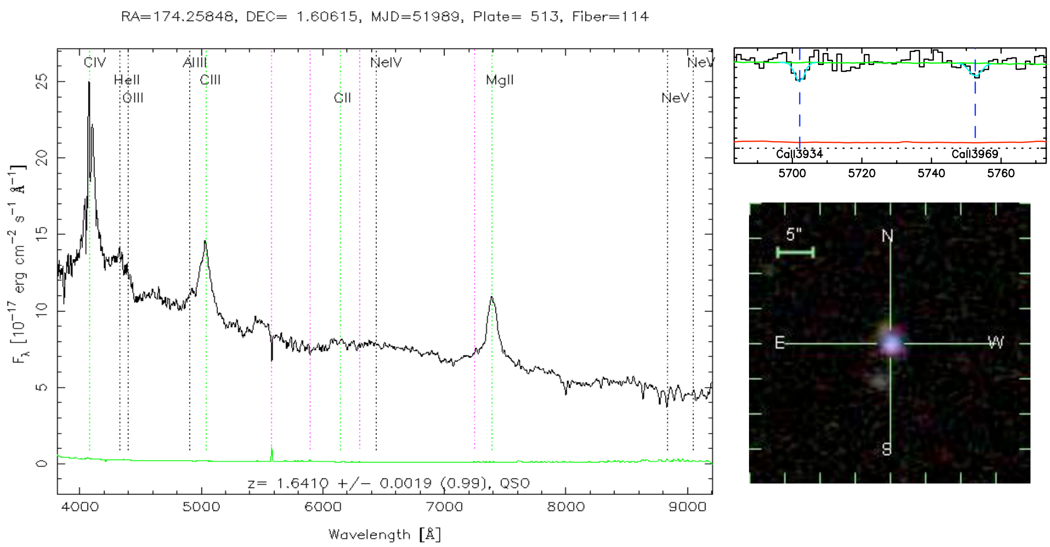

Figure 4.13: SDSS spectrum of SDSSJ113702.03+013622.1, the region around the Ca II lines (courtesy of Michael Murphy) and the SDSS image of the field.

Figure 4.13 shows that the J113702 appears slightly reddened and the image shows a possible candidate absorber closely associated with the QSO. Another non-detection, spectral regions surrounding λ4430 and λ5780 are shown in Figure 4.14, detection limits quoted in Table 4.5.

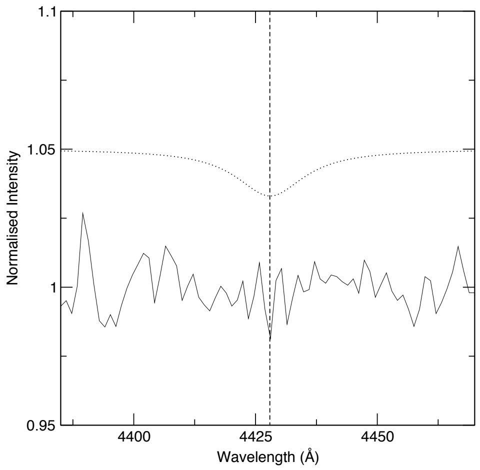

(a) λ4430

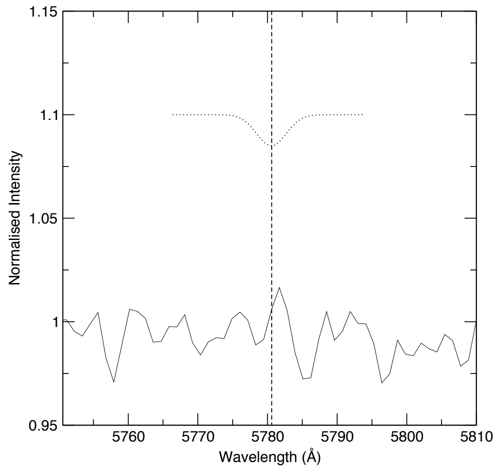

(b) λ5780

Figure 4.14: Plots of the spectral region encompassing λ4430 and λ5780 for SDSSJ113702.03+013622.1. The top trace is the predicted DIB profile based upon E_{B-V} and including the instrumental profile. The QSO spectrum is shown in black. All spectra have been shifted to rest.

SDSSJ122608.02-000602.2

The SDSS image of SDSSJ122608.02-000602.2 (J122608) appears extended in the East-West direction (Figure 4.15). Acquisition images taken by the VLT service mode astronomers confirmed this and so the orientation of the FORS2 slit was adjusted such that it was possible to record a spectrum of both targets.

The SDSS spectrum of J122608 appears to show significant reddening (Figure 4.15) although at $W_{\mathrm{Ca\,II}\ 3934} = 0.455$ Å the Ca II line is relatively weak compared with other targets.

Figure 4.16 shows one of the FORS2 acquisition images of the J122608 field (left) and a 'slice' in the spatial direction through the spectral trace of the FORS2 CCD data frames combined with the approximate orientation of the slit (right). As suggested in the SDSS and FORS2 images, there are clearly two objects in the field.

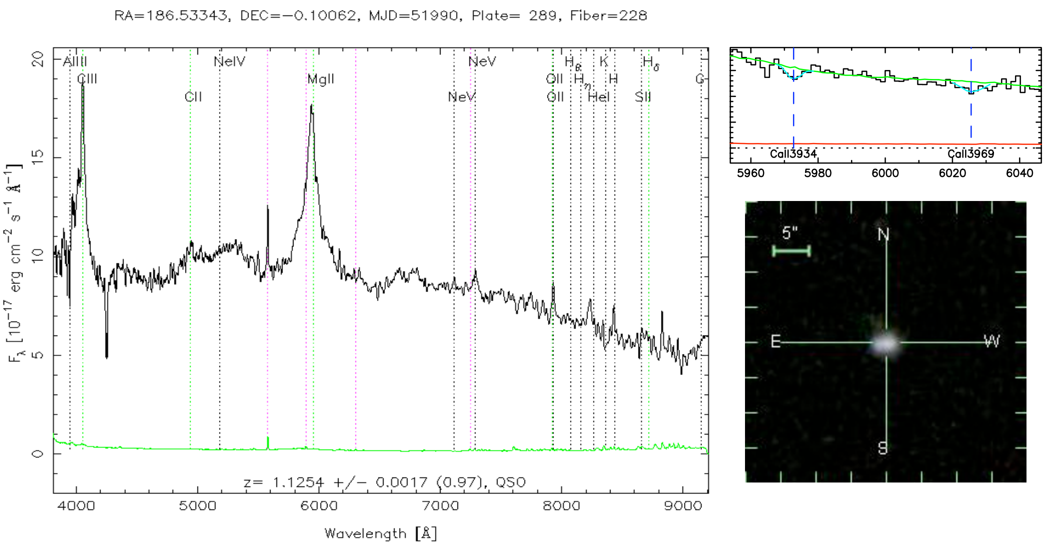

Figure 4.15: SDSS spectrum of SDSSJ122608.02-000602.2, the region around the Ca ɪɪ lines (courtesy of Michael Murphy) and the SDSS image of the field.

Figure 4.17 shows the spectral regions surrounding λ4430 for the QSO (black line) and the 'absorber' (red line). At the rest wavelength of λ4430 (4428 Å) there is no sign of a detection in either spectrum although there is a clear dip blue-ward of 4428 Å in the QSO spectrum. A check was made of the wavelength solution and of the relatively nearby Ca ɪɪ 3934 Å feature and no discrepancy was found in the wavelength solution.

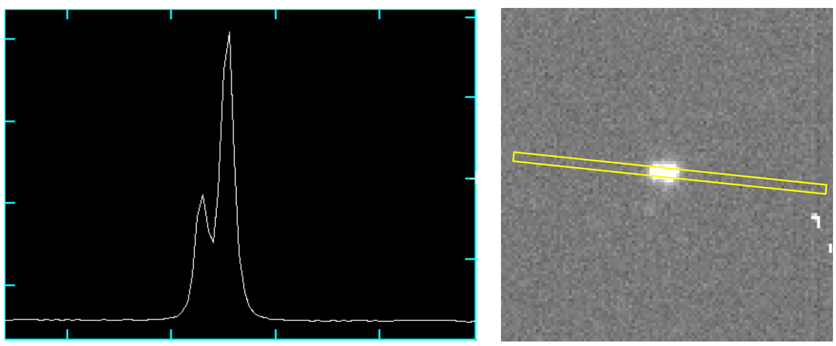

Figure 4.16: IRAF screen grab of a slice through a CCD frame of SDSSJ122608.02-000602.2 showing the galaxy profile (left) and the QSO profile (right) together with the FORS2 acquisition image and approximate slit position.

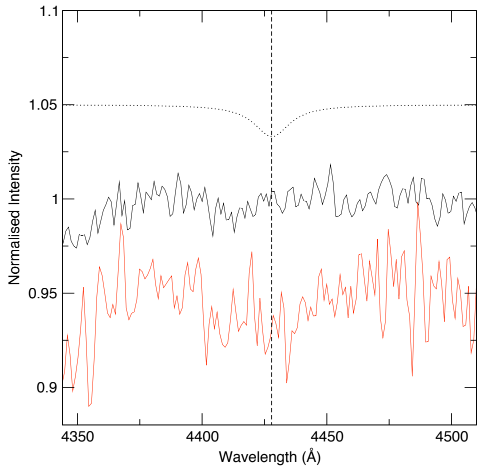

(a) $\lambda 4430$

Figure 4.17: Plot of the spectral region encompassing $\lambda 4430$ for SDSSJ122608.02-000602.2. The top trace is the predicted DIB profile based upon E_{B-V} and including the instrumental profile, the solid black line is the QSO spectrum, the red line the 'absorber'. All spectra have been shifted to rest.

4.4 Analysis and conclusions

Diffuse interstellar bands have not been detected in the five Ca II absorbers analysed. Observing requirements for the VLT/FORS2 observation were deliberately modest to ensure that, for as many targets as possible, the S/N requirements of the programme would be achieved. FORS2 data for SDSSJ213502.45+103823.5, SDSSJ001342.44-002412.6, SDSSJ104029.94+070528.3 and SDSSJ225913.74-084419.6 *have* all been recorded although since the early data release for this thesis. The results and analysis of these later targets will therefore be reported elsewhere.

Table 4.5 lists the limits for the DIB strengths in the Ca II absorbers.

The choice of which diffuse bands to observe in each target was determined by a number of factors including the redshift of the absorber, the redshift of the QSO, atmospheric 'windows' and the brightness of the target.

DIB strength estimates were based largely upon the relationship between DIB strength and E_{B-V}. In an effort to detect DIB signatures in DLA environments, the work of Lawton *et al.* (2005) demonstrated that the galactic $N(H\ \text{I}) - \lambda 5780$ relation (Herbig 1993) can not be relied upon to predict DIB strengths in extragalactic environments.

Target	$\lambda4430$	$\lambda5780$	$\lambda6284$	$\lambda6614$
SDSSJ143701.20-010418.0 (QSO)	–	< 40	< 45	< 15
SDSSJ143701.20-010418.0 (GAL)	–	Fe	< 65	< 17
SDSSJ100943.55+052953.8	< 140	< 45	–	–
SDSSJ121911.23-004345.5	< 175	< 50	–	–
SDSSJ113702.03+013622.1	< 240	< 80	–	–
SDSSJ122608.02-000602.2 (QSO)	< 220	–	–	–
SDSSJ122608.02-000602.2 (GAL)	< 450	–	–	–

Table 4.5: VLT/FORS2 limits on DIB detections in mÅ.

This finding is supported by the work of Cox *et al.* (2006) and Welty *et al.* (2006) who found that Magellanic Cloud $W_{\lambda5780}$ values were ~ 10 times lower than would have been expected based upon measurements of $N(H\ \text{I})$. Whatever physical and chemical factors result in the strength of $\lambda5780$ being related to $N(H\ \text{I})$ in the Galaxy do not hold for the Magellanic Clouds and beyond. Cox *et al.* (2006), Welty *et al.* (2006) and York *et al.* (2006) demonstrated that the E_{B-V}–$\lambda5780$ relationship holds for not only the Magellanic Cloud environments but also for a $z = 0.5$ DLA seen towards AO 0235+164 (York *et al.* 2006).

Wild & Hewett (2005) demonstrated that the average reddening for the stronger Ca II absorbers was $E_{B-V} \simeq 0.1$. Adopting this value $\lambda4430$, $\lambda5780$, $\lambda6284$ and $\lambda6614$ were predicted to have strengths of 220, 80, 85 and 30 mÅ respectively. At redshift z, the *observed FWHM* of a spectral feature is $FWHM_{\text{rest}} \times (1 + z)$ which should make the detection of a given feature easier. Table 4.5 demonstrates that, for the majority of cases, S/N requirements were achieved. In some cases (e.g. J143701, J100943 and J121911) the S/N of the spectra are sufficient to demonstrate that the DIBs are significantly weaker than might have been predicted for absorbers with $E_{B-V} \simeq 0.1$.

In the Galaxy, diffuse band strengths show little correlation with those species that are readily depleted onto grain surfaces e.g. Ca II and Ti II (Herbig 1993). The correlation between $W_{\text{Ca II}}$ and E_{B-V} in QSO absorption lines-of-sight can be interpreted more as an indication of the overall enrichment of the ISM of the absorber. The weakness of the Ca II line (minor ionisation state, heavily depleted) means that for the Ca II lines to be detected *at all* means there must be a significant quantity of material in the absorber either at high column densities or large volumes so that self-shielding can occur (Wild & Hewett 2005). Wild & Hewett (2005) argued strongly that their Ca II absorbers were likely some of the dustiest high-column density DLAs hence this search for DIBs in their spectra.

The non-detection of DIBs at their predicted strengths in the five targets presented here suggests that either the assumed E_{B-V} and hence DIB strength estimates are too high or that factors additional to E_{B-V} can affect the strength of the DIBs. In a complementary proposal metallicities and star formation rates of Ca II absorbers have been measured for those cases where the host is clearly visible. The metallicities of these absorbers are comparable to solar values (private communication, Michael Murphy) with the caveat that those Ca II absorbers where a host is visible are likely to be the most luminous dusty star-forming galaxies and therefore should not be considered representative of the sample as a whole.

In theory, a group of absorption-line-selected DLAs should be a more representative sample of the galaxy population in the early universe as selection effects associated with magnitude-limited galaxy surveys and dust obscuration biases should not be significant (e.g. Fall *et al.* 1989). A search for DIBs in the early universe is limited by the fact that the dustiest environments where a significant DIB carrier-population is likely to be present will be fainter than those DLAs without significant dust content. With the high-quality FORS2 spectra recorded for this project it should be possible to obtain a good measure of the amount of dust reddening of the background QSO. Combined with a careful extraction of those spectra where a foreground absorber is detected and the hence a metallicity estimate possible, it should be possible to determine with more certainty, those factors that are most significant in influencing DIB carrier abundances in these dusty DLAs.

Chapter 5

Post-AGB Stars with Dusty Discs

5.1 Introduction

A disc-like morphology is not uncommon in astrophysical objects: On the largest scales spiral galaxies like our own Milky Way resemble discs with a central bulge. On more modest scales and of more immediate interest for this work, are molecular clouds. During their collapse, conservation of angular momentum means that stars form from a rotating disc of material, the star becoming visible as the dusty disc is blown away by stellar winds and/or forms planetary systems.

There are two main populations of stars that are likely to be surrounded by a disc; young stars forming from a rotating disc of gas and dust and evolved stars where the outer layers of stellar atmospheres are lost as a consequence of low surface gravity. The weakly held outer layers of the stellar atmospheres in these evolved objects are often accreted by a binary companion or are driven out into the ISM by stellar pulsations and winds. These stars are responsible for much of the chemical enrichment of the ISM.

This Chapter is concerned with a subset of evolved exotic stars that have dusty discs. The J-silicate star IRAS 12311-3509 (Evans 1990, Lloyd Evans 1991) and post-AGB object U Equulei (U Equ, Fouque *et al.* 1992, Barnbaum *et al.* 1996, Lloyd Evans 1997b) have distinctive near- and mid-infrared (IR) colours, but their unusual spectra makes it difficult to place them within the known evolutionary tracks of post-AGB stars. Using the vast number of stars in the IRAS point source catalogue (PSC) and the near-IR 2MASS catalogue, an efficient extension of the work of Lloyd Evans (Lloyd

Evans 1997b) has been carried out to try to identify additional exotic post-AGB stars with dusty discs.

Before discussing in detail the specific set of stars under investigation a brief introduction to stellar evolution is given.

5.1.1 Stellar evolution

If a star is between 0.7 and 7 solar masses ($M_{\odot}$) then barring any cataclysmic event it will become a red giant (RG), and subsequently an AGB/post-AGB object. A star such as our own Sun will spend about 9 billion years on the main sequence (MS) before the hydrogen burning shell becomes of such a size that the star increases in size and decreases in temperature to become a red giant. Red giant stars are found on the red giant branch (RGB) running up the right-hand side of the Hertzsprung-Russell (HR) diagram and are known as 'convective' objects. This term is used as the stars have convection zones that reach down into the central regions of the star, transporting energy in the core to the surface. This convection also has a secondary effect inducing mass motion within the star. It is this mass motion that is responsible for the 'dredge up' of heavier (e.g. C, N, O) elements from deep within the stellar core to outer regions of the star.

On the RGB the primary source of energy for the star is still the nuclear fusion of hydrogen, although at progressively larger distances from the central region thus forming an ever larger helium core. Hydrogen fusion continues until a critical point in temperature and pressure when the helium core reaches such a size that helium fusion occurs; this is known as the 'helium flash'. Once a star has become a helium burner it moves down to the left on the HR diagram to join the horizontal branch (HB) and it remains there whilst there is helium burning in the core and a hydrogen burning shell. Stars on the HB develop instabilities in their outer envelopes leading to periodic pulsations of periods $\sim$ 0.5 days (RR Lyrae variables) which can be seen in the temperature, radius, etc. Stars on the HB evolve in a redward direction again towards the Hayashi Track whilst depositing carbon and oxygen (products of helium burning) into core regions. The stars follow an upward asymptotic path, hence the name given - the Asymptotic Giant Branch (AGB). Whilst on the AGB stars undergo further periodic helium flashes, although this time not in the core but in the outer layers of the star; helium deposited by the hydrogen burning shell causes periodic re-ignition of the helium layers. During these helium flashes there is a large increase in the energy coming from the helium layer causing convection between different regions of the star. Significantly, if the star is massive enough, i.e. $M > 2M_{\odot}$, then these convective regions extend downwards into the central regions of the star where carbon is synthesised and a 'third dredge-up' occurs, bringing carbon to the surface of the star. Current thinking suggests that it is this third dredge-up phase that explains why some stars acquire carbon-rich envelopes, while others remain oxygen-rich.

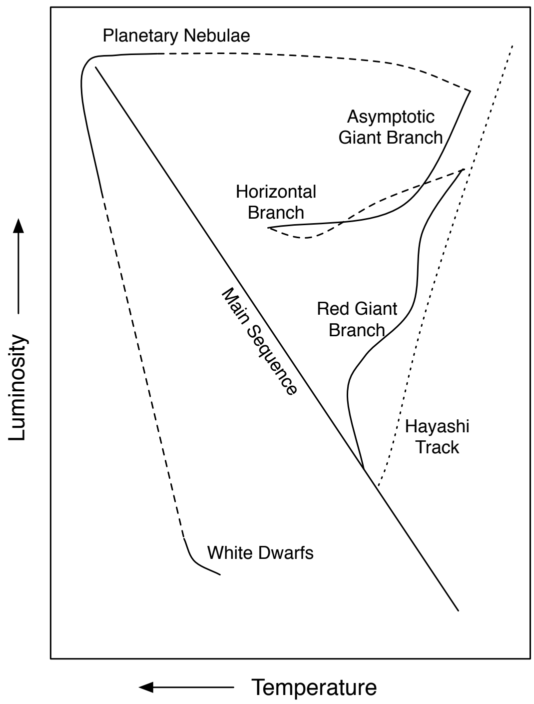

Figure 5.1: Hertzsprung-Russell diagram showing the path of a ~ 1 $M_{\odot}$ star.

Time spent on the AGB involves significant mass-loss for the star as it is many hundreds of times larger than when it was on the main sequence. Periodic pulsation combined with low surface gravity means that outer layers of the star are lost into surrounding regions. This ejected material can enshroud the star to such an extent that it becomes optically invisible and observations can only be made in the infra-red (IR) for photospheric, or microwave for circumstellar regions. A point is reached at which the star has undergone so great a mass loss that it can no-longer reside on the AGB and it becomes a post-AGB object. Post-AGB objects are stable in comparison with their AGB precursors. All significant mass-loss has ceased and the stars enter a much quieter stage in their life. The post-AGB phase is characterised by the expansion of gas and dust surrounding the star. This makes very new post-AGB objects difficult to see as they are often heavily obscured by the material ejected during the AGB phase. The rapid evolution of post-AGB stars means that they are rarely observed and the relationship between the range of post-AGB objects known poorly understood. Finding more post-AGB objects is therefore desirable.

Whilst the post-AGB phase is very short compared to the overall lifetime of the star (~10,000 years) it is one of the most interesting for astrochemistry. It is at this point that the heavier dust forming elements, once deep within the star, are able to form molecules and dust grains in the surrounding regions. As the star moves across the post-AGB branch the core heats up and irradiates the surrounding material with ever more energetic UV photons. The dissipation of the ejected material from the hot carbon/oxygen rich core of the star combined with the gradual increase in temperature of the core gives rise to a wide range of different objects.

5.1.2 Stars with discs

A wide variety of evolved stars have discs. Examples include RV Tauri stars such as those studied by Lloyd Evans 1997b, strong H-alpha emitters and some M giants. Exotic objects such as the carbon star IRAS 12311-3509 (Sarre *et al.* 1996, Lloyd Evans 1997a, Lloyd Evans *et al.* 2000) with its remarkable SiC_2 and C_2 emission have also been understood as systems with a disc; in this case the edge-on geometry of the disc is responsible for observation of the unusual emission spectrum as the starlight is observed indirectly *via* reflection off material out of the plane of the disc. Other examples of unusual objects include the stars U Equ (Fouque *et al.* 1992, Barnbaum *et al.* 1996, Lloyd Evans 1997b) and IRAS 08182-6000: (Lloyd Evans 1997b, Couch 2002, Couch *et al.* 2003) both discovered by Lloyd Evans in his search for RV Tauri objects in the IRAS Point Source Catalogue (PSC) (Lloyd Evans 1997b).

5.1.3 Identification of objects with discs - data sources

Stars with dusty discs are most readily identified by their near-IR and IR colours. The IR excess begins in the near-IR and extends to longer wavelengths (see Figure 5.2).

Identifying objects with an IR excess relies heavily upon the availability of large quantities of all-sky near-IR and IR photometry, the most significant of which are from the IRAS and 2MASS surveys.

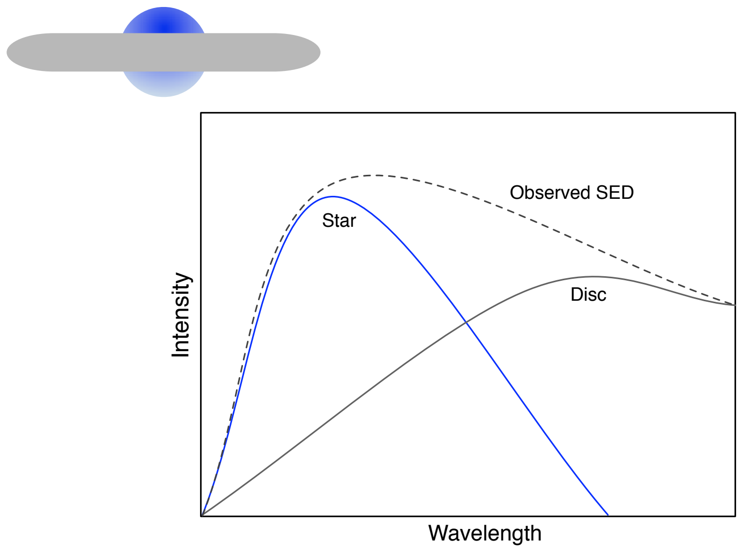

Figure 5.2: The spectral energy distribution (SED) of a star with a disc. The SED of the star is drawn in blue, the disc in grey and the sum of the two SEDs as a dashed line.

IRAS Point Source Catalog (IPSC)

In the 1970s astronomers began to consider the idea of placing an infrared telescope on a satellite in space. Such a telescope would be able to view the sky at wavelengths obscured by the Earth's atmosphere and so impossible to view with terrestrial instruments. By 1977 a international collaboration made up of scientists from the Netherlands, United States and United Kingdom had begun to develop an infrared space telescope named IRAS (The Infrared Astronomical Satellite).

After six years of development IRAS was launched on January 25 1983 and for ten months it scanned more than 96 percent of the sky four times at wavelengths of 12, 25, 60 and 100 microns. IRAS detected over 500,000 infrared sources thus increasing the number of catalogued astronomical sources by almost 70 percent.

Following the identification of more than 500,000 infrared sources, a catalogue of about 200,000 *point sources* was made. It was this catalogue (IPSC) with its unique infrared photometry, that Lloyd Evans used to construct two-colour diagrams and identified stars of an unusual nature (Lloyd Evans 1997b). This work also relied upon J, H, K and L photometry obtained at the SAAO for the near-IR colours of the programme stars.

The study presented here makes use of the 2MASS catalogue for near-IR photometry.

2MASS

Following the first large scale near-IR survey of the sky by Neugebauer & Leighton (1969: The Two Micron Sky Survey (TMSS)), nearly 6000 infrared sources were detected. This survey demonstrated the advantages of observing at infrared wavelengths. In particular, the Universe is more transparent at longer wavelengths with the selective extinction of optical flux by dust grains not affecting the longer wavelength IR photons. Following numerous subsequent near-infrared sky surveys of varying sky coverage and wavelengths and the completion of the aforementioned IRAS survey, it became apparent that a much deeper near-infrared all sky survey was required.

The University of Massachusetts and the Infrared Processing and Analysis Centre, together with The University of Arizona and The National Optical Astronomy Observatory set up the 2MASS (2 Micron All Sky Survey). This survey made calibrated observations of the entire sky at three wavelengths, J (1.24 μm), H (1.66μm) and K_s (2.16 μm) using two automated 1.3 m telescopes. With over 470,000,000 point sources detected, the 2MASS catalogue provided the near-IR photometric data required for this study.

5.1.4 Identification of objects with discs - methodology

With the advent of large all-sky IR surveys such as IRAS and 2MASS, the circumstellar environment of stars can be characterised by their IR colours and also by their IRAS LRS (Low Resolution Spectrograph) spectrum. Identification of the 10 μm silicate feature and whether it is found to be in emission or absorption has allowed classification of stars by their LRS spectrum - the presence of a 10 μm silicate absorption feature indicating the presence of a thick dust envelope. More directly related to this work is the classification of sources by their IR colours.

An alternative approach was used by Lloyd Evans (1997b), who demonstrated that by using the IRAS satellite measured fluxes at 12, 25, 60 and 100 μm, a two-colour plot of [12]-[25] against [25]-[60] could be used to classify stars. In particular the evolved RV Tauri stars[1] were shown to fall in a specific area of the the two-colour diagram. It was during this work that stars including the carbon star IRAS 12311-3509, IRAS 08182-6000 and U Equ were identified by their similar IRAS colours to RV Tauri stars and also by their near-IR excesses - indicating the presence of dusty discs (1997b).

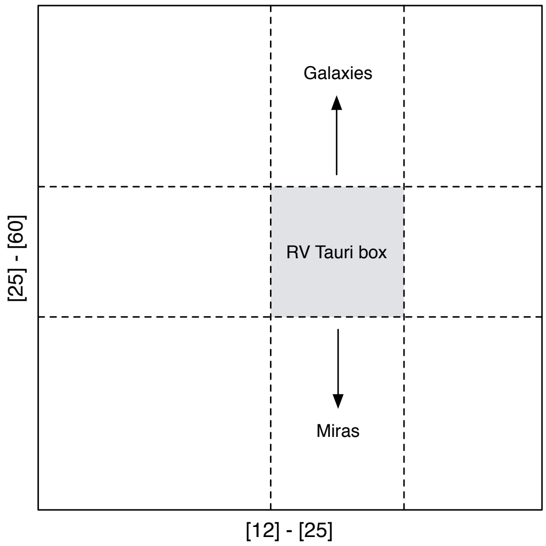

Figure 5.3: The IRAS two-colour diagram showing the location of the RV Tauri 'box' as described in Lloyd Evans (1997b).

Figure 5.3 shows the IRAS [12]-[25], [25]-[60] diagram and the position that the stars with colours similar to RV Tauri stars occupy compared to Mira variables and galaxies. The IRAS [12]-[25] & [25]-[60] colours are defined as follows:

$$[12] - [25] = 1.56 + 2.5 \log \frac{F_{25}}{F_{12}}$$

$$[25] - [60] = 1.88 + 2.5 \log \frac{F_{60}}{F_{25}}$$

where F_{12} is the IRAS 12 μm flux in Janskys. The correction for source temperature has not been applied to the observed fluxes in deriving these colours (1997b). In his original Lloyd Evans (1997b) survey, J, H , K and L photometry was undertaken in the search for objects of potential interest. It was found that the most interesting have an

[1]RV Tauri stars are a class of luminous variable supergiant with light curves showing alternating deep and shallow minima.

IR excess at L relative to the fiducial line for Miras (dusty objects without a disc, see Figure 5.4). Hence, in principle the 2MASS photometry can be used to select objects with an IR excess at K_s and hence identify potential objects of interest.

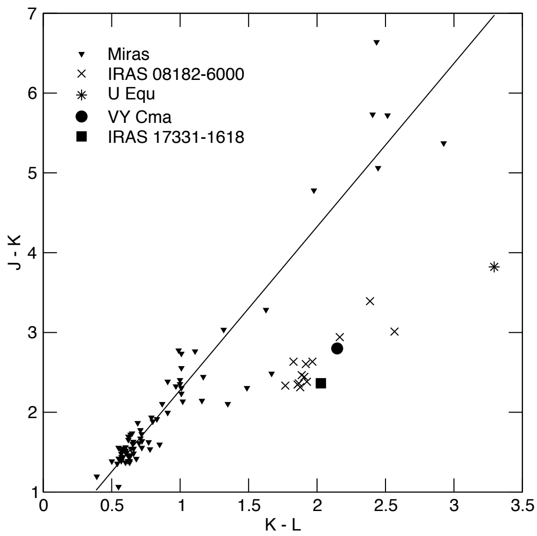

Figure 5.4: Near-IR two-colour plot demonstrating the excess in the L-band for those objects with discs compared to the normal colours of dusty Miras.

IRAS 12311-3509 (Sarre *et al.* 1996, Lloyd Evans 1997a, Lloyd Evans *et al.* 2000), U Equ (Fouque *et al.* 1992, Barnbaum *et al.* 1996, Lloyd Evans 1997b) and IRAS 08182-6000 (Lloyd Evans 1997b, Couch 2002, Couch *et al.* 2003) were all found to have unusual optical spectra (Sarre *et al.* 1996, Couch *et al.* 2003, Lloyd Evans *et al.* 2000). The carbon star IRAS 12311-3509 is unusual in that the Merrill-Sanford SiC_2 bands are seen in *emission* together with some Group I metals (Na, K, Rb). This remarkable spectrum can be explained by the light from the star being obscured by an edge-on disc, atomic and molecular species being identified through resonant scattering off gas lying out of the plane of the disc. U Equ and IRAS 08182-6000 were found to have very narrow TiO bands; in emission in U Equ and absorption in IRAS 08182-6000. Subsequent modeling of the TiO spectral features in these targets (Couch 2002, Couch *et al.* 2003, Hunter 2004) showed that the circumstellar (CS) environments of these stars is highly unusual with the TiO being at a temperature below that normally found in CS regions and well below that of the condensation temperature of TiO (~ 1600 K). Whilst both U Equ and IRAS 08182-6000 are thought to be post-AGB, it is clear that they are highly unusual stars (Couch 2002, Couch *et al.* 2003, Hunter 2004). Due to the relatively short lifetime of post-AGB stars (~ 10,000 yrs) they may represent an important phase in the evolution of post-AGB objects and so finding more stars of this type is therefore highly desirable.

5.2 Survey

In a survey of the IPSC for RV Tauri stars, (Lloyd Evans 1997b) the following criteria were used to select targets of potential interest:

I. Position in the two-colour IRAS [12]-[25], [25]-[60] diagram.

II. Near-IR excess at K (2.1 μm) and L (3.45 μm) compared to 'normal' near IR colours of sources without a disc.

III. A bright optical counterpart to the IR source. A star with the [12]-[25], [25]-[60] colour of a RV Tauri star, a near-IR excess and a bright optical counterpart is likely to be of interest for this study.

IV. Removal of objects with a high probability of variability (Miras) and checking for quality of flux data and various IRAS warning flags.

It was using these criteria the exotic objects U Equ and IRAS 08182-6000 were found aswell as a number of new RV Tauri stars (Lloyd Evans 1999). The number of targets selected was severely limited by the availability of good quality IRAS photometry at 60 μm.

Two different approaches have been used to increase the sample size. The methods employed are outlined below:

5.2.1 Selection by IRAS [12]-[25], [25]-[60] colour

Selecting targets by mid-IR ([12]-[25] & [25]-[60]) colour relies heavily upon the quality of the IRAS photometry. IRAS photometric data are categorised as 1, 2 or 3 (3 being the highest quality). Factors including the signal-to-noise, number of repeat observations and IR cirrus contamination affect the final quality of the data. There are also a number quality 'flags' assigned to those targets where the data quality gives cause for concern. Given the large number of targets in the ISPSC (~ 250,000), in the earlier work only those targets with quality category 3 for all three (12, 25, 60 μm) wavebands were considered. An obvious extension of this original study was to consider those targets where the quality of the IRAS data was less satisfactory , i.e. the 60 μm photometry was lacking, but for which it was possible to use near-IR data (2MASS) to establish the existence of an excess at K_s and $K_s-12 > 5.0$, a typical value for RV Tauri stars.

For the initial search of the IPSC, software was written to search the full catalogue based on criteria of [12]-[25] & [25]-[60] colour, the brightness of the target, photometric data quality and percentage likelihood of variability. The colour range was set to $0.9 <$ [12]-[25] < 1.9 and $0.2 <$ [25]-[60] < 1.0 and probability of variability to $< 50\%$. These limits produce a list of ~ 1000 targets within a given range in Right Ascension (RA) and Declination (Dec) suitable for a particular site at a given time of year (see Figure 5.5).

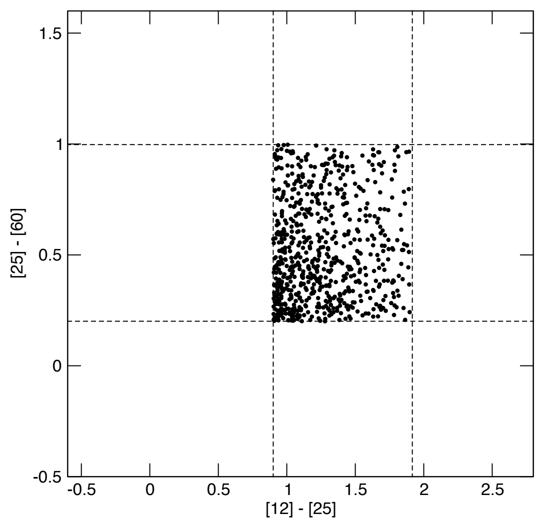

Figure 5.5: A plot demonstrating the distribution of IRAS colours for those targets selected from the IRAS catalogue.

For each of the IRAS targets selected further criteria were then applied to remove less promising targets: 2MASS near-IR photometry was obtained for the IRAS sources and a plot of J-H vs. H-K was made in order to detect those targets possessing a near IR excess (a characteristic of previous targets of interest). A visual inspection of Digitised

Sky Survey (DSS) V, R and I band images was made to check the optical colours of the star. Once all criteria, including a final check of the GCVS (General Catalogue of Variable Stars) and the list of stars already considered by Lloyd Evans had been applied, approximately 30 stars remained that were deemed suitable for a follow up spectroscopic investigation.

5.2.2 Selection by near-IR colour excess

Given that in the original survey of the IPSC *all* of the targets of interest within the RV Tauri 'box' possessing quality 3 data in all three wavebands were selected, an extension of the survey relied on relaxing the limits on flux quality and therefore increasing the number of 'unwanted' IR sources. The availability of all-sky near-IR photometry (2MASS) and DSS images allowed for removal of those targets not of immediate interest such as galaxies and ordinary M stars.

Once the criteria had been set and the software written the automated selection of targets from the IPSC was rapid. The most time consuming step in the process of producing a target list was identifying 2MASS sources[2] that matched the position of the IRAS targets. In order to search for near-IR excesses, a search for 2MASS targets within a 15″ radius of the IRAS position (typical difference in 2MASS and IRAS positions ~ 5″) was made. The IPSC contains ~ 250,000 IR sources, a number dwarfed by the much more sensitive 2MASS telescopes and the ~ 470,000,000 near-IR point source targets detected. A search within 15″ of the IRAS position often resulted in numerous possible near-IR sources matching the IRAS source. Identifying the correct target for many hundreds of IRAS sources was therefore a time consuming process.

In an attempt to search for targets in a more efficient fashion new software was written by the author to search the 2MASS catalogue directly for targets with a near-IR excess (see Figure 5.7). Searching the ~ 470,000,000 near-IR targets for an excess in K_s relative to the fiducial line for Mira variables (see Figure 5.6) produces a large list of potential targets of interest. Applying lower limits to the J band magnitude so that observations would be feasible on the chosen telescope and requiring an optical

[2]The online tool 'Gator' was used to obtain 2MASS photometry. Gator is part of the NASA/ IPAC Infrared Science Archive, which is operated by the Jet Propulsion Laboratory, California Institute of Technology, under contract with the National Aeronautics and Space Administration.

identification[3] of the 2MASS target significantly reduces the number of targets initially selected.

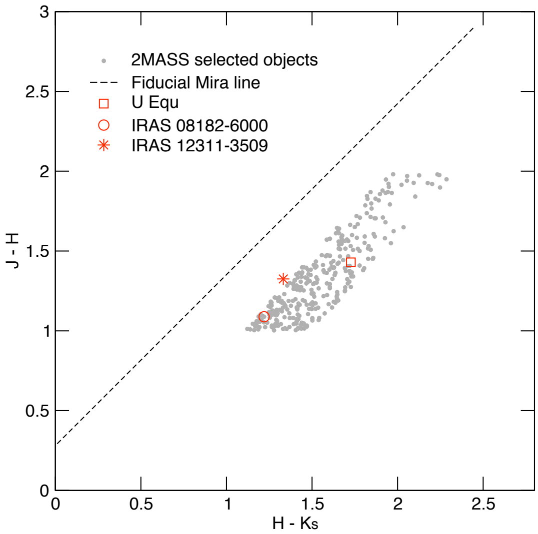

Figure 5.6: A plot demonstrating the selection of targets from the 2MASS catalogue based upon their near-IR excess relative to the fiducial Mira line.

Once the 2MASS targets had been identified, a search was made of the IPSC for the positions within 15″ radius of the 2MASS target. Given the lower limit in 2MASS J-band magnitude and the much smaller size of the IPSC, often only one IRAS target was found to match the position of the 2MASS target. Selections were then made based upon IRAS [12]-[25] colour (see Figure 5.5), probability of variability and an additional criterion of K_s-[12][4] > 5.0; the last of these a common feature of stars with dusty discs. Many targets were also rejected because of poor 2MASS photometry, with rare exceptions, only targets with 2MASS quality flags AAA were retained. After manual inspection of the DSS images, a final step in the refinement was to calculate the [25]-[60] colour of the selected targets. Given that the 60 μm flux for the majority of the targets selected (and not previously observed by Lloyd Evans) was poor, targets were *not* removed from the observing list if the [25]-[60] colour was outside the limits.

This alternative method for searching for potential objects of interest by searching directly for the near-IR excess was significantly more computationally intensive. As the

[3]2MASS targets are cross correlated by position with the TYCHO2 and USNO-A2.0 optical catalogues.

[4]The colour $K_s - [12]$ is defined as: $K_s - [12] = K_s - (3.63 + 2.5 \log F_{12})$

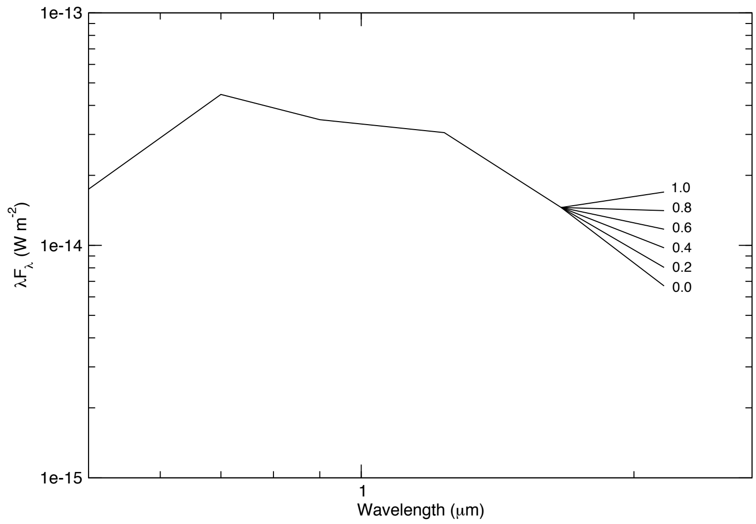

Figure 5.7: A sample SED plot demonstrating the effect of varying excesses in the K_s photometric band.

2MASS catalogue is split into 400MB zipped text files, each had to be un-compressed, analysed and then re-compressed to conserve computer hard disk space. Once the initial search had been made the application of further search criteria was significantly easier than when objects were searched for in the IPSC. The exact number of targets selected depended on the search criteria. Typically $\sim$ 3000 targets were initially selected from 2MASS, with $\sim$ 150 remaining (and deemed suitable for observation) once other criteria had been applied.

5.3 Observations

Data for this Chapter were recorded on the 1.9m Radcliffe Telescope at the Sutherland Observatory of the South African Astronomical Observatory (SAAO) using the Grating Spectrograph. Fourteen nights of telescope time were awarded to the project, the observations being made on two separate occasions; March 2004 and June 2005. Observations were made by the author and Dr. June McCombie for the 2004 run and the author and Dr. Tom Lloyd Evans in 2005.

The focus of these observations was to record spectra of a large number of targets in the most efficient mode possible. Low resolution spectra were recorded with sufficient S/N that distinctive signatures seen previously in objects such as the narrow TiO molecular bands of IRAS 08182-6000 or atomic emission lines in IRAS 12311-3509 could be identified. It was also important that the spectral regions recorded were sufficient for classification of the spectral types of the different stars observed.

Table 5.1 lists the grating configurations used and Table 5.2 the observations made in 2004 and 2005.

Grating	Grating Angle	λ Range (Å)	Blaze (Å)	Resolution (Å)
8	14°34′	4800-7700	7800	4
8	12°46′	6400-9100	7800	4
7	17°36′	3300-7100	4600	5
4	3°30′	4550-5400	4600	1

Table 5.1: A list of the gratings used in the Grating Spectrograph on the 1.9m Radcliffe telescope at the SAAO Sutherland observing site.

Target Name	RA(J2000)	Dec(J2000)	Date	Grating	Grating Angle	λ Range (Å)	Exp time (s)	R mag	[12]-[25]	K_s-[12]
				2004						
IRAS 06476-1114	06 50 02	-11 18 14	2004-03-10/11	Gr #8	14°34′	4800-7700	1000	15.9	1.31	6.77
IRAS 07377-2523	07 39 48	-25 30 28	2004-03-10/11	Gr #8	14°34′	4800-7700	1000	12.4	1.70	5.94
IRAS 08456-5216	08 05 47	-52 29 27	2004-03-10/11	Gr #8	14°34′	4800-7700	1000	13.5	1.94	5.92
IRAS 09258-6125	09 27 09	-61 38 16	2004-03-10/11	Gr #8	14°34′	4800-7700	1500	13.9	1.73	6.37
IRAS 10464-5935	10 48 27	-59 51 12	2004-03-10/11	Gr #8	14°34′	4800-7700	1500	–	1.81	6.19
IRAS 10545-6058	10 56 32	-61 14 09	2004-03-10/11	Gr #8	14°34′	4800-7700	1500	14.7	1.33	5.97
IRAS 11467-7003	11 08 49	-70 31 20	2004-03-10/11	Gr #8	14°34′	4800-7700	1500	13.9	1.86	6.12
IRAS 12400-6458	12 43 02	-65 14 35	2004-03-10/11	Gr #8	14°34′	4800-7700	1500	14.6	3.05	3.34
IRAS 12421-6217	12 45 07	-62 33 36	2004-03-10/11	Gr #8	14°34′	4800-7700	1500	12.0	1.32	9.53
IRAS 06126-0628	06 15 02	-06 29 25	2004-03-11/12	Gr #8	14°34′	4800-7700	1500	15.0	2.38	4.29
IRAS 07298-2228	07 31 57	-22 34 44	2004-03-11/12	Gr #8	14°34′	4800-7700	1800	–	2.05	4.59
IRAS 08425-4115	08 44 24	-41 26 04	2004-03-11/12	Gr #8	14°34′	4800-7700	1800	13.8	1.47	4.90
IRAS 09027-5325	09 04 13	-53 37 53	2004-03-11/12	Gr #8	14°34′	4800-7700	1800	–	0.27	3.95
IRAS 12421-6217	12 45 07	-62 33 36	2004-03-11/12	Gr #8	14°34′	4800-7700	1200	12.0	1.32	9.53
IRAS 13190-6704	13 22 32	-67 20 17	2004-03-11/12	Gr #8	14°34′	4800-7700	1800	12.1	1.19	6.84
IRAS 13317-6127	13 35 10	-61 43 06	2004-03-11/12	Gr #8	14°34′	4800-7700	1800	14.6	1.10	5.81
IRAS 14463-6300	14 50 24	-63 12 35	2004-03-11/12	Gr #8	14°34′	4800-7700	1800	14.1	1.18	5.63
IRAS 16497-4447	16 53 25	-44 52 53	2004-03-11/12	Gr #8	14°34′	4800-7700	1800	13.3	1.55	6.86
IRAS 16572-4037	17 00 43	-40 42 02	2004-03-11/12	Gr #8	14°34′	4800-7700	1800	15.0	1.54	7.11
IRAS 17034-3838	17 06 55	-38 42 19	2004-03-11/12	Gr #8	14°34′	4800-7700	1500	15.9	1.16	7.10
IRAS 08208-3330	08 22 47	-33 43 10	2004-03-12/13	Gr #8	14°34′	4800-7700	1800	13.9	0.80	4.85
IRAS 05307-6410	05 31 05	-64 08 31	2004-03-12/13	Gr #8	14°34′	4800-7700	1800	16.2	1.83	5.32
IRAS 07469-1806	07 49 11	-18 13 41	2004-03-12/13	Gr #8	14°34′	4800-7700	1800	15.6	0.62	5.61
IRAS 10082-5650	10 10 00	-57 04 52	2004-03-12/13	Gr #8	14°34′	4800-7700	1800	13.7	1.49	5.98
IRAS 12212-6115	12 24 00	-61 32 29	2004-03-12/13	Gr #8	14°34′	4800-7700	1500	–	0.76	5.17

Table 5.2: Detailed listings of the observations carried out during the 2004 and 2005 observing runs.

Target Name	RA(J2000)	Dec(J2000)	Date	Grating	Grating Angle	λ Range (Å)	Exp time (s)	R mag	[12]-[25]	K_s-[12]
IRAS 13508-6118	13 54 23	-61 33 26	2004-03-12/13	Gr #8	14°34′	4800-7700	1800	17.6	1.10	8.21
IRAS 13051-8408	13 10 56	-84 09 24	2004-03-12/13	Gr #8	14°34′	4800-7700	1800	15.7	1.37	6.01
IRAS 14465-6041	14 50 27	-60 53 23	2004-03-12/13	Gr #8	14°34′	4800-7700	1800	15.1	1.40	7.18
IRAS 16315-4642	16 35 13	-46 48 58	2004-03-12/13	Gr #8	14°34′	4800-7700	1800	14.3	1.00	6.17
IRAS 16329-4649	16 36 36	-46 55 32	2004-03-12/13	Gr #8	14°34′	4800-7700	1800	17.0	1.87	8.95
IRAS 12225-6050	12 25 18	-61 07 20	2004-03-12/13	Gr #8	14°34′	4800-7700	1800	13.9	1.23	5.25
IRAS 16521-4257	16 55 44	-43 02 33	2004-03-12/13	Gr #8	14°34′	4800-7700	1800	16.4	1.60	4.36
IRAS 16521-4311	16 55 40	-43 16 03	2004-03-12/13	Gr #8	14°34′	4800-7700	1800	14.3	1.73	6.28
IRAS 16569-4512	17 00 38	-45 17 20	2004-03-12/13	Gr #8	14°34′	4800-7700	1800	14.4	1.05	6.81
IRAS 06126-0628	07 31 57	-22 34 44	2004-03-13/14	Gr #8	12°46′	6400-9100	1800	15.0	2.38	4.29
IRAS 06476-1114	06 01 50	-11 14 18	2004-03-13/14	Gr #8	12°46′	6400-9100	3000	15.9	1.31	6.77
IRAS 07298-2228	07 31 57	-22 34 45	2004-03-13/14	Gr #8	12°46′	6400-9100	1800	–	2.05	4.59
IRAS 07377-2523	07 48 39	-25 28 30	2004-03-13/14	Gr #8	12°46′	6400-9100	1800	12.4	1.70	5.95
IRAS 08208-3330	08 22 47	-33 40 10	2004-03-13/14	Gr #8	12°46′	6400-9100	1800	13.9	0.80	4.85
IRAS 08425-4115	08 44 24	-41 26 04	2004-03-13/14	Gr #8	12°46′	6400-9100	1800	13.8	1.47	4.90
IRAS 09258-6125	09 27 09	-61 38 14	2004-03-13/14	Gr #8	12°46′	6400-9100	1800	13.9	1.18	6.37
IRAS 10082-5650	10 10 00	-57 04 52	2004-03-13/14	Gr #8	12°46′	6400-9100	1800	13.7	1.49	5.98
IRAS 11467-7003	11 49 09	-70 20 03	2004-03-13/14	Gr #8	12°46′	6400-9100	1800	13.9	1.86	6.12
IRAS 12212-6115	11 24 00	-61 32 29	2004-03-13/14	Gr #8	12°46′	6400-9100	1800	–	0.76	5.17
IRAS 13317-6127	13 35 10	-61 43 03	2004-03-13/14	Gr #8	12°46′	6400-9100	1800	14.6	1.10	5.81
IRAS 16497-4447	16 53 25	-44 52 53	2004-03-13/14	Gr #8	12°46′	6400-9100	1800	13.3	1.55	6.86
IRAS 16521-4257	16 55 43	-43 02 34	2004-03-13/14	Gr #8	12°46′	6400-9100	1800	16.4	1.60	7.36
IRAS 09540-5553	09 55 47	-56 07 55	2004-03-14/15	Gr #8	12°46′	6400-9100	600	14.5	0.59	3.13
IRAS 09584-4418	10 00 27	-44 33 19	2004-03-14/15	Gr #8	12°46′	6400-9100	1200	13.6	0.38	3.83
IRAS 11030-4942	11 05 17	-49 58 57	2004-03-14/15	Gr #8	12°46′	6400-9100	1200	12.2	1.23	4.06
IRAS 11556-6433	11 10 58	-64 49 53	2004-03-14/15	Gr #8	12°46′	6400-9100	1200	12.2	0.51	4.00

Table 5.2: Detailed listings of the observations carried out during the 2004 and 2005 observing runs.

Target Name	RA(J2000)	Dec(J2000)	Date	Grating	Grating Angle	λ Range (Å)	Exp time (s)	R mag	[12]-[25]	K_s-[12]
IRAS 14038-5909	14 07 22	-59 23 31	2004-03-14/15	Gr #8	12°46′	6400-9100	1200	15.7	0.93	4.98
IRAS 14122-5845	14 15 50	-58 59 18	2004-03-14/15	Gr #8	12°46′	6400-9100	1200	–	0.51	3.50
IRAS 14158-5050	14 19 12	-51 03 50	2004-03-14/15	Gr #8	12°46′	6400-9100	1200	12.1	0.87	3.47
IRAS 15180-5547	15 21 49	-55 58 43	2004-03-14/15	Gr #8	12°46′	6400-9100	1200	11.5	1.17	5.42
IRAS 16041-2332	16 07 08	-23 40 12	2004-03-14/15	Gr #8	12°46′	6400-9100	1500	13.7	2.40	4.02
IRAS 16090-4629	16 12 37	-46 37 37	2004-03-14/15	Gr #8	12°46′	6400-9100	1800	13.3	0.85	3.09
IRAS 16321-2512	16 35 11	-25 18 29	2004-03-14/15	Gr #8	12°46′	6400-9100	900	12.5	0.90	2.75
IRAS 16465-4129	16 50 04	-41 34 44	2004-03-14/15	Gr #8	12°46′	6400-9100	1200	13.8	1.36	4.36
IRAS 16446-1520	16 47 30	-15 25 23	2004-03-14/15	Gr #8	12°46′	6400-9100	1200	12.8	0.59	5.11
IRAS 16475-4658	16 51 15	-47 03 53	2004-03-14/15	Gr #8	12°46′	6400-9100	900	11.7	1.11	5.19
IRAS 17126-3812	17 16 02	-38 15 43	2004-03-14/15	Gr #8	12°46′	6400-9100	600	12.2	0.75	5.05
IRAS 16471-4650	16 50 50	-46 55 10	2004-03-15/16	Gr #8	12°46′	6400-9100	1800	–	1.23	7.07
IRAS 16518-4243	16 53 24	-42 48 21	2004-03-15/16	Gr #8	12°46′	6400-9100	1200	13.3	2.82	5.50
IRAS 16156-6605	16 20 27	-66 12 19	2004-03-15/16	Gr #8	12°46′	6400-9100	600	14.7	1.44	4.98
					2005					
IRAS 12497-5603	12 52 40	-56 19 25	2005-06-28/29	Gr #7	17°36′	3300-7100	3600	16.2	1.08	4.60
IRAS 15157-6054	15 19 48	-61 05 14	2005-06-28/29	Gr #7	17°36′	3300-7100	1500	12.0	1.34	5.19
IRAS 16011-5145	16 04 54	-51 53 13	2005-06-28/29	Gr #7	17°36′	3300-7100	1800	12.9	1.52	4.64
IRAS 17200-1355	17 22 51	-13 58 45	2005-06-28/29	Gr #7	17°36′	3300-7100	4800	14.0	1.70	5.50
IRAS 18372-0247	18 39 53	-02 44 21	2005-06-28/29	Gr #7	17°36′	3300-7100	2400	12.1	1.65	6.04
IRAS 00350-7436	00 37 00	-74 19 47	2005-06-28/29	Gr #7	17°36′	4450-5400	4000	14.0	1.23	5.32
IRAS 09258-6125	09 27 09	-61 38 16	2005-06-29/30	Gr #7	17°36′	3300-7100	2700	13.9	1.73	6.37
IRAS 15500-4917	15 53 40	-49 26 13	2005-06-29/30	Gr #7	17°36′	3300-7100	5400	13.9	1.27	5.66
IRAS 17339-2821	17 37 07	-28 23 23	2005-06-29/30	Gr #7	17°36′	3300-7100	2400	13.5	1.27	5.17
IRAS 17378-1446	17 40 40	-14 47 36	2005-06-29/30	Gr #7	17°36′	3300-7100	1800	14.2	1.13	6.19
IRAS 19094+0006	19 11 58	+00 11 51	2005-06-29/30	Gr #7	17°36′	3300-7100	1800	12.7	1.74	6.30

Table 5.2: Detailed listings of the observations carried out during the 2004 and 2005 observing runs.

Target Name	RA(J2000)	Dec(J2000)	Date	Grating	Grating Angle	λ Range (Å)	Exp time (s)	R mag	[12]-[25]	K_s-[12]
IRAS 20057+1507	20 08 05	+15 16 43	2005-06-29/30	Gr #7	17°36′	3300-7100	3000	11.6	1.08	5.25
IRAS 18254-1038	18 28 16	-10 36 10	2005-06-29/30	Gr #7	17°36′	3300-7100	1800	15.2	1.64	5.36
IRAS 00350-7436	00 37 00	-74 19 47	2005-06-29/30	Gr #4	3°30′	4450-5400	3500	14.0	1.23	5.32
IRAS 13051-8408	13 10 56	-84 24 09	2005-07-01/02	Gr #7	17°36′	3300-7100	4800	15.7	1.37	6.01
IRAS 16429-3109	16 46 12	-31 15 18	2005-07-01/02	Gr #7	17°36′	3300-7100	300	–	1.05	5.14
IRAS 18280-1201	18 30 51	-11 59 37	2005-07-01/02	Gr #7	17°36′	3300-7100	2400	14.5	1.67	6.94
IRAS 18418-0951	18 44 39	-09 48 01	2005-07-01/02	Gr #7	17°36′	3300-7100	1200	13.6	1.62	5.68
IRAS 18322-1345	18 35 07	-13 43 18	2005-07-01/02	Gr #7	17°36′	3300-7100	1800	15.8	1.49	4.67
IRAS 18486-0435	18 51 18	-04 31 37	2005-07-01/02	Gr #7	17°36′	3300-7100	1800	–	1.49	5.68
IRAS 19285+1620	19 30 47	+16 27 16	2005-07-01/02	Gr #7	17°36′	3300-7100	1800	13.7	1.06	5.40
IRAS 18422+0621	18 44 41	+06 24 58	2005-07-01/02	Gr #7	17°36′	3300-7100	1800	–	1.37	6.02
IRAS 20282+1756	20 30 29	+18 06 27	2005-07-01/02	Gr #7	17°36′	3300-7100	1800	14.3	1.11	5.33
IRAS 19521+0515	19 54 40	+05 23 53	2005-07-01/02	Gr #7	17°36′	3300-7100	1800	13.7	1.56	6.18
IRAS 00350-7436	00 37 00	-74 19 47	2005-07-01/02	Gr #4	3°30′	4450-5400	7500	14.0	1.23	5.32
IRAS 09260-5238	09 27 40	-52 51 19	2005-07-02/03	Gr #7	17°36′	3300-7100	4800	14.2	1.63	6.91
IRAS 17495-3303	17 52 50	-33 04 19	2005-07-02/03	Gr #7	17°36′	3300-7100	2400	16.6	1.58	8.26
IRAS 18302-0450	18 32 57	-04 47 42	2005-07-02/03	Gr #7	17°36′	3300-7100	2400	15.2	1.43	5.98
IRAS 19157-0355	19 18 21	-03 49 45	2005-07-02/03	Gr #7	17°36′	3300-7100	2400	15.6	1.19	5.07
IRAS 18526+0612	18 55 05	+06 16 37	2005-07-02/03	Gr #7	17°36′	3300-7100	2400	16.3	1.76	5.56
IRAS 19029+0933	19 05 22	+09 38 23	2005-07-02/03	Gr #7	17°36′	3300-7100	2400	14.6	1.40	7.58
IRAS 19078+0647	19 10 17	+06 52 58	2005-07-02/03	Gr #7	17°36′	3300-7100	2400	15.3	1.43	5.06
IRAS 00350-7436	00 37 00	-74 19 47	2005-07-02/03	Gr #4	3°30′	4450-5400	6000	14.0	1.23	5.32
IRAS 15500-4917	15 53 40	-49 26 13	2005-07-03/04	Gr #8	12°45′	6400-9100	2400	13.9	1.27	5.66
IRAS 17331-1618	17 36 03	-16 20 43	2005-07-03/04	Gr #8	12°45′	6400-9100	900	13.7	1.76	6.86
IRAS 17200-1355	17 22 51	-13 58 45	2005-07-03/04	Gr #8	12°45′	6400-9100	1200	14.0	1.70	5.50
IRAS 17339-2821	17 37 07	-28 23 23	2005-07-03/04	Gr #8	12°45′	6400-9100	1200	13.5	1.27	5.17

Table 5.2: Detailed listings of the observations carried out during the 2004 and 2005 observing runs.

Target Name	RA(J2000)	Dec(J2000)	Date	Grating	Grating Angle	λ Range (Å)	Exp time (s)	R mag	[12]-[25]	K_s-[12]
IRAS 17378-1446	17 40 40	-14 47 36	2005-07-03/04	Gr #8	12°45′	6400-9100	1200	14.2	1.13	6.19
IRAS 18254-1038	18 28 16	-10 36 10	2005-07-03/04	Gr #8	12°45′	6400-9100	1200	15.2	1.64	5.36
IRAS 18372-0247	18 39 53	-02 44 21	2005-07-03/04	Gr #8	12°45′	6400-9100	900	12.1	1.65	6.04
IRAS 18422+0621	18 44 41	+06 24 58	2005-07-03/04	Gr #8	12°45′	6400-9100	1800	–	1.37	6.02
IRAS 20057+1507	20 08 05	+15 16 43	2005-07-03/04	Gr #8	12°45′	6400-9100	1200	11.6	1.08	5.25
IRAS 19094+0006	19 11 58	+00 11 52	2005-07-03/04	Gr #8	12°45′	6400-9100	1200	12.7	1.74	6.30
IRAS 18322-1345	18 35 07	-13 43 18	2005-07-03/04	Gr #8	12°45′	6400-9100	1800	15.8	1.34	5.45
IRAS 00350-7436	00 37 00	-74 19 47	2005-07-03/04	Gr #4	3°30′	4450-5400	5400	14.0	1.23	5.32
IRAS 09258-6125	09 27 09	-61 38 16	2005-07-04/05	Gr #8	12°45′	6400-9100	1800	13.9	1.73	6.37
IRAS 09260-5238	09 27 40	-52 51 19	2005-07-04/05	Gr #8	12°45′	6400-9100	1800	14.2	1.63	6.91
IRAS 12225-6050	12 25 18	-61 07 20	2005-07-04/05	Gr #8	12°45′	6400-9100	1000	13.9	1.23	5.25
IRAS 13051-8408	13 10 56	-84 24 09	2005-07-04/05	Gr #8	12°45′	6400-9100	1800	15.7	1.37	6.01
IRAS 15157-6054	15 19 48	-61 05 14	2005-07-04/05	Gr #8	12°45′	6400-9100	800	12.0	1.34	5.19
IRAS 16011-5145	16 04 54	-51 53 13	2005-07-04/05	Gr #8	12°45′	6400-9100	1800	12.9	1.52	4.65
IRAS 18280-1201	18 30 51	-11 59 38	2005-07-04/05	Gr #8	12°45′	6400-9100	1800	14.5	1.67	6.94
IRAS 18486-0435	18 51 18	-04 31 37	2005-07-04/05	Gr #8	12°45′	6400-9100	1800	–	1.49	5.68
IRAS 17495-3303	17 52 50	-33 04 19	2005-07-04/05	Gr #8	12°45′	6400-9100	1800	16.6	1.58	6.34
IRAS 19029+0933	19 05 22	+09 38 23	2005-07-04/05	Gr #8	12°45′	6400-9100	2400	14.6	1.40	7.58
IRAS 19521+0515	19 54 40	+05 23 53	2005-07-04/05	Gr #8	12°45′	6400-9100	2400	13.7	1.56	6.18
IRAS 19285+1620	19 30 47	+16 27 16	2005-07-04/05	Gr #8	12°45′	6400-9100	2400	13.7	1.06	5.40
IRAS 00350-7436	00 37 00	-74 19 47	2005-07-04/05	Gr #4	3°30′	4450-5400	4300	14.0	1.23	5.32

Table 5.2: Detailed listings of the observations carried out during the 2004 and 2005 observing runs.

5.4 Results and discussion

Fifty-one stars were observed in 2004 and thirty-nine in 2005 giving a total sample size of ninety objects. The focus of the initial observations were on the yellow (4800 – 7700 Å) spectral regions using Grating 8 at an angle of 14°34′. This relatively narrow spectral region allows for easy identification of emission features (e.g. Na D lines, indicative of a edge-on disc) or narrow molecular features (e.g. TiO, unusual CS environment), but does not provide sufficient wavelength coverage for formal spectral-type classification of the stars. Further spectra were recorded in the blue (Gr #7 17°36′, 3300 – 7100 Å) and/or red (Gr #8 12°46′, 6400 – 9100 Å) for a significant fraction of the stars observed so that their spectral type could be determined.

The selection criteria used to search the IRAS and 2MASS catalogues were tailored to the distinctive colours of the peculiar stars already known (IRAS 12311-3509, IRAS 08186-6000. U Equ etc., see section 5.1.4). Whilst the criteria applied are characteristic of these targets they do not uniquely identify them and so objects with similar near- and mid-IR colours invariably contaminate the sample set.

Of the 90 objects observed it has been possible to identify the spectral type or at least constrain the likely nature of the source for 48 of the stars. None of the $\sim$ 90 objects observed displayed narrow molecular bands of TiO (IRAS 08182-6000, U Equ) or emission bands of C_2 (IRAS 12311-3509) although many targets did show emission features including the Na I D lines (5890 & 5896 Å), K I (7699 Å) and H-α (6563 Å).

5.4.1 Na I D emission line targets

Four targets were found to have Na I D emission lines with two having K I emission also. The Na I D emission line targets are listed in Table 5.3 together with the parameters used to select the targets and spectral type classifications[5].

Lloyd Evans *et al.* (2000) identified atomic emission lines (Na, K, Rb, Ca) in the spectrum of the carbon star IRAS 12311-3509. The origin of these emission features can be explained as a ‘resonance fluorescence’ effect whereby the central star is hidden by the edge-on disc; the star seen by reflection of starlight off material out of the plane

[5]Spectral type classifications were performed by Dr. Tom Lloyd Evans.

IRAS	[12] - [25]	[25] - [60]	K_s - [12]	Na D	K I	Spec
09258-6125	1.73	1.18	6.37	Y	Y	F8Ibe
11467-7003	1.19	1.46	6.12	Y	N	A2Ib/A5III
13051-8408	1.37	0.87	6.01	Y	Y	M5Ve
19521+0515	1.55	1.00	6.18	Y	N	A3Ia

Table 5.3: Stars with Na I D lines in emission identified in this project.

of the disc (see Figure 5.8). Light from the central star pumps an electron from a lower atomic energy energy level to an excited upper level. Subsequent relaxation (fluorescence) back down to the lower energy level scatters photons in all directions therefore giving rise to the emission lines observed.

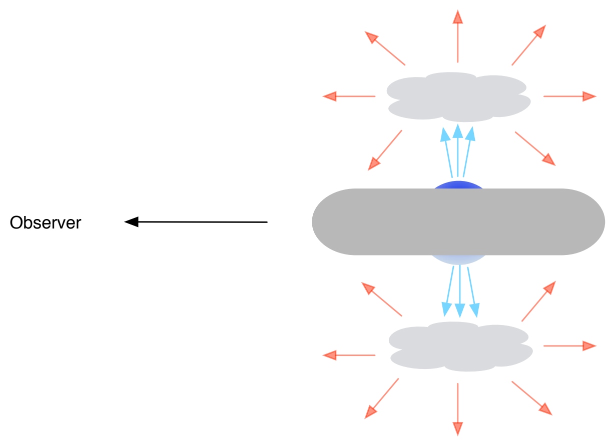

Figure 5.8: Diagram to explain the geometry required to give rise to a star with emission lines. Star is occluded by the edge-on disc and so is seen by reflection off material out of the plane of the disc also giving rise to resonance emission of atomic species.

This edge-on disc geometry has also been used to explain the emission lines present in the spectrum of the M star VY CMa (Herbig 1970) and is often accompanied by a large near-IR excess (Lloyd Evans *et al.* 2000). Figure 5.9 shows the excess in K_s relative to a large number of dusty Mira variables[6] that do not have a disc and therefore no near-IR excess. The dashed line is the cut-off used to select the targets for this observing program, the line being defined as an excess relative to the best fit to the Mira data (Figure 5.6).

The four new emission line targets have an excess in K_s equal to or greater than those of

[6]Mira variables are evolved stars that have periods of between 80 – 1000 days. Used as a reference colour for this work they are dust reddened but generally do not have a disc and therefore also lack the near-IR excess.

VY CMa and IRAS 12311-3509. The $K_s-[12] > 5$ colour limit, thought to differentiate between objects with discs and those without also appears to be true for these four new stars (Table 5.3). VY CMa and IRAS 12311-3509 have $K_s - [12]$ values of 6.65 and 7.62 respectively.

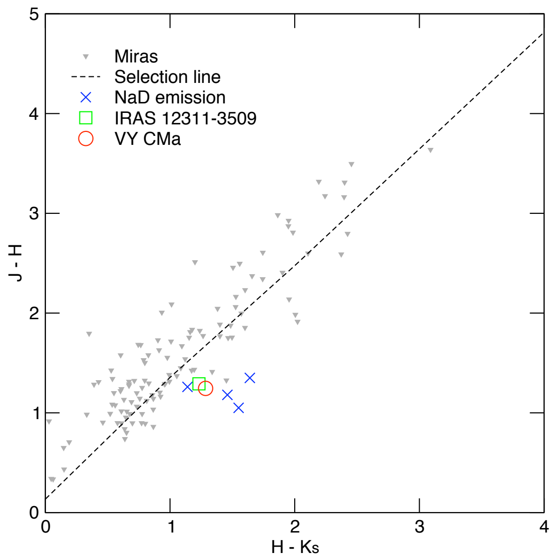

Figure 5.9: K_s excess for Na I D emission line stars and those of IRAS 12311-3509 and VY CMa.

Three of the four (IRAS 11467-7003, IRAS 13051-8408 and IRAS 19521+0515) fall within the original 'RV Tauri box' IRAS [12] − [25] colour limits defined as $1.00 < [12] - [25] < 1.55$ (Lloyd Evans 1997b) although only two (IRAS 13051-8408 and IRAS 19521+0515) lie between the [25]−[60] colour limits of $0.20 < [25]-[60] < 1.00$. Selected firstly by their near-IR excess and later by an extension of [12] − [25] limits to 0.9 – 1.9, the relaxation of the [25] − [60] colour limits appears to have been justified, as two of the targets (IRAS 09258-6125 and IRAS 11467-7003) have [25] − [60] colours outside of the RV Tauri box.

Figure 5.10 shows spectra for the four Na I D emission line stars for the yellow/blue spectral regions. IRAS 09258-1625 is probably a supergiant with IRAS 11467-7003 and IRAS 19521+0515 being less luminous (bright giants) A-type stars. The 'stepped' appearance caused by the molecular bands of TiO in the spectrum of IRAS 13051-8408 is characteristic of M-type stars. A mid M-type dwarf, IRAS 13051-8408 is classified spectral type M5Ve due to the emission lines also present (Na I D, K I, O I and Ca II H & K) and is probably a M dwarf and a T Tauri star.

A near-IR excess for stars with discs can be demonstrated by colour-colour diagrams like Figure 5.9 or can be more readily understood in the form of a spectral energy distribution (SED) plot. SED plots describe the flux distribution of a source as a function of wavelength and are routinely used to infer the presence of dust-discs (e.g. de Ruyter *et al.* 2006).

Figure 5.11 is an SED plot for IRAS 13051-8408. The red squares are flux measurements at different wavelengths in the optical, near- and mid-IR. The longest wavelength IRAS 100 μm measurement is an upper limit hence the downward arrow. The solid black line is a scaled Kurucz model atmosphere[7] for a M5 dwarf. Figure 5.11 demonstrates that the SED of the underlying M5V star cannot account for the rising IR flux and must be due to cooler dust surrounding the star.

Figure 5.12 is an SED plot for IRAS 09258-6125. As for Figure 5.11 the red squares are photometric measurements from various optical and IR surveys. The solid line is the Kurucz model for a G0 supergiant (G0Ib) and is the closest match available to the spectral type of IRAS 09258-6125 (F8Ibe). The match to the optical flux measurements and the Kurucz model is not as good as for IRAS 13051-8408 although the dramatic excess in K_s is clear ($\sim 2.16\ \mu$m). Even with the discrepancies between the model atmosphere and the optical photometry it is clear that there is a significant IR component to the SED that cannot be accounted for by the stellar SED alone.

[7]Kurucz model atmospheres of Robert L. Kurucz, Harvard-Smithsonian Center for Astrophysics (http://kurucz.harvard.edu/)

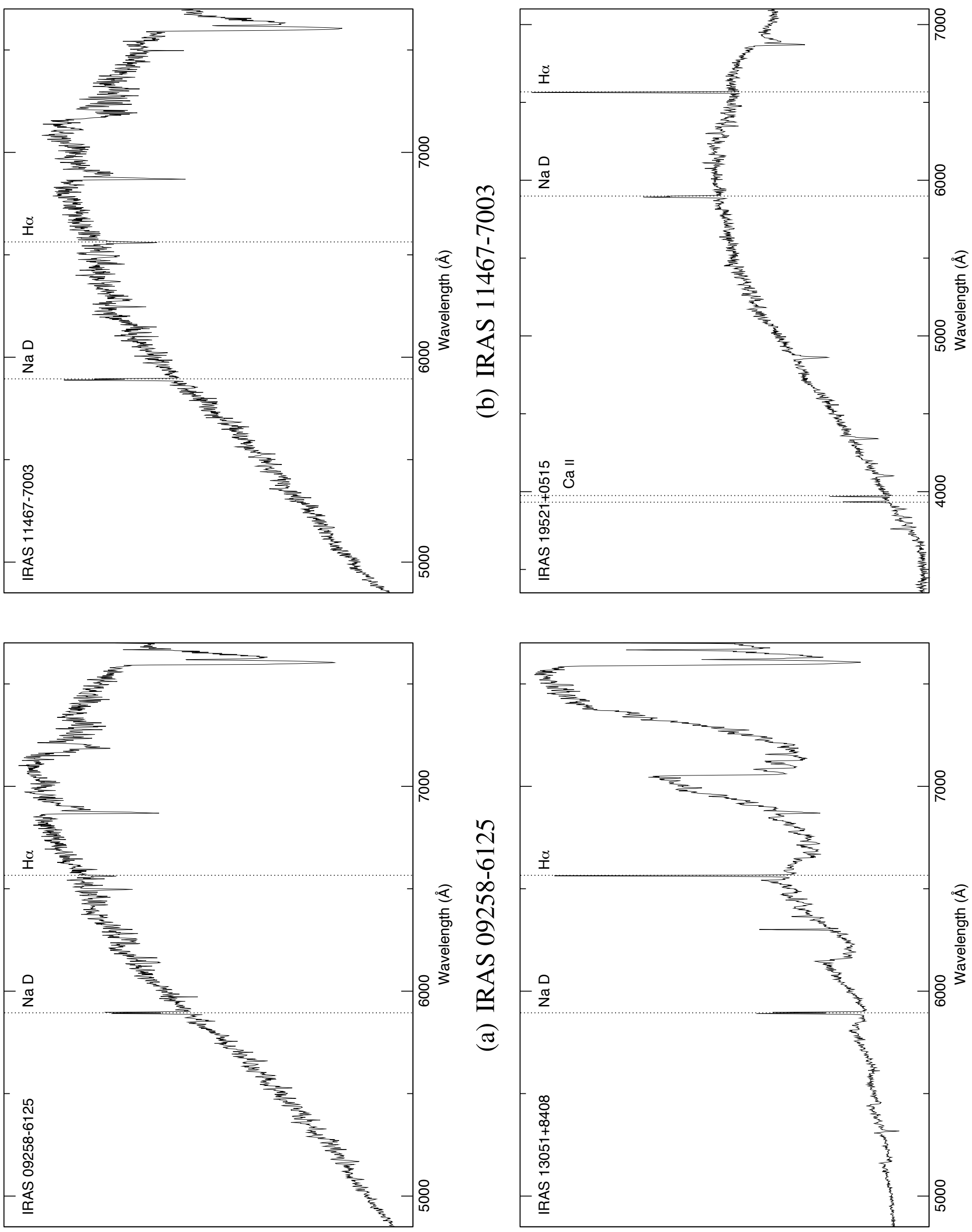

(a) IRAS 09258-6125

(b) IRAS 11467-7003

(c) IRAS 13051-8408

(d) IRAS 19521+0515

Figure 5.10: Spectra of the four Na I D emission line stars discovered in this work.

Model atmosphere 'grids' have been calculated for a variety of spectral types (e.g Kurucz 1979) and where possible for the Na ɪ D emission line stars SED plots has been constructed. Suitable matches to the spectral types of IRAS 11467-7003 and IRAS 19521+0515 could not be found and so SED plots are not presented.

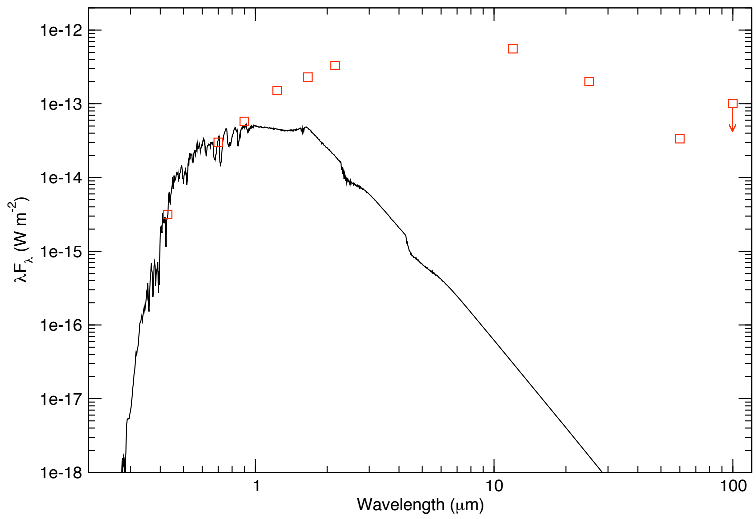

Figure 5.11: SED plot for IRAS 13051-8408 incorporating optical, near-IR and mid-IR photometry (boxes).

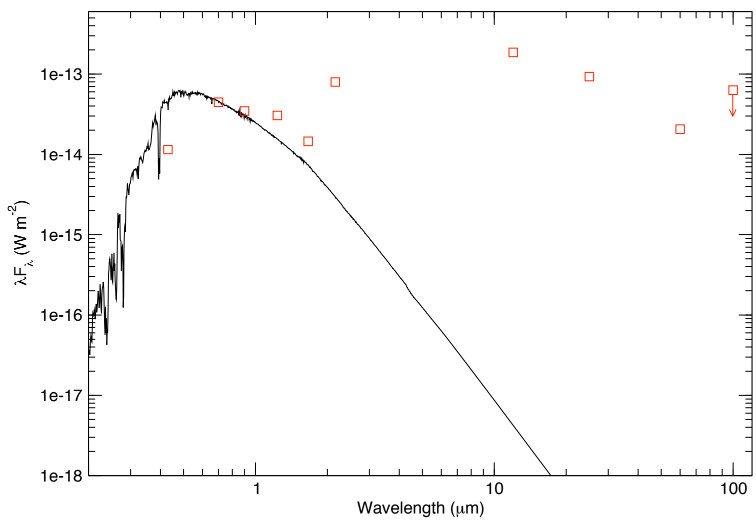

Figure 5.12: SED plot for IRAS 09258-6125 incorporating optical, near-IR and mid-IR photometry (boxes).

5.4.2 Hα emission line targets

A significant fraction of the stars selected for observation had spectra dominated by strong Hα emission. Composed mostly of A or earlier spectral type, this group also includes a number of stars with Ca II emission (8498, 8542 & 8662 Å) which are possibly Herbig Ae/Be stars. Higher mass (2–8 $M_\odot$) counterparts of the lower mass ($\sim 1M_\odot$) T Tauri stars, Herbig Ae/Be stars are pre-main sequence stars with spectral types A and B and have near-IR excesses arising from dust discs left over from star formation. The presence of the dust disc and the accompanied near-IR excess has led to their inclusion in this sample of stars. HST imaging of young stars has led to the recent creation of a new class of stellar object. So called 'proplyds', where a proto-planetary disc is seen edge-on, are often Herbig Ae/Be stars and presumably similar to those identified although not necessarily with the same edge-on disc geometry (see Figure 5.13).

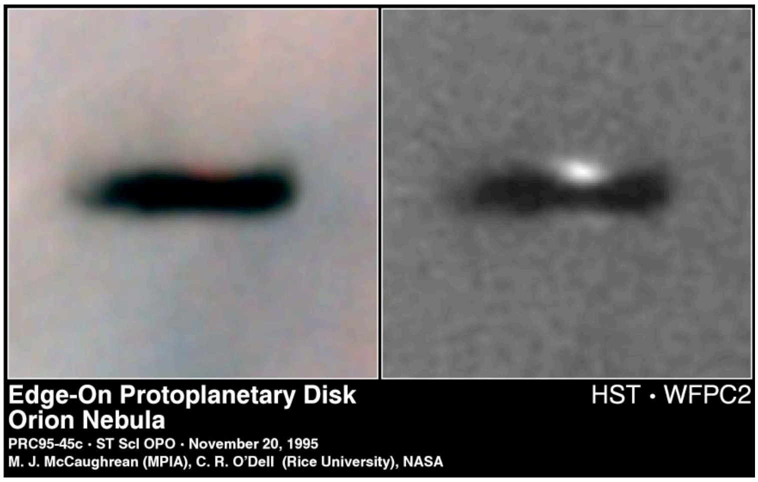

Figure 5.13: HST WFPC2 images of the proplyd (proto-planetary disc) PRC95-45c as seen through different filters. The presence of an edge-on disc is clear.

Candidate Herbig Ae/Be stars including those identified in this study are listed in Table 5.4 and have been included in a Spitzer proposal for follow-up observation by Bram Acke, University of Leuven and the spectra of which are shown in Figure 5.14. All three of the stars have strong Hα (6563 Å) emission. Two of the three stars in Figure 5.14 also have Ca II in emission (8498, 8452 & 8662 Å) which is an indicator of their young nature.

Figure 5.15 demonstrates the range in near-IR excess of the stars with strong Hα emis-

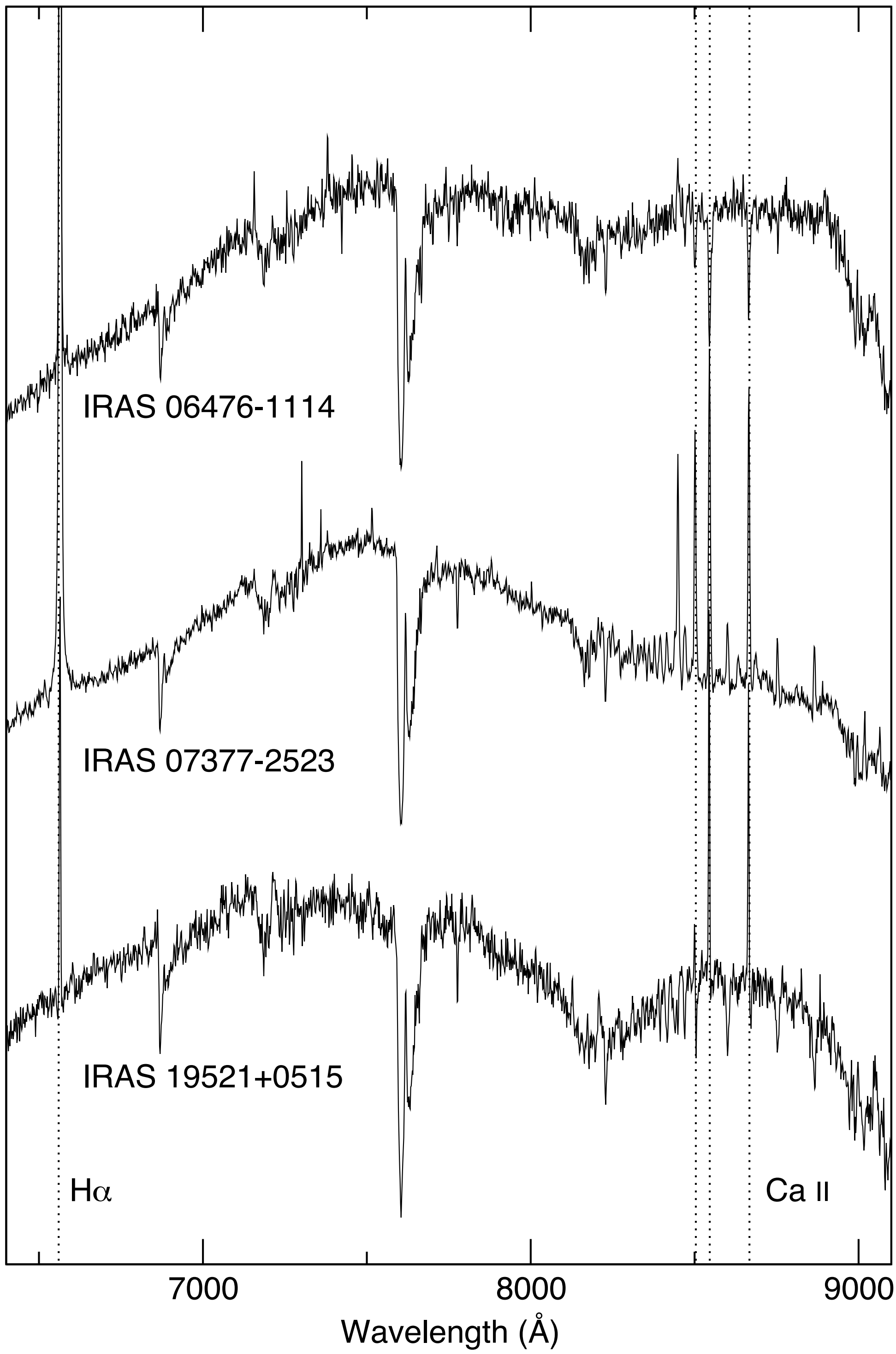

Figure 5.14: Spectra of three possible Herbig Ae/Be stars identified in this survey.

sion. The candidate Herbig Ae/Be stars (marked with a red cross) fall well within the range of K_s excesses of the other Hα emission objects (green star symbol) and do not form a distinct population.

IRAS	α	δ
06476-1114	06 50 02	-11 18 14
07377-2523	07 39 48	-25 30 28
10082-5650	10 10 00	-57 04 52
19521+0515	19 54 40	+05 23 53

Table 5.4: Candidate Herbig Ae/Be stars in this survey.

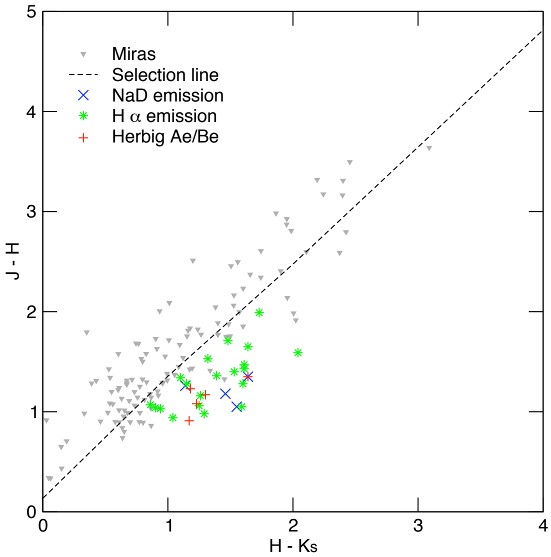

Figure 5.15: K_s excess for Hα emission targets, possible Herbig Ae/Be stars and Na I D emission lines stars relative to dusty Miras and survey selection line.

5.4.3 'Ordinary' stars

It was inevitable that given the many thousands of potential targets considered for observation there would be a fraction of 'ordinary' objects contaminating the sample set. Many steps were taken to limit the number of 'unwanted' stars including inspection of DSS images, constraints on the IRAS P_{var} (probability of variability) value and the construction of numerous IR colour plots. Of the 90 stars observed 16 were deemed 'ordinary'. Composed mainly of K and M giants and some dwarfs the 'ordinary stars' are listed in Table 5.5.

IRAS	α	δ	Spec
092690-5238	09 27 40	-52 51 18	M1III
11030-4942	11 05 17	-49 58 56	M
11556-6433	11 58 10	-64 49 51	A5V
12212-6115	12 24 00	-61 32 33	M0III
12400-6458	12 43 02	-65 14 37	M
13190-6704	13 33 31	-67 20 19	F3V
14154-6136	14 19 09	-61 50 21	–
14158-5050	14 19 12	-51 03 54	F3V
15180-5547	15 21 50	-55 58 41	F3V
16465-4129	16 50 04	-41 34 44	F2III
16471-4650	16 50 51	-46 55 08	K1III
16518-4243	16 55 24	-42 48 23	F6V
16521-4257	16 55 43	-43 02 34	K2III
19029+0933	19 05 22	+09 38 23	K4III
19157-0355	19 18 21	-03 49 48	M
20282+1756	20 30 29	+18 06 29	M

Table 5.5: 'Ordinary' stars identified in this survey.

Possible reasons for some the stars in Table 5.5 being selected are poor quality photometry, confusion as to which IRAS source matches the 2MASS source and human error. Compared to the more modern 2MASS data the positional accuracy of the IRAS satellite was significantly lower. In the selection of targets for observation a search was made 15″ around the 2MASS position for a corresponding IRAS source. Where there was more than one IRAS source the possibility arose that the wrong IRAS target was chosen leading to incorrect values for [12] – [25], K_s–[12] for the 2MASS source with a K_s excess.

5.4.4 Review of selected targets

Although unsuccessful in identifying new stars with unusual molecular spectra like those of IRAS 12311-3509 and U Equ, a significant fraction of the (~ 30%) of the targets observed are found to have unusual atomic line spectra. Figure 5.16 is a plot of the optical and IR photometry for those program stars where reliable photometry is available. All photometric values have been normalised to the same value for the J-band (1.235 μm) flux so that they may be easily compared. As expected the 'shape' of the near- to mid-IR flux distributions to the red of 1.235 μm are broadly similar, reflecting the selection criteria used. To the blue of 1.235 μm, where the stellar SED flux is expected to dominate (see Figures 5.11 & 5.12) there is a large range in the SED distributions. This variation in stellar SEDs confirms the broad range of stellar types that have been selected and observed for this project.

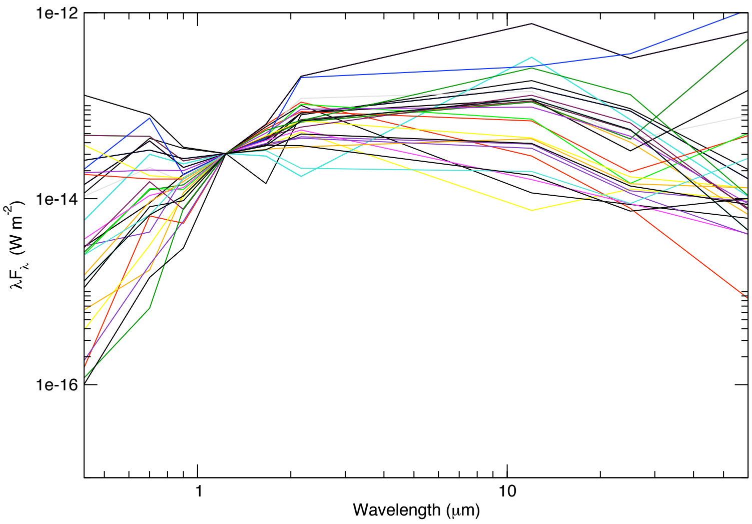

Figure 5.16: Optical, near and mid-IR photometry for all targets observed and normalised to a J-band magnitude to allow for comparison of the SEDs of the targets.

The variable quality of the IRAS 60 μm flux measurements was one of the main obstacles preventing an extension to the original Lloyd Evans survey. A search of the 2MASS catalogue to identify all potential sources with near-IR excesses, an indication of a disc, combined with IRAS [12] − [25] colours shows promise as an efficient method for identifying stars with discs. Figure 5.17 shows the distribution of K_s-[12] values as a function of IRAS [12] − [25] colour for targets believed to have discs (VY CMa, IRAS 12311-3509 and U Equ) compared to those selected for this project. The red crosses represent those targets believed to be possible Herbig Ae/Be stars (Table 5.4) and the blue crosses are the Na I D emission line stars listed in Table 5.3. Clearly the stars with discs occupy a fairly sparsely populated region of this two-colour plot. Only one of the 11 'disc' stars has a value of K_s−[12] of less than 6.

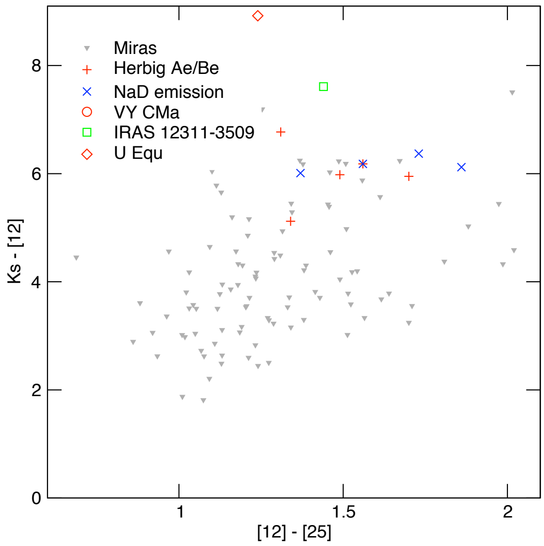

Figure 5.17: $K_s - [12]$ values as a function of $[12] - [25]$ colour for 'exotic' targets and dusty Miras.

5.5 Conclusions and future strategy

Stars have been selected from the 2MASS near-IR catalogue by their near-IR excess in K_s-band relative to the 'normal' near-IR colours of dusty Mira variables. Stars with near-IR excesses have been selected from the 2MASS catalogue and matched with the corresponding IRAS source. A selection has been made based upon $[12] - [25]$ colour, the presence of an optical counterpart, probability of variability, the $K_s-[12]$ colour index and appearance on DSS images.

No stars with unusual *molecular* spectra have been identified from the sample of ~ 90 observed stars although $\sim 10\%$ *are* believed to have edge-on or near-edge-on discs. Figure 5.17 has shown that $K_s-[12]$ is likely an important factor for selecting objects with discs.

Many thousands of IRAS sources lie within the bounds of the RV Tauri Box but only a small fraction have a near-IR excess. Searching directly for a near-IR excess as a first step in selecting potential targets appears to have been an improvement over relying primarily upon IRAS photometry. Figure 5.18 demonstrates that the near-IR excess due to a disc is more pronounced in the L photometric band (3.54 μm) than in K_s (2.159 μm). There is no all-sky L-band photometry available but a search for an excess in 2MASS-K_s seems justified given the distinct region of the J-H, H-K_s plot that the exotic stars occupy.

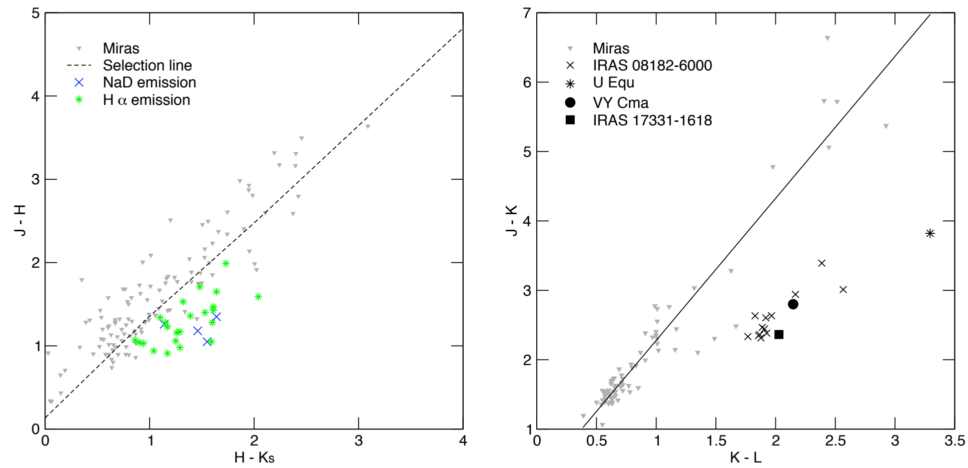

Figure 5.18: K_s-band excess compared with L-band excess for select targets.

The detection of in particular the Na I D emission line and possible Herbig Ae/Be stars underlines the value of this method for detecting stars with discs. In future it is recommended that no potential sources of $K_s-[12] < 6$ are observed as this value appears to represent a cut-off for normal stars. An extension of this survey into the Northern hemisphere is recommended as objects of $\delta > 15°$ N are inaccessible from the SAAO Sutherland observatory. Targets with good quality IRAS 12, 25 and 60 μm photometry could be selected as well as those with more marginal IRAS data as Lloyd Evans did not attempt an extension of his survey in the Northern hemisphere.

Limits on the 2MASS J-band magnitude were used so that observations were possible on a 2-metre class telescope. Many promising sources were identified but were too faint for the telescope-spectrograph configuration in use. This problem would be easily rectified by using a larger telescope, the enormous collecting area of the Southern African Large Telescope (SALT) combined with the low-medium resolution Robert Stobie Spectrograph (RSS) being an ideal configuration.

An additional source of potential targets for this project could come from the Sloan Digital Sky Survey (SDSS). The recently released SDSS data release 5 spectroscopic catalogue contains spectra (R ~ 1800) of 1,048,960 targets including 154,925 stars. Using techniques similar to those used to detect metal lines in quasar absorption lines-of-sight (e.g. Hewett *et al.* 1985), it may be possible to search for the pattern of narrow TiO absorption bands in SDSS stellar spectra.

Chapter 6

Conclusions

This thesis presented the results and analysis of three separate, albeit related pieces of work. A unifying theme for all three chapters has been the role of dust and molecules in astronomical environments.

Contrary to early beliefs, in-depth study of different phases of the ISM over the last ~ 50 years, has revealed a rich and diverse chemistry (e.g. Hartquist & Williams 1978). To date, approximately 130 different molecular species have been detected in the ISM and although the reaction mechanisms in many cases for their formation remain uncertain, it is clear that dust plays an important role in the formation of many species (e.g. Whittet 2003).

Given the significance of dust in facilitating the chemistry of the ISM, surprisingly little is known about its spatial distribution: Chapter 3 of this thesis investigated this question by searching for differences in strengths of the DIBs between closely spaced lines-of-sight. Although current thinking (Herbig 1993) would suggest that the DIB carriers are not due to actual interstellar dust grains, their strong linear relationship with line-of-sight dust reddening, E_{B-V}, means that they *can* be used to infer the dust distribution. Primarily an investigation of the strengths of blue ($\lambda < 5700$ Å) DIBs, this work has also confirmed that the result of Cordiner (2005) holds for the majority of blue and red DIBs analysed. The result is emphatic; there exists small-scale structure in the majority of DIB strengths over scales of 300 – 25,000 AU. This remarkable result means that future chemical models of diffuse interstellar environments should incorporate structure of this size-scale. Efforts to include small-scale-structure variations detected towards κ Velorum in the modelling of these regions (Bell *et al.* 2005) have predicted detectable amounts of previously undetected species suggesting that structure/density variations in the diffuse ISM could give rise to a significant abundance of molecules not previously considered to have a significant abundance.

Chapter 4 continued the theme the DIB-dust relation by searching for DIBs in the spectra of QSO absorption lines-of-sight. Studies of extragalactic environments have shown that the galactic DIB–E_{B-V} relation appears, at least for the limited number of cases tested, to be universal (e.g. Welty *et al.* 2006). DIB signatures have so far only been detected in one extremely reddened QSO sightline (Junkkarinen *et al.* 2004). The routine detection of DIBs at cosmological distances would be significant as the DIB carrier species are thought to be closely related to biological-type molecules (e.g. Ehrenfreund). Although this would be of interest, the primary motivation for this chapter was to ascertain whether the DIBs could be used as a *spectroscopic* signature of dust in damped Lyman-alpha systems. Although the reader is directed to the introduction of Chapter 4 for a more comprehensive review of motivations for this study, it is important to realise that the quantity of dust present in DLAs is far from certain (Murphy & Liske 2004). Any additional methods for probing this question are therefore potentially extremely important: understanding the role that dust has to play in the early universe is key to our evolution of primordial gas clouds and the formation of early stars and galaxies. Although at the time of writing, only limited amounts of data for this chapter were available, none of the QSO absorption sightlines investigated showed DIB absorptions. Further careful analysis of this data is required although it is, at this stage, possible to say that the non-dectection of DIBs in those targets discussed means that the DIB strengths are below the predicted values based upon the 'universal' DIB–E_{B-V} relationship.

Whilst chapters 3 and 4 have provided an opportunity to investigate the DIB–dust relationship it has also been possible to study the relationship between the abundances of known species (e.g. small molecules and atoms) and the strengths of the DIBs. Systematic analysis of the blue and red DIBs has shown that the blue DIBs, on average, favour significantly denser environments than their red cousins. This result is in agreement with the findings of Thorburn *et al.* (2003), who identified a subset of weak blue DIBs that show a significant correlation with C_2, a species that only resides in the most dense phases of the diffuse ISM. Although the number of lines-of-sight available for analysis was limited, there does appear to be a real difference in the behaviour of those DIBs that favour dense (blue DIBs) and more diffuse (red DIBs) regions. New methods pioneered for here and by Cordiner (2005) have demonstrated what is possible when S/N of target spectra routinely exceed 1000. The robust and objective method of ratioing spectra to search for variations in weak features (DIBs) has proved to be highly successful and worth pursuing in further lines-of-sight.

Chapter 5 documented a search of near- and mid-IR catalogues for evolved stars with dusty discs. Searching directly for signatures of dust reddening (mid-IR excess) combined with a disc-like geometry (near-IR excess) the aim was to increase a currently extremely small sample of stars with exotic atomic and molecular spectra whose evolutionary tracks and position within the HR diagram are currently unclear. The stellar winds and outflows of evolved low–medium mass stars enrich the ISM with significant quantities of dust and molecules. Whilst the DIBs have not been detected in the outflow of a nearby carbon star (Kendall *et al.* 2004), it is possible that the parent species of the DIB carriers *are* present, requiring some level of processing before the DIB carriers are formed. Although no new examples of evolved stars similar to those already known were detected this work demonstrated that the methodology was sound and showed the potential for searching publicly available catalogues in a systematic fashion.

Eighty-four years after their discovery, the Diffuse Interstellar Band spectrum remains unassigned. Over the last few decades significant progress has been made in identifying at least the class of species giving rise to the DIB spectrum. However, this work has shown that there are still many ‘unknowns’ in DIB research, established DIB ‘families’ may be in need of further refinement and local DIB correlations may not hold in all extragalactic environments. With the ever increasing quality of spectroscopic data and advances in terrestrial laboratory techniques, it can surely not be another eighty years before the DIB spectrum is assigned? Only once the identity of the DIB carriers is known, will the true significance of these elusive molecules and their place within the chemistry of the ISM be fully understood.

Bibliography

Adams, W. S., 1943, ApJ, **97**, 105+.

Adamson, A. J., Whittet, D. C. B., Duley, W. W., 1991, MNRAS, **252**, 234–245.

Allamandola, L. J., Tielens, G. G. M., Barker, J. R., 1989, ApJS, **71**, 733–775.

André, P., Ward-Thompson, D., Barsony, M., 1993, ApJ, **406**, 122–141.

Appenzeller, I., Fricke, K., Furtig, W., Gassler, W., Hafner, R., Harkl, R., Hess, H.-J., Hummel, W., Jurgens, P., Kudritzki, R.-P., Mantel, K.-H., Meisl, W., Muschielok, B., Nicklas, H., Rupprecht, G., Seifert, W., Stahl, O., Szeifert, T., Tarantik, K., 1998, The Messenger, **94**, 1–6.

Barnbaum, C., Omont, A., Morris, M., 1996, A&A, **310**, 259–270.

Bell, T. A., Viti, S., Williams, D. A., Crawford, I. A., Price, R. J., 2005, MNRAS, **357**, 961–966.

Black, J. H., van Dishoeck, E. F., 1991. Chemistry and Small-Scale Structure of Diffuse and Translucent Clouds. In E. Falgarone, F. Boulanger, and G. Duvert, editors, *IAU Symp. 147: Fragmentation of Molecular Clouds and Star Formation*, pages 139+.

Cami, J., Sonnentrucker, P., Ehrenfreund, P., Foing, B. H., 1997, A&A, **326**, 822–830.

Chlewicki, G., de Groot, M. S., van der Zwet, G. P., Greenberg, J. M., Alvarez, P. P., Mampaso, A., 1987, A&A, **173**, 131–136.

Collings, M. P., Dever, J. W., Fraser, H. J., McCoustra, M. R. S., Williams, D. A., 2003, ApJ, **583**, 1058–1062.

Cordiner, M. A., 2005, Ph.D. Thesis.

Cordiner, M. A., Sarre, P. J., Fossey, S. J., 2005, AAT Newsletter, **107**, 9.

Couch, P. A., 2002, Ph.D. Thesis.

Couch, P. A., Lloyd Evans, T., Sarre, P. J., 2003, MNRAS, **346**, 153–162.

Cox, N. L. J., Cordiner, M. A., Cami, J., Foing, B. H., Sarre, P. J., Kaper, L., Ehrenfreund, P., 2006, A&A, **447**, 991–1009.

Crawford, I. A., 2002, MNRAS, **334**, L33–L37.

Crawford, I. A., 2003, Ap&SS, **285**, 661–675.

Crawford, I. A., Howarth, I. D., Ryder, S. D., Stathakis, R. A., 2000, MNRAS, **319**, L1–L6.

Crawford, M. K., Tielens, A. G. G. M., Allamandola, L. J., 1985, ApJ, **293**, L45–L48.

de Ruyter, S., van Winckel, H., Maas, T., Lloyd Evans, T., Waters, L. B. F. M., Dejonghe, H., 2006, A&A, **448**, 641–653.

Diamond, P. J., Goss, W. M., Romney, J. D., Booth, R. S., Kalberla, P. M. W., Mebold, U., 1989, ApJ, **347**, 302–306.

Diego, F., Fish, A. C., Barlow, M. J., Crawford, I. A., Spyromilio, J., Dryburgh, M., Brooks, D., Howarth, I. D., Walker, D. D., 1995, MNRAS, **272**, 323–332.

Dieter, N. H., Welch, W. J., Romney, J. D., 1976, ApJ, **206**, L113–L115.

Douglas, A. E., 1977, Nature, **269**, 130.

Duley, W. W., 1968, Nature, **218**, 153.

Duley, W. W., Williams, D. A., 1986, MNRAS, **223**, 177–182.

Ehrenfreund, P., Foing, B. H., 1997, Advances in Space Research, **19**, 1033–1042.

Evans, T. L., 1990, MNRAS, **243**, 336–348.

Eyster, E. H., 1937, ApJ, **86**, 486–488.

Fall, S. M., Pei, Y. C., McMahon, R. G., 1989, ApJ, **341**, L5–L8.

Federman, S. R., Strom, C. J., Lambert, D. L., Cardelli, J. A., Smith, V. V., Joseph, C. L., 1994, ApJ, **424**, 772–792.

Foing, B. H., Ehrenfreund, P., 1994, Nature, **369**, 296+.

Fouque, P., Le Bertre, T., Epchtein, N., Guglielmo, F., Kerschbaum, F., 1992, A&AS, **93**, 151–171.

Galazutdinov, G., Moutou, C., Musaev, F., Krełowski, J., 2002, A&A, **384**, 215–224.

Galazutdinov, G. A., Gnaciński, P., Han, I., Lee, B.-C., Kim, K.-M., Krełowski, J., 2006, A&A, **447**, 589–595.

Gamow, G., 1948, Nature, **162**, 680.

Gredel, R., Lepp, S., Dalgarno, A., Herbst, E., 1989, ApJ, **347**, 289–293.

Hartquist, T. W., Williams, D. A., 1978. *The Molecular Astrophysics of Stars and Galaxies*. Clarendon Press, Oxford.

Heckman, T. M., Lehnert, M. D., 2000, ApJ, **537**, 690–696.

Heger, M. L., 1922, Lick Observatory Bulletin, **10**, 141–148.

Herbig, G. H., 1963, ApJ, **137**, 200+.

Herbig, G. H., 1970, ApJ, **162**, 557–+.

Herbig, G. H., 1993, ApJ, **407**, 142–156.

Herbig, G. H., 1995, ARA&A, **33**, 19–74.

Hewett, P. C., Irwin, M. J., Bunclark, P., Bridgeland, M. T., Kibblewhite, E. J., He, X. T., Smith, M. G., 1985, MNRAS, **213**, 971–989.

Hunter, R., 2004, Ph.D. Thesis.

Johnstone, D., Wilson, C. D., Moriarty-Schieven, G., Joncas, G., Smith, G., Gregersen, E., Fich, M., 2000, ApJ, **545**, 327–339.

Junkkarinen, V. T., Cohen, R. D., Beaver, E. A., Burbidge, E. M., Lyons, R. W., Madejski, G., 2004, ApJ, **614**, 658–670.

Kendall, T., Mauron, N., McCombie, J., Sarre, P., 2004, Ap&SS, **289**, 203–206.

Kerr, T. H., Hibbins, R. E., Miles, J. R., Fossey, S. J., Somerville, W. B., Sarre, P. J., 1996, MNRAS, **283**, L105+.

Kerr, T. H., Hibbins, R. E., Fossey, S. J., Miles, J. R., Sarre, P. J., 1998, ApJ, **495**, 941+.

Krelowski, J., Schmidt, M., 1997, ApJ, **477**, 209+.

Krełowski, J., Sneden, C., 1995. *Diffuse Interstellar Bands in Individual Sightlines*, pages 13+. ASSL Vol. 202: The Diffuse Interstellar Bands.

Krelowski, J., Walker, G. A. H., 1987, ApJ, **312**, 860–867.

Kurucz, R. L., 1979, ApJS, **40**, 1–340.

Lawton, B., York, B., Ellison, S. L., Churchill, C. W., Johnson, R. A., Snow, T. P., 2005. A search for organic molecules in intermediate redshift DLAs. In P. Williams, C.-G. Shu, and B. Menard, editors, *IAU Colloq. 199: Probing Galaxies through Quasar Absorption Lines*, pages 430–432.

Leger, A., d'hendecourt, L., 1985, A&A, **146**, 81–85.

Lequeux, J., 2005. *The Interstellar Medium*. Springer.

Liszt, H., Lucas, R., 2000, A&A, **355**, 333–346.

Lloyd Evans, T., 1991, MNRAS, **249**, 409–416.

Lloyd Evans, T., 1997, MNRAS, **286**, 839–847.

Lloyd Evans, T., 1997, Ap&SS, **251**, 239–242.

Lloyd Evans, T., 1999. The Nature of RV Tauri Stars. In T. Le Bertre, A. Lebre, and C. Waelkens, editors, *IAU Symp. 191: Asymptotic Giant Branch Stars*, pages 453–+.

Lloyd Evans, T., Hurst, M. E., Sarre, P. J., 2000, MNRAS, **319**, 111–120.

Lodén, L. O., 1973, Ap&SS, **24**, 511+.

Lowrance, J. L., Morton, D. C., Zucchino, P., Oke, J. B., Schmidt, M., 1971, BAAS, **3**, 238+.

Lowrance, J. L., Morton, D. C., Zucchino, P., Oke, J. B., Schmidt, M., 1972, ApJ, **171**, 233+.

Malhotra, S., 1997, ApJ, **488**, L101+.

Marscher, A. P., Moore, E. M., Bania, T. M., 1993, ApJ, **419**, L101+.

McCall, B. J., Rachford, B. L., Snow, T. P., Sonnentrucker, P., Friedman, S., Thorburn, J., Oka, T., Welty, D., Hobbs, L. M., York, D. G., 2002. Early Results from the APO Diffuse Interstellar Band Survey. In F. Salama and et al., editors, *NASA Laboratory Astrophysics Workshop*, pages 138+.

McCall, B. J., Hinkle, K. H., Geballe, T. R., Moriarty-Schieven, G. H., Evans, II, N. J., Kawaguchi, K., Takano, S., Smith, V. V., Oka, T., 2002, ApJ, **567**, 391–406.

McCall, B. J., Rachford, B. L., Snow, T. P., Friedman, S. D., Sonnentrucker, P., Thorburn, J. A., Hobbs, L. M., Oka, T., Welty, D. E., York, D. G., 2005. *Correlations among the Diffuse Interstellar Bands, Atoms and Small Molecules*. 60th Ohio State University International Symposium on Molecular Spectroscopy.

Merrill, P. W., 1934, PASP, **46**, 206–207.

Merrill, P. W., 1936, ApJ, **83**, 126+.

Merrill, P. W., Wilson, O. C., 1938, ApJ, **87**, 9+.

Meyer, D. M., 1990, ApJ, **364**, L5–L8.

Meyer, D. M., Blades, J. C., 1996, ApJ, **464**, L179+.

Motta, V., Mediavilla, E., Muñoz, J. A., Falco, E., Kochanek, C. S., Arribas, S., García-Lorenzo, B., Oscoz, A., Serra-Ricart, M., 2002, ApJ, **574**, 719–725.

Moutou, C., Krełowski, J., D'Hendecourt, L., Jamroszczak, J., 1999, A&A, **351**, 680–688.

Murphy, M. T., Liske, J., 2004, MNRAS, **354**, L31–L36.

Nestor, D. B., Turnshek, D. A., Rao, S. M., 2005, ApJ, **628**, 637–654.

Neugebauer, G., Leighton, R. B., 1969. *Two-micron sky survey. A preliminary catalogue*. NASA SP, Washington: NASA, 1969.

Pan, K., Federman, S. R., Cunha, K., Smith, V. V., Welty, D. E., 2004, ApJS, **151**, 313–343.

Pan, K., Federman, S. R., Sheffer, Y., Andersson, B.-G., 2005, ApJ, **633**, 986–1004.

Pei, Y. C., Fall, S. M., 1995, ApJ, **454**, 69+.

Pei, Y. C., Fall, S. M., Bechtold, J., 1991, ApJ, **378**, 6–16.

Penzias, A. A., Wilson, R. W., 1965, ApJ, **142**, 419–421.

Péroux, C., Dessauges-Zavadsky, M., D'Odorico, S., Kim, T.-S., McMahon, R. G., 2003, MNRAS, **345**, 480–496.

Pettini, M., Smith, L. J., Hunstead, R. W., King, D. L., 1994, ApJ, **426**, 79–96.

Pettini, M., Smith, L. J., King, D. L., Hunstead, R. W., 1997, ApJ, **486**, 665+.

Prochaska, J. X., Herbert-Fort, S., 2004, PASP, **116**, 622–633.

Rank, D. M., Townes, C. H., Welch, W. J., 1971, Science, **174**, 1083.

Rao, S. M., Turnshek, D. A., 2000, ApJS, **130**, 1–35.

Richter, P., Sembach, K. R., Howk, J. C., 2003, A&A, **405**, 1013–1023.

Salama, F., 1999, Bulletin of the American Astronomical Society, **31**, 881+.

Sarre, P. J., Miles, J. R., Kerr, T. H., Hibbins, R. E., Fossey, S. J., Somerville, W. B., 1995, MNRAS, **277**, L41–L43.

Sarre, P. J., Hurst, M. E., Lloyd Evans, T., 1996, ApJ, **471**, L107+.

Savage, B. D., Sembach, K. R., 1996, ARA&A, **34**, 279–330.

Słyk, K., Galazutdinov, G. A., Musaev, F. A., Bondar, A. V., Schmidt, M. R., Krełowski, J., 2006, A&A, **448**, 221–229.

Snow, T. P., 2001, Spectrochimica Acta, **57**, 615–626.

Snow, T. P., 2002, ApJ, **567**, 407–411.

Snow, T. P., McCall, B. J., 2006, ARA&A, **44**, 367–414.

Snow, T. P., Zukowski, D., Massey, P., 2002, ApJ, **578**, 877–884.

Sollerman, J., Cox, N., Mattila, S., Ehrenfreund, P., Kaper, L., Leibundgut, B., Lundqvist, P., 2005, A&A, **429**, 559–567.

Stanke, T., Smith, M. D., Gredel, R., Khanzadyan, T., 2006, A&A, **447**, 609–622.

Swings, P., 1937, MNRAS, **97**, 212+.

Thorburn, J. A., Hobbs, L. M., McCall, B. J., Oka, T., Welty, D. E., Friedman, S. D., Snow, T. P., Sonnentrucker, P., York, D. G., 2003, ApJ, **584**, 339–356.

Tokunaga, A. T., 1997. A summary of the ”UIR” bands. In H. Okuda, T. Matsumoto, and T. Rollig, editors, *ASP Conf. Ser. 124: Diffuse Infrared Radiation and the IRTS*, pages 149+.

Tuairisg, S. Ó., Cami, J., Foing, B. H., Sonnentrucker, P., Ehrenfreund, P., 2000, A&AS, **142**, 225–238.

van Dishoeck, E. F., Black, J. H., 1986, ApJS, **62**, 109–145.

Wang, J., Hall, P. B., Ge, J., Li, A., Schneider, D. P., 2004, ApJ, **609**, 589–596.

Watson, J. K., Meyer, D. M., 1996, ApJ, **473**, L127+.

Welty, D. E., Federman, S. R., Gredel, R., Thorburn, J. A., Lambert, D. L., 2006, ApJS, **165**, 138–172.

Westerlund, B. E., Krelowski, J., 1988, A&A, **203**, 134–144.

Whittet, D. C. B., 2003. *Dust in the Galactic Environment.* Institute of Physics Publishing.

Wild, V., Hewett, P. C., 2005, MNRAS, **361**, L30–L34.

Wolfe, A. M., Lanzetta, K. M., Foltz, C. B., Chaffee, F. H., 1995, ApJ, **454**, 698+.

Wolfire, M. G., McKee, C. F., Hollenbach, D., Tielens, A. G. G. M., 2003, ApJ, **587**, 278–311.

York, B. A., Ellison, S. L., Lawton, B., Churchill, C. W., Snow, T. P., Johnson, R. A., Ryan, S. G., 2006, ApJ, **647**, L29–L32.

List of Figures

1.1 The Milky Way 7

1.2 Reaction pathway for an exothermic reaction with and without an activation barrier. 10

1.3 λ5780 strength as a function of E_{B-V}. Figure from Herbig (1993). . . 17

2.1 Basic light path for a reflecting telescope and spectrograph. 21

2.2 CCD images with and without fringing. 27

2.3 Synthetic spectral feature outlining key defining parameters. 30

3.1 Photographic plate images of Ca II lines seen towards HD 167264 from Adams (1943). 32

3.2 Binary stars giving rise to different lines-of-sight through interstellar clouds. 35

3.3 Proper motion displacement of binary stars giving rise to very slightly different lines-of-sight through interstellar clouds. 36

3.4 Overlaid profiles of λ6614 towards ρ Oph A, B, C and DE. 38

3.5 An example division of ρ Oph A and B λ6614 spectra. 39

3.7 λ4726 towards ρ Oph A, B, C and DE and select spectral ratios. . . . 44

3.8 λ4734 towards ρ Oph A, B, C and DE and select spectral ratios. . . . 45

3.9 λ4964 towards ρ Oph A, B, C and DE and select spectral ratios. . . . 46

3.10 λ4984 towards ρ Oph A, B, C and DE and select spectral ratios. . . . 47

3.11 $\lambda 5170$ towards ρ Oph A, B, C and DE and select spectral ratios. . . . 48

3.12 $\lambda 5418$ towards ρ Oph A, B, C and DE and select spectral ratios. . . . 49

3.13 $\lambda 5512$ towards ρ Oph A, B, C and DE and select spectral ratios. . . . 50

3.14 $\lambda 5541$, $\lambda 5544$ and $\lambda 5546$ towards ρ Oph A, B, C and DE and select spectral ratios. 51

3.15 $\lambda 5780$ and $\lambda 5797$ towards ρ Oph A, B, C and DE and select spectral ratios. 52

3.16 $\lambda 5850$ towards ρ Oph A, B, C and DE and select spectral ratios. . . . 53

3.17 $\lambda 6090$ towards ρ Oph A, B, C and DE and select spectral ratios. . . . 54

3.18 $\lambda 6196$ towards ρ Oph A, B, C and DE and select spectral ratios. . . . 55

3.19 $\lambda 6270$ towards ρ Oph A, B, C and DE and select spectral ratios. . . . 56

3.20 $\lambda 6284$ towards ρ Oph A, B, C and DE and select spectral ratios. . . . 57

3.21 $\lambda 6376$ and $\lambda 6379$ towards ρ Oph A, B, C and DE and select spectral ratios. 58

3.22 $\lambda 6614$ towards ρ Oph A, B, C and DE and select spectral ratios. . . . 59

3.23 $\lambda 6660$ towards ρ Oph A, B, C and DE and select spectral ratios. . . . 60

3.24 Plots of the ratios of $\lambda 5418$ in 2004 and 2005 and their ratio. 63

3.25 Plots of the ratios of $\lambda 5493$ in 2004 and 2005 and their ratio. 64

3.26 Plots of the ratios of $\lambda 5512$ in 2004 and 2005 and their ratio. 65

3.27 Plots of the ratios of $\lambda 5541$, $\lambda 5544$ and $\lambda 5546$ in 2004 and 2005 and their ratio. 66

3.28 Plots of the ratios of $\lambda 5780$ and $\lambda 5797$ in 2004 and 2005 and their ratio. 67

3.29 Plots of the ratios of $\lambda 5850$ in 2004 and 2005 and their ratio. 68

3.30 Plots of the ratios of $\lambda 6090$ in 2004 and 2005 and their ratio. 69

3.31 Plots of the ratios of $\lambda 6196$ and $\lambda 6203$ in 2004 and 2005 and their ratio. 70

3.32 Plots of the ratios of $\lambda 6270$ in 2004 and 2005 and their ratio. 71

3.33 Plots of the ratios of $\lambda 6284$ in 2004 and 2005 and their ratio. 72

3.34 Plots of the ratios of λ6376 and λ6379 in 2004 and 2005 and their ratio. 73

3.35 Plots of the ratios of λ6614 in 2004 and 2005 and their ratio. 74

3.36 Plots of the ratios of λ6660 in 2004 and 2005 and their ratio. 75

3.37 Enlargement of the λ6614 ρ Oph B/A ratios in 2004 and 2005. 76

3.38 Enlargement of the λ6614 ρ Oph C/A ratios in 2004 and 2005. 77

3.39 Enlargement of the λ6614 ρ Oph DE/A ratios in 2004 and 2005. . . . 78

3.40 Enlargement of the λ6614 ρ Oph C/DE ratios in 2004 and 2005. . . . 79

3.41 Additional ρ Oph C/B and DE/B ratios of λ6614. 81

3.42 Enlargement of the λ6614 ρ Oph C/B ratios in 2004 and 2005. 82

3.43 Enlargement of the λ6614 ρ Oph DE/B ratios in 2004 and 2005. . . . 83

3.44 Comparison of the 2004 and 2005 seeing profiles for ρ Oph A and B. . 85

3.45 Comparison of the original 2004 λ6614 spectrum with a version 'degraded' to the lower 2005 spectral resolution. 86

3.46 Enlarged λ6614 ρ Oph B / A ratios from 2004 simulating the increased 'contamination' in 2005. 87

3.47 K I and Na I D spectra towards ρ Oph A, B, C and DE in 2004 and 2005. 90

3.48 K I and Na I D spectra towards β Sco in 2004 and 2005. 92

3.49 K I spectra towards ν Sco in 2004 and 2005. 93

3.50 Na I D spectra towards ν Sco in 2004 and 2005. 94

3.51 Plots of summed equivalent width pairs of select 'C_2' DIBs. 95

3.52 Combined profiles of λ4726, λ4734, λ4964 and λ4984 towards ρ Oph A and B. 97

3.53 Combined profiles of , λ5170, λ5176 λ5418, λ5541, λ5544 and λ5546 towards ρ Oph A and B. 98

3.54 Correlation plot for 22 DIB equivalent widths in the ρ Oph suite of stars. 103

3.55 Correlation plot for 22 DIB equivalent widths in the ρ Oph suite of stars with KW families marked. 104

3.56 Correlation plot for yellow/red DIB equivalent widths in a selection of stars. 106

3.57 Correlation plot for yellow/red DIB equivalent widths in a selection of stars highlighting strong correlations. 106

3.58 Atomic and molecular species plotted as a function of 'blue' DIB strengths. 112

3.59 Atomic and molecular species plotted as a function of 'blue' DIB strengths. 113

3.60 Atomic and molecular species plotted as a function of yellow/red DIB strengths. 114

3.61 Atomic and molecular species plotted as a function of yellow/red DIB strengths. 115

3.62 Comparison of the H I vs. W_{5780} and Ca I vs. W_{5780} relations. 121

3.63 Overview of atomic and molecular velocity components towards the ρ Oph stars. 124

3.64 Illustration (from Pan *et al.* (2005)) of the different density environments that atomic and molecular species occupy. 125

4.1 λ5780 strength as a function of N(H I) from Herbig (1993). 128

4.2 λ5780 strength as a function of $E_{B-V}$from Herbig (1993). 129

4.3 A representation of a QSO absorption line-of-sight with an intervening DLA. 131

4.4 Comparison of a reddened and un-reddened SDSS QSO spectrum. . . 137

4.5 SDSS images of the QSOs observed in this study. 138

4.6 SDSS spectrum and image of SDSSJ143701.20-010418.0. 142

4.7 IRAF screen grab of SDSSJ143701.20-010418.0 showing QSO and galaxy profiles. 143

4.8 λ5780, λ6284 and λ6614 spectra of SDSSJ143701.20-010418.0. . . . 144

4.9 SDSS spectrum and image of SDSSJ100943.55+052953.8. 145

4.10 λ4430 and λ5780 spectra of SDSSJ100943.55+052953.8. 146

4.11 SDSS spectrum and image of SDSSJ121911.23-004345.5. 147

4.12 λ4430 and λ5780 spectra of SDSSJ121911.23-004345.5. 147

4.13 SDSS spectrum and image of SDSSJ113702.03+013622.1. 148

4.14 λ4430 and λ5780 spectra of SDSSJ113702.03+013622.1. 149

4.15 SDSS spectrum and image of SDSSJ122608.02-000602.2. 150

4.16 IRAF screen grab of a slice through a CCD frame of SDSSJ122608.02-000602.2 showing the galaxy profile (left) and the QSO profile (right) together with the FORS2 acquisition image and approximate slit position. 150

4.17 λ4430 spectrum of SDSSJ122608.02-000602.2. 151

5.1 Hertzsprung-Russell diagram 156

5.2 Spectral energy distribution of a star with a disc 158

5.3 IRAS two-colour diagram showing the Lloyd Evans RV Tauri ‘Box’ . 160

5.4 Near-IR colour plot demonstrating the excess in the L-band for objects with discs. 161

5.5 Sample of targets selected by their IRAS colours. 163

5.6 Sample of targets selected by their near-IR 2MASS colours. 165

5.7 Sample SED plots demonstrating different excesses in K_s 166

5.8 Diagram to explain emission lines in spectra of stars with discs. . . . 174

5.9 Near-IR two colour plot showing the K_s excesses for the newly identified Na I D emission line stars. 175

5.10 Optical spectra of the four newly identified Na I D emission line stars. 177

5.11 SED plot for IRAS 13051-8408 incorporating optical, near-IR and mid-IR photometry. 178

5.12 SED plot for IRAS 09258-6125 incorporating optical, near-IR and mid-IR photometry. 178

5.13 HST images of proplyd PRC95-45c 179

5.14 Spectra of three possible Herbig Ae/Be stars. 180

5.15 Near-IR two-colour plot showing the K_s excesses for the candidate Herbig Ae/Be stars, Na I D emission line stars and Hα emission objects. 181

5.16 Optical, near and mid-IR photometry for all targets observed and normalised to a J-band magnitude. 183

5.17 $K_s - [12]$ values as a function of $[12] - [25]$ colour for 'exotic' targets and dusty Miras. 184

5.18 K_s-band excess compared with L-band excess for select targets. 185

List of Tables

1.1 Phases of the ISM 9

3.1 Overview of 2005 UCLES targets observed. 36

3.2 'Blue' DIBs studied in this work. 41

3.3 Yellow/red DIBs studied in this work. 42

3.4 ρ Oph DIB equivalent widths and atomic species column densities. . . 61

3.4 DIB strengths in ρ Oph stars 61

3.5 ρ Oph λ6614 TSS measurements 81

3.6 Fractional contamination of the ρ Oph A and B profiles in 2004 and 2005. 88

3.7 ρ Oph λ5780 and λ5797 TSS measurements 88

3.8 Equivalent width measurements of K I towards ρ Oph A, B, C and DE in 2004 and 2005 89

3.9 Equivalent width measurements of Na I D towards ρ Oph A, B, C and DE in 2004 and 2005 89

3.10 What am I 91

3.11 Equivalent width measurements of Na I D and K I towards β Sco in 2004 and 2005 91

3.12 Equivalent width measurements of Na I D and K I towards ν Sco in 2004 and 2005 93

3.13 'C_2' DIB splittings. 96

3.14 Krełowski and Walker DIB family groupings. 100

3.15 AMS DIB groupings 108

3.16 KW DIB groupings 109

3.17 Pan *et al.* (2004) atomic and molecular data 111

3.18 Pan *et al.* (2005) model values for the ρ Oph region. 117

3.19 Predicted C_2 strengths based upon relationship with CH and CH^+ (Federman *et al.* (1994)). 117

3.20 Total predicted C_2 column densities and observed values from Thorburn *et al.* (2003). 118

3.21 Total predicted C_2 column densities taking into account differences in CH distributions as explained in Pan *et al.* (2005). 119

4.1 VLT targets observed in program ID 077.C-0737 for this work. 139

4.2 Gratings available for use on the FORS2 spectrograph. 139

4.3 Targets observed with FORS2, gratings used and DIBs targeted. . . . 140

4.4 Predicted S/N requirements for DIB detections. 141

4.5 DIB strength limits for targets observed. 152

5.1 Diffraction gratings used on the grating spectrograph of the 1.9m Radcliffe telescope at the SAAO. 167

5.2 List of targets observed in 2004 and 2005 168

5.2 List of targets observed in 2004 and 2005 169

5.2 List of targets observed in 2004 and 2005 170

5.2 List of targets observed in 2004 and 2005 171

5.2 List of targets observed in 2004 and 2005 172

5.3 Na I D emission line stars identified during this study. 174

5.4 Table of candidate Herbig Ae/Be stars. 181

5.5 ‘Ordinary’ stars identified in this survey. 182